Devices, Structures, and Processes for Optical MEMS

Hyuck Choo

Electrical Engineering and Computer Sciences
University of California at Berkeley

May 5, 2007

Devices, Structures, and Processes for Optical MEMS

by

Hyuck Choo

B.S. (Cornell University) 1996
M.Eng. (Cornell University) 1998

A dissertation submitted in partial satisfaction of the

requirements for the degree of

Doctor of Philosophy

in

Engineering-Electrical Engineering and Computer Sciences

in the

Graduate Division

of the

University of California, Berkeley

Committee in charge:

Professor Richard S. Muller, Chair
Professor Jeffrey Bokor
Professor James R. Graham

Spring 2007

The dissertation of Hyuck Choo is approved:

Chair   **Date**

University of California, Berkeley

Spring 2007

Abstract

Devices, Structures, and Processes

for Optical MEMS

by

Hyuck Choo

Doctor of Philosophy in Electrical Engineering and Computer Sciences

University of California, Berkeley

Professor Richard S. Muller, Chair

High-precision microlenses have been fabricated utilizing hydrophobic effects and polymer-jet printing technology. The lenses are formed precisely at desired locations on a wafer using a polymer-jet system in which hydrophobic effects define the lens diameter and surface tension creates a high-quality optical surface. They have 200–1000-μm diameters and 343–7862-μm focal lengths. At 635 nm, wavefront aberrations (measured using a Shack-Hartmann sensor of $\lambda/100$ accuracy) are $\lambda/5$-$\lambda/80$, and the variation in focal length is less than 4.22%. Using WYKO NT3300, the maximum deviation of the surface profile from an ideal circle was measured to be approximately 0.15 μm for most cases (range ~ 0.05–0.23 μm). The average p-v optical-path-length-difference values were 0.14, 0.25, 0.33, and 0.46 μm for 200 μm-, 400 μm-, 600 μm-, and 1mm-diameter microlenses, respectively.

Using micromachining techniques, polarization beam splitters (PBS), important optical components to separate the orthogonal TE and TM components of light, have been batch-processed and characterized. The devices were fabricated from thin-film,

low-stress silicon nitride membranes and showed excellent performance. Measurements using NANO Deep-UV System showed that the final thickness of the membranes varied from 418.8 to 419.5 nm. Using a WYKO NT3300, the radius-of-curvature of a typical nitride membrane was measured to be 51 m: the membrane is virtually flat. Very good performance has been demonstrated by the new MEMS-PBS structures at 635 nm: extinction ratios (for reflected and transmitted light) of (21dB, 10dB), (21dB, 14dB), and (21dB, 16dB) for single-, double-, and triple-layer systems, respectively with corresponding insertion losses of 3, 10, and 13%.

A new, straightforward, CMOS-compatible, three-mask process is used to fabricate high-performance torsional microscanners driven by self-aligned, vertically offset comb drives. Both the moving and fixed combs are defined using the same photolithography mask and fabricated in the same device layer, a process allowing the minimum gap between comb fingers to be as small as twice the alignment accuracy of the photolithography process. The fabricated microscanners have torsional resonant frequencies between 58 Hz and 24 kHz and maximum optical-scanning angles between 8 and 48° with actuation voltages ranging from 14.1 to 67.2 $V_{ac\text{-}rms}$. The yields on two separate fabrication runs have been better than 70%. To demonstrate an application for these scanners, laser-ablation patterns suitable for ocular cornea surgery have been generated. First, a two-dimensional scanning system has been assembled by orienting, two identical microscanners at right angles to one another. Next, when driven by two 90° out-of-phase 6.01-kHz sine waves, the cross-coupled scanners produce circular patterns having radii fixed by the amplitude of the driving voltage. Then, a small pattern from the surface topography found on a US Roosevelt dime has been chosen and emulated to

generate a cumulative ablation pattern that compares favorably with similar emulations reported by earlier researchers who used larger, more-complicated ablation systems.

Various wavefront sensing techniques to evaluate their suitability for precisely characterizing high-order wavefront aberrations of large magnitude have been examined. An appropriate wavefront sensor must be able to characterize corneal scarring, tear film effects, LASIK flap wrinkles, and keratoconics and post-LASIK corneas. The following sensors are discussed: phase-shifting interferometry (including sub-Nyquist interferometry and two-wavelength interferometry), curvature sensing, phase-diversity method, lateral shearing interferometry, star test, Ronchi test, and knife-edge test. Their fundamental operating principles and theoretical limitations as well as their past and current wavefront-sensing abilities are presented and discussed.

An addressable array (5-by-5) of high-quality microlenses suitable for application in a Shack-Hartmann (SH) sensor in a micro-optical system has been demonstrated. Specific lenses in the array can be addressed using a new selection scheme (that we have designed, built, and tested) in which the mechanical resonant frequencies of individual lens-support carriages are varied. Thus, by changing the frequency of the drive voltage, only two electrical connections per row are required in the lens system to identify the selected lens by its resonating focal image. Using this lens-identification method will allow us to improve the dynamic range of SH sensors by a factor of 12-46 above values reported for conventional SH designs.

A MEMS-based, phase-shifting interferometer (MBPSI) that is much faster than conventional phase-shifting interferometers (PSI) has been demonstrated. The conventional interferometers use piezoelectric actuators to obtain phase-shifted signals.

In contrast, the MEMS-based system takes measurements using a comb-driven vertically resonating micromachined mirror that is illuminated by synchronized laser pulses (1 µsec duration at $\lambda = 660$ nm). The MBPSI employs a four-frame phase-shifting technique (four CMOS-imager frames for each profile measurement) at a rate of 23 profile measurements-per-second (43.5 msec per measurement). At this rate, the MBPSI can capture more than 700 PSI measurements of a time-varying phenomenon in a 30.5-second interval which compares to 1 measurement in 1 second in conventional systems. The MBPSI in Twyman-Green configuration has accurately tracked the fast-changing, transient motion of a PZT actuator, with a precision of $\pm \lambda/220$ ($\pm$ 3 nm). Measurements to check the repeatability of the system, performed in a 20-minute period, show that it is accurate to within $\pm$ 10 nm.

Signature: _____

Committee Chairman

Devices, Structures, and Processes for Optical MEMS

Copyright © 2007

by

Hyuck Choo

DEVICES, STRUCTURES, AND PROCESSES
FOR OPTICAL MEMS

by

Hyuck Choo

To my parents, my grandparents,

and

to my family, Inhwa and Seungheon

ACKNOWLEDGEMENTS

I would like to express my deepest appreciation to my advisor, Professor Richard S. Muller. I first got to know him through his renowned book on device physics – *Device Electronics for Integrated Circuits*, which kept me awake at night during my last year at Cornell University. As my research advisor, he has consistently provided guidance, support, and encouragement in the course of my PhD. His enthusiasm in MEMS and his caring personality always helped me stay highly motivated. He carefully revised (and also added many hyphens in) all the technical articles that we published and also thoroughly advised all my talks at conferences. I will always remember the great times that we shared together – snorkeling in Kona, Hawaii, tennis games in Hilton Head Island, presentation practice at 11pm in a hotel room, bike trip to the Richmond Marina, and his 70th birthday party (and the 40th year at UC Berkeley) for which many of his former students gathered and celebrated together. Moreover, as a senior in life, he has always been available to give me invaluable advice whenever I needed one. Together with the late Mrs. Joyce Muller, he has shown me and Inhwa (my wife) how happiness is "engineered" in one's life.

I would also like to express my sincerest gratitude to Professor Jeffrey Bokor. His courses in optics served as the foundation for my research, and his constructive criticism sharpened my research focus. I would not have gotten this far without his instruction, advice, and guidance. I also enjoyed working as a teaching assistant in his class. Taking and teaching his classes helped me embody my teaching philosophies and methods.

plan. Professor Howe has also been very supportive of us and our work in many occasions.

My EE199 students, Kishan Gupta and Katherine Yiu, have done outstanding work as undergraduate researchers. I have learned quite a bit from these young, highly talented students and also thank them for our lasting friendship.

I give my special thanks to Ruth Gjerde, Mary K. Byrnes, and Shareena Samson in the EECS administrative office. Ruth has always welcomed students with her warm personality and handled the administrative hassle with such grace that it will be very difficult to find a better successor. I also give my thanks to the BSAC administrative team: Tom Parsons, Helen Kim, Richard Lossing, and John Huggins. Their excellent administrative work greatly assisted me in carrying out my research.

I thank Professor Chenming Hu for superb device-physics courses and great help on my preliminary-exam preparation. His honorable work ethics and exemplary services to students have left lasting impression in my mind.

I wish to thank my former research advisor, Professor Clifford R. Pollock, at Cornell University for continual support and encouragement even after graduation. I hope my achievements at UC Berkeley have met his expectations.

I am deeply indebted to my parents and grandparents who have given me their unconditional love and support throughout my life. My wife, Inhwa, has been an endless reservoir of patience, love, and support in the course of my graduate studies. And, my son, Seungheon, who arrived in the midst of my graduate studies, has immeasurably boosted my morale with his cheerful doings. I am grateful to Inhwa and Seungheon. They will always be the source of my happiness.

Table of Contents

CHAPTER 1

Optical Properties of Microlenses Fabricated
Using Hydrophobic Effects and Polymer-Jet-Printing Technology

1.1 Introduction

Major opportunities have existed in optical microelectromechanical systems (MEMS), and despite the economic setback in the year 2002, concentrated research optical MEMS has been underway at many locations. However, most of the research reported thus far has been focused on activated-mirror-micro-optical systems, which have instantly recognizable applications in the display and fiber-optic-switching fields. Optical components other than activated mirrors must, however, be available for designers to produce micro-optical systems for other applications that are already of proven value in macro designs. Chief among the needed components are lenses with high optical quality that can be accurately formed and placed at specified locations in an optical system. For example, the ability to integrate high-quality microlenses onto optical-MEMS structures will serve as a foundation for MEMS-based optical applications such as Shack-Hartmann wavefront sensor with improved dynamic range [1] and more advanced endoscopic imaging systems with flexible magnifications and higher resolutions. In order to achieve these goals, the microlens-fabrication method must be highly repeatable and should provide an easy way to batch-fabricate high-quality microlenses on movable MEMS structures for various applications.

Microlenses have a wide range of potential applications such as imaging systems, optical communication networks, and miniaturized hybrid digital/optical computing

systems [2-4]. Up to present, several microlens-fabrication methods have been developed and used [5-8]. Binary-amplitude and binary-phase micro-Fresnel lenses, which show low theoretical diffraction efficiencies (limited to 10% and 41%, respectively) have been demonstrated [5]. Refractive microlenses have been in use for some time in various forms [6-8]. They have been fabricated by using photoresist-reflow method or gray-scale-mask photolithography technique. But, for these methods, adjusting the microlens radius or precisely controlling the reactive-ion etching process has been challenging. Therefore, a simpler yet more reliable fabrication method has been constantly demanded.

The fabrication of microlenses using surface tension with or without hydrophobic effects has attracted considerable research because of this method's potential applicability to various micro-optical systems [9-10]. Because of the vast amount of interest that the scientific community paid to this research subject, we occasionally come across researchers who claim that they have pioneered the microlens fabrication using surface tension. However, the credit for first reporting this method should be given to M. C. Hutely who, back in 1991, demonstrated the fabrication of microlenses based on regular, surface-minimizing shapes observed in liquids under the influence of surface tension [11-12]. Then in 1994-1996, Prof. George M. Whitesides of Harvard University utilized the method for more general applications (as known as self-assembly techniques) [13-14]. Using hydrophobic method, Prof. S. C. Esener's group reported dipping-method produced lenses in 2000 [15], but did not provide a reliable means to vary or control optical properties if, for example, several lenses at differing locations on a wafer or chip were needed in a microsystem. The dipping technique is especially cumbersome when

(as in the usual case) microstructures have already been fabricated onto the wafer surface. If, instead of dipping, a polymer-jet-printing technique is used without hydrophobic pattern definition, it is difficult to obtain uniform diameters or to build closely packed microlens arrays because uncured liquid polymer tends to flow and merge with adjacent microlens patterns [10]. Recent research described polymer-jet-printing of microlenses having a range of focal lengths for a single fixed diameter [16]. The authors mentioned the use of 'surface treatments,' but without fully describing the process.

In this chapter, a fabrication method for high-precision microlenses with excellent optical characteristics is discussed. Our method combines the strengths of two different fabrication methods that were reported earlier [17-18]. The desired lens diameter and locations are precisely determined by hydrophobic effects while the volume of the lens is accurately controlled by using a polymer-jet system. Then the surface tension creates a high-quality optical surface, and the deposited liquid polymer is cured using an UV lamp to form solid microlenses. This fabrication concept is graphically illustrated in Figure 1.1.
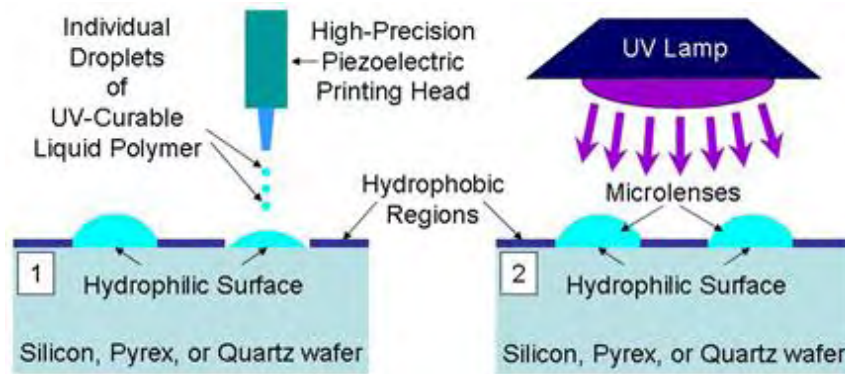
Figure 1.1   Microlens-fabrication concept

In this chapter, the fabrication method (the microlens-template fabrication and polymer-jet-printing setup/operation), the characterization methods for optical and physical properties of the fabricated microlenses, and the characterization results (optical

aberrations, focal lengths, f-numbers, and surface roughness) measured by using several precise physical- and optical-characterization systems including the atomic force microscope (AFM), a white-light interferometric profiler (WYKO NT3300), and the CLAS-2D Shack-Hartmann sensor will be discussed.

1.2 Microlens-Template Fabrication

To position and size microlenses precisely, we need to create hydrophilic circular regions at the desired locations on the surface of Pyrex and/or quartz wafers. The process can be divided into three major parts: Teflon coating, Teflon roughening, and Teflon patterning. The fabrication process is illustrated in Figure 1.2.
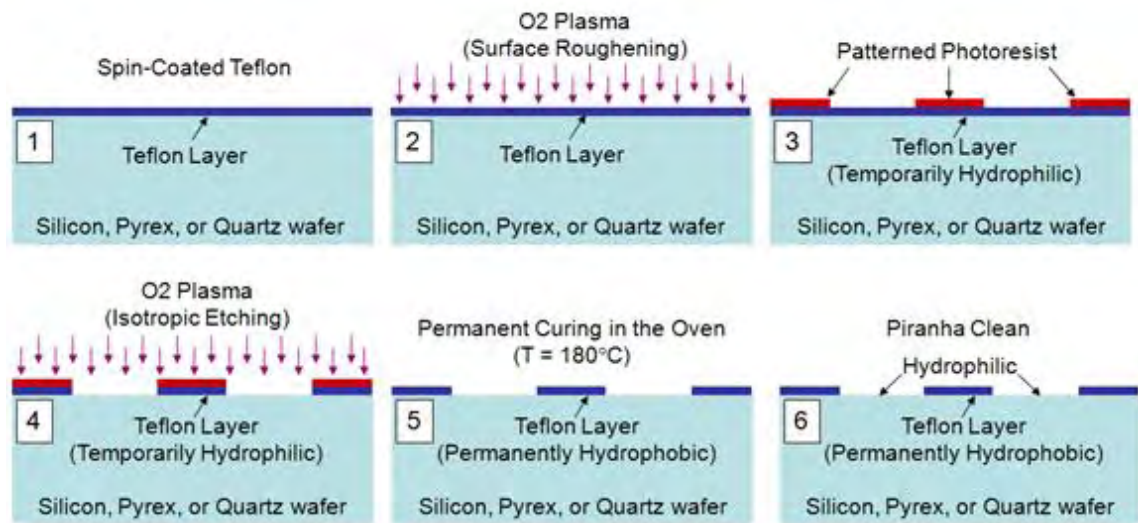
Figure 1.2   Microlens-template fabrication

1. Figure 1.2-1: The Teflon in liquid form is spin-coated on the wafer surface. The chosen liquid Teflon is CYTOP CTL-809M manufactured by Asahi Glass, Japan. This Teflon in liquid form is designed to show excellent adhesion to Pyrex and silicon surfaces and is highly resistant to virtually all chemicals, including the Baker's PRS-3000, photoresist developers, acetone, IPA, methanol, and various acids & bases. In

order to coat a 4-inch wafer, approximately 5 gm of CTL-809M is dispensed onto a pre-cleaned wafer. Then, the wafer is spun at 2000 rpm for 1 min on the manual spinner, followed by soft-bake at 100 °C for 90 seconds on a hotplate. (Please refer to Table 1.1 for coated-Teflon-layer thickness vs. coating-spin speed.) This yields a 1-μm thick Teflon layer on the wafer.

2. Figure 1.2-2: After completing the step 1, the Teflon layer is very hydrophobic (contact angle = 135°), making it impossible to coat it with photoresist. Hence we need to modify the surface property of the Teflon layer: convert the hydrophobic layer into a temporarily hydrophilic layer. This can be achieved by a "surface modification" process in an O_2-plasma etcher [19]. Table 1.2 shows how the contact angle changes with respect to the roughening-process duration. For our purpose, we used oxygen plasma at P = 50W for 30-second in the Technics-C plasma etcher. After the surface treatment, the contact angle becomes 104.1°, which makes it possible to coat the Teflon surface with photoresist.

3. Figure 1.2-3: We coat the treated Teflon surface with photoresist (Shipley's OiR 897-10i) with thickness of 2μm followed by softbake at 90°C for 1 minute and then perform photolithography. The same exposure and development conditions used to process the photoresist layers coated on bare silicon surfaces can be used.

4. Figure 1.2-4: Next, using the photoresist layer as a masking layer, we etch and pattern the Teflon layer using the isotropic oxygen plasma in the Technics-C plasma etcher (Power = 50W, Time = 7 minutes).

5. Figure 1.2-5: After removing the remaining photoresist with acetone or the Baker's PRS-3000, the wafer is placed inside a 200-°C oven for an hour in order to cure the

Teflon layer permanently. After this step, the Teflon layer exhibits surface-contact angles larger than 150°, which is an extreme hydrophobic property.

6. Figure 1.2-6: Finally the completed microlens templates are cleaned in the 4:H_2SO_4/1:H_2O_2 bath for 10 minutes. This removes any organic residues (such as photoresist remnants) left on the wafer surface and also greatly improves the hydrophilic property of the areas (quartz surfaces) on which microlenses will be formed.

Occasionally quartz and Pyrex wafers can present adhesion problems: the coated Teflon film may come off the wafer surface very easily. In order to prevent this, a very thin layer of PSG/LTO (≤ 0.1 μm) can be deposited and annealed on the quartz and Pyrex wafers before coating them with the Teflon.

Table 1.1 Thickness vs. the coating-spin speed for CTL-809M (measurements made by using the NANODUV with the following options: Positive PR on Si and n = 1.29; the measurements were made at its center and at locations, 2 cm from the outer edge of the wafer.)

Viscosity in cps	Spin Speed (in rpm)	Spin Duration (in seconds)	Center (μm)	Top (μm)	Left (μm)	Flat (μm)	Right (μm)
300	2000	30	1.19	1.14	1.14	1.14	1.14
300	3000	30	0.75	0.71	0.72	0.71	0.70
300	4000	45	0.52	0.50	0.50	0.50	0.50
300	8000	30	0.42	0.41	0.41	0.41	0.41
150	2000	30	0.55	0.54	0.54	0.54	0.54

Table 1.2 Contact angles vs. the O2-plasma-etch duration: Technics-C

Etch Duration (in sec)	0	30	60	90	120	150	180	210	240
Etch Depth (in Å)	0	1323	1540	3130	4513	6484	8041	9842	10321
Contact Angle (in degree)	135	104.1	105.3	104.2	102.7	111.4	119.2	117.1	118.2

Figure 1.3 below shows microlens templates patterned on a quartz wafer. Because the oxygen-plasma-etch process is isotropic, the process etches the Teflon layer both into the lateral and vertical directions. Hence, it is more advantageous to use a thinner Teflon layer in order to define the bases of the microlenses more precisely.
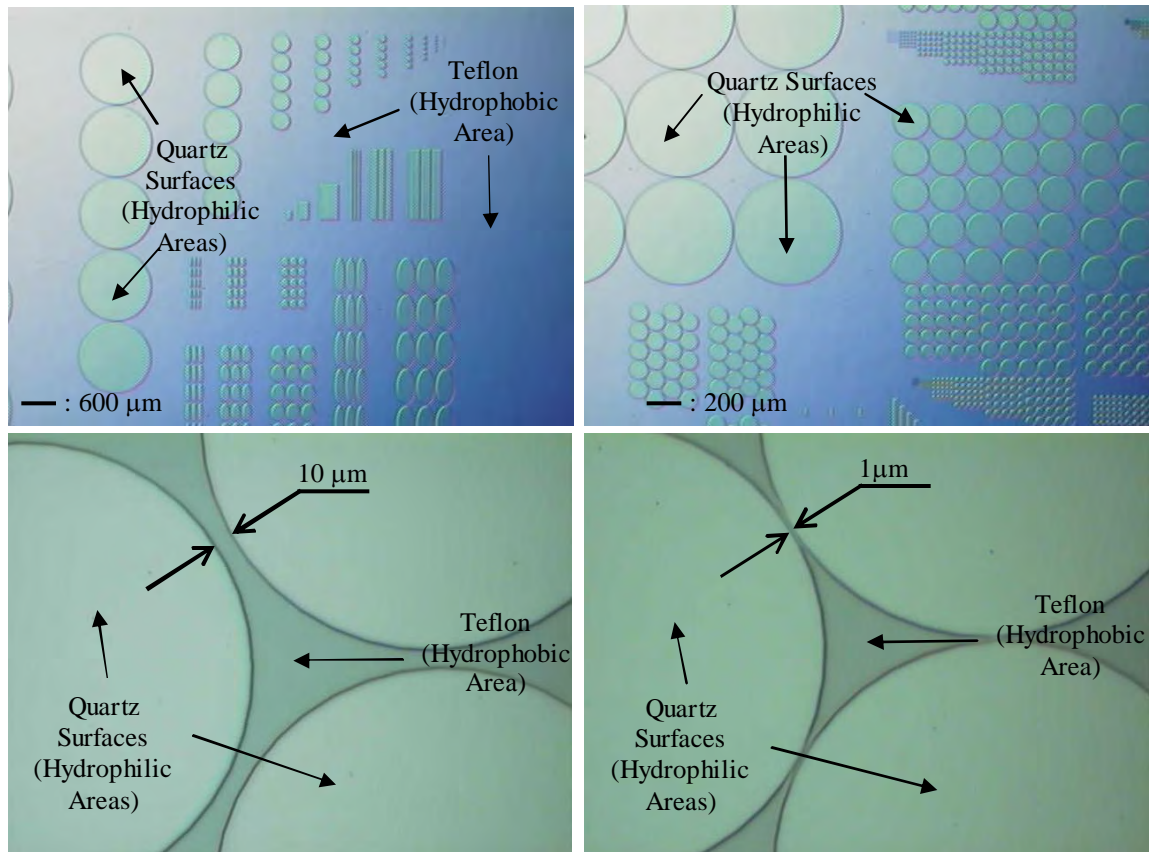
Figure 1.3   Microlens templates fabricated on a quartz wafer: A template contains base patterns for microlenses, microlens arrays, ovals, and rectangles.

Because the base patterns are defined photolithographically, it is possible to create very precisely aligned, narrowly spaced microlens arrays (1-µm gap) as shown in Figure 1.3. Such microlens arrays show significant improvements in optical fill-factors, up to 90%, which are considered to be very important parameters in optical-sensing systems and applications.

1.3 Polymer-Jet Printing Setups

The polymer-jet printing head is manufactured and sold by MicroFab, Inc. in Plano, Texas. The print head MJ-AT, which is shown in Figure 1.4, has been used in our setup. The schematic diagram of the setup is shown in Figure 1.5.
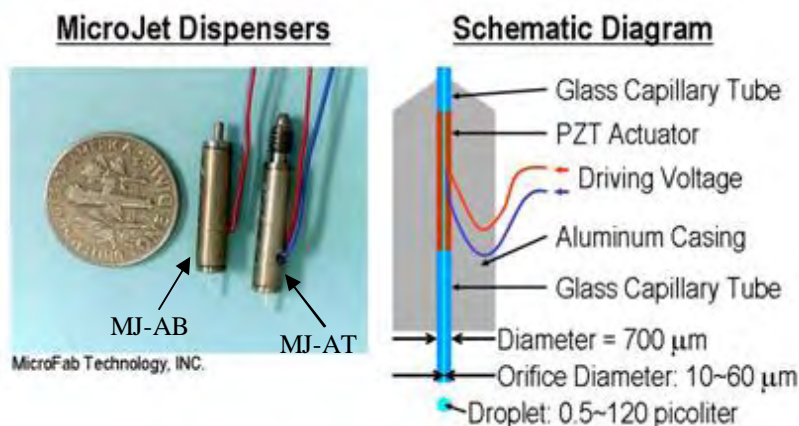
Figure 1.4 MicroJet dispensers (piezoelectric print heads): MJ-AT, which is used in our setup, has the threaded head, achieving more secure delivery of the printing fluid.
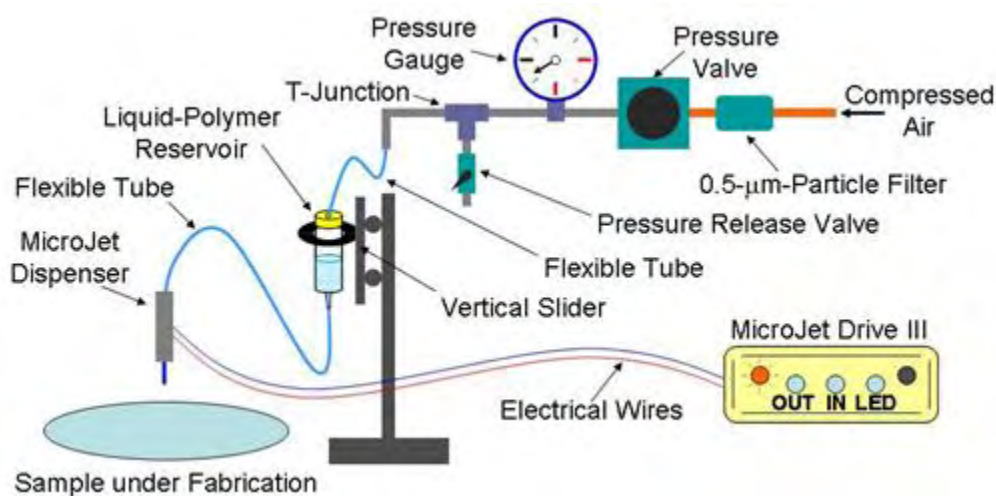
Figure 1.5 Schematic diagram of MicroJet-dispenser printing setup: Visual observation systems have been omitted from this diagram.

Figure 1.6 below shows the physical setup.
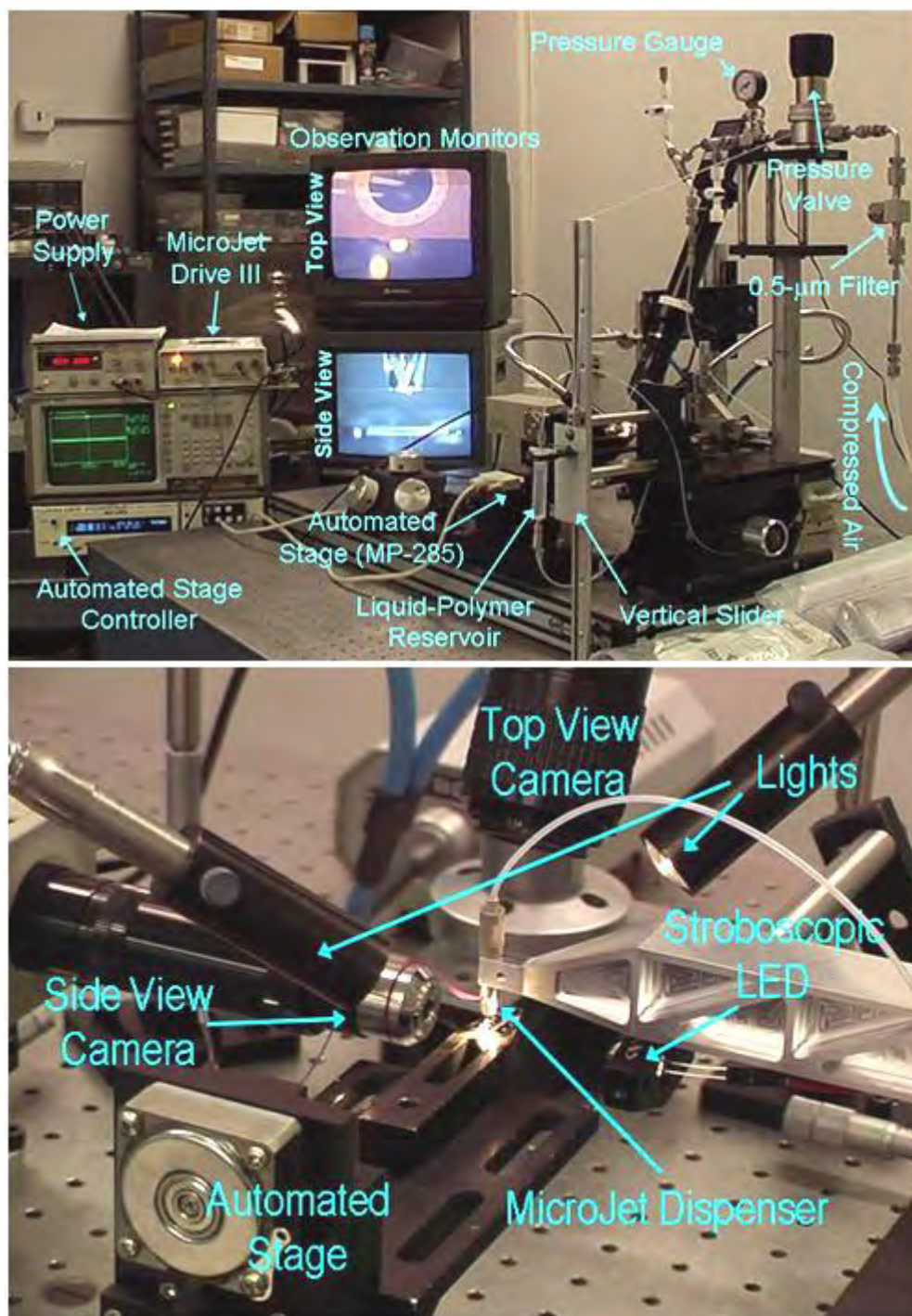
Figure 1.6   Pictures of the microlens-fabrication setup: The bottom picture shows the close-up picture of the area surrounding the MJ-AT.

The MJ-AT has the threaded head and is designed to work with the MINSTAC fittings

and tubes provided by The Lee Company in Westbrook, Connecticut. A 062 MINSTAC

tubing union (The Lee Company Part Number TMUA3201950Z) has been used to interface the MINSTAC fitting on the MJ-AT with a MINSTAC male coupling screw attached to a MINSTAC Teflon tubing (Figure 1.7).
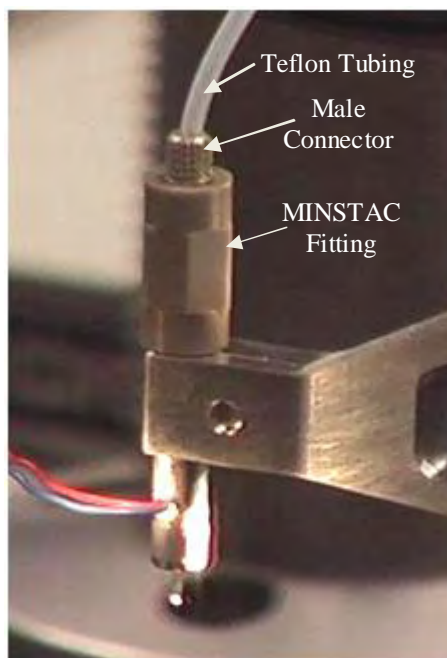
Figure 1.7   Picture of the MINSTAC-fitting assembly on the MJ-AT print head

Because the MINSTAC fittings and tubing are originally developed for use in aircraft, they require a set of expensive, specialized tools to assemble male/female screws on them. However, in order to save time and money, one can simply order Teflon tubing with pre-assembled MINSTAC male coupling screws.   Some suggestions for tubing with pre-assembled coupling screws are listed in Table 1.3. Please notice that the smaller inner-diameter requires more pressure to drive the liquid through the tubing while it reduces the amount of polymer wasted in the tubing (dead volume). For our setup, we chose the 60-cm-long tubing with the 0.032" inner-diameter (TUTC3216960L).

Table 1.3   Examples of MINSTAC pre-assembled tubing list

Part Number	Description
TUTC3216915L	15-cm long, 0.032" Inner-Diameter Tubing with Two 062 Fittings
TUTC3216930L	30-cm long, 0.032" Inner-Diameter Tubing with Two 062 Fittings
TUTC3216960L	60-cm long, 0.032" Inner-Diameter Tubing with Two 062 Fittings
TUTC3216910D	100-cm long, 0.032" Inner-Diameter Tubing with Two 062 Fittings
TUTC1226930L	30-cm long, 0.012" Inner-Diameter Tubing with Two 062 Fittings
TUTC1226910D	100-cm long, 0.012" Inner-Diameter Tubing with Two 062 Fittings

Since the droplets are generated at rates between 1-20000 droplets per second, it is necessary to build a stroboscopic optical viewing system to monitor the proper operation of the apparatus. This is achieved by building the following simple viewing system shown in Figure 1.8. The LED (Super Red MV 9100 by Fairchild Semiconductor) is placed approximately one focal length (of the LED) away from the droplet position. A microscope objective lens (4X or 5X, PLAN quality) is used as an imaging lens. This is an inexpensive yet highly effective solution for building a high-quality imaging system.
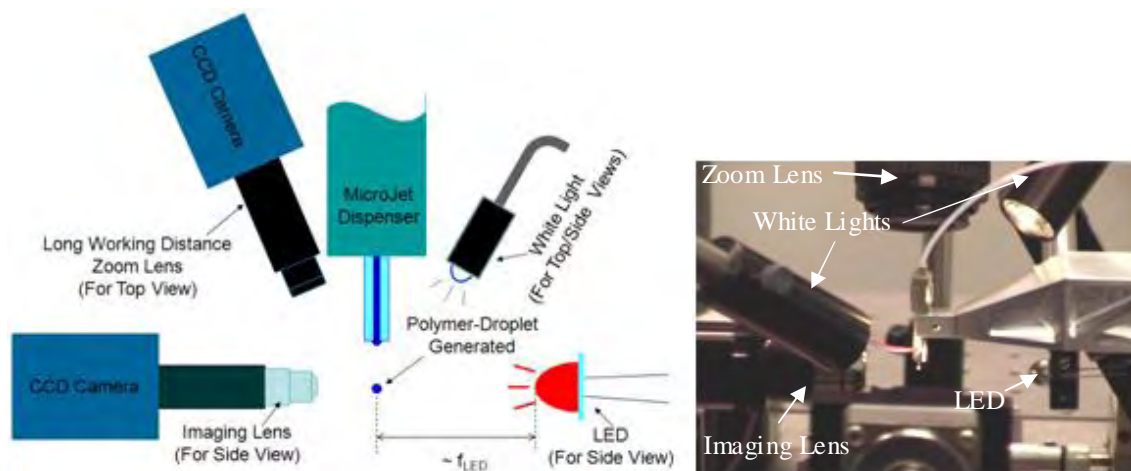
Figure 1.8   Optical viewing setup for observing MicroJet-droplet generation

It requires an extremely low level of pressure (on the order of a few mbar) to drive the liquid (lens material) from the reservoir to the MJ-AT print head. Since a digital/analog pressure controller that can achieve such a fine level of pressure is very expensive and rare, the best option is to use a slight difference in the height (and thereby

utilizing the gravitational force) to make the delivery. So the reservoir was mounted on a vertical slide as shown in Figure 1.9, and its height was adjusted in order to apply the proper level of pressure.

There is no particle filter integrated onto the reservoir because attaching one in the delivery path makes it very difficult to control the pressure through the delivery path. Hence the liquid that will be poured into the reservoir was filtered beforehand. Using a 0.45-µm Pall-Gelman Nylon-Disc filter (Pall Corporation, East Hills, New York) has proven to be sufficient because the inner diameters of the orifices at the printing end of MJ-ATs range between 10-60 µm. When using a disc particle filter, one must be aware that a disc filter releases a large amount of debris (originated from the filtering fibers) into the filtered liquid on its first use. Hence, it is important to run sufficient amount (approximately 1 liter) of clean dummy liquid such as acetone or distilled water through the disc filter before starting to use it to purify the lens material that will be poured into the reservoir.

The volumes of the droplets generated by MJ-ATs with larger orifices tend to be larger than those generated by MJ-ATs with smaller orifices. A smaller orifice would provide a better step-volume resolution for microlens-fabrication process, but it may result in more frequent blockage at the printing tip. In our setup, we chose a MJ-AT with a 40-µm orifice because it gives a good balance between the droplet-volume resolution and ease of maintenance.
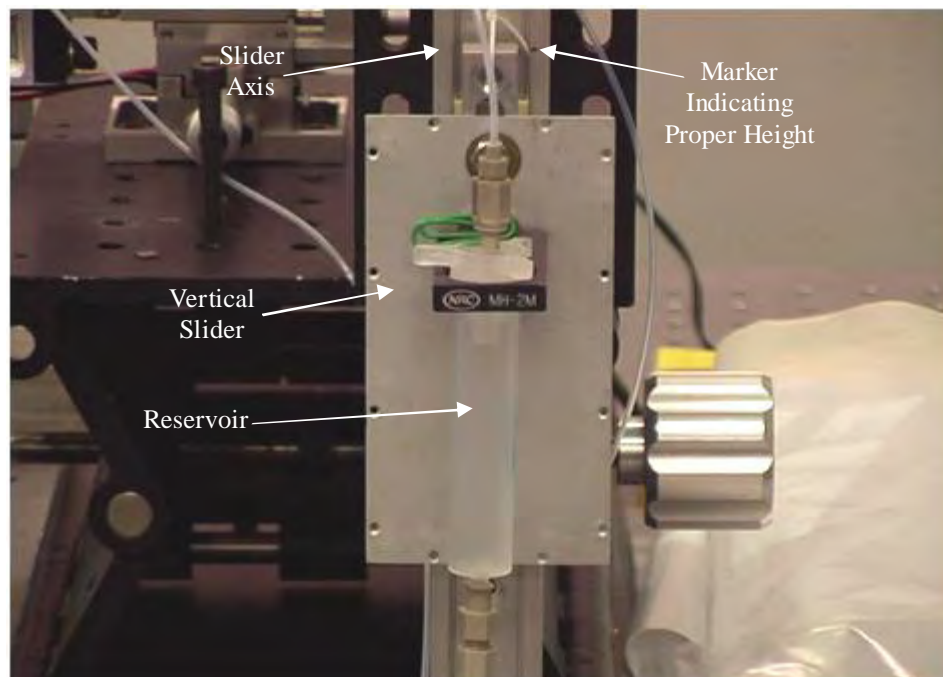
Figure 1.9   Reservoir mounted on a slider

The MJ-AT can handle liquid with viscosity up to 40 cps at a room temperature (20 °C), and this significantly limits the number of optical-purpose epoxies that can be used in the system. Our lens material used is an optically transparent epoxy called, "EPOTEK OG146" manufactured by Epoxy Technology, Inc., in Billerica, Massachusetts. It is the only off-the-shelf optical epoxy with viscosity less than 40 cps at 23 °C. To cure the epoxy, the company recommends to use a 100 mW/cm^2 UV-light source (wavelength between 300-400nm) for 1-2 minutes.

The OG146 shows excellent transmission rates of 82-96% for 350-449 nm and rates higher than 96% for 450-900 nm, which makes it highly desirable for optical applications. The MSDS of OG146 is available from the website of Epoxy Technology. Figure 1.10 shows the simulated prediction of the refractive index vs. wavelength for the OG146 before and after UV-curing.
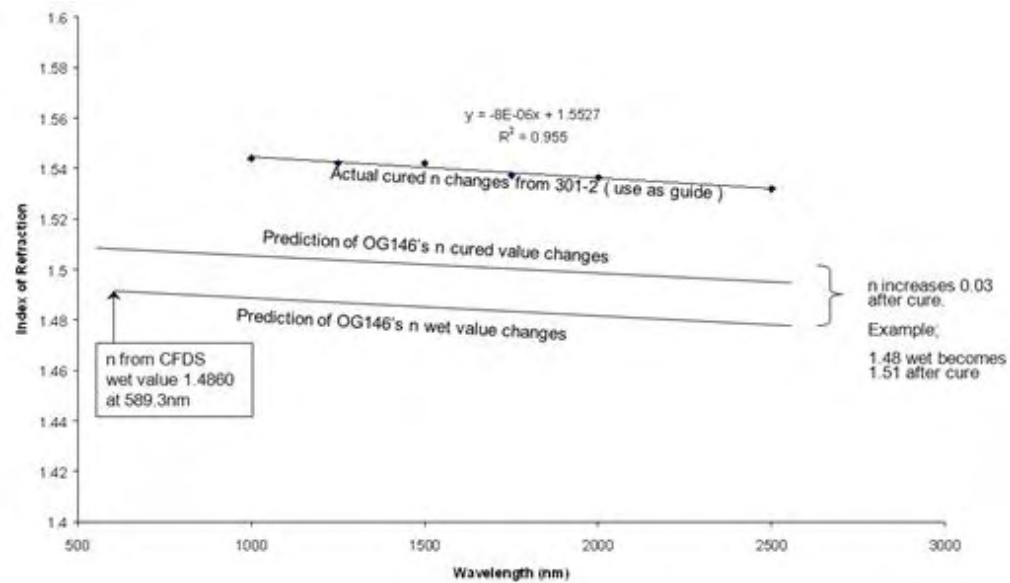
Figure 1.10   Predicted refractive index (n) of OG146 Vs. wavelengths before and after curing (Courtesy: Epoxy Technology)

1.4 Operation of MJ-AT: Printing Microlenses

In order to start printing microlenses, the liquid lens material must fill all the way from the reservoir to the tip of the MJ-AT print head. This can be achieved by adjusting the relative height of the reservoir with respect to the tip of the MJ-AT While observing the liquid meniscus formed at the tip of the MJ-AT. The MJ-AT is driven by the periodic trapezoidal waves as shown in Figure 1.11. The LED is programmed to flash 200 μs after the ejection of the droplet. If stable dispensing is achieved, then the droplet will also appear stationary on the viewing screen.
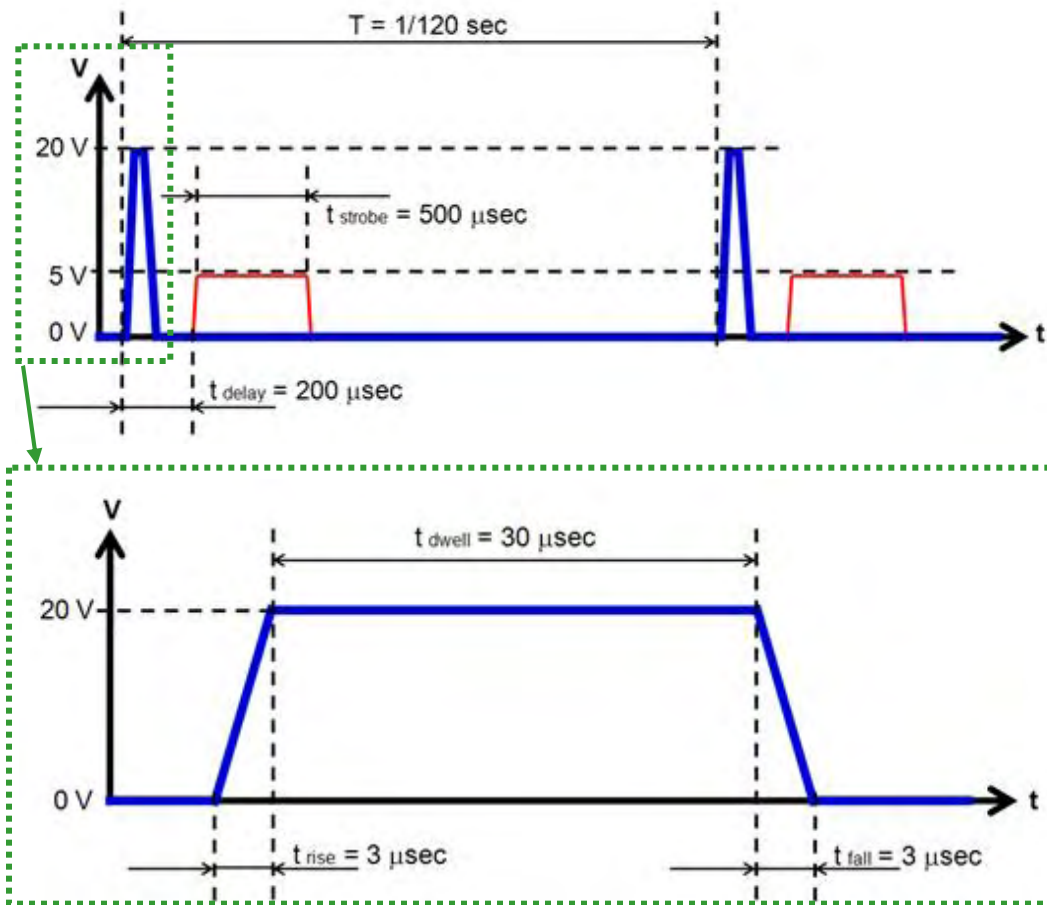
Figure 1.11   MJ-AT driving waveform for droplet generation: Top – periodic trapezoidal waveforms; Bottom – individual trapezoidal waveform

The optimal driving condition depends on the properties, especially viscosity, of the liquid being dispensed. The goal is to generate a very stable stream of clean individual droplets without satellite formation as shown on the left side of Figure 1.12 as well as in Figure 1.13. In order to calculate the volume of an individual droplet, we deposit a large number of droplets (usually 3000-5000 droplets) on the surface of a silicon wafer and measure its volume using a white-light interferometer. Then the volume is divided by the number of droplets dispensed. The volume of the individual droplet is measured to be 24 pL, and the diameter of the individual droplet, which can be calculated from the

individual volume, is 35.8 µm, which is slightly less than the inner diameter of the MJ-

AT's orifice (40 µm).
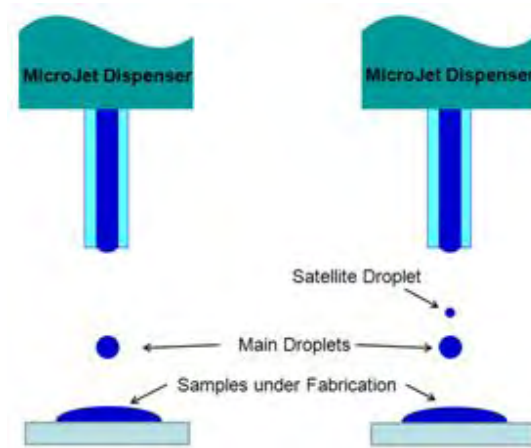
Figure 1.12   Clean droplet generation (left) and undesired satellite-droplet formation
(right)
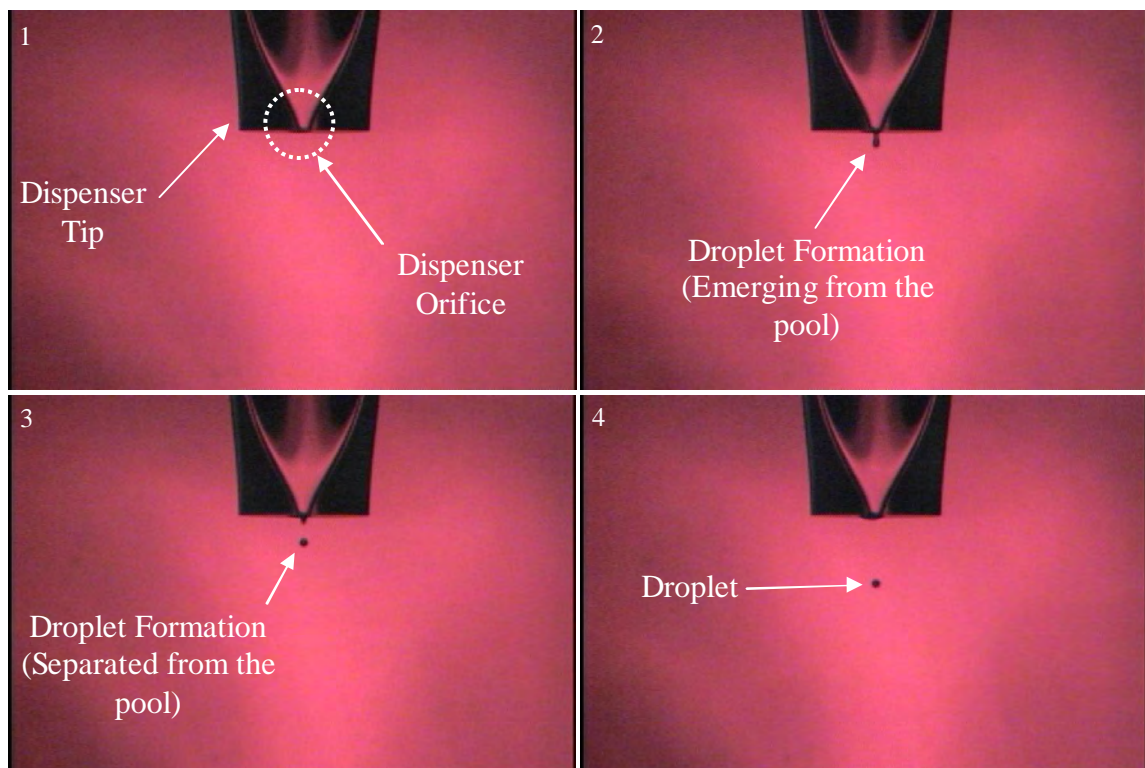
Figure 1.13   Sequential images of clean droplet formation captured by a stroboscopic
viewing system

Satellite formation mentioned earlier can cause fluctuation in droplet volume and makes

it difficult to achieve good repeatability for the microlens fabrication process since the

fluctuation in microlens volume will directly influence the optical properties of the microlens. If the satellite formation becomes problematic, then it is necessary to increase or decrease t_{dwell} in order to prevent it. Changing the driving voltage usually changes the volume of a droplet and has little effect on satellite formation.

The higher the driving voltage is, the larger the droplet becomes. The droplet size also depends on the ambient temperature because the polymer's viscosity decreases as the temperature increases and so does the volume of the droplet. Hence, it is necessary to make sure that the ambient temperature remains as stable as possible whenever microlenses are fabricated. Since our lab (173 Cory) was not equipped with an air conditioner until 2003, microlens fabrication was carried out between 10 pm – 9 am to improve the uniformity of the microlenses. The sequential images of the microlens-fabrication process are shown in Figures 1.14 and 1.15.
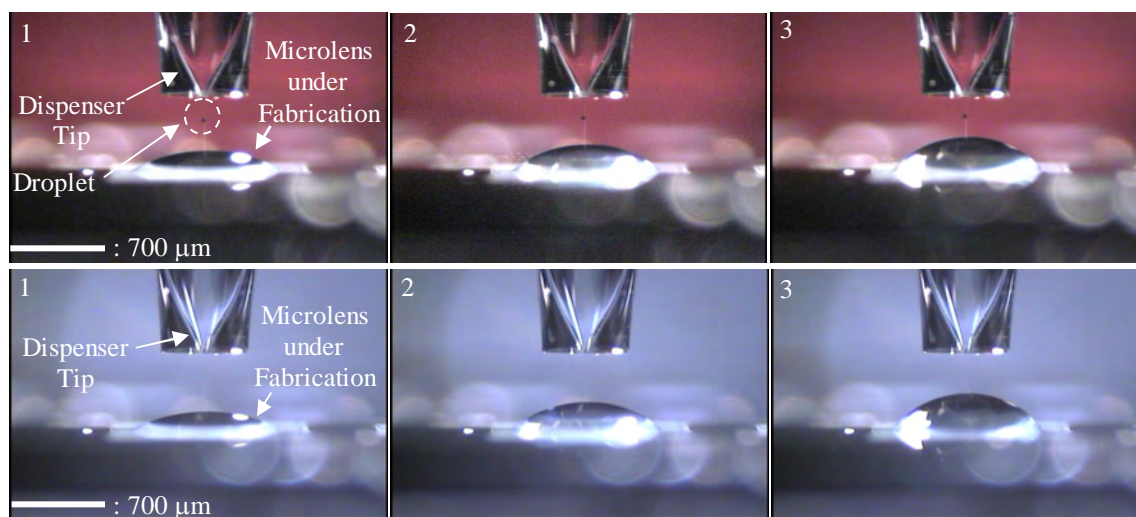
Figure 1.14 Observation of microlens fabrication: Top three images – combination of white-light and stroboscopic observation, which makes it possible to observe individual droplets being dispensed as well as the progress of microlens fabrication; Bottom three images – white-light observation
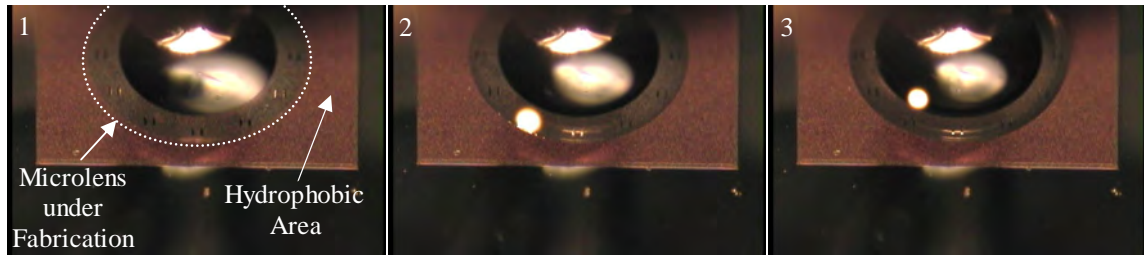
Figure 1.15 Top-view observation of microlens fabrication: One can clearly observe the change in the curvature of the microlens under fabrication as more lens material is added.

1.5 Physical and Optical Properties of Fabricated Microlenses

1.5.1 SEM Pictures of Various Microlenses Fabricated

Microlenses and microlens arrays of various sizes and properties have been fabricated, and, in this section, their scanning-electron-microscope (SEM) images are shown. For the analysis work, we concentrate on 200-µm, 400-µm, 600-µm, and 1000-µm diameter microlenses.
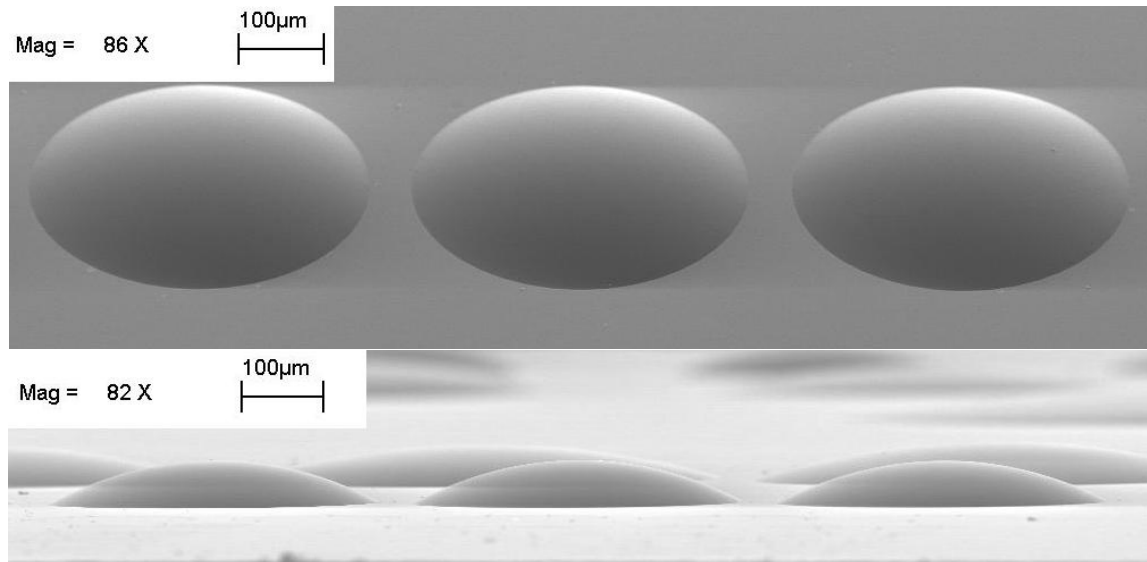
Figure 1.16 Three identical microlenses with base diameter of 400 µm, viewed at an angle (top) and from the side (bottom)
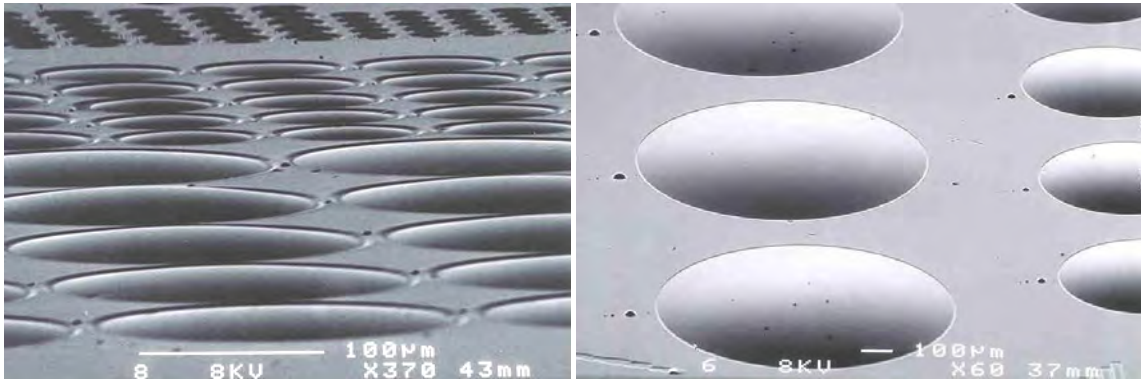
Figure 1.17 Left – Various microlens arrays of uniform microlenses; Right – Microlenses with base diameters of 1000 and 600 μm
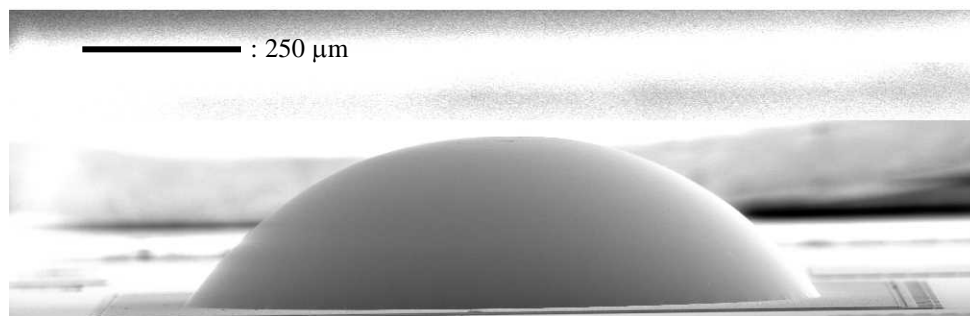
Figure 1.18 Side view of a microlens with a base diameter of 1000 μm
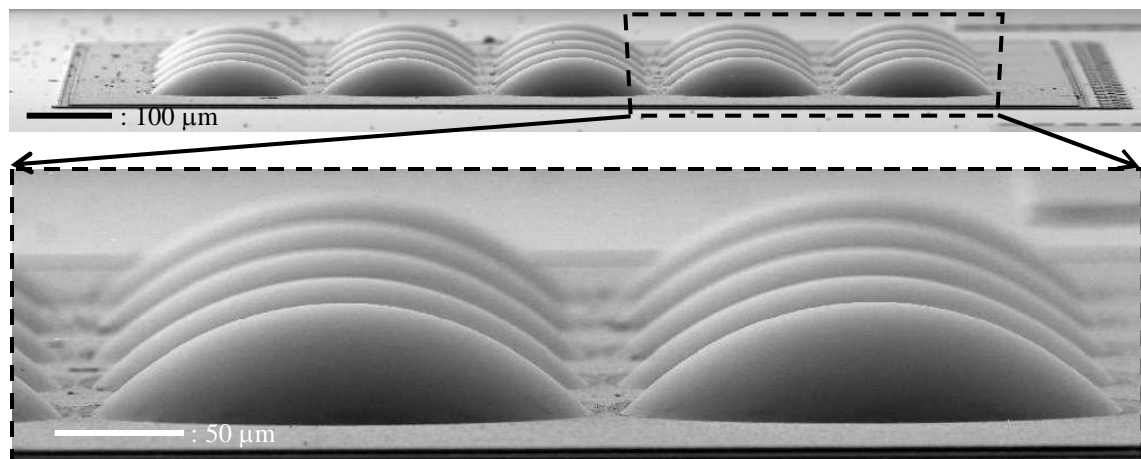
Figure 1.19 5-by-5 microlens array (base diameter = 200 μm, spacing between microlenses = 10 μm): In the SEM images, these microlenses in the array look extremely uniform.

1.5.2 Surface Roughness of Microlenses

The surface roughness of microlenses is an important property if the microlenses are to be used as imaging elements. Rough microlens surface can scatter incoming light,

and the light efficiency of the microlens becomes poor. The measurement using the DI AFM Nanoscope Dimension 3100, an atomic-force microscope (AFM), at the selected areas, showed that the surface roughness of our microlenses was measured to be less than 5 nm. This measurement result is in agreement with what other research groups have previously reported on the surface roughness of polymer microlenses fabricated using surface tension [9, 15]. Figure 1.20 shows the images of the microlens-polymer surface and high-temperature-annealed phosphosilicate glass (PSG) at the same magnification (×25000). From the images, it's clear that the surface of the polymer microlens is almost as smooth as that of the PSG.
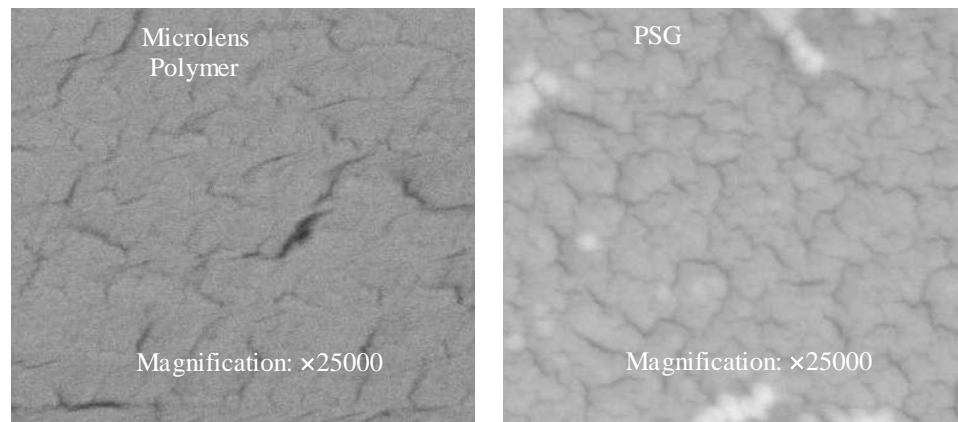
Figure 1.20   25000X SEM images of the surfaces of a microlens (left) and annealed phosphor-silicate glass (PSG) (right): The smoothness of the polymer surface is similar to that of PSG annealed at 950 °C.

1.5.3 Volume vs. Effective Focal Length (EFL)

We have created microlenses of different volumes and measured their focal lengths as a function of volume. The focal length of a microlens can be varied by controlling its volume. Figure 1.21 shows one such case, in which microlenses with a base diameter of 400 μm have different volumes, and consequently, they have different focal lengths.
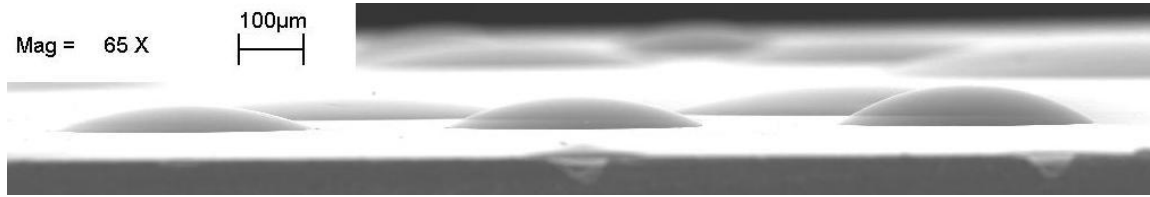
Figure 1.21 Microlenses with base diameter of 400 μm: three different volumes and focal lengths

To measure the effective focal lengths of different microlenses fabricated, we built a setup consisting of a laser source, optical fiber, automated stage with position readout, and a viewing system. The drawings in Figure 1.22 illustrate the measurement method. The optical fiber, which is connected to a laser diode, is mounted on an automated stage (not shown in Figure 1.22) with highly accurate distance-movement readout. First, the tip of the optical fiber is brought into contact with the top surface of the microlens along its optical axis. The initial position of the automated stage is noted by reading the numerical value off the stage's display. Then, by controlling the automated stage, the optical fiber is slowly moved away from the microlens until the light that emerges from the microlens becomes completely collimated (or the spot projected on the wall, which is ~ 6 meters away, is the smallest). The spot will be the smallest only if the tip of the optical fiber is precisely 1 EFL away from the microlens. Again, the final position of the automated stage is noted by reading the numerical value off the stage display. The difference between the initial and final positions is the effective focal length.
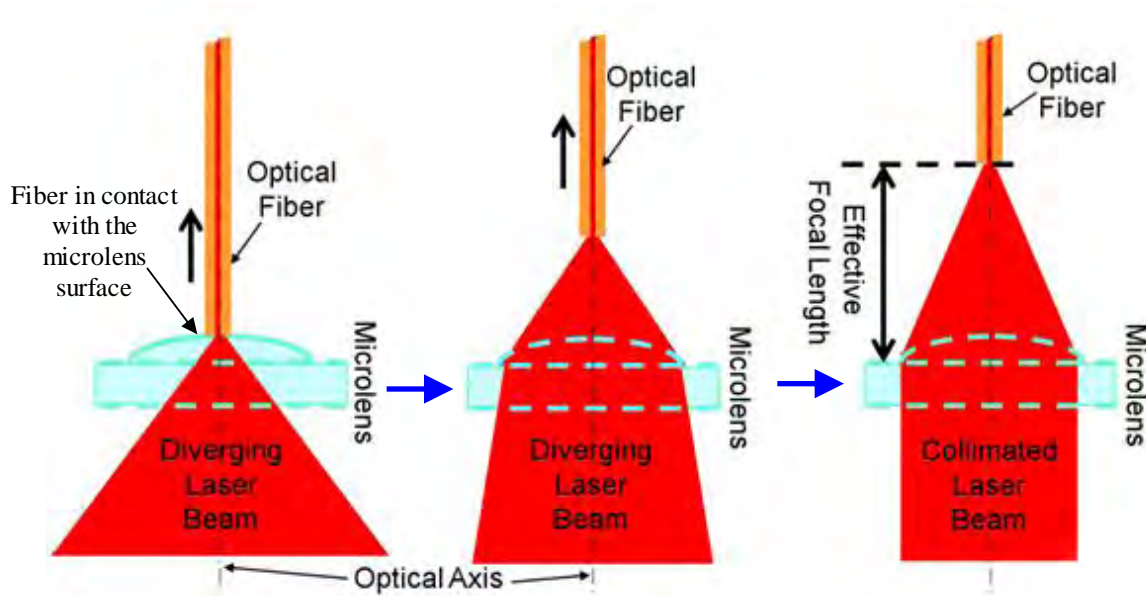
Figure 1.22   Method for measuring effective focal lengths: The optical fiber is mounted on an automated stage, which is not shown in the diagram.

The physical setup is shown in Figure 1.23.   The 3-degree-of-freedom-automated stage (Sutters MP285) in the setup has a travel range of ±12.5 mm (or 25 mm in one direction) and displays the position within ±0.04μm accuracy.   Figure 1.24 shows the measurement process in progress.   The CCD imager combined with the imaging lens and the display monitor plays important role in positioning the optical fiber.   To prevent scratches on the microlens surface, it is important to avoid that the optical fiber forcefully presses against the surface of the microlenses during measurement.   Also, the tip of the optical fiber, which is cleaved using the Fujikura CT-04B High-Precision Fiber Cleaver, is equally sensitive and fragile.   If the tip of the optical fiber is damaged by pressing against the microlens surface, then the fiber does not function as a point source anymore, and it becomes very difficult to make proper measurements.
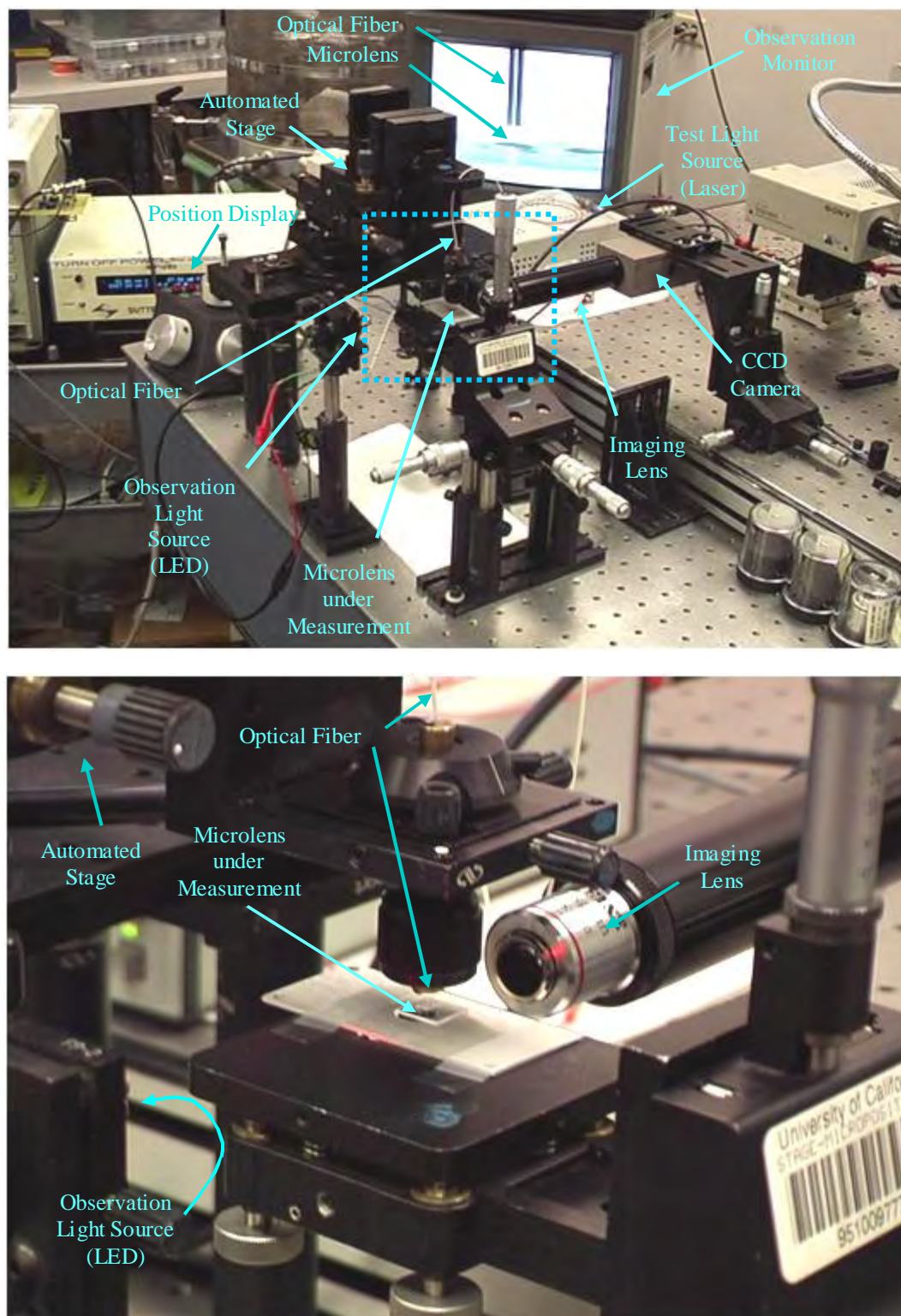
Figure 1. 23 EFL measurement setup: The bottom picture shows the detailed image of the area covered by the dotted rectangle in the upper picture.
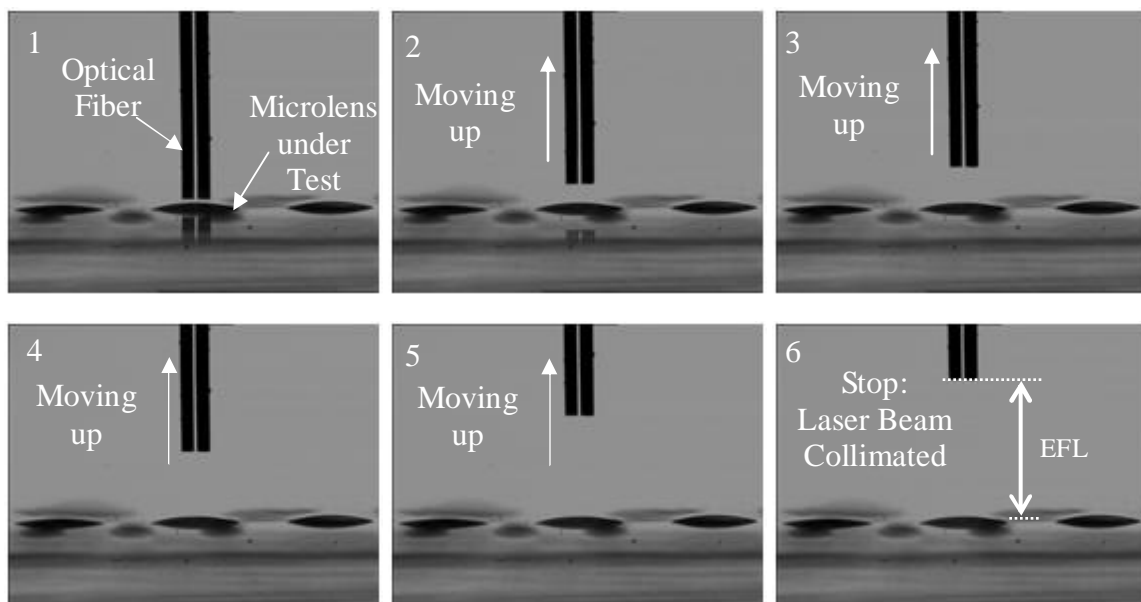
Figure 1.24   Pictures showing the measurements of effective focal lengths

The Figure 1.25 shows the distribution of the effective focal lengths measured from 200-μm, 400-μm, 600-μm, and 1000-μm diameter microlenses. As shown in Figure 1.25, we can obtain microlenses with focal lengths ranging from 0.34 to 7.86 mm, depending on the volume of the polymer dispensed as well as the base diameters of the microlenses.
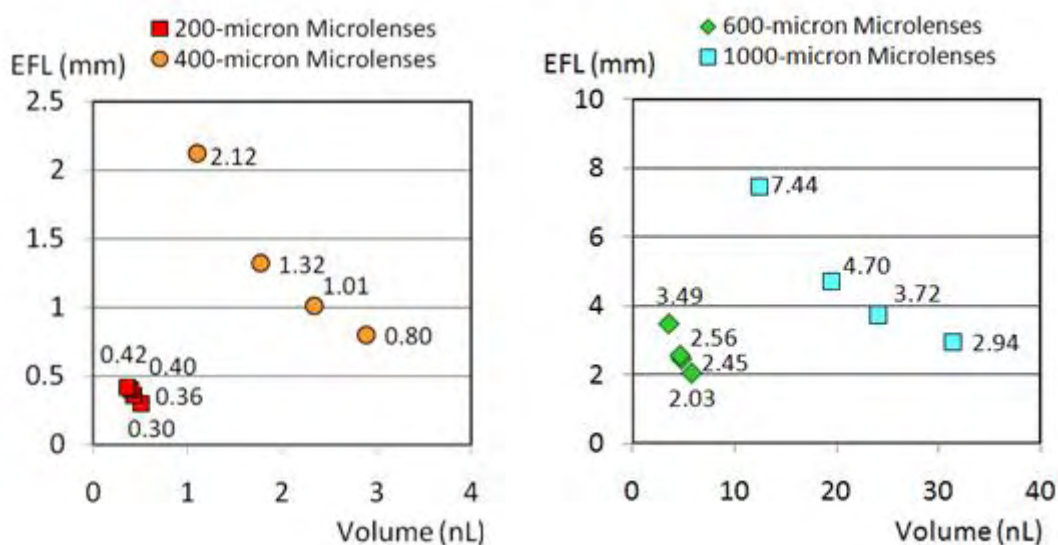
Figure 1.25   Volume vs. effective focal length for 200-μm, 400-μm, 600-μm, and 1000-μm diameter microlenses

The f-numbers range from 1.5-2.1, 2.0-5.5, 3.4-6.3, and 2.9-7.4 for 200 μm-, 400 μm-, 600 μm-, and 1 mm-diameter microlenses, respectively (Table 1.4). The values are calculated from the microlens base diameters and the corresponding focal lengths.

Table 1.4   Range of f-Number for microlenses with different base-diameters

Microlens Diameter	200 μm	400 μm	600 μm	1000 μm
Range of f-Number	1.5-2.1	2.0-5.3	3.4-5.8	2.9-7.4

1.5.4 Microlens Profile

We compared the surface profile of the microlenses to that of an ideal circle as shown in Figure 1.26.
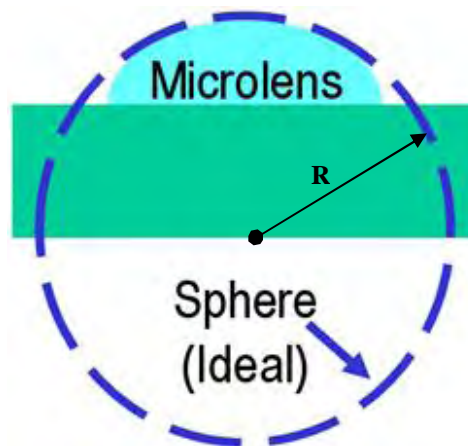
Figure 1.26   Comparison between ideal sphere and microlens surface profile

Having spherical profiles is not ideal for lenses in general because sphericity causes spherical aberration. Here we compare the microlens profiles to ideal spheres because spheres are mathematical objects that everyone is familiar with - Spheres can serve as good reference profiles.

Using WYKO NT3300 (a white light interferometer or an optical surface profiler), we first measure the profile of a microlens as shown in Figure 1.27. Figure 1.28 shows

the comparison between ideal and measured radii of curvatures. Areas defined by ≥ 90 %

of the microlens' base diameters (from the center) are measured and used for analysis.
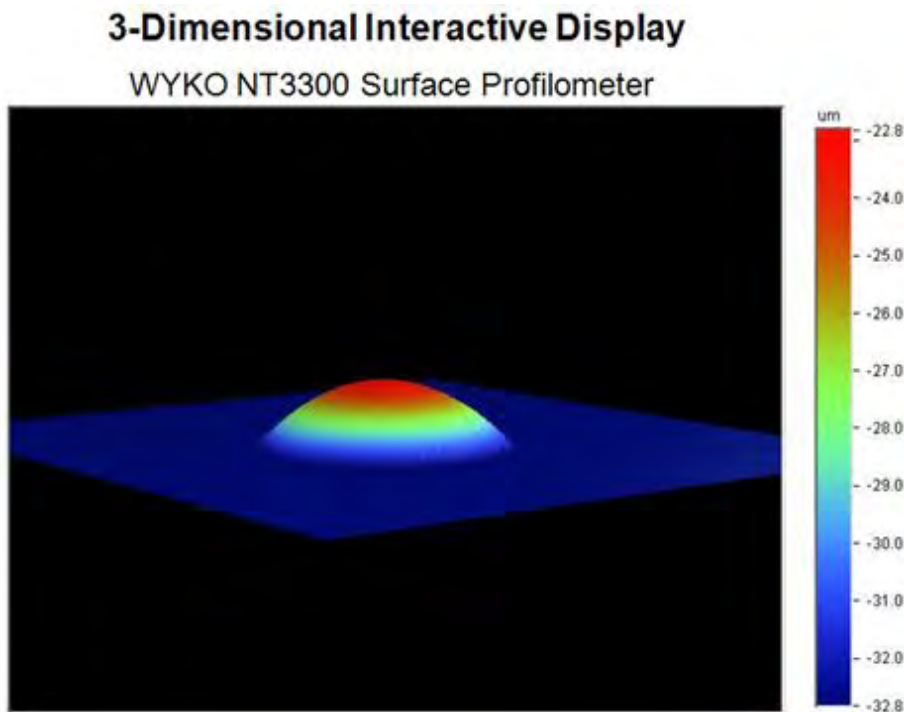
Figure 1.27   3-dimensional interactive display of a microlens-surface profile measured using WYKO NT330
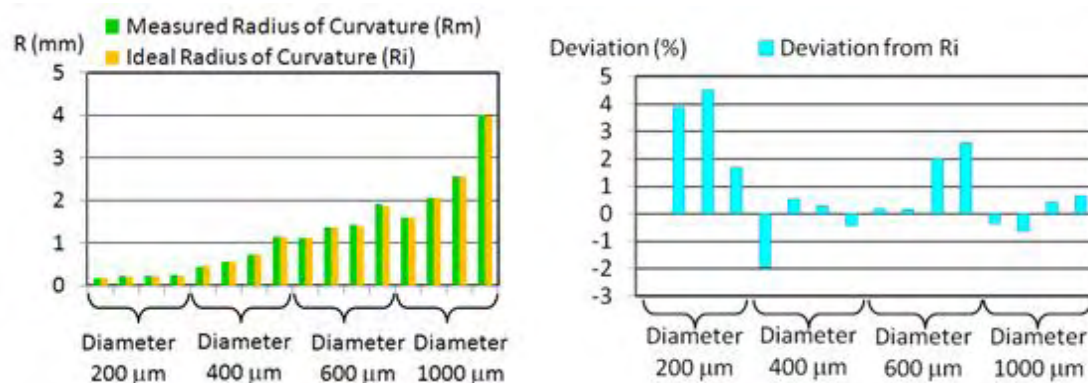
Figure 1.28   Comparison of ideal radii of curvatures (predicted by the volumes of the microlenses) to the measured radii of the microlens-surface profile: The deviation is less than 5 %.

Figures 1.29 shows 2-D view of the deviation of a 1000μm-diameter microlens profile

from an ideal sphere. The figure was generated by using the spherical-curvature-removal

option in WYKO's VISION32 program: Figure 1.29 shows the difference between the

microlens profile and the ideal spherical profile. Any changes in height are depicted by using different colors, and the deviation from an ideal sphere is extremely small because the color is highly uniform in the circular area.
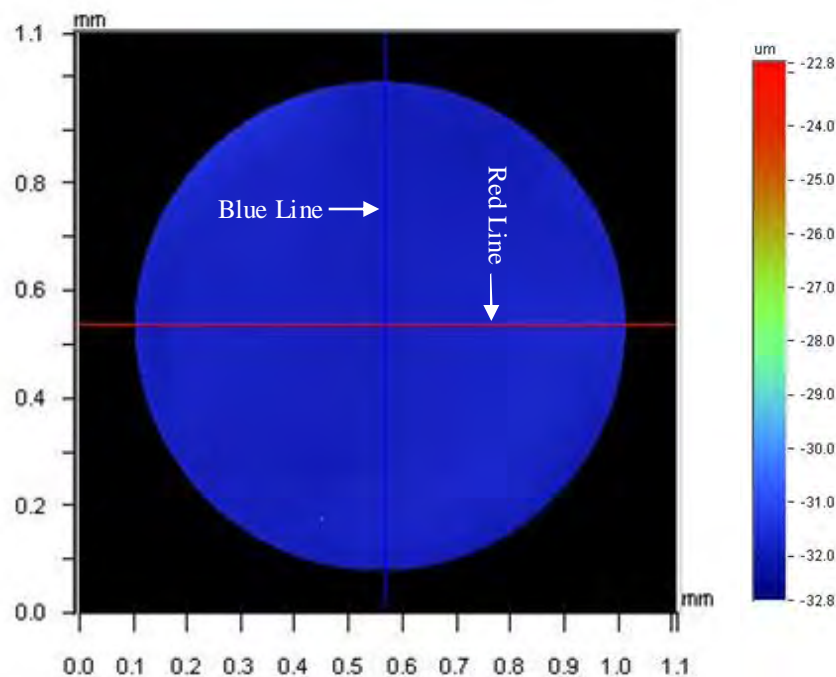
Figure 1. 29 2-D plot showing the deviation of the microlens-surface profile from an ideal sphere: It looks very flat.

Figure 1.30 shows the profiles of the circular area along the blue vertical and red horizontal lines (shown in Figure 1.29). The maximum deviation of the surface profile from an ideal circle was approximately 0.15μm for most cases (range ~0.05-0.23μm). Having a spherical profile may not be the best case for lenses due to the potential presence of spherical aberrations. However, this highly spherical profile implies that it is easy to model and predict the optical property of the polymer microlenses. Tables 1.5 – 1.8 summarize the properties of 200-μm, 400-μm, 600-μm, and 1000-μm diameter microlenses tested.
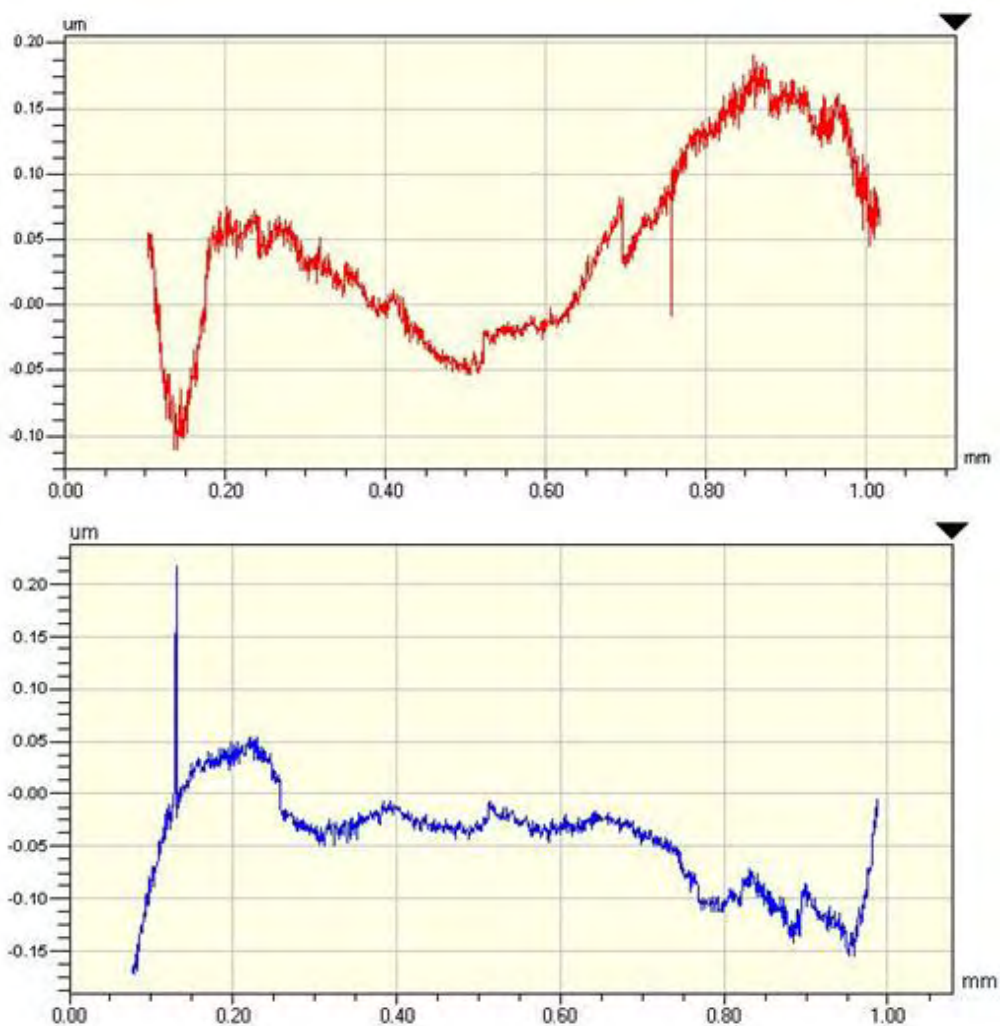
Figure 1.30   Cross-sections along the red and blue lines shown in Figure 1.29: The maximum deviation of the profile in each case is less than ±0.2 μm.

Table 1.5   Properties of 200-μm diameter microlenses

Lens Number	200-1	200-2	200-3	200-4
EFL (mm)	0.30	0.36	0.40	0.42
f-Number	1.5	1.8	2.0	2.1
Volume (nL)	0.51	0.43	0.40	0.36
Measured R of Curvature (μm)	175	215	232	242
Ideal R of Curvature (μm)	175	207	222	238
Deviation from Ideal R (%)	0.0	3.87	4.51	1.68

Table 1.6   Properties of 400-µm diameter microlenses

Lens Number	400-1	400-2	400-3	400-4
EFL (mm)	0.80	1.01	1.32	2.12
f-Number	2.0	2.5	3.3	5.3
Volume (nL)	2.89	2.34	1.77	1.10
Measured R of Curvature (µm)	447	566	733	1140
Ideal R of Curvature (µm)	456	563	731	1145
Deviation from Ideal R (%)	-1.97	0.53	0.27	-0.44

Table 1.7   Properties of 600-µm diameter microlenses

Lens Number	600-1	600-2	600-3	600-4
EFL (mm)	2.03	2.45	2.56	3.49
f-Number	3.4	4.1	4.3	5.8
Volume (nL)	5.84	4.81	4.73	3.52
Measured R of Curvature (µm)	1120	1350	1420	1920
Ideal R of Curvature (µm)	1118	1348	1392	1872
Deviation from Ideal R (%)	0.18	0.15	2.01	2.56

Table 1.8   Properties of 1000-µm diameter microlenses

Lens Number	1000-1	1000-2	1000-3	1000-4
EFL (mm)	2.94	3.72	4.70	7.44
f-Number	2.9	3.7	4.7	7.4
Volume (nL)	31.48	24.12	19.58	12.47
Measured R of Curvature (µm)	1600	2050	2560	4010
Ideal R of Curvature (µm)	1606	2063	2550	3984
Deviation from Ideal R (%)	-0.37	-0.63	0.39	0.65

1.5.5. Microlens Uniformity

In order to test the uniformity of the microlens-fabrication process, we fabricated 20 microlenses - ten identical 400-µm and ten identical 600-µm microlenses. For 600-µm microlenses, 250 droplets were dispensed to make each microlens and then cured. For 400-µm, 125 droplets were dispensed for each microlens and then cured. Figure 1.31 shows the EFLs of these 20 microlenses.
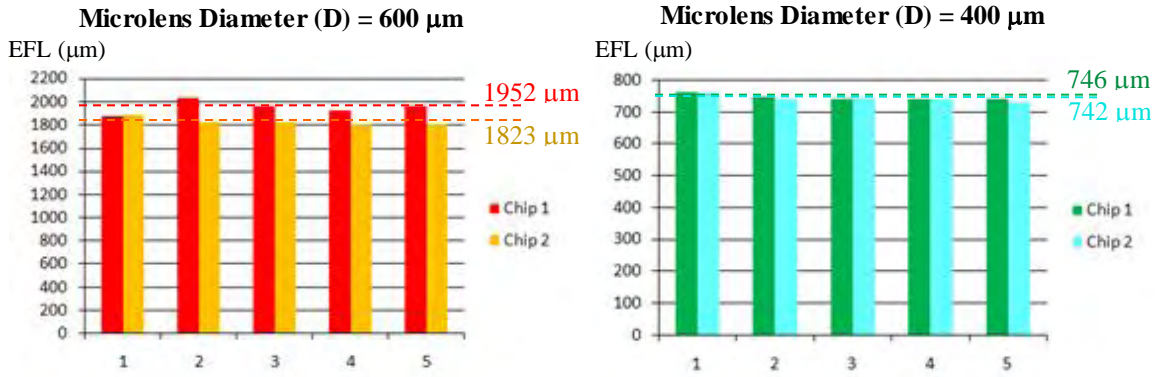
Figure 1.31 Uniformity of focal lengths: The dotted lines show the average EFL for each set of microlenses, indicated by the color.

Table 1.9 EFL uniformity data: 100% ×Standard deviation ÷ Average EFL

	Microlens (D = 400 μm)	Microlens (D = 600 μm)
Within Chip 1 (5 lenses each)	1.22 %	3.09 %
Within Chip 2 (5 lenses each)	1.44 %	1.86 %
Chip1 to Chip 2 (10 lenses each)	1.29 %	4.22 %

Table 1.10 EFL maximum deviation: 100% × [(Max or Min EFL) – Average EFL] ÷ Average EFL

	Microlens (D = 400 μm)	Microlens (D = 600 μm)
Within Chip 1 (5 lenses each)	1.97 %	4.33 %
Within Chip 2 (5 lenses each)	2.16 %	3.20 %
Chip1 to Chip 2 (10 lenses each)	2.26 %	7.74 %

Table 1.11 EFL Peak-to-valley deviation: 100% × (Max EFL – Min EFL) ÷ Average EFL

	Microlens (D = 400 μm)	Microlens (D = 600 μm)
Within Chip 1 (5 lenses each)	2.82 %	8.48 %
Within Chip 2 (5 lenses each)	3.99 %	4.67 %
Chip1 to Chip 2 (10 lenses each)	4.36 %	12.42 %

Examining the results shown in Tables 1.9-1.11, one can clearly see that the uniformity is well maintained within the same chip. The variation becomes larger as the volume of the microlenses increase. Also notice that within the chip uniformity is better than the chip-to-chip uniformity.

1.5.6 Wavefront-Aberration Measurements

We measured spherical aberrations, coma, astigmatism, root-mean-square wavefront errors (rms WFE), and peak-to-valley optical-path differences (p-v OPD) of the microlenses on microlenses fabricated using hydrophobic effects and polymer-jet-printing technique. We used the commercially available CLAS-2D Shack-Hartmann sensor from Wavefront Sciences, Inc. in Albuquerque, New Mexico, with the help of Dr. Paul D. Pulaski [20]. A Shack-Hartmann sensor is made of a microlens array and a CCD imager. For our measurements, we used the 31×24 microlens array in the CLAS-2D Shack-Hartmann sensor. The diameter of the microlenses in the array was 198 μm, and the focal length was 15.5 mm. The wavelength (λ) of the laser diode used as a light source was 635 nm. Using the 31×24 microlens array as a sensing element, the CLAS-2D sensor achieves the sensitivity (accuracy) of $\lambda/100$ (rms), dynamic range of 40λ, and the repeatability of $\lambda/120$ (rms). A schematic diagram that depicts the measurement setup is shown in Figure 1.32.
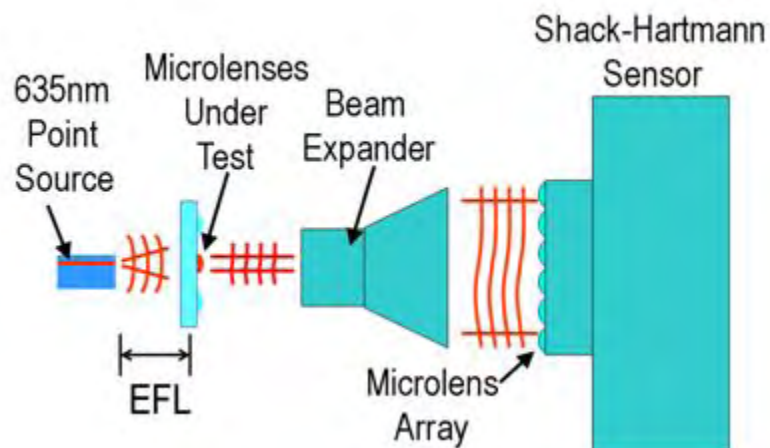
Figure 1.32   Schematic diagram of the optical-aberration-measurement setup

The laser-diode output was coupled into a single-mode fiber which served as a point source. The microlens under measurement was placed precisely its EFL away from the tip of the optical fiber, so that the diverging beam emerging from the optical fiber was collimated by the microlens. The diameter of the beam that emerges from the microlens under test is as wide as the diameter of the microlens, which is between 200 μm and 1 mm. In order to take the full advantage of the Shack-Hartmann sensor, this collimated beam from the microlens under test must occupy the maximum number of microlenses in the microlens array used in the sensor, without clipping the beam, as shown in Figure 1.33.
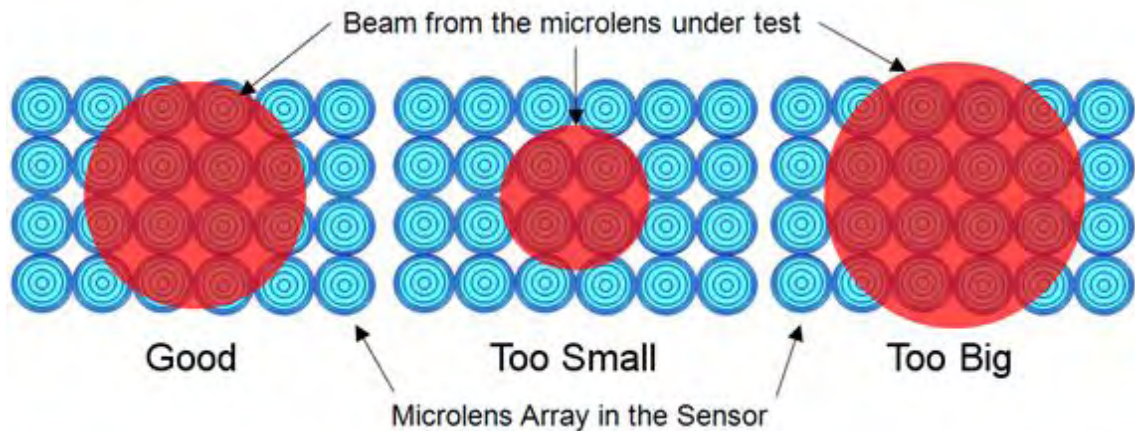
Figure 1.33   Filling up the microlens array in the sensor with the beam from the microlens under test: The beam size on the left is proper for measurement.

The length and the width of the microlens array used in the sensor are 6.14 and 4.75 mm, respectively. Hence, in order to perform more accurate measurements on microlenses with 200, 400, 600, 1000-μm diameters, we used ×8, ×8, ×4, and ×4 beam expanders, respectively. These custom-made beam expanders were carefully tested and calibrated using the CLAS-2D sensor (as shown in Figure 1.34). Then, a reference measurement is made only with the beam expander in the setup, as shown in Figure 1.34, and then is

subtracted from the measurement made with our microlenses in place, as shown in Figure 1.32. This subtraction cancels out the influence of the beam expander's native optical aberrations to the microlens measurements.
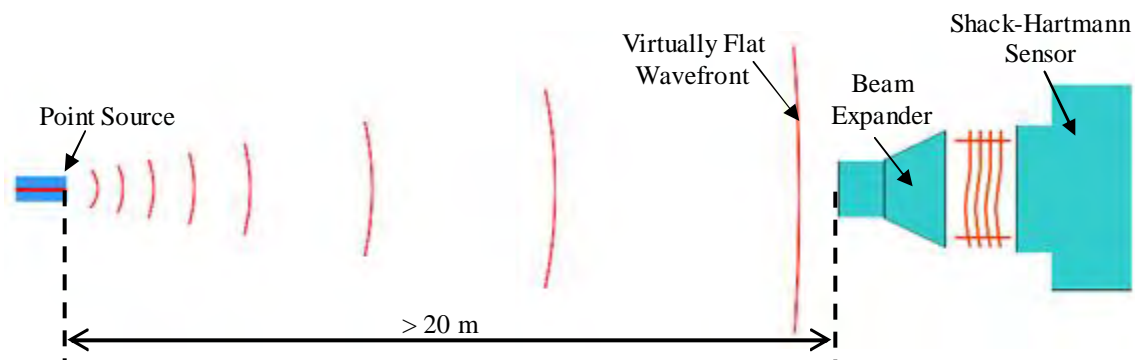
Figure 1.34   Calibration setup for a beam expander

The wavefront generated by the point-laser source is placed at least 20 meters away from the beam expander and is virtually flat (with a radius of curvature larger than 20 meters) by the time it reaches the beam expander. First, a measurement is made without a test microlens in place and saved onto the machine. This is the reference measurement. Then the second measurement is made with the test microlens in place and after the light source is brought up closer to the test microlens, exactly the lens' EFL away. Finally, the reference measurement is subtracted from the second measurement. (The CLASS-2D software performs this operation automatically.)

For 200-μm diameter microlenses, the use of a beam expander with a magnification of ×12 would have been more appropriate, but it was not possible to calibrate it. The point source was 20 meters away, and the beam-expander's aperture on the entering side was too small to accept any detectable amount of laser light from the point source. Hence, we used the ×8 beam expander for the measurements, which sacrificed the spatial resolution of the measurements by 50%.

The detailed results of optical aberration measurements are shown in Tables 1.12-1.15. The rms WFE values of our microlenses were between $\lambda/5$ and $\lambda/80$, depending on the aperture size, diameter, and volume of the microlenses. The average p-v OPD values were 0.14, 0.25, 0.33, and 0.46 μm for 200 μm-, 400 μm-, 600 μm-, and 1mm-diameter microlenses, respectively. Decreasing the aperture size of the microlenses produced much smaller rms WFE and p-v OPD values. These values were sometimes as low as $\lambda/80$.
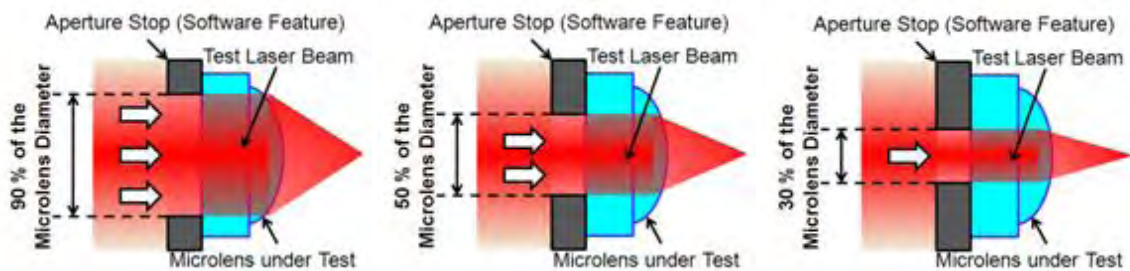
Figure 1.35   Aperture size vs. optical aberrations: The aperture stop shown here is not a physical aperture stops. This is a feature that comes with the CLAD-2D software.

Table 1.12 Optical aberrations and peak-to-valley optical-path difference (P-V OPD) of 200-µm diameter microlenses

(All Values in µm)	Lens Number	200-1	200-2	200-3	200-4
Aperture Size: 90% of the Diameter	Spherical Aberration	-0.3198	-0.3859	0.2797	-0.3384
	Coma	0.0790	0.0905	0.1054	0.1343
	Astigmatism	0.0066	0.0256	0.0216	0.0232
	rms WFE	0.0346	0.0317	0.0288	0.0340
	P-V OPD	0.1773	0.1315	0.1229	0.1384
Aperture Size: 50% of the Diameter	Spherical Aberration	-0.0034	-0.0342	0.2956	0.0094
	Coma	0.0089	0.0203	0.1778	0.0037
	Astigmatism	0.0164	0.0224	0.0798	0.0133
	rms WFE	0.0167	0.0189	0.0406	0.0068
	P-V OPD	0.0529	0.0757	0.1452	0.0289

Table 1.13 Optical aberrations and peak-to-valley optical path difference of 400-µm diameter microlenses

(All Values in µm)	Lens Number	400-1	400-2	400-3	400-4
Aperture Size: 90% of the Diameter	Spherical Aberration	-0.2053	0.1044	-0.0099	0.3143
	Coma	0.1062	0.0665	0.1276	0.3684
	Astigmatism	0.0699	0.0608	0.0391	0.3368
	rms WFE	0.0429	0.0274	0.0395	0.1269
	P-V OPD	0.1468	0.1453	0.1712	0.5392
Aperture Size: 50% of the Diameter	Spherical Aberration	-0.0322	-0.0076	-0.0303	-0.0163
	Coma	0.0183	0.0054	0.0313	0.0343
	Astigmatism	0.0147	0.0106	0.0386	0.1433
	rms WFE	0.0080	0.0055	0.0108	0.0322
	P-V OPD	0.0339	0.0255	0.0496	0.1633
Aperture Size: 30% of the Diameter	Spherical Aberration	0.0115	-0.0134	0.0345	-0.0037
	Coma	0.0099	0.0241	0.0123	0.0182
	Astigmatism	0.0217	0.0044	0.0107	0.0631
	rms WFE	0.0074	0.0071	0.0056	0.0140
	P-V OPD	0.0303	0.0308	0.0278	0.0589

Table 1.14 Optical aberrations and peak-to-valley optical path difference of 600-µm diameter microlenses

(All Values in µm)	Lens Number	600-1	600-2	600-3	600-4
Aperture Size: 90% of the Diameter	Spherical Aberration	-0.1895	-0.1411	-0.0361	0.6044
	Coma	0.0734	0.2359	0.2433	0.1747
	Astigmatism	0.0189	0.0727	0.0738	0.1419
	rms WFE	0.1008	0.0859	0.0539	0.0702
	P-V OPD	0.3772	0.3419	0.2175	0.3952
Aperture Size: 50% of the Diameter	Spherical Aberration	-0.0089	0.0164	-0.0041	0.0051
	Coma	0.0153	0.0235	0.0315	0.0413
	Astigmatism	0.0367	0.0313	0.0465	0.1004
	rms WFE	0.0097	0.0128	0.0156	0.0242
	P-V OPD	0.0394	0.0632	0.0643	0.1314
Aperture Size: 30% of the Diameter	Spherical Aberration	-0.0089	0.0058	-0.0245	0.007
	Coma	0.0071	0.0107	0.0128	0.0209
	Astigmatism	0.0511	0.0106	0.0196	0.0418
	rms WFE	0.0120	0.0045	0.0072	0.0106
	P-V OPD	0.0564	0.0193	0.0334	0.0502

Table 1.15   Optical aberrations and peak-to-valley optical path difference of 1000-µm diameter microlenses

(All Values in µm)	Lens Number	1000-1	1000-2	1000-3	1000-4
Aperture Size: 90% of the Diameter	**Spherical Aberration**	-2.1196	-0.4324	-0.1089	-0.3491
	Coma	0.2367	0.1167	0.1973	0.2737
	Astigmatism	0.0112	0.2596	0.3206	0.1158
	rms WFE	0.1054	0.0752	0.0996	0.1115
	P-V OPD	0.4147	0.3237	0.6232	0.4612
Aperture Size: 50% of the Diameter	**Spherical Aberration**	0.0378	0.0175	-0.0372	-0.0135
	Coma	0.0701	0.0153	0.0495	0.0339
	Astigmatism	0.1172	0.1029	0.1052	0.0343
	rms WFE	0.0359	0.0309	0.0263	0.0119
	P-V OPD	0.1339	0.1230	0.1378	0.0575
Aperture Size: 30% of the Diameter	**Spherical Aberration**	0.0213	0.0234	0.0103	0.0005
	Coma	0.0272	0.0095	0.0040	0.0191
	Astigmatism	0.0367	0.0363	0.0391	0.0190
	rms WFE	0.0101	0.0108	0.0088	0.0066
	P-V OPD	0.0397	0.0409	0.0435	0.0285

The optical aberration measurement results are plotted and shown in Figures 1.36 – 1.39. The negative values were plotted using their absolute values to make the comparison easier. Two trends emerge from these plots. First, the optical aberrations generally decrease as we use smaller aperture stops, or only the center region of the microlenses. Decrease in optical aberrations is exactly what one would expect as the aperture size is decreased. This is also observed in other imaging lenses, including commercial photographic lenses. Second, shorter focal lengths generally result in smaller optical aberrations, especially in spherical aberration. In order to create microlenses with longer focal lengths, it is necessary to decrease the volumes of the microlenses accordingly within the same base diameter. Sometimes, the amount of liquid polymer dispensed within the microlens area is below the minimum level required to form a high-quality spherical surface, and the surface profile of the microlens deviates further away from spherical surface, and this is responsible for general increase in optical aberrations in longer-focal-length microlenses. This effect becomes more pronounced as the diameter

of the microlens becomes larger ($\geq$ 400 µm), and it can be ignored if the diameter of the

microlens is small ($<$ 200 µm).
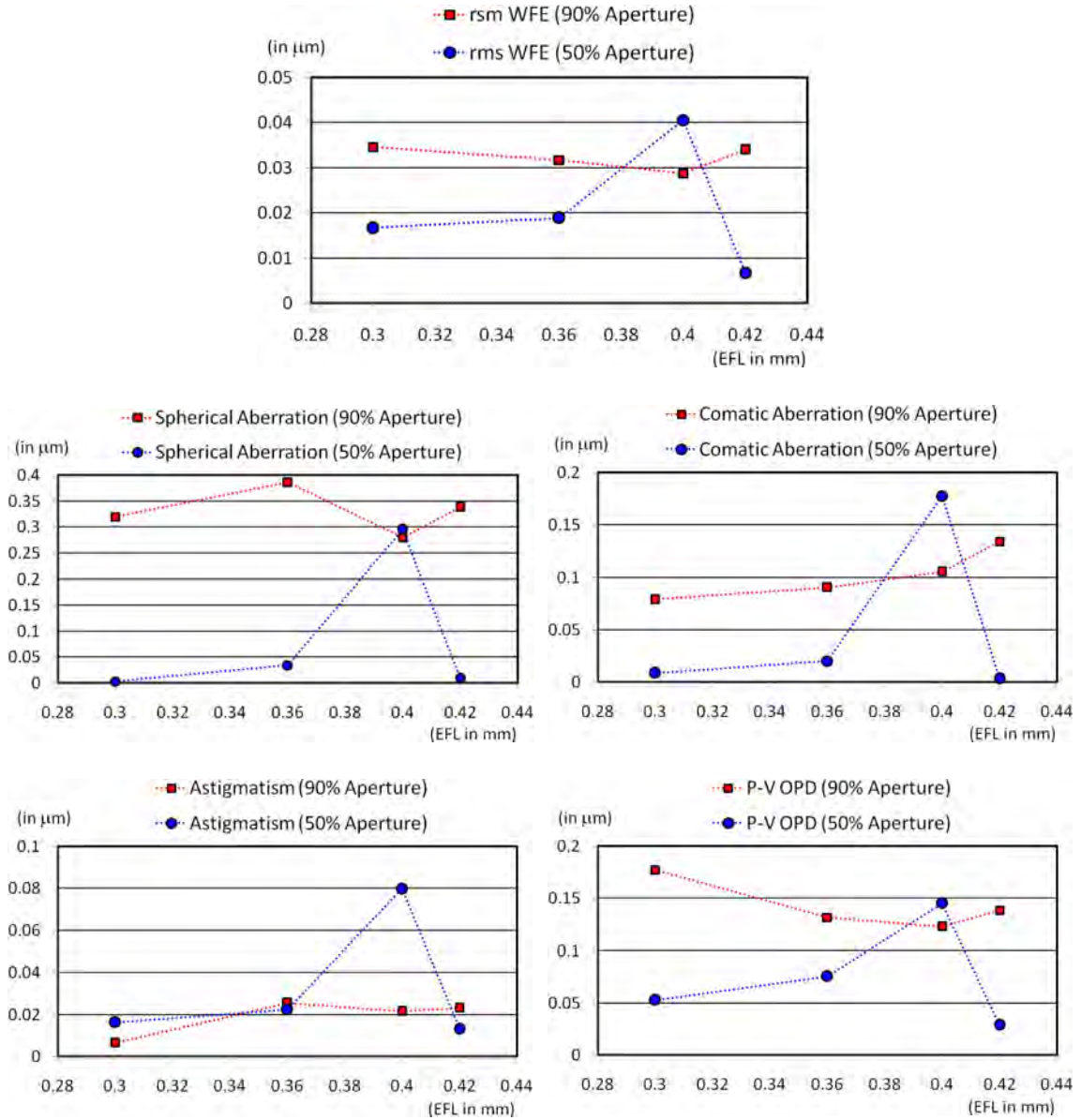
Figure 1.36   Optical aberration measurements for 200-µm diameter microlenses
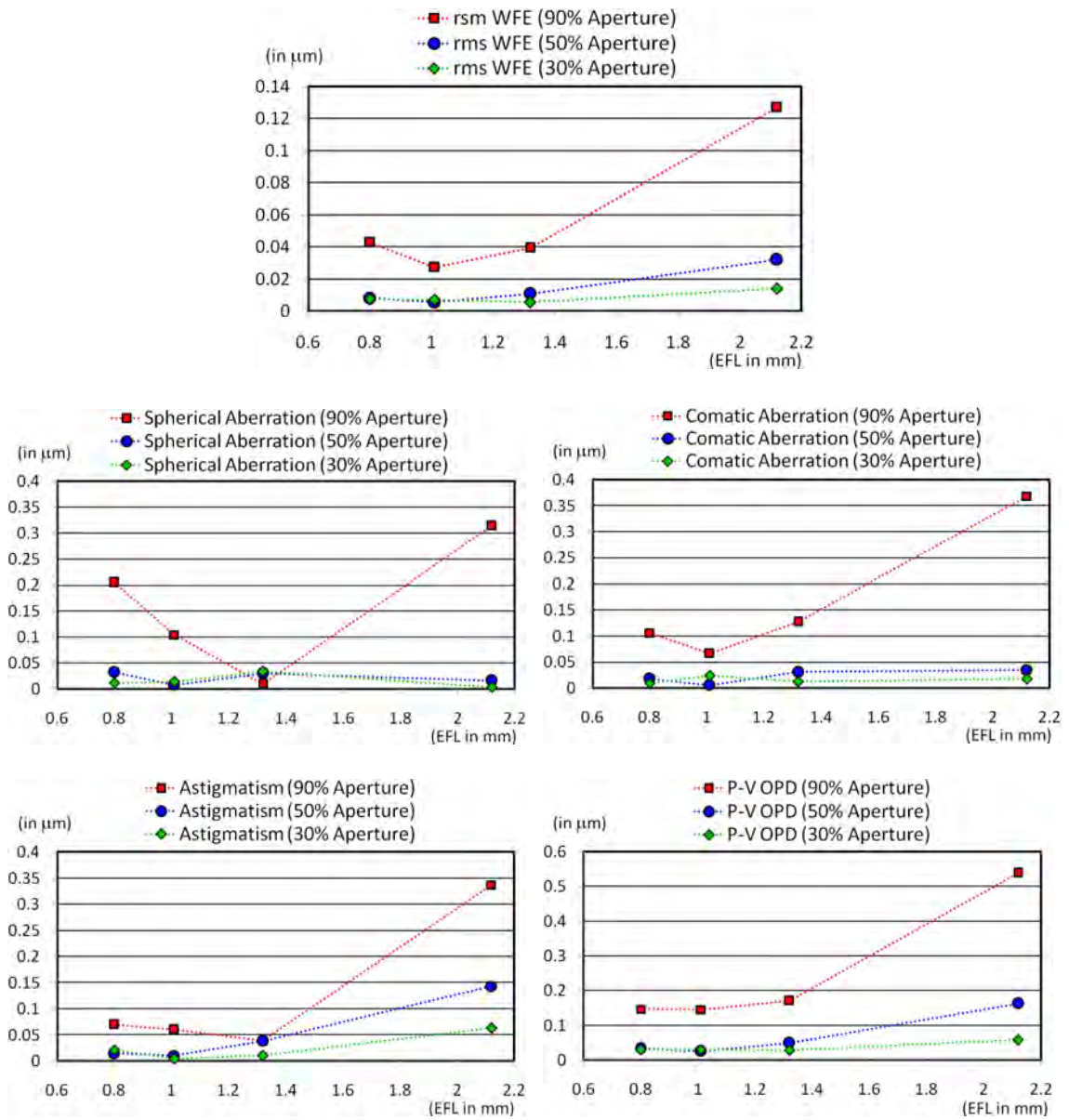
Figure 1.37   Optical aberration measurements for 400-μm diameter microlenses
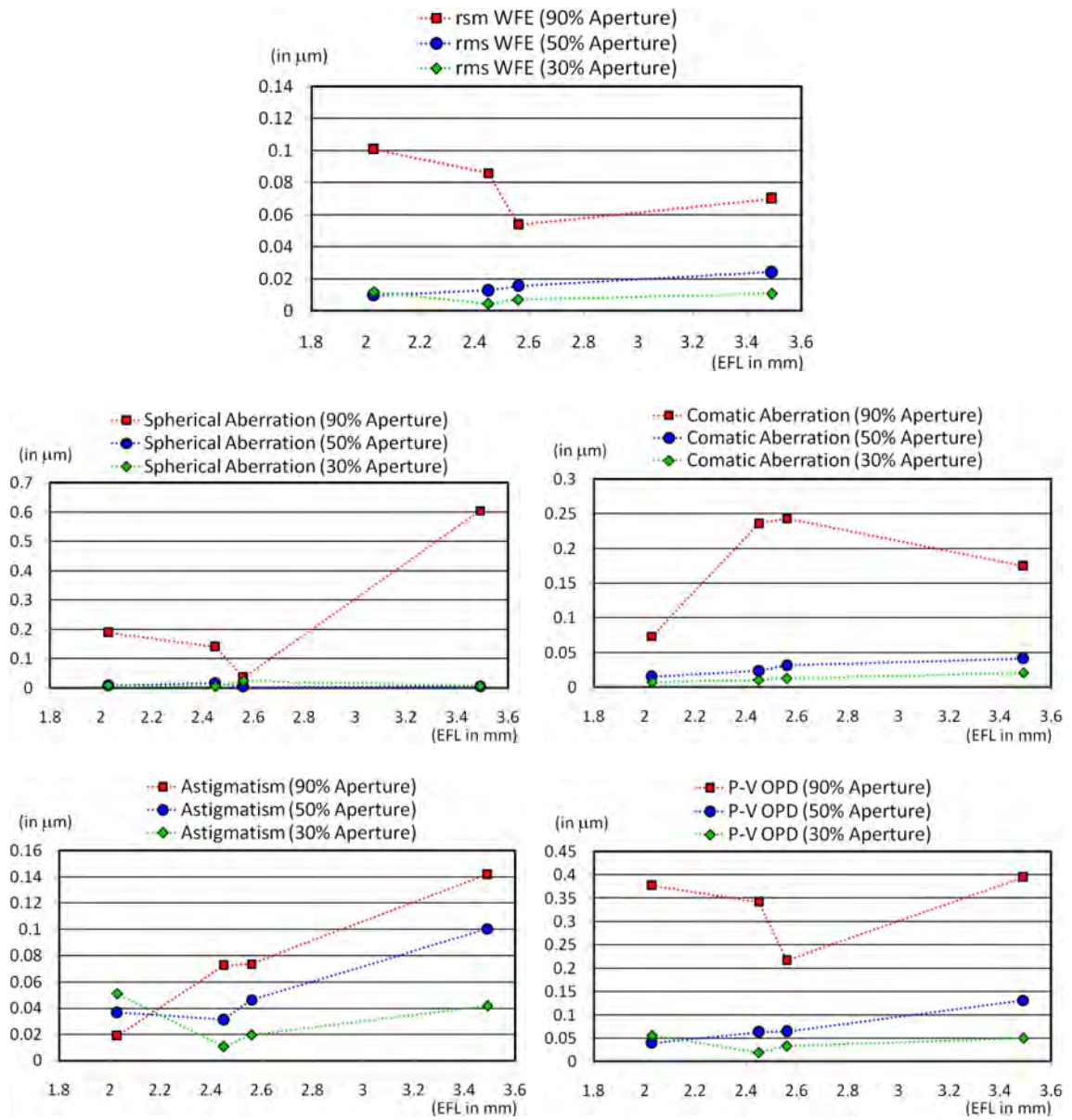
Figure 1.38   Optical aberration measurements for 600-µm diameter microlenses
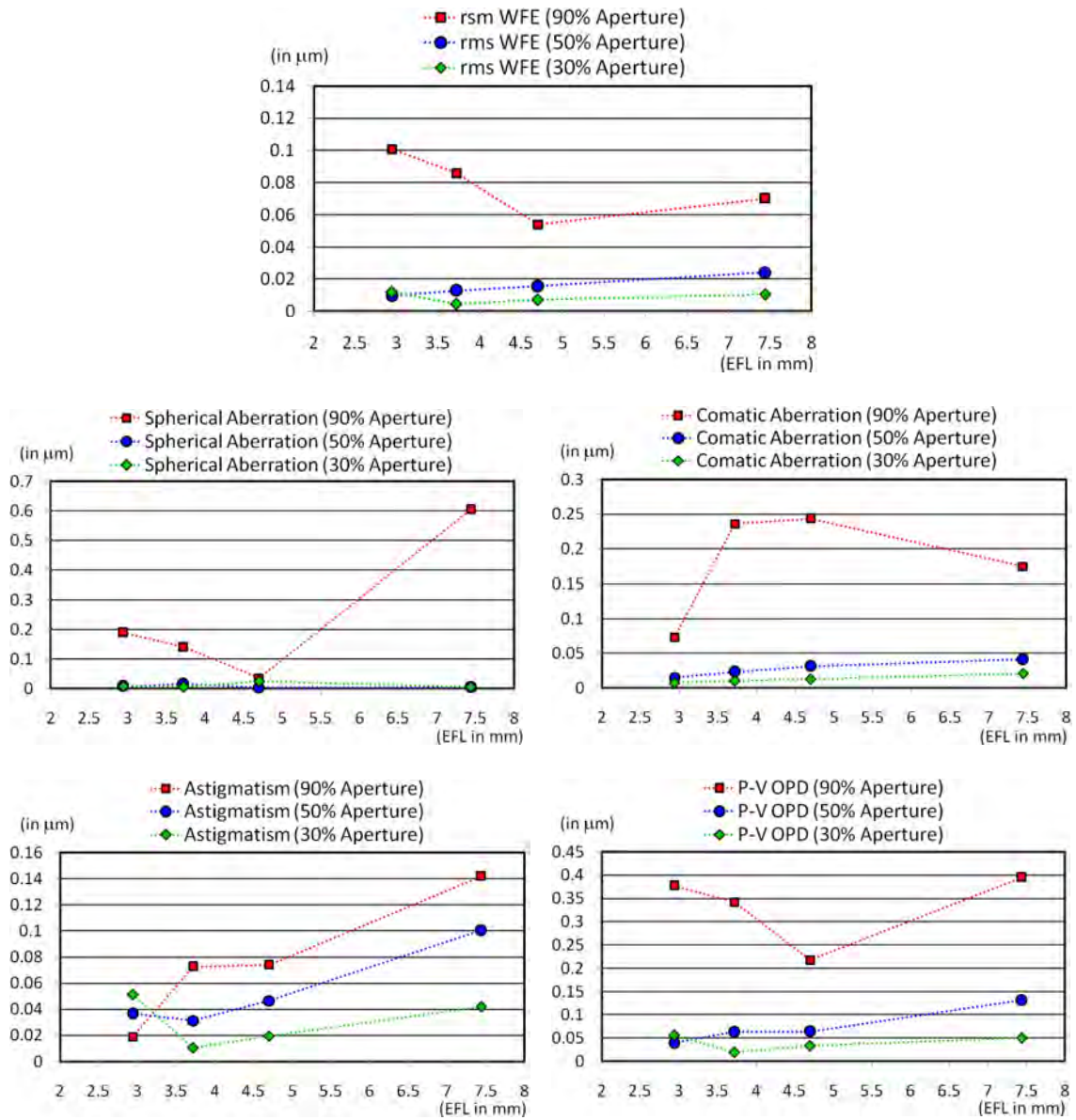
Figure 1.39   Optical aberration measurements for 1000-μm diameter microlenses

One can also observe some unexpected deviation in optical aberrations. Optically examing these microlenses using reflection-based characterization tools (such as SEM, WYKO, and optical microscopes) reveals no problems - they look fine. This unexpected variation must be due to the presence of refractive-index fluctuation typically observed in polymer materials, which mainly depends on the quality of the polymer material used.

1.5.7 Image Gallery

We have built a rudimentary imaging system consisting of a microlens, an aluminum-foil aperture stop, and a miniaturized ¼" CCD. The schematic diagram of the setup is shown in Figure 1.40. A white-light from a desktop lamp with 25W halogen bulb was used in order to illuminate the samples. (Hence, the illumination is not very uniform across the sample.) Please note that we are not viewing through the microlenses using a commercial microscope, as a few other researchers have done previously [21]. Viewing through microlenses with a commercially available microscope is not a proper way to evaluate or estimate the imaging capability of the microlenses since the optical components inside the microscope play considerable roles in determining the quality of the final image. In our setup, the optical rays from the object under observation pass through the microlenses and form the images directly on the CCD. Using this simple imaging system, we have observed the black grid lines drawn on a Panasonic 9V battery (Figure 1.41), which is commonly available at any electronics shops around the world. We also imaged two sets of lines/gaps, one with periodic 5-um wide lines and gaps, and the other with 2.5-um wide lines and gaps, on a photolithography mask (chrome). All the images created using our microlens imaging system were compared with those generated by a Reichert-Jung PolyLite microscope (Figures 1.42-44). Detailed information on the CCDs is given below. Clearly, the CCD used in our microlens imaging system is inferior to one used with the Reichert-Jung PolyLite microscope.

Specifications of the CCD cameras used for the imaging experiments:

CCD Imager for Microlens Imaging System
Name: WAT660D Monochrome Imager with ¼" Interline Transfer CCD Image Sensor
Effective Picture Elements: 537 (H) × 505 (V)
Pixel Size: 7.15 µm (H) × 5.55 µm (V)
Signal-to-Noise Ratio: > 46 dB
Distance between the CCD imager and the lens: ~ 7.5mm
Street Price: $160

CCD Imager for Reichert-Jung PolyLite Microscope
Name: jai CV-730NCD High-resolution Color CCD Camera with ½" Hyper HAD
        Interline Transfer CCD Image Sensor
Effective Picture Elements: 768 (H) × 494 (V)
Pixel Size: NA
Signal-to-Noise Ratio: > 50 dB
Street Price: $1500
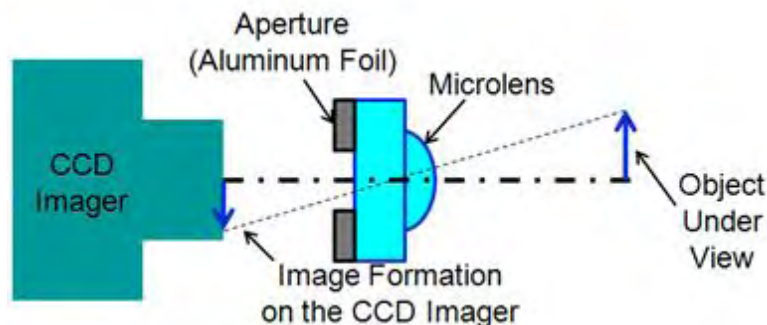
Figure 1.40   Microlens imaging system: The diameter of the aluminum-aperture stop is 800 µm.

Although the microlenses in the system have much smaller aperture sizes than microscope objective lenses and they lack anti-reflection coatings, the microlens imaging system have produced good-quality pictures. The maximum magnification demonstrated by one of the microlenses we used is comparable to that of Reichert microscope with the 5X objective lens. Also, our microlenses also showed a superior ability in resolving small patterns for 2.5-um wide lines/gaps. When we digitally enlarge the images, we can observe the line/gap patterns in the picture taken with our microlens imaging system (Figure 1.44).
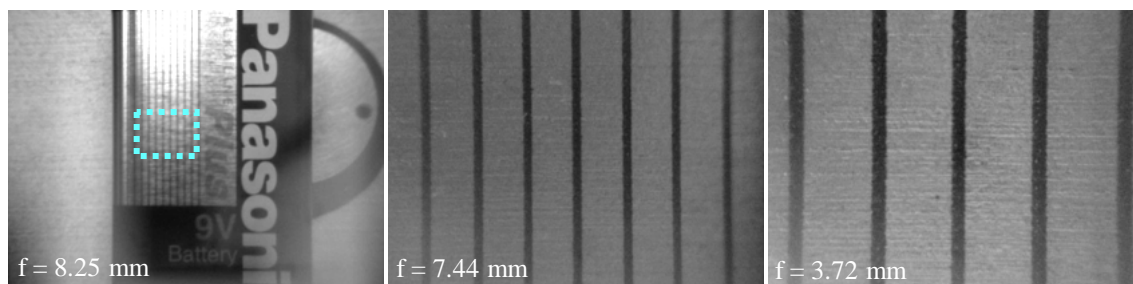
Figure 1.41 Images of a Panasonic 9V battery captured (at different magnifications) using our microlens imaging system (Diameter of the microlenses used: 1000 μm, Illumination: bright field, top): Vertical stripes shown in the two right pictures come from the area inside the blue dotted box in the picture on the left.
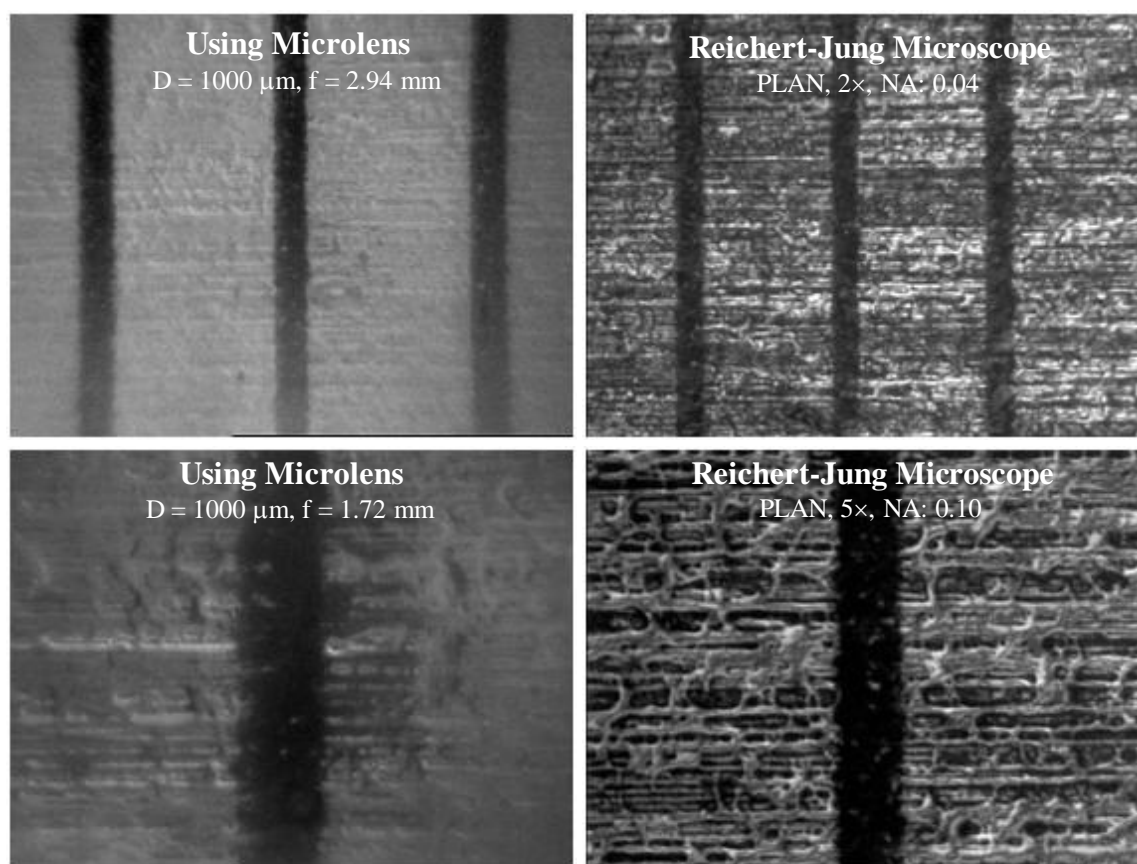
Figure 1.42 Images of a Panasonic battery captured using our microlens imaging system and Reichert-Jung PolyLite microscope (Both used bright field, top illumination)
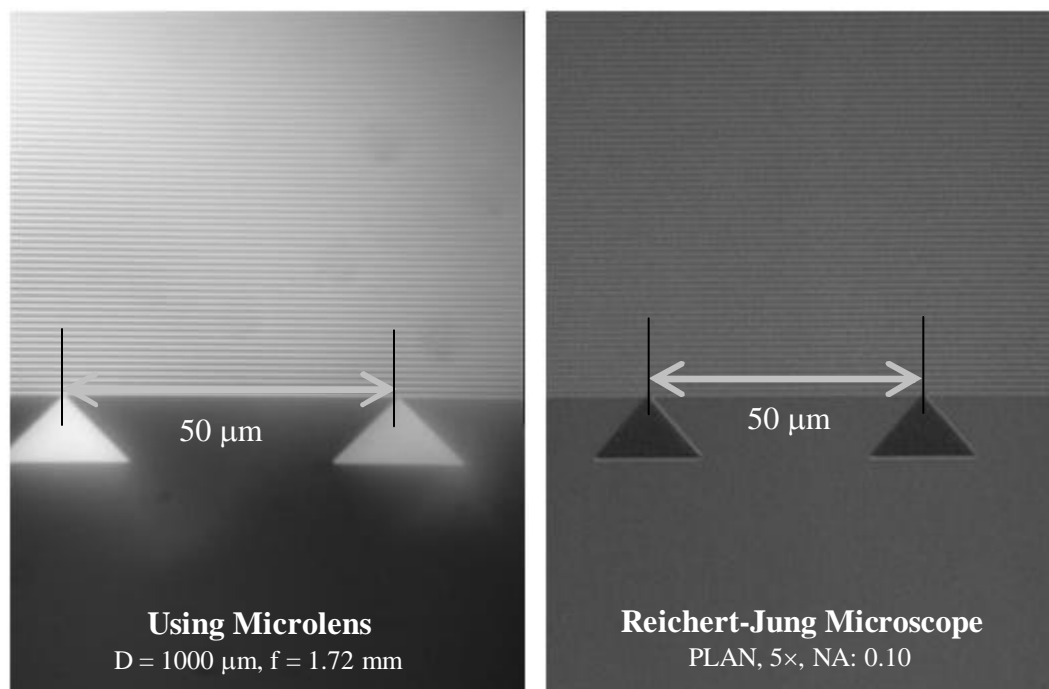
Figure 1.43   Images of 5 µm-wide lines/gaps captured using our microlens imaging system (bright field, bottom illumination) and Reichert-Jung PolyLite microscope (bright field, top illumination)
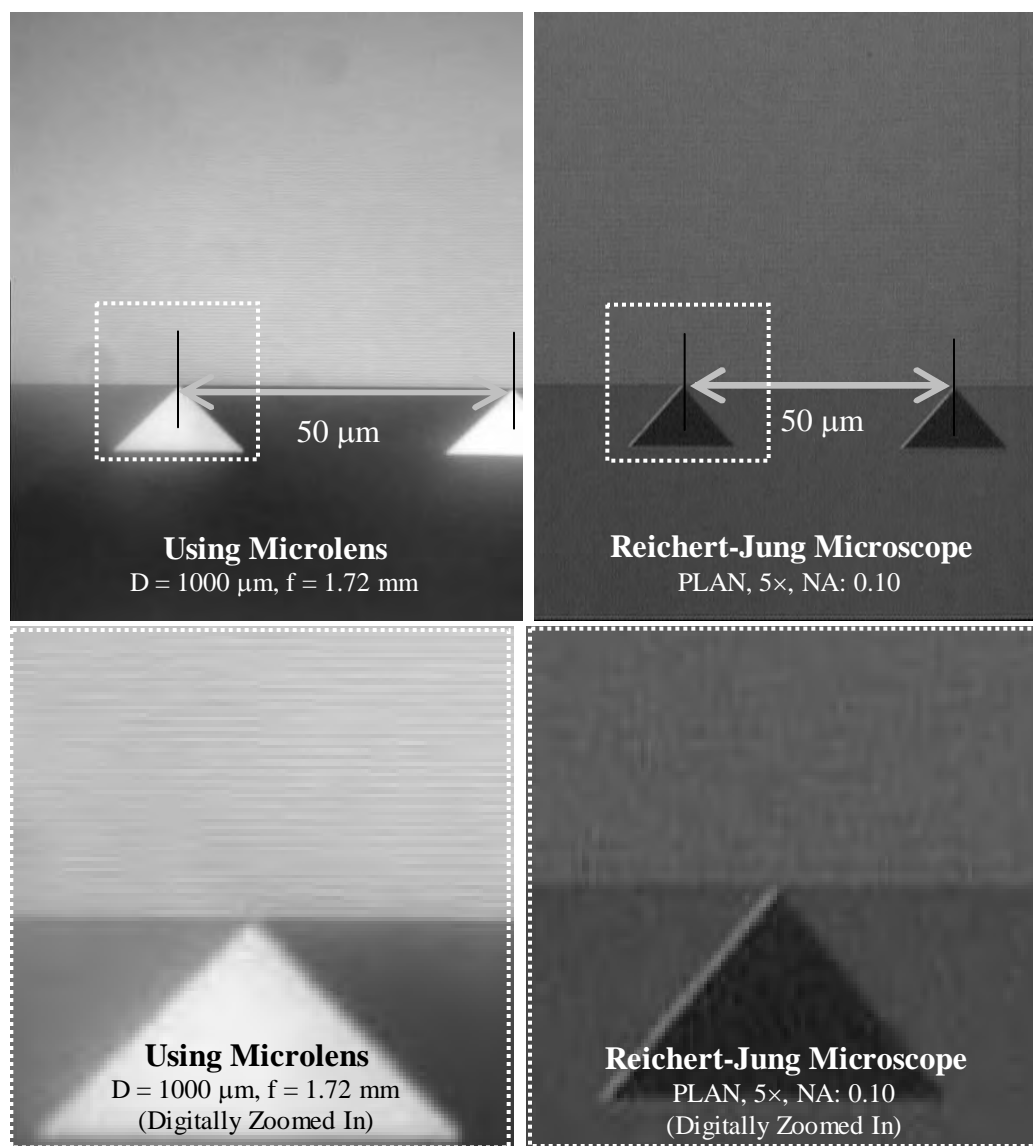
Figure 1.44   Images of 2.5 µm-wide lines/gaps captured using our microlens imaging system (bright field, bottom illumination) and Reichert-Jung PolyLite microscope (bright field, top illumination): Two pictures in the bottom are digitally enlarged, approximately by a factor of 3. It's quite clear that the image generated by the Reichert-Jung microscope does not show the 2.5 µm-wide lines/gaps.
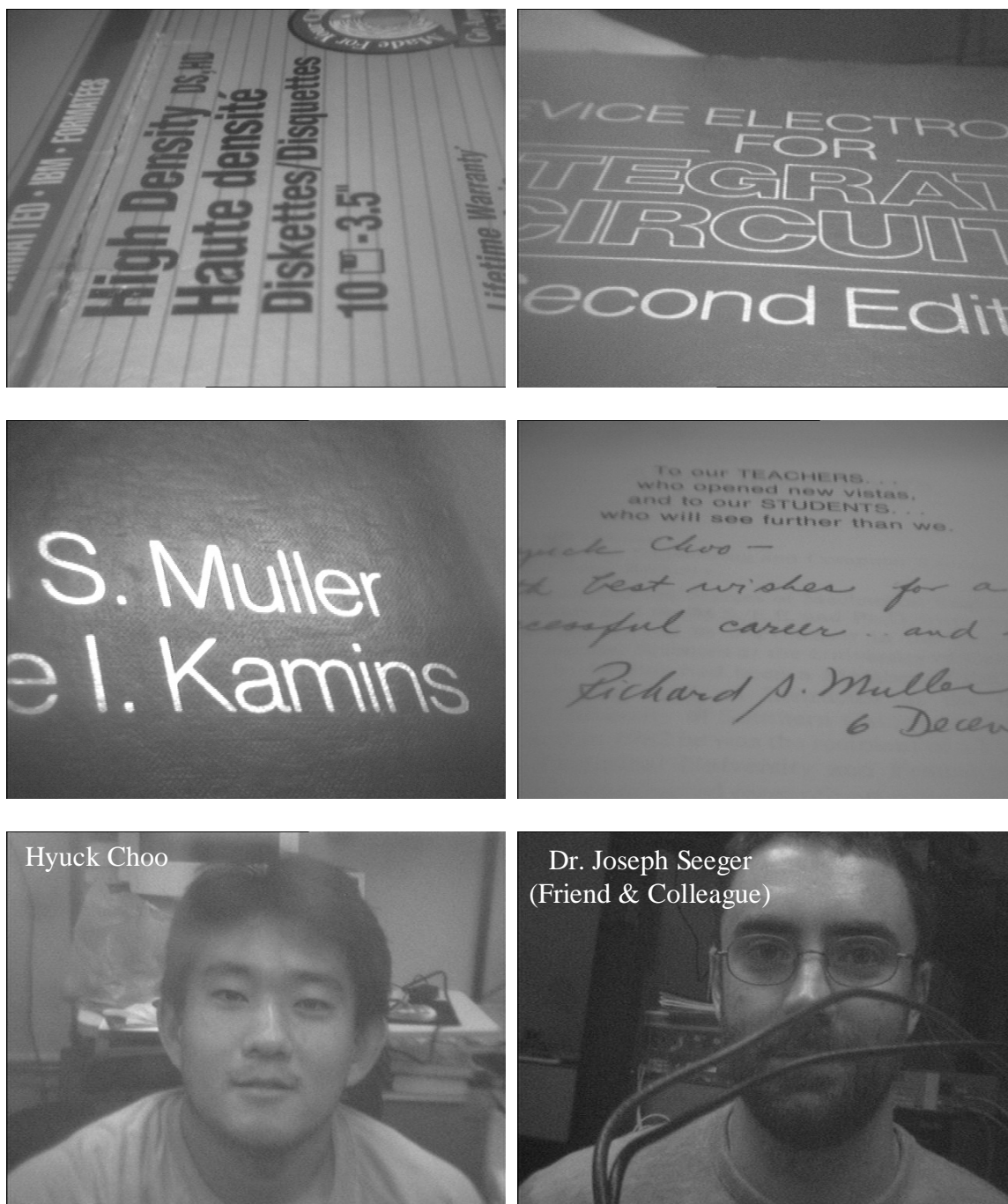
Figure 1.45 Microlens imaging capability on macro-scale objects: microlens diameter = 1000 μm, f = 8.25 mm

1.6 Conclusions

Microlenses have been fabricated using polymer-jet printing technique and hydrophobic effects. Fabricated microlenses, whose diameters are 200, 400, 600, and

1000 μm, have focal lengths ranging between 0.3 and 7.44 mm. The f-numbers range from 1.5-2.1, 2.0-5.5, 3.4-6.3, and 2.9-7.4 for 200 μm-, 400 μm-, 600 μm-, and 1 mm-diameter microlenses, respectively. The uniformity of the focal lengths within the chip is 3.09%, and that of chip-to-chip is 4.22 %. The microlens profiles are highly spherical – The maximum deviation from an ideal radius of curvature has been less than 5 %. The rms WFE of the microlenses are also excellent, too. Over the microlens area included by 90% of its diameter, all the microlenses show rms WFEs less than $\lambda/6$, which is the quality one would expect from high-end commercial camera lenses. The low optical aberration proves that microlenses are capable of imaging very fine features. The microlens imaging system was compared with a commercial microscope side by side. The microlens can resolve 2.5-μm wide lines and gaps when paired with a miniature CCD. Finally, the microlenses have demonstrated good-imaging qualities with macro-scale objects.

References

[1]   H. Choo and R. S. Muller, "Addressable Microlens Array to Improve Dynamic Range of Shack-Hartmann Sensors," *Journal of Microelectromechanical Systems*, vol. 15, no. 6, December 2006, pp. 1555-1567.

[2]   L. Y. Lin, S. S. Lee, K. S. J. Pister, and M. C. Wu, "Three-dimensional micro-Fresnel optical elements fabricated by micromachining technique," *Electronics Letters*, vol. 30, no. 5, 1994, pp. 448-449.

[3]   L. Y. Lin, S. S. Lee, K. S. J. Pister, and M. C. Wu, "Micromachined three dimensional micro-optics for integrated free-space optical system," *IEEE Photonics Technology Letters*, vol. 6, no. 12, 1994, pp 1445-1447.

[4]   O. Solgaard, M. Daneman, N. C. Tien, A. Friedberger, R. S. Muller, and K. Y. Lau, "Optoelectronic packaging using silicon surface-micromachined alignment mirrors," *IEEE Photonics Technology Letters*, vol. 7, no. 1, pp.41-43, 1995

[5]   K. Rastani, A. Marrakchi, S. F. Habiby, W. M. Hubbard, H. Gilchrist, and R. E. Nahory, "Binary phase Fresnel lenses for generation of two-dimensional beam arrays," *Applied Optics*, vol. 30, no. 11, 1991, pp.1347-1354.

[6]   H. Sankur, E. Motamedi, R. Hall, w. J. Gunning, M. Khoshnevisan, "Fabrication of refractive microlens arrays," *Proc. SPIE, Micro-Optics/Micromechanics and Laser Scanning and Shaping*, vol. 2383, 1995, pp.179-183.

[7]   Z. D. Popovic, R. A. Sprague, and G. A. Neville Connell, "Technique for monolithic fabrication of microlens arrays," *Applied Optics*, Vol. 27, no. 7, 1988, pp. 1281-1284.

[8]   N. J. Phillips and C. A. Barnett, "Micro-optic studies using photopolymers," *Proc. SPIE, Miniature and Micro-Optics*, vol. 1544, 1991, pp. 10-21.

[9]   D. M. Hartmann, O. Kibar, S. C. Esener, "Optimization and theoretical modeling of polymer microlens arrays fabricated with the hydrophobic effect," *Applied Optics, vol.40, no.16,* June 1, 2001, pp.2736-46

[10]   D. L. MacFarlane, V. Narayan, J. A. Tatum, W. R. Cox, T. Chen, and D. J. Hayes, "Microjet fabrication of microlens arrays," *IEEE Photonics Technology Letters, vol.6, no.9,* September 1994, pp.1112-14.

[11]   M. C. Hutley, "Microlens Arrays," *Proceedings IOP Short Meet*, series vol. 30, IOP Publishing, Tendington, UK, 1991.

[12]   J. S. Legatt and M. C. Hutley, "Microlens arrays for interconnection of singlemode fiber arrays," *Eletronics Letters*, vol. 29, 1991, pp.238-240.

[13]   E. Kim and G. M. Whitesides, "Use of Minimal Free Energy and Self-Assembly To Form Shapes," *Chemistry of Materials*, vol. 7, 1995, pp.1257-1264.

[14]   N. Bowden, A. Terfort, J. Carbeck, and G. M. Whitesides, "Self-Assembly of Mesoscale Objects into Ordered Two-Dimensional Arrays," *Science*, vol. 276, 1997, pp. 233-235.

[15]   D. M. Hartmann, O. Kibar, and S. C. Esener, "Characterization of a polymer microlens fabricated by use the hydrophobic effect", *Optics Letters*, vol. 25, 2000, pp. 975-977.

[16]   T. Chen, W. R. Cox, D. Lenhard, and D. J. Hayes, "Microjet printing of high-precision microlens array for packaging of fiber optic components," *SPIE-Int. Soc. Opt. Eng. Proceedings of Spie - the International Society for Optical Engineering, vol.4652,* 2002, pp.136-41.

[17]   H. Choo and R. S. Muller, "Optical Properties of Microlenses Fabricated Using Hydrophobic Effects and Polymer-jet-printing Technology," *2003 IEEE/LEOS International Conference on Optical MEMS and Their Applications*, 2003, pp. 169-170, Kona, Hawaii USA.

[18]   H. Choo and R. S. Muller, "Devices, Structures, and Processes for Optical MEMS," *Invited Paper, Special Issue on IEEJ (Institute of Electrical Engineers of Japan) Transactions of Electrical and Electronic Engineering* (To be published in May 2007).

[19]   A. Dekker, K. Reitsma, T. Beugeling, A. Bantjes, J. Feijen, and W. G. van Aken, "Adhesion of endothelial cells and adsorption of serum proteins on gas plasma-treated polytetrafluoroethylene," *Biomaterials*, vol. 12, issue 2, 1991, pp.130-138.

[20]   P. D. Pulaski, D. R. Neal, J. P. Roller, "Measurement of aberrations in microlenses using a Shack-Hartmann wavefront sensor," *SPIE-Int. Soc. Opt. Eng. Proceedings of Spie - the International Society for Optical Engineering, vol.4767,* 2002, pp. 44-52. USA.

[21]   A. Picard, W. Ehrfeld, H. Lowe, H. Muller, J. Schulze, "Refractive microlens arrays made by contactless embossing," *SPIE-Int. Soc. Opt. Eng. Proceedings of Spie - the International Society for Optical Engineering,* vol.3135, 1997, pp.96-105.

CHAPTER 2

Micromachined Polarization Beam Splitters for the Visible Spectrum

2.1 Introduction

Polarization beam splitters (PBS), which separate the orthogonal TE and TM components of light (Figure 2.1), are important components in a number of optical systems and applications, especially in interferometers which have a very wide range of applications. In order to create useful optical systems using MEMS technology, we need an ability to integrate PBS easily and reliably onto micro-optical structures.   However, commercially available PBS's (Figure 2.1) are just too large, bulky, and expensive to be integrated into MEMS systems in microscale. Most of all they require painfully challenging manual assembly process. Hence, using the materials and technologies that are readily available to MEMS researchers, we need to develop a simple yet reliable method to fabricate PBS directly on the MEMS structures.
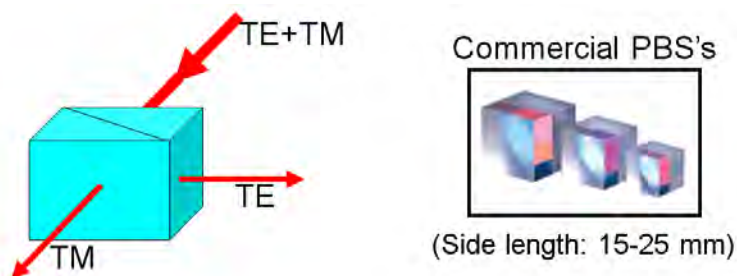
Figure 2.1 Right: TE and TM modes separation by a PBS; Left: Pictures of commercially available PBS's

A literature search led us to 1998 work by Pu, Zhu and Lo who investigated a MEMS-compatible surface-micromachined PBS made using thin-film polycrystalline silicon [1]. They achieved extinction ratios of 21 and 10 dB for reflected and transmitted light with an insertion loss of ~50% at a 1.3μm laser beam. For visible as well as infrared

light, this polysilicon PBS is excessively lossy due to the presence of etch holes and dimples.   And, clearly it is not suitable for use in the visible spectrum since polycrystalline as well as single-crystal silicon is partially transparent only in the infrared range.

Based upon our background in surface micromachining at Berkeley Sensor & Actuator Center (BSAC), we have seen and exploited a method to produce them using thin-film, low-stress silicon nitride (LSN) membranes deposited using low-pressure chemical-vapor-deposition (LPCVD) technique [2].   Another reason for choosing the LPCVD-LSN film is that it has good transmission rates in the visible spectrum, as shown in Figure 2.2.
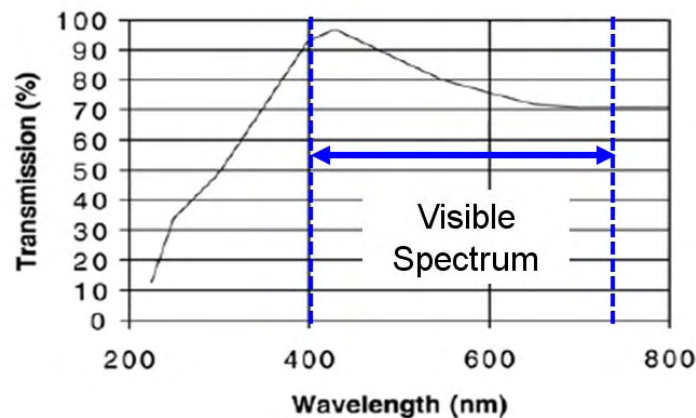
Figure 2.2   Transmission rate vs. wavelength for LPCVD low-stress silicon-nitride film: The refractive index is 2.1. (Source: D. R. Ciarlo, *Biomedical Microdevices*, 4: 1: 63-68, 2002 [2])

The author of the reference [2] also reports that the fabricated films are physically very robust.   The PBS fabrication steps involve only the well-established processing techniques widely used in MEMS community.   By stacking membranes, we have demonstrated a triple-layer PBS that produced extinction ratios of 21 and 16dB for

reflected and transmitted light rays, respectively, which matches the performance of commercially available PBS at a fraction of the cost.

2.2 Design of MEMS PBS

Figure 2.3 shows the optical principles for thin-film-based PBS. The light (TE and TM modes) incidents on the thin film's surface from the media 1 at the Brewster's angle (θ_B) - TE mode of the light reflects back into the media 1 while the TM mode of the light passes through the thin film (media 2) and enters the media 3.
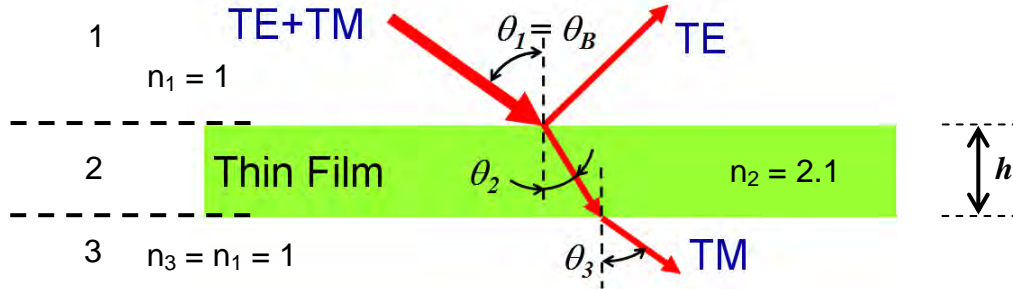
Figure 2.3   Optical principles of PBS made of LPCVD-LSN thin film

And, the performance of PBS is described by using extinction ratios, σ_R and σ_T.

$$\sigma_R = 10 \, \log(R_{TE}/R_{TM}) \tag{2.2.1}$$

$$\sigma_T = 10 \, \log(T_{TM}/T_{TE}) \tag{2.2.2}$$

R_{TE} and R_{TM} are reflection coefficients for TE and TM modes, and T_{TE} and T_{TM} are transmission coefficients for TE and TM modes, respectively. The higher the extinction ratios are, the better the performance of the PBS is. For commercial PBS, σ_R and σ_T are typically equal to or larger than 15 dB.

In order to produce a thin-film PBS of optimal performance, one needs to consider four design and fabrication issues. First, the film thickness must be accurately controlled. Second, the thin-film PBS must be extremely flat to minimize any optical

aberrations introduced by the PBS. Third, the film must be sufficiently thick and mechanically robust. Finally, the area of the window must be big enough for optical beam but not too large to process.

The first step for designing a thin-film PBS is to find the Brewster's angle (θ_B) at the interface between the air and silicon-nitride film [2].

$$\theta_B = \tan^{-1}(n_2/n_1) \tag{2.2.3}$$

For n_1 = 1 (air) and n_2 = 2.1 (LPCVD LSN film), the Brewster's angle (θ_B) is 64.54°, and this is equal to θ_1 in Figure 2.3. We also need to find θ_2 using Snell's Law [2].

$$\theta_2 = \sin^{-1}(n_1 \cdot \sin\theta_1/n_2) \tag{2.2.4}$$

θ_2 is 25.46°. θ_3 is equal to θ_1, which is 64.54°.

Next, we need to calculate the optimal thickness for the film's use as PBS. For 635-nm light and a thin-film membrane of low-stress silicon nitride, the thickness should be an integral multiple of 83.5 nm. This can be calculated using the equations given in the reference [3], which are listed here for the readers' convenience.

$$R_{TE} = \left| \frac{R_{TE:1\to2} + R_{TE:2\to3} \cdot e^{2i\beta}}{1 + R_{TE:1\to2} \cdot R_{TE:2\to3} \cdot e^{2i\beta}} \right|^2 \tag{2.2.5}$$

$$T_{TE} = \frac{p_3}{p_1} \left| \frac{T_{TE:1\to2} \cdot T_{TE:2\to3} \cdot e^{i\beta}}{1 + R_{TE:1\to2} \cdot R_{TE:2\to3} \cdot e^{2i\beta}} \right|^2 \tag{2.2.6}$$

$$R_{TM} = \left| \frac{R_{TM:1\to2} + R_{TM:2\to3} \cdot e^{2i\beta}}{1 + R_{TM:1\to2} \cdot R_{TM:2\to3} \cdot e^{2i\beta}} \right|^2 \tag{2.2.7}$$

$$T_{TM} = \left| \frac{T_{TM:1\to2} \cdot T_{TM:2\to3} \cdot e^{i\beta}}{1 + R_{TM:1\to2} \cdot R_{TM:2\to3} \cdot e^{2i\beta}} \right|^2 \tag{2.2.8}$$

where

$$R_{TE:1\to2} = \frac{p_1 - p_2}{p_1 + p_2}; \quad R_{TE:2\to3} = \frac{p_2 - p_3}{p_2 + p_3} \tag{2.2.9 \& 2.2.10}$$

$$T_{TE:1\to2} = \frac{2p_1}{p_1 + p_2}; \quad T_{TE:2\to3} = \frac{2p_2}{p_2 + p_3} \tag{2.2.11 \& 2.2.12}$$

$$R_{TM:1 \to 2} = \frac{q_1 - q_2}{q_1 + q_2}; \ R_{TM:2 \to 3} = \frac{q_2 - qp_3}{q_2 + q_3} \qquad \text{(2.2.13 \& 2.2.14)}$$

$$T_{TM:1 \to 2} = \frac{2q_1}{q_1 + q_2}; \ T_{TM:2 \to 3} = \frac{2q}{q_2 + q_3} \qquad \text{(2.2.15 \& 2.2.16)}$$

and

$$\beta = \left(\frac{2\pi}{\lambda}\right) \cdot n_2 \cdot h \cdot \cos\theta_2 \qquad \text{(2.2.17)}$$

$$p_j = n_j \cdot \cos\theta_j \qquad (j = 1, 2, 3) \qquad \text{(2.2.18)}$$

$$q_k = \frac{1}{n_k} \cdot \cos\theta_k \qquad (k = 1, 2, 3) \qquad \text{(2.2.19)}$$

It is easier to find optimal values for h if one plots R_{TE}, R_{TM}, T_{TE} and T_{TM} as a function of h. We used the *Mathematica* to plot the graphs. Please notice that the requirement on the film-thickness precision is more generous than what one would expect. T_{TE} remains below 0.2 ($< +10\%$ from the minimum value) even if the thickness fluctuates between 67.7 nm and 99.3 nm. This will make it much easier to fabricate the PBS with high extinction ratios. In order to obtain reasonable yield in our processing, we aim for desired thicknesses of 250.5 nm (83.5 nm + 1× 167 nm) and 417.5nm (83.5 nm + 2× 167 nm) instead of 83.5 nm, trading off transmission through the film with membrane strength.

Based on this design, we can predict the extinction ratios of $\sigma_R = \infty$ dB and $\sigma_T = 7.3$ dB. While the value of σ_R is more than acceptable, σ_T needs to be improved. A disadvantage of a thin-film PBS, as shown in our prediction, is that it shows a low extinction ratio for the transmitted TM mode since transmitted light still contains some TE mode. This disadvantage can be alleviated by employing multi-layer thin-film PBS to filter out more of the remaining TE mode in the transmitted light (Figure 2.5).

R$_{TE}$ and T$_{TE}$
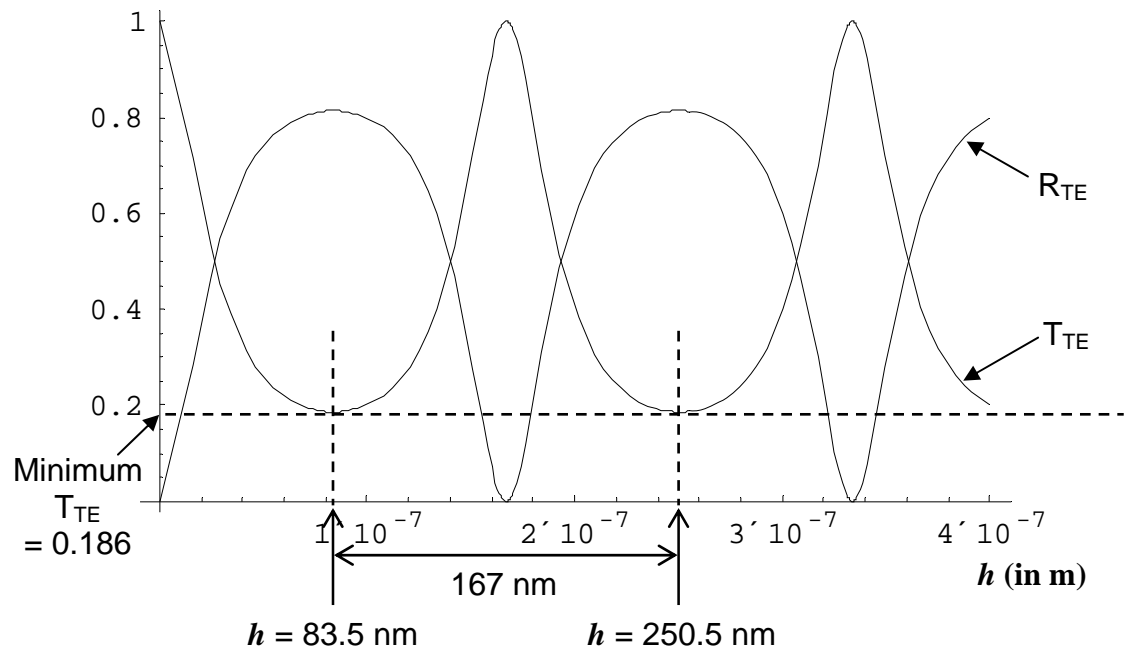
R$_{TM}$ and T$_{TM}$
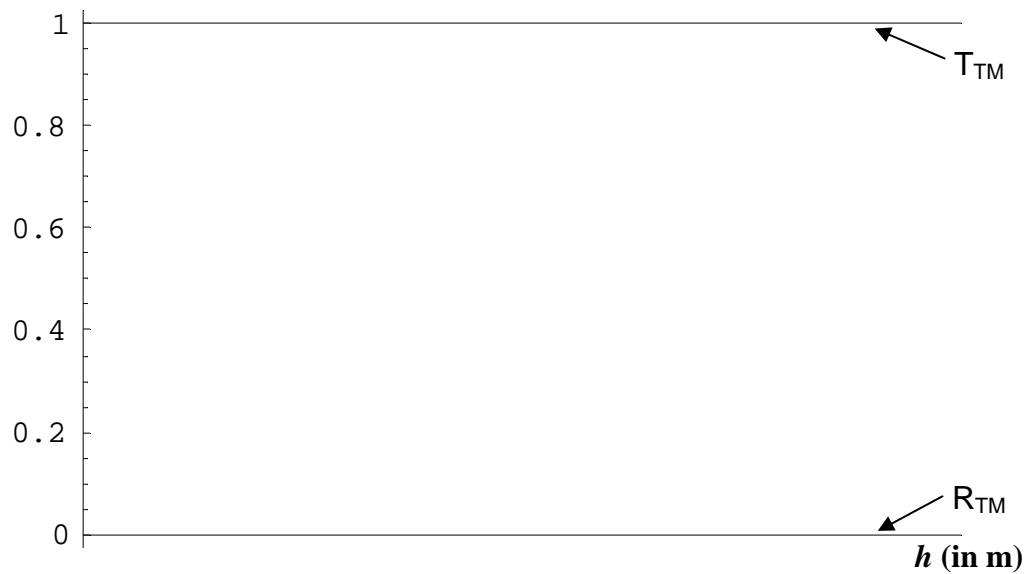
Figure 2.4   Plots of R_{TE}, R_{TM}, T_{TE} and T_{TM} as functions of h: The minimum T_{TE} (or maximum of R_{TE}) happens at 83.5 nm + $y \times$ 167 nm (where y = 0, 1, 2, 3, …). R_{TM} and T_{TM} show minimum reflection and maximum transmission, respectively, at this angle.
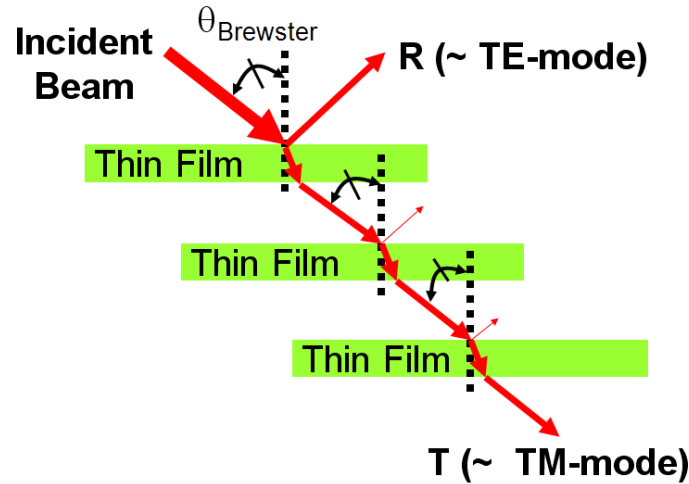
Figure 2.5   Stacked thin-film PBS for improved σ_T.

2.3 Fabrication of MEMS PBS

The fabrication steps we use to make the PBS are shown in Figure 2.6. Using low-pressure chemical-vapor deposition (LPCVD), we deposit a low-stress silicon nitride layer on *p*-type (or *n*-type) silicon wafers, aiming for a thickness slightly greater than the target value (Figure 2.6-1). This fabrication step produces a low-stress silicon nitride layer with tensile stress of ~200 MPa. According to our experiences, the proper range of tensile stress for producing very flat, mechanically robust nitride membrane is between 150 MPa and 200 MPa. If the stress is larger than this range, then the nitride membrane tends to tear off the silicon-wafer surfaces easily. If the stress is too low (< 150 MPa), then the nitride membrane wrinkles up and loses its flatness. After depositing the low-stress nitride layer, we slowly and uniformly reduce the nitride thickness down to the target value in a 160°C, phosphoric acid bath (Figure 2.6-2), at a rate of 4.2 nm per minute. Measurements using NANO Deep-UV System show that the final thickness of the membranes varies from 418.8 to 419.5 nm. Next, we create etch windows by photolithographic-patterning and dry-etching the nitride layer on the backside of the

wafers (Figure 2.6-3). To open the window cavity (4.25mm square), we use 80°C KOH

to etch through 530-μm (+/-5 μm) Si, leaving only the nitride membrane over the cavity

(Figure 2.6-4). On taking the structures out of the KOH bath, it is important to rinse the

structures in cold, running DI water for at least 10 minutes. Although the underlying

mechanism is not clear, this rinsing step greatly improves the cleanness and most of all

the flatness of the silicon-nitride film.
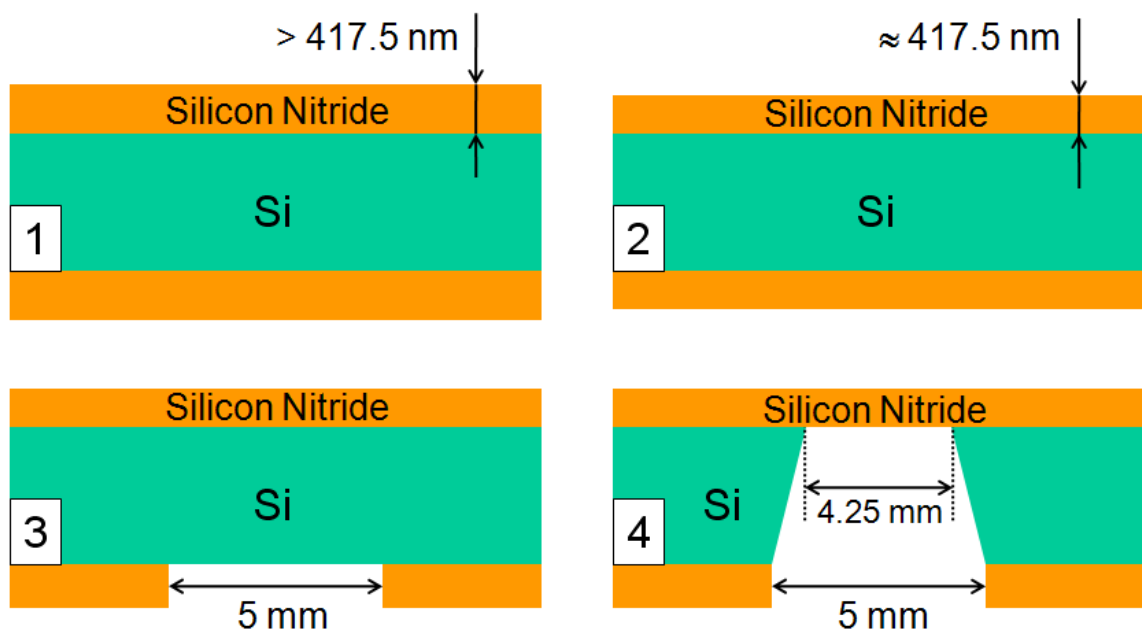
Figure 2.6   Fabrication process for micromachined thin-film PBS

2.4 Test Results of PBS

Our thin-film PBS showed <40% yield (98 out of 256) for thickness of 250.5 nm

and > 60% yield (158 out of 256) for 417.5 nm. As we expected, the thicker film, which

tends to be physically more robust, produced a better yield. Using a WYKO NT3300, we

measure the radius-of-curvature of a typical nitride membrane to be 51 m; the membranes

are virtually flat! Figure 2.7 shows several of the fabricated membranes: single-, double-,

and triple-layer nitride membrane PBS. For a multi-layered PBS, membranes are stacked at an angle to clear the optical path for transmitted light.
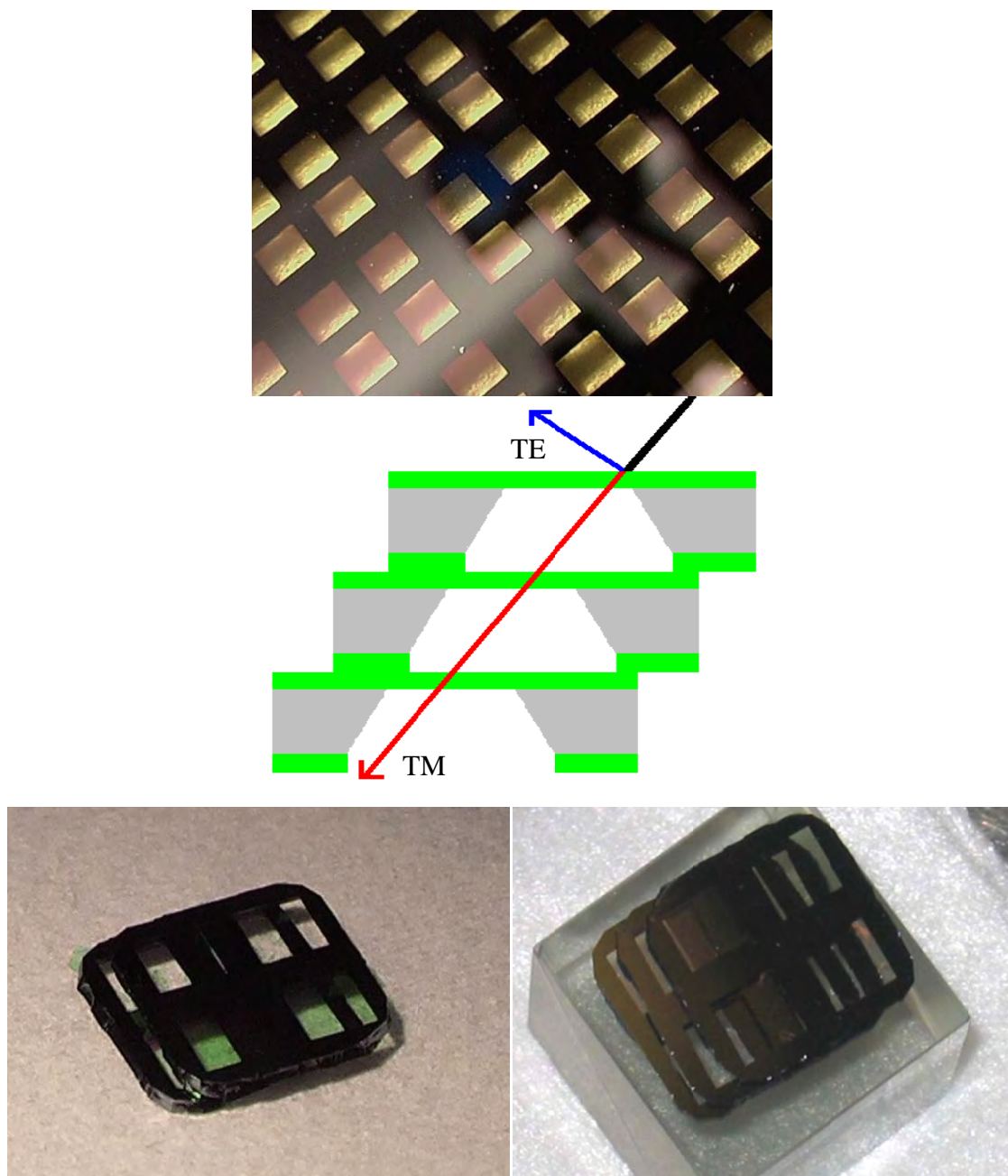
Figure 2.7   Pictures of fabricated PBS's

To test our silicon nitride membrane PBS, a 635-nm beam from a laser diode was directed at the surfaces of both single- and stacked-PBS devices at the film Brewster angle (64.5°) (Figures 2.8 and 2.9). The transmitted and reflected rays from the test structures were then passed through two Tech Spec™ 15mm High-Efficiency Polarizing-Cube-Beam Splitters (reflection efficiency > 99.5%, transmission efficiency > 95%, Edmund Optics Part No. C47-125) using the system shown in Figures 2.8 and 2.9. The intensities of both TE and TM components were then measured using a photo detector. The insertion losses and extinction ratios derived from these measurements are listed in Table 2.1. Very good performance is demonstrated by the new MEMS PBS structures: extinction ratios (σ_R for reflected and σ_T for transmitted light) of (21dB, 10dB), (21dB, 14dB), and (21dB, 16dB) for single-, double-, and triple-layer systems, respectively with corresponding insertion losses of 3, 10, and 13%. The stacked PBS devices clearly exhibit the expected improvements over single-layer splitters in the transmitted extinction ratios. Also, as shown in Table 2.2, the performance of the stacked-PBS devices is comparable to that of a commercially available PBS.
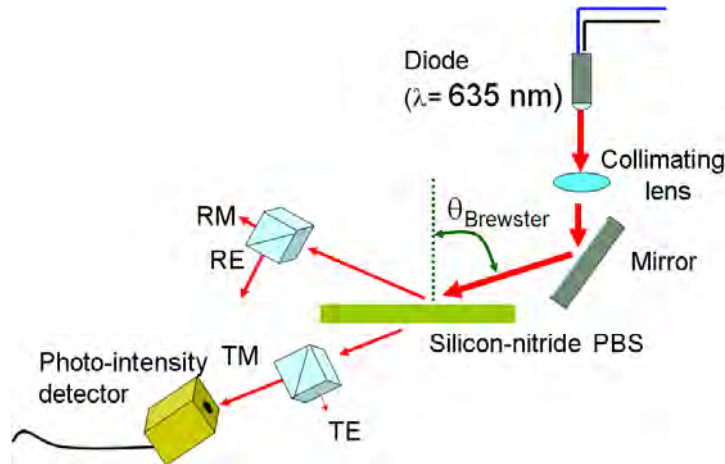
Figure 2.8   Schematic diagram of the measurement setup for silicon-nitride PBS
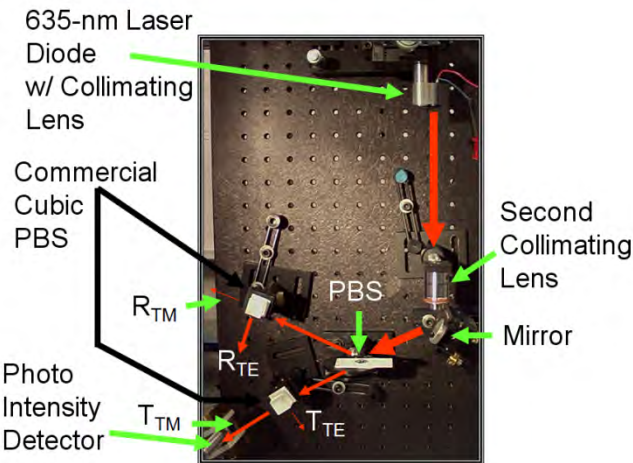
Figure 2.9   Picture of the measurement setup for silicon-nitride PBS

Table 2.1   Performance of single-, double-, and triple-layer silicon-nitride PBS's
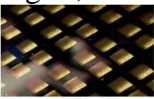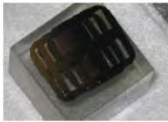
	Single-Layer	Double-Layer	Triple-Layer
σ_R (dB)	21	21	21
σ_T (dB)	10	14	16
Insertion Loss (%)	3	10	13

Table 2.2   Comparison between silicon-nitride PBS and commercially available PBS

Operating Wavelength (nm)	632.8	632.8
σ_R (dB)	21	>20
σ_T (dB)	16	15-30
Cost per PBS	US $1.14*	US $100-200

2.5 Conclusions

      We have built and characterized batch-processed polarization beam splitters (PBS), important optical components to separate the orthogonal TE and TM components of light. The devices were fabricated from thin-film, low-stress silicon nitride membranes

and showed excellent performance. Extinction ratios (σ_R for reflected and σ_T for transmitted light) of (21dB, 10dB), (21dB, 14dB), and (21dB, 16dB) for single-, double-, and triple-layer systems, respectively with corresponding insertion losses of 3, 10, and 13%. The stacked devices clearly showed improved in performance, especially in the extinction ratio for the transmitted light.

References

[1]   C. Pu, Z. Zhu, and Y.-H Lo, "Surface Micromachined Integrated Optic Polarization Beam Splitter," *IEEE Photonics Technology Letters*, 1998, pp. 988–990.

[2]   D. R. Ciarlo, "Silicon Nitride Thin Windows for Biomedical Microdevices," *Biomedical Microdevices*, vol. 4, no. 1, 2002, pp.63-68.

[3]   M. Born, and E. Wolf, *Principles of Optics, Seventh Edition*. Cambridge, UK; Cambridge University Press, E.1999.

CHAPTER 3

Simple Fabrication Process for Self-Aligned, High-Performance Microscanners;
Demonstrated Use to Generate a Two-Dimensional Ablation Pattern

3.1 Introduction

Many researchers have been motivated to develop simpler, more cost-effective scanner-fabrication technologies because the commercial markets that have resulted from the macro-scale torsional-scanner (galvano-scanner) technology are mature and lucrative. The scanners are labeled "torsional" because they consist of mirrors supported by beams that are torsionally flexed in order to direct a light beam through an arc. Scanners are essential components for applications such as optical switches in telecommunication networks [1], high-definition and retinal displays for entertainment, engineering, and educational markets [2, 3, 4, 5], bar-code scanning for inventory monitoring, endoscopic, confocal, and coherent tomography imaging in biomedical fields [6, 7, 8], range-finding systems for safe-vehicular navigation, and free-space laser communications [9].

A number of previous researchers have used the methods that are generally identified as "microelectromechanical-system (MEMS) technologies" to fabricate microscanners in order to exploit the precise-design and mass-production advantages afforded by this choice. Specific results as reported for this earlier research demonstrate, however, that there are pitfalls that lead to undesirable complexity, lowered processing yields, and other difficulties. A major problem area is centered on actuation of the microscanners.

Torsional microscanners typically require substantial torque and to produce this torque by electrostatic drivers, previous research [10] has shown the effectiveness of using vertically offset comb pairs for the drivers. Fabrication of these vertically offset combs has been a considerable challenge to earlier MEMS technologists, who have found solutions using demanding procedures such as: (a) carrying through critical-alignment steps in a two-wafer process [10]; (b) controlling and replicating the properties of materials like photoresist or bimorph layers so that these materials can function as hinges [11]; (c) post-process-annealing in a high-temperature furnace following the hand assembly of lids on device chips [12]; and (d) depositing multiple-masking layers (composed of silicon dioxide and silicon nitride) [13] to create the offset combs. We decided to focus our research on the development of fabrication methods that would produce vertically offset comb pairs using more conventional IC processing tools.

In this chapter, we discuss a CMOS-compatible MEMS technology that we have developed and demonstrated for batch-fabricating high-performance torsional microscanners. Our microscanner-fabrication technology employs only conventional silicon-processing tools that have proven their effectiveness and user-friendliness through large-scale use in the integrated-circuits industry. The required temperatures for all of our processing steps are low enough to allow pre-fabrication of CMOS electronics directly on the same wafer as the microscanner devices. The yield for this new scanner process has exceeded 70% on two fabrication runs (*116 devices per wafer, 2 wafers per run*) made in the UC-Berkeley Microlab.

Operational tests on the fabricated microscanners show that they easily meet the performance requirements for many applications in the biomedical, telecommunication,

and imaging-systems areas. To demonstrate the microscanner performance, we have investigated a particular application for which we find our design to be well suited: refractive laser surgery of ocular corneas where small spot size and high scan speeds are important assets [14]. In ocular refractive surgery, surgeons need to steer and control laser pulses to reshape a patient's corneas in order to improve his vision. To demonstrate this use with our microscanners, we have employed them to generate ablation-emulation results that are superior to published emulation patterns that had been produced by commercial, state-of-the-art, eye-surgery microscanners [14].

There are potentially many additional MEMS applications for the robust, high-performance comb drivers introduced in this chapter. As a result of their fabrication using only conventional IC-processing tools, there is excellent control of critical dimensions such as comb-finger spacings. These spacings are determined by a single photomasking step which allows them to be as small as two-times the alignment accuracy of the photolithography process (which is 2×7 nm = 14 nm for Nikon NSR-S609B). However, the practical minimum gap sizes are typically 1 μm wide or larger because they are determined by the fabrication process limitations and variations such as an achievable aspect ratio of a DRIE process as well as the side-wall erosions commonly observed in plasma-etch processes. Minimizing gap spacing reduces the driving voltage needed to provide a given force. As an example we consider a typical design in which vertical combs having gaps of 3 μm, widths of 5 μm, and lengths of 100 μm, are laid out using 25 % of the comb-drive area for supporting structures. With this design, finished combs will exert an out-of-plane force density of 13.8 μN / cm^2 / V^2. Comb drives having this force density can be used advantageously in many ways; for example, in adaptive optics

for mirror-curvature adjustments [15], in vertical inch-worm motors [16], in phase-shifting interferometers [17], and also, in acoustic speakers. In yet another application, by producing a capacitance change of 27.6 pF/cm^2 per μm of out-of-plane motion, the combs can gainfully be applied to the design of *z*-axis accelerometers, to innovative microphone technologies, and to microstage positioning systems.

3.2 Design, Fabrication, and Characterization

3.2.1 Microscanner Design

We have investigated three different designs of microscanners as pictured in Figure 3.1.
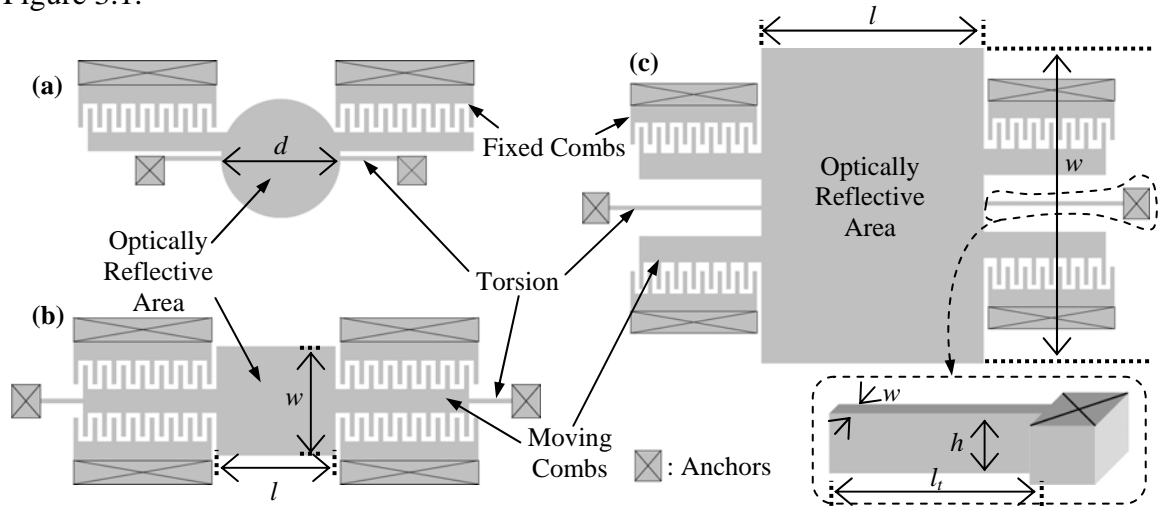
Figure 3.1   Three different microscanner designs: (a) fast microscanner with a circular scanning area (or optically reflective area); (b) very fast microscanner with a rectangular scanning area; and (c) slow microscanner with an extra large scanning area; inset at lower right is a plan view showing the dimensions of the microscanner support beams

For each of these three designs, we have varied the dimensions (diameters of circular reflective areas or lengths and widths of rectangular reflective areas) of the optically reflective areas as along with the lengths and the widths of the torsion beams. To predict

the resonant frequencies of these designs, we calculate the torsional stiffness of the beams using Timoshenko's equation [18].

$$k_t = \frac{1}{3} G(w_t)^3 \left(\frac{h_t}{l_t} \right) \left[1 - \frac{192}{\pi^5} \frac{w_t}{h_t} \sum_{n=1,3,5,...}^{\infty} \frac{1}{n^5} \tanh \left(\frac{n \cdot \pi \cdot h_t}{2 w_t} \right) \right]; \; h_t > w_t \qquad (3.2.1)$$

In Eq. 3.2.1, G is the torsional modulus for silicon, and w_t and h_t are the width and height of the beam, as indicated in the bottom-right inset to Figure 3.1. The microscanner resonant frequency is given by

$$f_r = \frac{1}{2\pi} \sqrt{\frac{k_t}{I_m}} . \qquad (3.2.2)$$

where I_m is the mass-moment of inertia of the microscanner (given in Table 3.2), the value of which depends on the microscanner geometry and is readily calculated [19].

Table 3.1 lists the dimensions of the microscanner embodiments investigated and their predicted resonant frequencies (using Eq. 3.2.2). By making various combinations of reflective areas of different sizes and torsion beams of differing dimensions (resulting in different torsional stiffnesses) as listed in Table 3.1, we designed microscanners having predicted resonant frequencies ranging from 50 Hz to 26 kHz. This wide range of resonant frequencies can address the requirements for microscanners having many different applications.

Table 3.1 Parameter Variations for Microscanner Embodiments

	Large Rectangular Microscanners	Circular Microscanners	Rectangular Microscanners
Dimensions: Reflective Area*	l: 3 mm w: 6, 7, or 8 mm t_{SOI}: 50 μm	d: 0.5 or 1 mm t_{SOI}: 30 μm	l: 1, 1.5, or 3 mm w: 0.5, 1, or 1.5 mm t_{SOI}: 50 μm
Dimensions: Torsion Beams	l_t: 1 mm w_t: 10, 15, 20, or 30 μm h_t: 25 or 50 μm	l_t: 0.2, 0.3, 0.4, or 0.5 mm w_t: 10 or 20 μm h_t: 30 μm	l_t: 0.4, 0.6, 0.8, or 1 mm w_t: 33.3, 40, or 50 μm h_t: 50 μm
Moment of Inertia*	$\dfrac{\rho_{Si} \cdot t_{SOI} \cdot l \cdot w^3}{12}$	$\dfrac{\pi \cdot \rho_{Si} \cdot t_{SOI} \cdot d^3}{64}$	$\dfrac{\rho_{Si} \cdot t_{SOI} \cdot l \cdot w^3}{12}$
Predicted f_r	50-230 Hz	1-10 kHz	4-26 kHz

*t_{SOI}: Thickness of the device layer of SOI wafer; and ρ_{Si}: Density of silicon (2330 kg/m^3)

3.2.2 Microscanner Fabrication

The microscanner fabrication process, which involves the use of three photolithography masks (two for defining features in the device layer of a SOI wafer and one for opening the backside of the microscanners), is illustrated in Figure 3.2.

a. We start with an <100> n-type SOI wafer (device-layer thickness: 30 or 50 μm, resistivity: 0.005-0.01 Ω-cm) and grow 0.5μm thermal oxide at 900 °C or deposit low-temperature oxide (LTO) at 400 °C. LTO must be chosen if it is necessary to ensure that the fabrication process remains completely CMOS-compatible. Because the oxide layers serve only as protective layers, the LTO layer does not need to go through a densification process at high temperatures (which would typically exceed 950 °C). Next, using the photolithography mask #1, we pattern and remove the oxide (thermal or LTO) selectively where fixed combs will be later fabricated and vertically thinned (Figure 3.2-a).

b. Using mask #2, we define patterns for the microscanners, including moving/fixed combs, flexures, and the geometries of the reflective area, on the top surface of the device layer (Figure 3.2-b). The fixed combs must be defined within the windows from which the oxide has been removed to expose the silicon surface in the

previous step, and the minimum gap between the moving and fixed comb fingers can be as small as twice the alignment accuracy of the photolithography system.

c. After hard-baking the patterned photoresist at 120°C for one hour, we first perform anisotropic oxide etch and then use deep-reactive-ion-etch (DRIE) to pattern the microscanner structures (including the optically reflective area, comb fingers, and flexures) in the device layer of the SOI wafer (Figure 3.2-c).

d. Once the DRIE etching is complete, we remove the photoresist layer and deposit a very thin layer (~0.2 μm) of thermal oxide or LTO, in order to stop erosion of the sidewalls of the structures that were created in the previous step (Figure 3.2-d). After this thin oxide has been deposited, there are 0.2μm-thick oxide layers on top of the fixed-comb fingers and approximately 0.7μm-thick oxide layers on all other surfaces including, especially, the top surfaces of the movable-comb fingers and of optically reflective surfaces.

e. Following the oxide growth (or deposition), we perform a timed anisotropic-plasma-oxide etch to remove the 0.2μm-thick oxide from the top-facing surfaces. This step exposes the silicon surface on top of the fixed combs, but leaves all other surfaces covered by an approximately 0.5μm-thick oxide layer (Figure 3.2-e).

f. In a next step, we use a timed plasma etch that erodes silicon isotropically to etch the exposed top surfaces of the fixed combs, thinning only these fingers because all other surfaces of the structures are still protected by an oxide layer (see Figures 3.2-f, 3.3-b, and 3.4).

g. Using mask #3, we then pattern and open the backside of the microscanners, and release the devices in concentrated HF followed by critical-point drying (CPD) (Figure 3.2-g).

70

Top View   **Cross-section View**

Handling Layer of
SOI Wafer

Device Layer of
SOI Wafer

Photoresist

Buried Oxide

Thermal Oxide
(Or LTO)
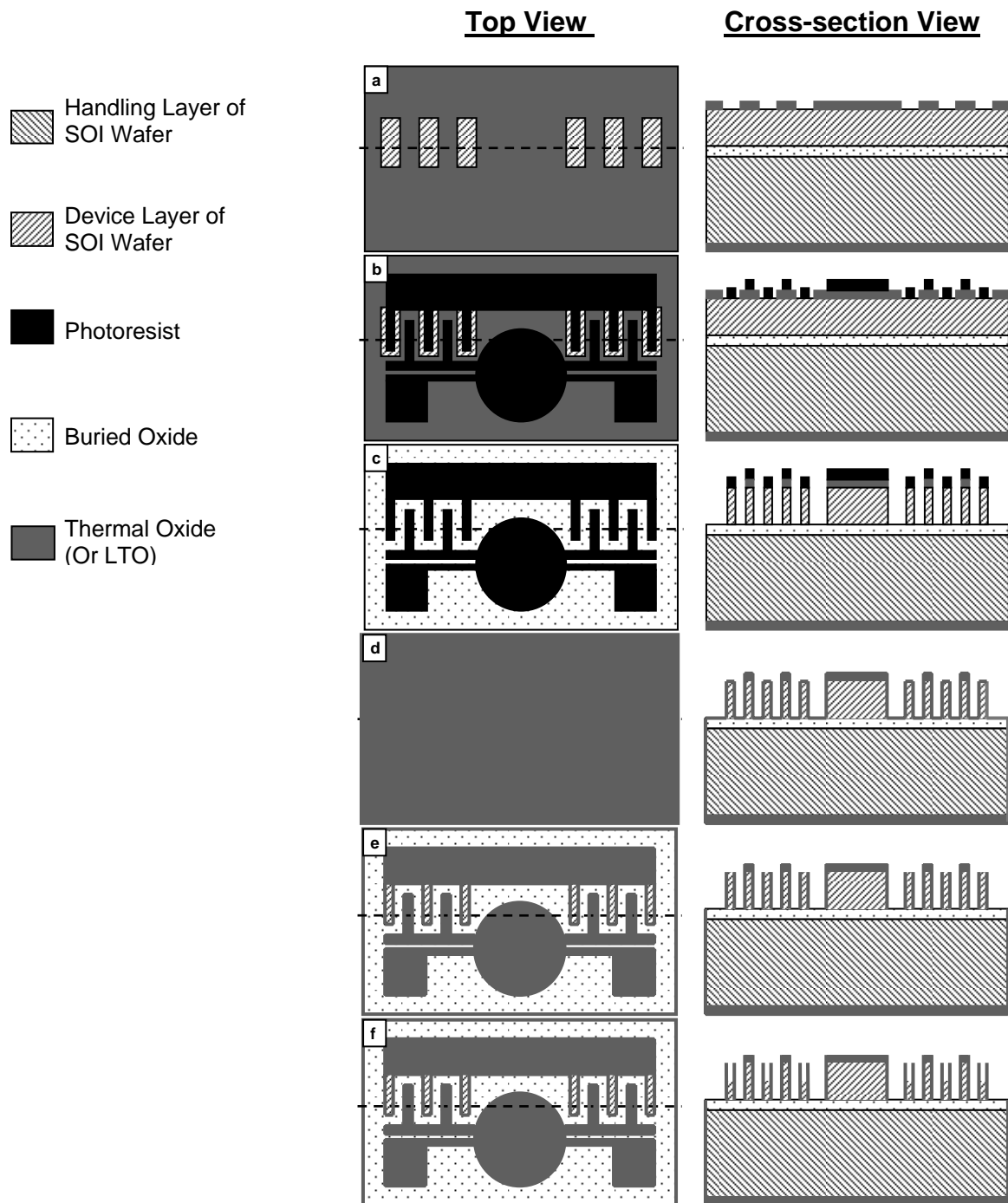
(Figure 3.2 continued on the next page)

(Figure 3.2 continued)
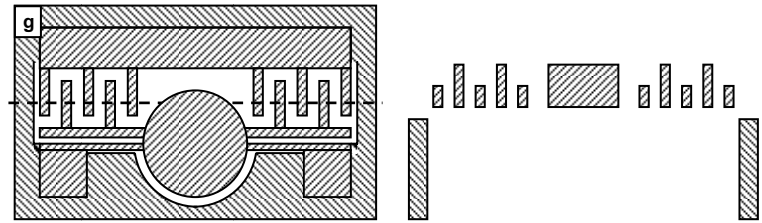
Figure 3.2   Fabrication process for torsional microscanners with self-aligned, vertically offset combs: The left column shows top views while the right column shows cross-sectional views along the dotted lines following completion of the processing steps described in the previous section.

Comment on the need for steps d and f, thin-oxide deposition and selective removal: In theory, the process described above might be simplified through omission of steps d through f, replacing them by an anisotropic etch which should erode only the exposed fixed-comb tops. In practice, we have found, however, that anisotropic silicon etch does, in fact, erode surfaces that are not perpendicular to the beam causing considerable silicon removal from the comb sidewalls.

(a) Using anisotropic silicon etch   **(b)** Using oxide layer and isotropic silicon etch
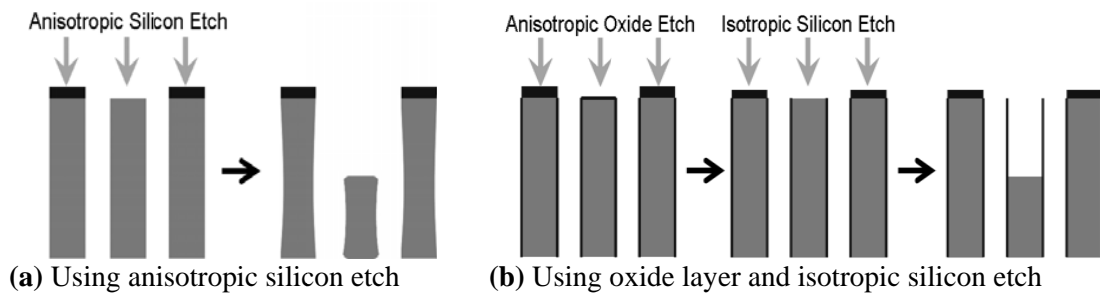
Figure 3.3   Etch methods to produce offsets to the comb fingers

This erosion leads to unacceptable control of comb-finger widths and of the gaps separating the fingers. Accordingly, we have added the thin-oxide deposition and selective removal steps to produce our microscanners.

Figure 3.4 shows SEM images of moving- and fixed-combs taken immediately following completion of the timed-isotropic silicon etch described in process step f and shown in Figure 3.2-f. The vertically etched top surfaces as well and the remaining oxide

shells are clearly visible. Compressive stress in the silicon dioxide layer is the source for the waviness of the vertical oxide shell. The oxide waviness does not have any effect on the final shape of the silicon comb fingers, as shown in Figure 3.5.
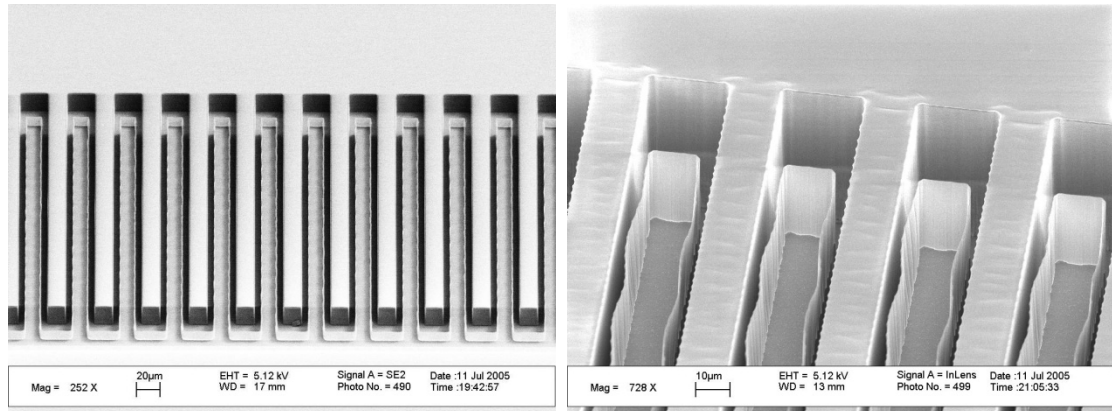
Figure 3.4   SEM images of moving- and fixed-comb fingers after completing fabrication step f (Figure 3.2-f): The upper two images show offset combs being processed on SOI wafers with a 30-µm device layer (offset height: 15 µm) while the lower two images show offset combs being processed on SOI wafers with a 50-µm device layer (offset height: 25 µm).

Figure 3.5 shows SEM images of released combs (following step g above); the comb fingers are clearly vertically offset, sharply defined, and precisely aligned. The top surfaces of the isotropically etched fixed-comb fingers are visually as smooth as the surfaces of the adjacent unprocessed comb-fingers that form the moving-comb pair.
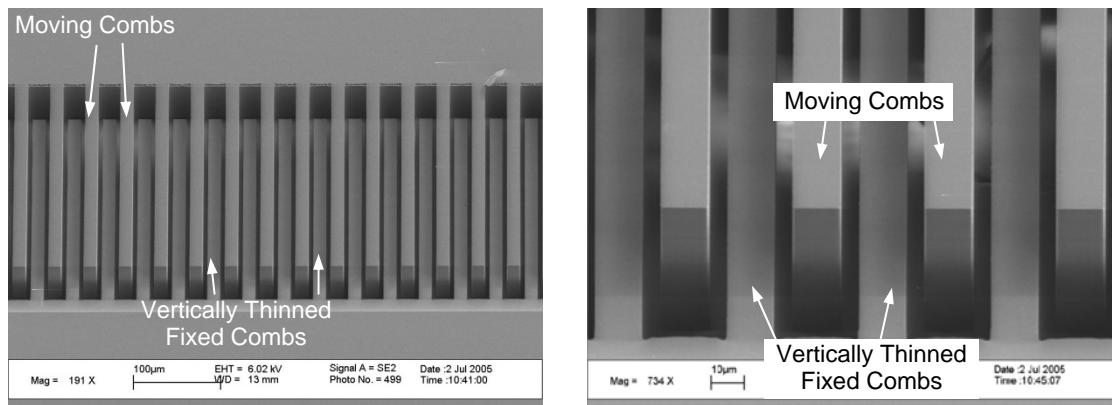
Figure 3.5   SEM images of moving- and fixed-comb fingers after HF release (process step g) – The completely processed comb fingers have sharp, well-defined rectangular shapes with very smooth surfaces, regardless of having undergone the silicon isotropic etch step or not.

Using a WYKO NT3300 Optical Surface Profiler, we measured the offset heights of vertically offset comb fingers around the wafers. The measurements were made at five locations, 2 cm from the outer perimeter of 10-cm processed wafers (Figure 3.6). The peak-to-peak deviations at five locations shown in Table 3.2 are smaller than the thickness fluctuations stated in the specifications for the device layers of SOI wafers (typically 0.5 - 2 μm), and they show excellent uniformity for the new process.

3-D Profile
(WYKO Measurement)
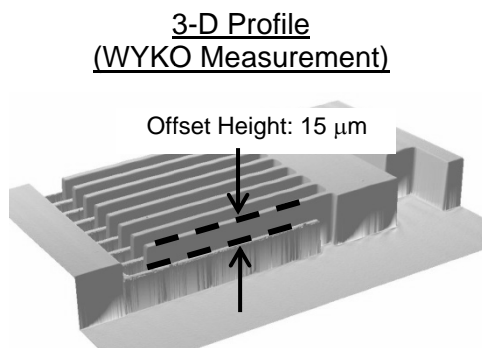
Offset Height: 15 μm

Table 3.2   Deviation from the Average Value (15μm)

Center	Left	Right	Top	Flat
+1.53%	-1.38%	+0.13%	+0.90%	-0.28%
+0.23μm	-0.21μm	+0.02μm	+0.14μm	-0.04μm

Figure 3.6   3-D profile measurements of vertically offset combs and the uniformity of offset heights at five locations on a 10-cm processed wafer: The measurements were made at its center and at locations, 2 cm from the outer edge of the wafer. The values are peak-to-peak deviations from the average value.

3.2.3 Properties of Fabricated Microscanners

SEM pictures of fabricated microscanners are shown in Figure 3.7.
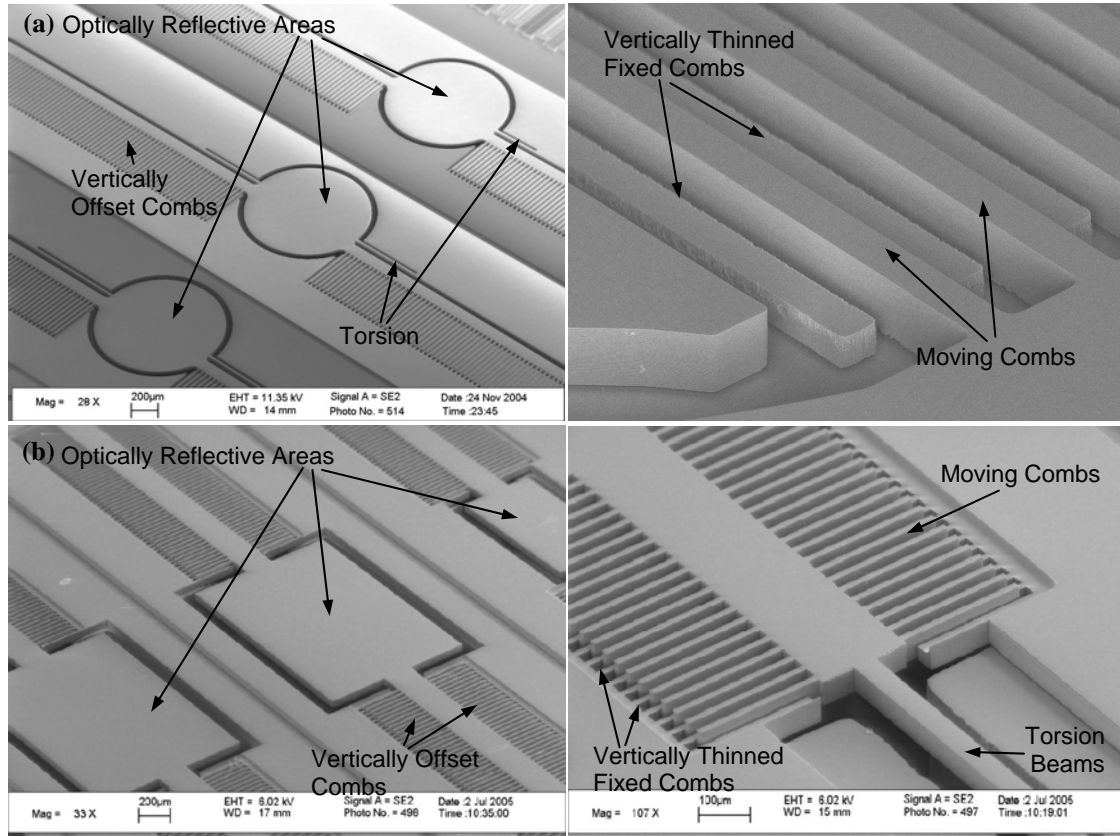
Figure 3.7   SEM pictures of fabricated microscanners: (a) fast circular microscanners – only LTO has been used in the fabrication process; and (b) very fast rectangular microscanners – only thermal oxide has been used in the fabrication.

Our fabrication process has produced high yields on two separate fabrication runs (116 micromirrors per wafer, 2 wafers per run). Between 70 and 85% of tested microscanners perform properly on all of the wafers. Damages to microscanners mostly occurred during step g, the final HF-release/rinsing/critical-point-drying step as a consequence of rough handling.

Table 3.3 shows the resonant frequencies (f_r), quality factors (Q), and maximum optical-scan angles (OSA) at resonance measured for selected microscanners driven with

sine waves having the tabulated rms amplitudes. Here, OSA is defined as an angle that is twice the mechanical-scan angle that a microscanner physically rotates. Resonant frequencies of the fabricated microscanners ranged from 58 Hz to 24 kHz. The maximum resonant amplitudes achieved by the microscanners ranged from 8 to 48°, with most microscanners exhibiting OSA of 20° ± 5°. The actuation voltages ranged from 14.1 – 67.2 V_{ac_rms}. Figure 3.8 shows the frequency response measured for five different microscanners

Table 3.3   Resonant-motion properties of representative microscanners

f_r	Q	OSA	V_{ac} (rms)	Dimensions
58 Hz*	40	20.8 °	14.1	l = 3 mm w = 8 mm
6.01 kHz**	67	24.2 °	26.4	d = 1 mm (Circular Microscanner)
8.89 kHz**	70	22 °	34.9	d = 1 mm (Circular Microscanner)
12.5 kHz ***	180	48 °	67.2	l = 1.5 mm w = 1 mm
24 kHz***	300	17 °	35.2	l = 1 mm w = 0.5 mm

*: Slow large rectangular microscanner; **: Fast circular microscanners;
***: Very fast rectangular microscanners
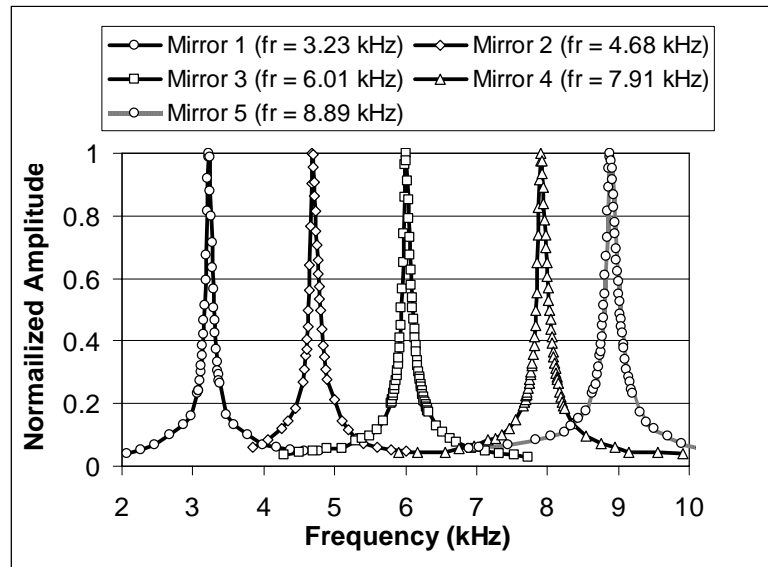
Figure 3.8   Frequency responses of selected microscanners with circular reflective areas

3.3 Microscanner-Application Example: Emulating a Cornea-Ablation Process

In order to evaluate our microscanners in a "real-world" application, we investigated their possible application to the task of refractive laser surgery of ocular corneas. Scanners used for this purpose should be effective in steering very small laser beams at high scan speeds [14]. The purpose of the surgery is to reshape optical corneas by ablating tissue in order to correct optical aberrations as shown in Figure 3.9.
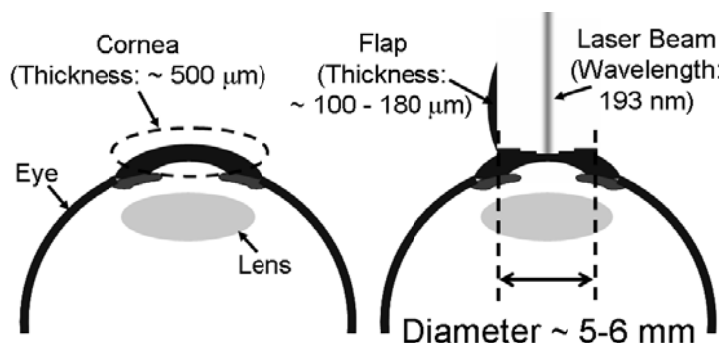
Figure 3.9   Ocular refractive surgery: Using a microkeratome (a very fine blade), a corneal flap is cut open. Then using a laser (wavelength: 193-208 nm), the exposed inner tissue of the cornea is selectively ablated to correct optical aberrations and thereby improve the patient's vision.

Ablation of human corneas is a cumulative process, as shown in Figure 3.10. Only the section of the laser pulse having an energy level higher than the threshold value (50-60 mJ/cm^2) causes ablation [14, 20]. The depth of the ablated tissue is proportional to the logarithm of the laser-pulse energy [20].

(a) Pulse Energy

Ablation Threshold

Pulse Diameter

(b) No Ablation — Ablation Target

(c) Single Ablation — Single Ablation

(d) Two Ablations

(e) Multiple Ablations — Spherical Profile
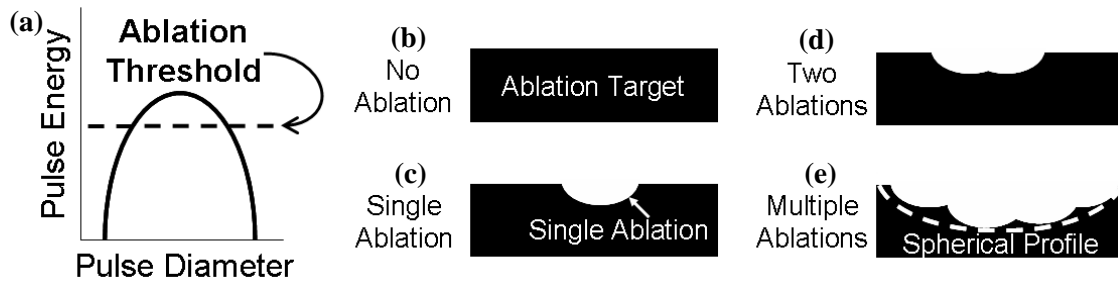
Figure 3.10 Summary of ablation process for refractive surgery: (a) only that part of the laser pulse having energy density above an Ablation-Threshold value, will ablate the target; (b) no ablation performed; (c) ablation pattern generated by applying a single laser pulse having the pulse-energy distribution shown in (a); (d) ablation pattern generated by applying two subsequent laser pulses; (e) spherical profile generated by applying multiple, coordinated laser pulses

To demonstrate this application, we assembled a two-dimensional scanning system by orienting two identical microscanners at right angles to one another (Mirror #3 in Figure 3.8, mirror diameter = 1 mm, resonant frequency = 6.01 kHz) and scanned a pulsed laser beam (670nm wavelength). The cross-coupled scanners were driven by two 6.01-kHz sine waves that were 90° out of phase, producing circular patterns having radii fixed by the amplitude of the driving voltage with an intensity governed by the modulated laser. For cornea ablation, circular scanning provides for an excellent match to the cornea's geometry and is therefore favorable over the more typical raster scanning which uses linear sweeps by horizontal- and vertical-scanning mirrors to trace out a pattern.

Circular Raster Scanning
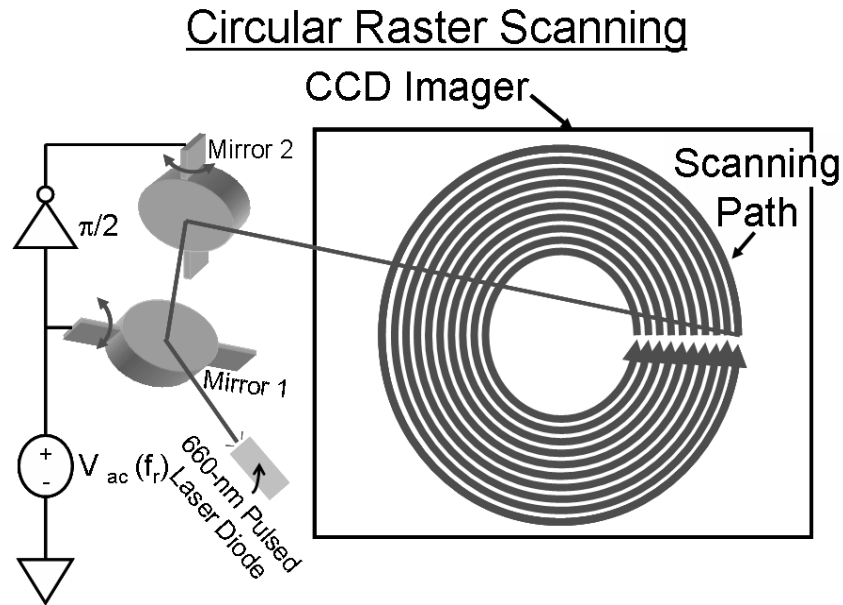
Figure 3.11 Two-dimensional scanning system realized using a pair of identical microscanners
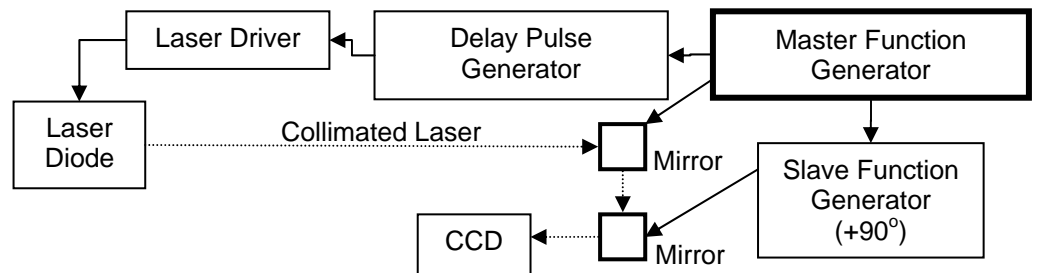
Figure 3.12 Schematic diagram of experimental set-up using scanners to generate cornea ablation patterns

In the ablation system, laser spots forming the pattern persist for 0.4μsec and have a 220-μm diameter (full width/half maximum) as measured with a CCD optical sensor. The wavelength of the laser is 660 nm. A CCD sensor, positioned in place of the ocular cornea, allows us to assess performance of the system. As mentioned earlier, refractive laser surgery is a cumulative ablation process [14]. To mimic the real process, we capture the scanning pattern at each CCD frame and then sum the intensity profiles which are proportional to the final ablation pattern. The usual period of time for optical laser surgery is shorter than 20 minutes so we measured the repeatability and stability of our

system over a period of 30 minutes (Figure 3.13). Our system demonstrates excellent repeatability in pulse position (standard deviation less than 0.56μm) as well as in pulse diameter (standard deviation less than 0.68μm) around the ablation zone.
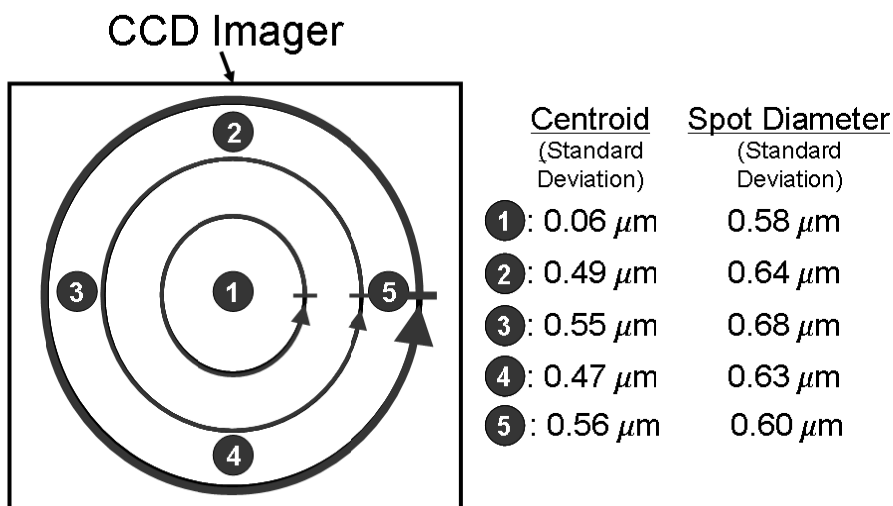
Figure 3.13   The stability and repeatability of our 2-D scanning system within 30 minutes

To demonstrate the versatility of our area scanner, we have emulated a small pattern from the surface topography found on a US Roosevelt dime. The 3-D topology of the region of interest on the US dime was measured using a WYKO NT3300 and is shown in Figure 3.14 (b) and (c) as well as in Figure 3.15 (a). The height information was then converted into a gray-scale image (0-255 level), which is easier to utilize for ablation process.
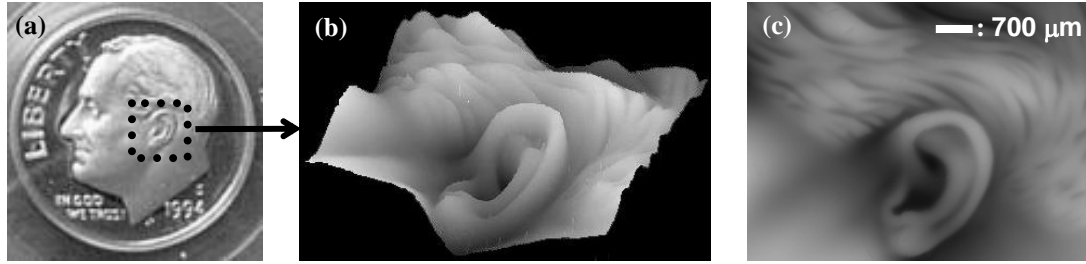
Figure 3.14   Selected ablation target pattern: (a) picture of a US dime; (b) 3-dimensional profile of the region of interest indicated by the dotted circle (measurements by using WYKO NT 3300); and (c) 3-dimensional profile converted to a gray-scale image (based on height information), which is more convenient for emulating the ablation process

Next, according to the gray-scale image, we have built up an ablation pattern over a 40-minute interval. The resultant pattern is shown in Figure 3.15 (b). Because the scanning spot was 220 μm in diameter, some of the very fine details were lost. Yet, overall, the emulated ablation image contains many details and shows good-quality depiction of the original target pattern.
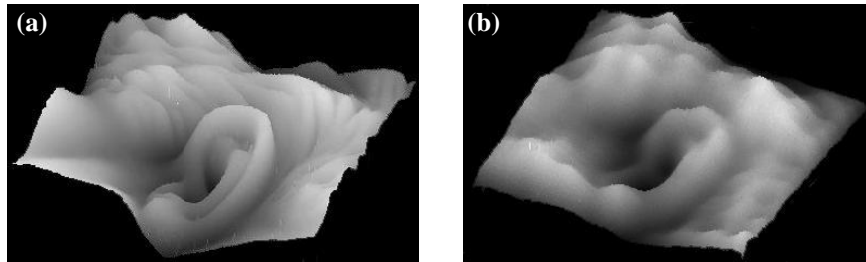
Figure 3.15   (a) WYKO 3-D surface profile (Figure 3.14(b) repeated); (b) 3-D ablation replica of the dime surface captured by our microscanner and CCD system (peak-to-valley height difference is approximately 93 μm on the original surface)

Figure 3.16 shows a similar result presented by researchers to demonstrate their ablation capabilities using a state-of-the-art refractive surgery system [14]. By comparing Figure 3.15 (b) with the images shown in Figures 3.16 (b) and (c), we can judge at least qualitatively that the microscanner ablation system that we have presented performs very well as compared to presently available macro-sized tissue-ablation systems.
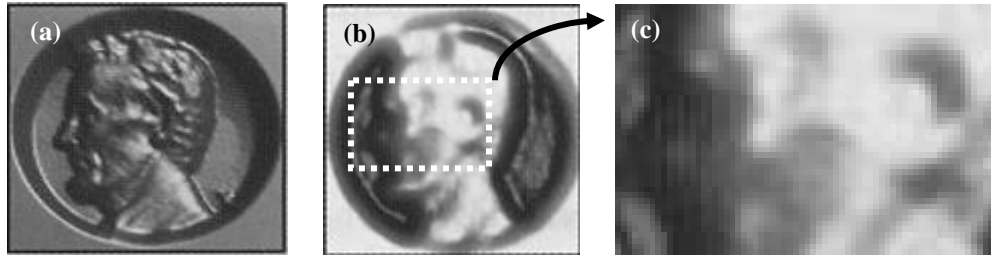
Figure 3.16 Laser-ablation pattern produced by a commercially available system: (a) surface topology of an US penny (target pattern); (b) reproduced pattern using a state-of-the-art refractive surgery system; (c) magnified image zoomed in around the ear of the reproduced pattern (after J. F. Bille, C. F. H. Harner, and F. H. Loesel [14]) Figure 3.15 (b) can be compared to Figure 3.16(c) for an evaluation of performance of our ablation scanning system with the performance of a commercial system (VISX STAR S4).

3.4 Conclusions

We have designed, fabricated, and tested microscanners using our new fabrication techniques. The process uses well-developed integrated-circuit processing tools, and is simple, high-yielding, and reliable. The major advance in our fabrication process results from its straightforward method to produce vertically offset comb pairs that provide for robust electrostatic drive of torsion-bar suspensions. In practice, we achieve uniform offset-heights for vertical comb fingers processed across the 10-cm wafers. We have produced microscanners having resonant frequencies ranging from 50 Hz to 24 kHz having OSA values typically approximating 20° but varying from 8 to 48°. The actuation voltages required were from 14.1 to 67.2 V_{ac_rms}.

A 2-D scanning system, built using these microscanners, produced emulated ablation patterns that compare favorably to results published by researchers to illustrate the performance of a state-of-the-art macro-scale ablative surgery system.

References

[1] M. Ward and F. Briarmonte, "Lucent's new All-Optical Router uses Bell Labs Microscopic Mirrors," *Bell Labs innovations in the news*, Nov. 10, 1999 (http://www.bell-labs.com/news/1999/november/10/1.html).

[2] Microvision, Inc., 6222 185th Ave NE, Redmond, WA, 98052 USA (http://www.microvision.com).

[3] H. Urey, "MEMS Scanners for Display and Imaging Applications," *Proceedings of SPIE – Volume 5604: Optomechatronic Micro/Nano Components, Devices, and Systems*, pp. 218-229, October 2004.

[4] Y. C. Ko, J. W. Cho, Y. K. Mun, H. G. Jeong, W. K. Choi, J. H. Lee, J. W. Kim, J. B. Yoo, and J. H. Lee, "Eye-type scanning mirror with dual vertical combs for laser display," *Proceedings of SPIE – Volume 5721: MOEMS Display and Imaging Systems III*, pp. 14-22, January 2005.

[5] M. Yoda, K. Isamoto, C. Chong. H. Ito, A. Murata, S. Kamisuki, M. Atobe, and H. Toshiyoshi, "A MEMS 1D optical scanner for laser projection display using self-assembled vertical combs and scan-angle magnifying mechanism," *The 13th International Conference on Solid-State Sensors, Actuators and Microsystems - TRANSDUCERS 2005*, vol. 1, pp. 968-971, June 2005.

[6] Y. Haga and M. Esashi, "Biomedical microsystems for minimally invasive diagnosis and treatment," *Proceedings of the IEEE*, Vol. 92, No. 1, pp. 98-114, January 2004.

[7] U. Hofmann, S. Muehlmann, M. Witt, K. Dörschel, R. Schütz, and B. Wagner, "Electrostatically driven micromirrors for a miniaturized confocal laser scanning microscope," *Proceedings of SPIE – Volume 3878: Miniaturized Systems with Micro-Optics and MEMS*, pp. 29-38, September 1999.

[8] H. Miyajima, M. Nishio, Y. Kamiya, M. Ogata, and Y. Sakai, "Development of two dimensional scanner-on-scanner for confocal laser scanning microscope LEXT series," *IEEE/LEOS International Conference on Optical MEMS and Their Applications 2005*, pp.23-24, Oulu, Finland, August 2005.

[9] L. Zhou, M. Last, V. Milanovic, J. M. Khan, and K. S. J. Pister, "Two-axis scanning mirror for free-space optical communication between UAVs," *IEEE/LEOS International Conference on Optical MEMS and Their Applications 2003,* pp. 157-158, Hawaii, USA, August 2003.

[10] R. A. Conant, J. T. Nee, K. Y. Lau, and R. S. Muller, "A flat high-frequency scanning micromirror," *Hilton Head Solid-State Sensor and Actuator Workshop 2000*, pp.6-9, Hilton Head, South Carolina, USA, June 2000.

[11] P. R. Patterson, D. Hah, H. Nguyen, H. Toshiyoshi, R. Chao, and M. C. Wu, "A scanning micromirror with angular comb drive actuation.", *International Conference on Micro Electro Mechanical Systems 2002*, pp.544-7, Las Vegas, NV, USA, January 2002.

[12] J. Kim, H. Choo, L. Lin, and R. S. Muller, "Microfabricated torsional actuator using self-aligned plastic deformation," *The 12th International Conference on Solid-State Sensors, Actuators and Microsystems - TRANSDUCERS 2003*, pp1015-1018, Boston, MA, USA, June 2002.

[13] D. T. McCormick and N. C. Tien, "Multiple Layer Asymmetric Vertical Comb-Drive Actuated Trussed Scanning Mirrors," *IEEE/LEOS International Conference on Optical MEMS and Their Applications 2003*, pp.12-13, Hawaii, USA, August 2003.

[14] J. F. Bille, C. F. H. Harner, and F. H. Loesel, "Aberration-Free Refractive Surgery," 2nd Edition, Springer-Verlag, 2004, Chap.10, Page 182, New York, USA.

[15] J. Mansell and R. L. Byer, "Micromachined silicon deformable mirror," *Proceedings of SPIE – Volume 3353: Adaptive Optical System Technologies*, Editors: D. Bonaccini and R. K. Tyson, pp. 896–901, 1998.

[16] R. Yeh, S. Hollar, and K. S. J. Pister, "Single mask, large force, and large displacement electrostatic linear inchworm motors," *International Conference on Micro Electro Mechanical Systems 2001,* pp. 260-264, Interlaken, Switzerland, January 2001.

[17] H. Choo, R. Kant, D. Garmire, J. Demmel, and R. S. Muller, "Fast, MEMS-based, Phase-Shifting Interferometer," *Hilton Head Solid-State Sensor and Actuator Workshop 2000*, pp. 94-95, Hilton Head, South Carolina, USA, June 2006.

[18] S. Timoshenko and J. N. Goodier, "Theory of Elasticity," Second Edition, McGraw-Hill Book Company, Inc, 1951, Page 278, New York, USA.

[19] A. C. Ugural, "Mechanics of Materials," McGraw-Hill Book Company, Inc, 1991, Appendix A, New York, USA.

[20] M. Mrochen, "Converting wavefronts into corrections," *3rd International Congress of Wavefront Sensing and Aberration-free Refractive Correction*, Interlaken, Switzerland, February 2002.

CHAPTER 4

Review of Wavefront Sensors

4.1 Introduction

An extensive background study was carried out to explore previous research on wavefront sensing. All of the material in this chapter derives from published research. Based on this study, we examine, in this chapter, various wavefront-sensing techniques to evaluate their suitability for precisely characterizing high-order wavefront aberrations of large magnitude. For the applications we are focusing on in this study, an appropriate wavefront sensor must be able to characterize corneal scarring, tear-film effects, LASIK flap wrinkles, and keratoconics and post-LASIK corneas. The following sensors are discussed: phase-shifting interferometry (including sub-Nyquist interferometry and two-wavelength interferometry), curvature sensing, phase-diversity-method, lateral shearing interferometry, star test, Ronchi test, and knife-edge test. The fundamental operating principles, theoretical limitations, and performance of these methods are presented and discussed in this summary; for details, the reader is directed to references listed at the end of this chapter

A qualifying wavefront sensor must be able to accommodate the following requirements [1-3]:

- Aberration Measurement Range per Diameter: $\geq 200\lambda$

- Sensitivity / Accuracy / Precision: $\leq \lambda/100$

- Zernike Terms: ≥ 60 terms

- Spatial Resolution: $\leq 400\ \mu m$

- Local Wavefront Slope: >> 20 mrad (surface with discontinuity)

- Measurement Time: ≤ 0.2 sec

- Highly-Precise, Quantitative Measurements Only

We discuss the fundamental operating principles of the following wavefront sensors and wavefront-sensing algorithms

1. Phase Shifting Interferometers

2. Lateral Shearing Interferometers

3. Curvature Sensing

4. Phase-Diversity Method

5. Brief summary of Foucault (knife-edge) test, Ronchi test, and Star test

Then we discuss the present status of these wavefront sensors and algorithms, and their suitability for measuring high-order aberrations of large magnitude.

4.2. Phase Shifting Interferometry

Phase-shifting interferometry (PSI) electronically records a series of interferograms as the reference phase of the interferometer undergoes stepwise changes. The wavefront phase is encoded in the variations in the intensity pattern of the recorded interferograms, and a straightforward point-by-point calculation recovers the phase. Our theoretical treatment of the conventional PSI algorithms follows that given by D. Malacara in *Optical Shop Testing* [4].

4.2.1 Basic Concept of Phase-Shifting Interferometry

The concept behind PSI is relatively simple. A time-varying phase shift is introduced between the reference wavefront and the test or sample wavefront in the interferometer (Figure 4.1).
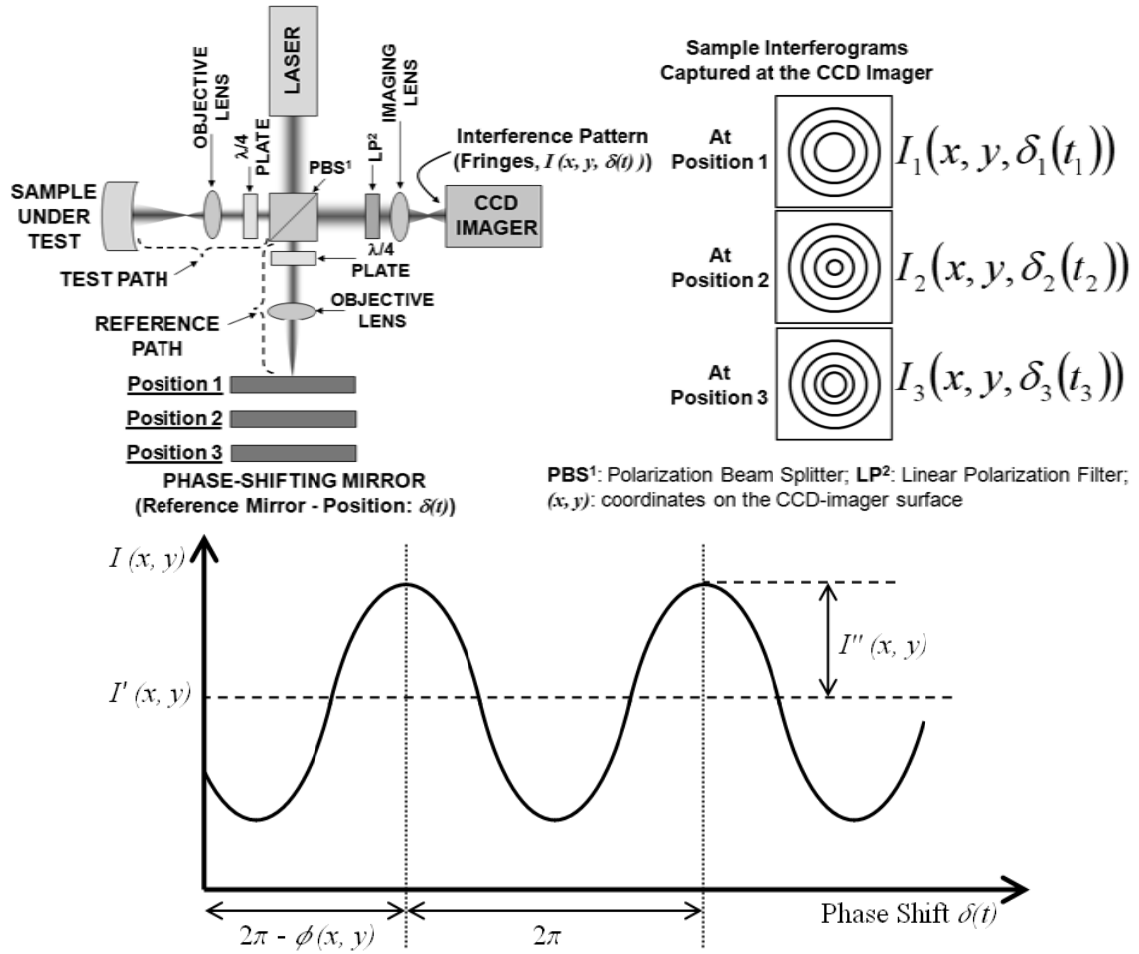
Figure 4.1 Example of a Twyman-Green phase-shifting interferometer (top) and the variation of intensity with the reference phase at a point in an interferogram (bottom, after D. Malacara [4])

A time-varying signal is then produced at each measurement point in the interferogram, and the relative phase between the two wavefronts at that location is encoded in these signals. Assume a surface with height errors $h(x, y)$ tested in reflection. Height errors are the deviations from the reference surface. For normal incidence, the difference between the reference surface and the test surface will result in a wavefront error

$$\phi(x, y) = \frac{4\pi h(x, y)}{\lambda} \qquad (4.2.1)$$

where x and y denote the spatial coordinates, and λ is the wavelength. The reference and test wavefronts can be expressed as

$$w_r(x, y, t) = a_r(x, y)e^{i[\phi_r(x,y)-\delta(t)]} \tag{4.2.2}$$

and

$$w_t(x, y, t) = a_t(x, y)e^{i[\phi_t(x,y)]} . \tag{4.2.3}$$

where: $a_r(x, y)$ and $a_t(x, y)$ are the wavefront amplitudes, $\phi_r(x, y)$ and $\phi_t(x, y)$ are the wavefront phases, and $\delta(t)$ is a time-varying phase shift between the two beams. Let $\delta(t)$ be the relative phase shift between the two beams. The resulting intensity pattern is

$$I(x, y, t) = |w_r(x, y, t) + w_t(x, y)|^2 \tag{4.2.4}$$

$$I(x, y, t) = I'(x, y) + I''(x, y)\cos[\phi_t(x, y) - \phi_r(x, y) + \delta(t)] \tag{4.2.5}$$

where

$$I'(x, y) = a_r^2(x, y) + a_t^2(x, y) \tag{4.2.6}$$

is the average intensity, and

$$I''(x, y) = 2a_r(x, y)a_t(x, y) \tag{4.2.7}$$

is the fringe or intensity modulation. If we define $\phi(x, y)$ as

$$\phi(x, y) = \phi_t(x, y) - \phi_r(x, y), \tag{4.2.8}$$

then the fundamental equation for PSI can be written

$$I(x, y, t) = I'(x, y) + I''(x, y)\cos[\phi(x, y) + \delta(t)]. \tag{4.2.9}$$

The intensity at each point varies as a sinusoidal function of the introduced phase shift $\delta(t)$. Refer to the intensity plot shown in the bottom of Figure 4.1. The three unknowns in the fundamental equation for PSI can be readily identified. The constant

term $I'(x, y)$ is the intensity bias, $I''(x, y)$ is half the peak-to-valley intensity modulation, and the unknown phase $\phi(x, y)$ is related to the temporal phase shift of this sinusoidal variation. The entire map of the unknown wavefront phase $\phi(x, y)$ can be recorded by monitoring and comparing this temporal delay at all the required measurement points in the interferogram. Note that the period is independent of the wavefront phase; it is the same for all data points.

4.2.2 Methods of Phase Shifting

The most common method used to introduce the time-varying phase shift in a PSI system is to translate one of the mirrors or optical surfaces in the interferometer with a piezoelectric transducer. Since the reference wavefront is planer, a relatively small lateral displacement (such as in a Mach-Zehnder interferometer, where the axes of the propagation direction of the reference wavefront and that of the phase-shifting mirror's movement meet at 45°, rather than being congruent) can be ignored. Depending on the configuration, up to a few hundred volts may be needed to obtain to actuate typical piezoelectric drives over the required motions (lengths on the order of 1μm, approximate wavelengths). By changing the applied voltage in a series of steps, the induced-phase-shifts vary in the same way.

An alternative method for producing either a stepped or continuous phase shift is to use a tilted plane that is positioned parallel to the reference beam of the interferometer. The optical path within the plate increases as the tilt angle is increased. To avoid introducing aberrations such as astigmatism and spherical distortions to the reference beam, this method can only be used for collimated or nearly collimated reference beams.

A continuous phase shift can also be produced between the reference and test beams by introducing an optical frequency difference between these two beams. Such shift can be introduced by using translating/rotating diffraction gratings or rotating polarization phase retarders. Directly modulating the output wavelength of a laser diode is another way to produce phase shifts.

4.2.3 PSI Algorithms

In this section, we briefly discuss various PSI algorithms. The algorithms with fewer steps require shorter measurement times and generate smaller amounts of measurement data, but the accuracy of the results is more sensitive to any position errors arising from the phase-shifting mirror. Those algorithms having more steps require longer measurement times and more complex computation, but they are less sensitive to position errors of the phase-shifting mirror. Hence, the choice of the algorithm should follow the measurement needs. The algorithm that is most frequently used in reported research is a four- or five-step algorithm (Hariharan algorithm) that offers a good balance between accuracy and complexity in data handling.

4.2.3.1 Four-Step Algorithm

The four-step Hariharan algorithm makes use of four separate interferograms that are recorded and digitized in each half-cycle of motion. A 90° optical-phase shift is introduced into the reference beam between each of the sequentially recorded interferograms. Since these are discrete measurements, the time dependence has been changed to the phase-step index *i*. The function $\delta(t)$ now takes on four discrete values:

$$\delta_i = 0, \pi/2, \pi, 3\pi/2; \qquad i = 1, 2, 3, 4$$

Substituting each of these four values into

$$I(x, y, t) = I'(x, y) + I''(x, y)\cos[\phi(x, y) + \delta(t)],$$ (4.2.10)

we obtain four equations describing the four measured interferogram intensity patterns:

$$I_1(x, y) = I'(x, y) + I''(x, y)\cos[\phi(x, y)]$$ (4.2.11)

$$I_2(x, y) = I'(x, y) + I''(x, y)\cos[\phi(x, y) + \pi/2]$$ (4.2.12)

$$I_3(x, y) = I'(x, y) + I''(x, y)\cos[\phi(x, y) + \pi]$$ (4.2.13)

$$I_4(x, y) = I'(x, y) + I''(x, y)\cos[\phi(x, y) + 3\pi/2]$$ (4.2.14)

After some arithmetic manipulations, we obtain

$$\phi(x, y) = \tan^{-1}\left[\frac{I_4 - I_2}{I_1 - I_3}\right]$$ (4.2.15)

The wavefront φ can be easily related to the surface deviation of the test sample from the reference surface or the optical path difference (OPD):

$$OPD(x, y) = \lambda\phi(x, y)/2\pi.$$ (4.2.16)

4.2.3.2 Three-Step Algorithm

Since there are three unknowns in the fundamental equation for PSI, the minimum number of the interferogram-intensity measurements that are required to reconstruct the unknown wavefront phase is three. The general case can be solved using equal phase steps of size α. In this case,

$$\delta_i = -\alpha, 0, \alpha; \qquad i = 1, 2, 3$$

and

$$I_1(x, y) = I'(x, y) + I''(x, y, \Delta)\cos[\phi(x, y) - \alpha]$$ (4.2.17)

$$I_2(x, y) = I'(x, y) + I''(x, y, \Delta)\cos[\phi(x, y)]$$ (4.2.18)

and

$$I_3(x, y) = I'(x, y) + I''(x, y, \Delta)\cos[\phi(x, y) + \alpha] \qquad (4.2.19)$$

Δ is the integration period, indicating the use of the Integrating-Bucket-Data-Collection technique. Using trigonometric addition identities and performing some arithmetic manipulations, we obtain the following expression for the unknown phase at each location:

$$\phi(x, y) = \tan^{-1}\left\{\left[\frac{1 - \cos(\alpha)}{\sin(\alpha)}\right]\frac{I_1 - I_3}{2I_2 - I_1 - I_3}\right\}. \qquad (4.2.20)$$

Two phase-step sizes that are commonly used with the three-step algorithm are 90° and 120°, which (when inserted into the previous equation) leads, respectively, to

$$\phi(x, y) = \tan^{-1}\left(\frac{I_1 - I_3}{2I_2 - I_1 - I_3}\right), \qquad (4.2.21)$$

and

$$\phi(x, y) = \tan^{-1}\left(\sqrt{3}\,\frac{I_1 - I_3}{2I_2 - I_1 - I_3}\right). \qquad (4.2.22)$$

4.2.3.3 Hariharan Five-Step Algorithm

In many applications, researchers have found the five-step Hariharan algorithm provides a good balance between computational complexity, on the one hand, and susceptibility to errors, on the other. For the five-step Hariharan algorithm, we initially assume a linear phase shift of α between frames:

$$\delta_i = -2\alpha, -\alpha, 0, \alpha, 2\alpha; \qquad i = 1, 2, 3, 4, 5.$$

Then,

$$I_1(x, y) = I'(x, y) + I''(x, y, \Delta)\cos[\phi(x, y) - 2\alpha], \qquad (4.2.23)$$

$$I_2(x, y) = I'(x, y) + I''(x, y, \Delta)\cos[\phi(x, y) - \alpha], \qquad (4.2.24)$$

$$I_3(x, y) = I'(x, y) + I''(x, y, \Delta)\cos[\phi(x, y)], \qquad (4.2.25)$$

$$I_4(x, y) = I'(x, y) + I''(x, y, \Delta)\cos[\phi(x, y) + \alpha], \qquad (4.2.26)$$

and

$$I_5(x, y) = I'(x, y) + I''(x, y, \Delta)\cos[\phi(x, y) + 2\alpha]. \qquad (4.2.27)$$

If we differentiate the intermediate result obtained by expanding and combining the five equations above, we obtain

$$\frac{d}{d\alpha}\left\{\frac{\tan[\phi(x, y)]}{2\sin(\alpha)}\right\} = \frac{-\cos(\alpha)\tan[\phi(x, y)]}{2\sin^2(\alpha)}. \qquad (4.2.28)$$

Eq. (4.2.28) goes to zero when $\alpha = \pi/2$. If we substitute $\pi/2$ for α, the final expression for the unknown phase at a point becomes

$$\phi(x, y) = \tan^{-1}\left(\frac{2(I_2 - I_4)}{2I_3 - I_5 - I_1}\right). \qquad (4.2.29)$$

4.2.3.4 Other Algorithms

In addition to the algorithms discussed above, other PSI algorithms are least-squares algorithms, Carré algorithm (less susceptible to reference-phase-shift error, averaging 3 + 3 algorithm (less sensitive to linear phase shift errors caused by sinusoidal errors in the reconstruction of the wavefront phase that has frequency twice the interferogram fringe frequency), and 2+1 algorithm (less sensitive to vibrations).

4.2.4 Phase Unwrapping

In order to unwrap the phase information properly from PSI measurements, the so-called Nyquist criteria must be met: *at least two imaging pixels of the CCD/CMOS imager are covered within one fringe period.* Nyquist frequency is defined as

$$f_{N\_x} \equiv \frac{1}{2x_S} \qquad\qquad (4.2.30)$$

$$f_{N\_y} \equiv \frac{1}{2y_S} \qquad\qquad (4.2.31)$$

where x_s and y_s indicate the pixel pitches (in the horizontal and vertical directions, respectively) of the imaging sensor. If the interference-fringe frequency exceeds the Nyquist frequency, aliasing in the recorded interferogram, makes it impossible to interpret the interferogram with certainty. Usually, four or more pixels-per-fringe are recommended.

The arctangent in any of the PSI equations interprets the intensities and returns a value of phase between $-\pi/2$ and $\pi/2$ at each pixel. These values can be easily corrected to produce the wavefront phase modulo 2π.

Table 4.1   Example of modulo 2π phase correction: for four-step algorithm (after D. Malacara [4])

Sine	Cosine	Corrected Phase $\phi(x, y)$	Phase Range
0	+	0	0
+	+	$\phi(x, y)$	0 to $\pi/2$
+	0	$\pi/2$	$\pi/2$
+	−	$\phi(x, y) + \pi$	$\pi/2$ to π
0	−	π	π
−	−	$\phi(x, y) + \pi$	π to $3\pi/2$
−	0	$3\pi/2$	$3\pi/2$
−	+	$\phi(x, y) + 2\pi$	$3\pi/2$ to 2π

Then the 2π discontinuities in these numbers must be corrected to obtain a usable result. If the Nyquist criteria are met, the change in wavefront phase per pixel is no more than π. If the phase-change between two pixels is larger than π, then 2π or multiples of 2π are added to or subtracted from the calculated value of the second pixel until this condition is met.
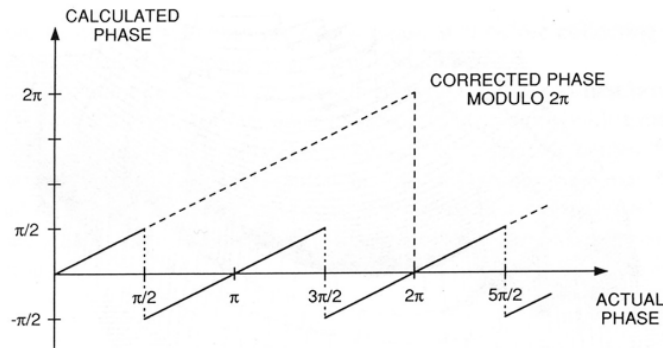
Figure 4.2   The conversion of the phase calculated by the arctangent to the wavefront phase modulo 2π (after D. Malacara [4])
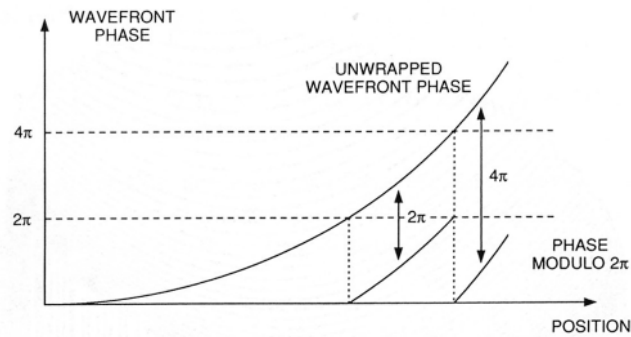
Figure 4.3   The phase unwrapping process in one dimension (after D. Malacara [4]): The entire wavefront map is calculated by working outward from the starting location (usually the center). The phase unwrapping process in one dimension is graphically represented in Figure 4.4.
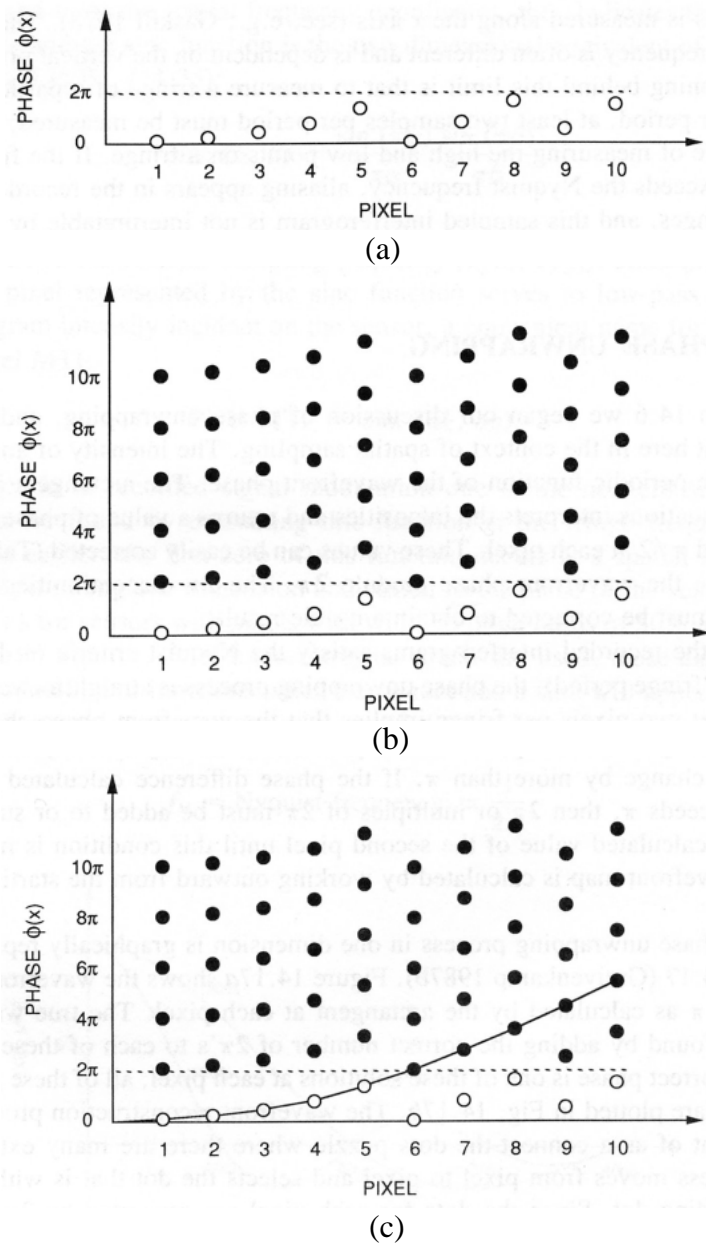
Figure 4.4   The PSI phase-unwrapping process: (a) the wavefront data modulo 2π at each pixel; (b) all of the possible solutions for the wavefront phase; and (c) the reconstructed wavefront

Because of the Nyquist criteria, standard PSI systems are limited to testing surfaces with no more than 10-20 waves of *asphericity*. The exact number of aspheric waves is not possible to predict because the maximum fringe frequency is related to slope, not to peak excursion.

4.2.5 Sub-Nyquist Phase-Shifting Interferometry

Sub-Nyquist interferometry (SNI) was devised by J. E. Greivenkamp to handle aliased fringes that occur above the Nyquist frequency [5]. SNI is based on the assumption that the wavefront from or surface of an optical element is smooth (in general) and therefore has continuous derivatives. With this *a priori* additional information on derivatives, it becomes possible to interpret fringes that occur at frequencies well in excess of the Nyquist frequency. Unlike PSI which depends on wavefront height constraint, SNI requires that derivatives of the reconstructed wavefront not exhibit any large changes from pixel to pixel. Hence, for SNI, the change of the wavefront slope is limited to π from pixel to pixel, but the change of the wavefront height can now be considerably larger as long as it does not violate the SNI's derivative constraint [5]. The appropriate numbers of 2π's are added to each pixel to satisfy this condition, and there is only a single solution at each pixel that produces this result [5]. The slope continuity constraint correctly reconstructs the wavefront from the aliased data until the second derivative of the actual wavefront exceeds the limit imposed by the constraint. When this situation arises, further correction is possible by requiring that the second, or even higher-order, derivative be continuous, and adding more 2π's. The SNI phase unwrapping process for aspherics is graphically demonstrated in Figure 4.5 [5].

To calculate initial values of the various surface derivatives, there must be a small block of pixels that appear in the data set without aliasing. A block of 2-by-2 pixels is needed to implement first-derivative continuity, a 3-by-3 block is needed for second-derivative continuity, etc. One of the fundamental limits to the measurement range of an SNI system is in the ability of the sensor to respond to the high-frequency fringes: the

pixel MTF [5]. The measured data modulation must be high, and the sensor must be able to respond to fringes well beyond the Nyquist frequency. Hence, the pixel-width-to-pitch-ratio must be small such as that found in a sparse-array sensor. The maximum measurable slope of a SNI system with a sparse-array sensor can be up to 20 times that of a PSI system [4]. Like conventional PSI, SNI is also unsuitable for measuring discontinuities or steps larger than a half-wave (or a quarter-wave in reflection) even with the concept of using a priori information with interferometers.
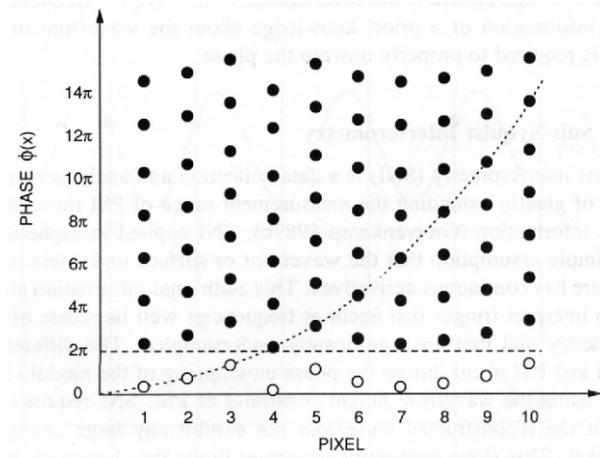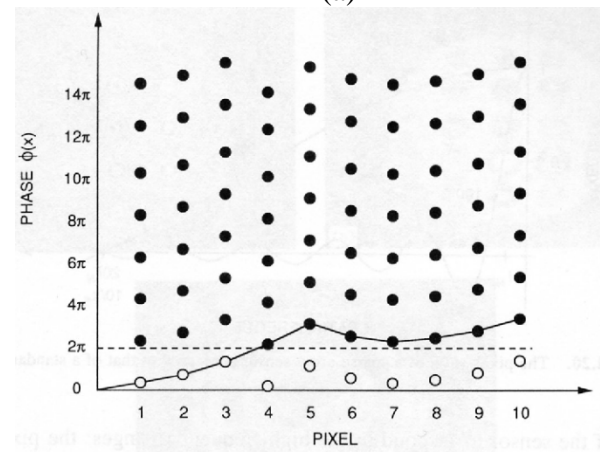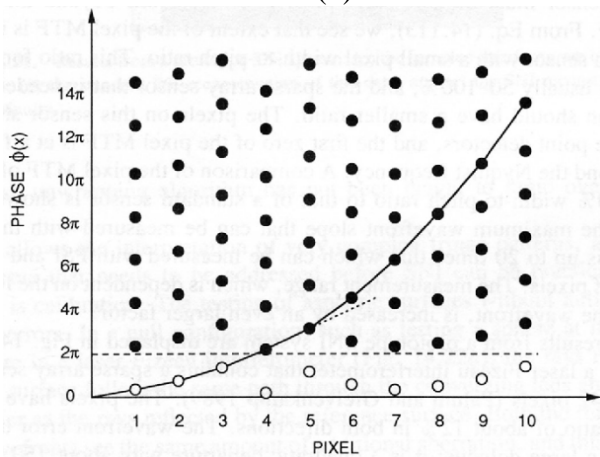
Figure 4.5 The SNI reconstruction process: (a) the possible solutions for the wavefront phase at each pixel, (b) the standard PSI reconstruction of this data; and (c) the SNI reconstruction using slope continuity (after J. E. Greivenkamp [5])

The optical step height of the surface (or optical elements) under test must be known ahead of time to within a half-wave of the actual value [5], which may be impractical in some situations. Calibrating a SNI system can be quite challenging, especially in a form of null testing [6]. No SNI papers that report successful measurements of large-magnitude, high-order aberrations with large local gradients (surface containing unknown discontinuity) are found. And, SNI will be too slow for refractive measurements of human eyes.

4.2.6 Two-Wavelength Phase-Shifting Interferometry

J. C. Wyant reported the two-wavelength interferometry (TWI) in 1971 and TWI using digital electronic technique in 1984 [7-9]. An excellent summary of two-wavelength interferometry can be found in the paper written by J. E. Greivenkamp [5]. In two-wavelength interferometry (TWI), two separate measurements of the same part are made at two different wavelengths to expand the measurement range beyond the Nyquist frequency. First, two complete sets up phase-shifted interferometric data are collected at two different wavelengths, and the phase modulo 2π at each wavelength is computed. Since a phase of 2π is a different optical path difference (OPD) at each wavelength, only one choice of wavefront deformation will satisfy both data sets. The graphical representation of the TWI concept is shown in the figure below. Please notice that the vertical scale is OPD instead of phase so that is not wavelength dependent.
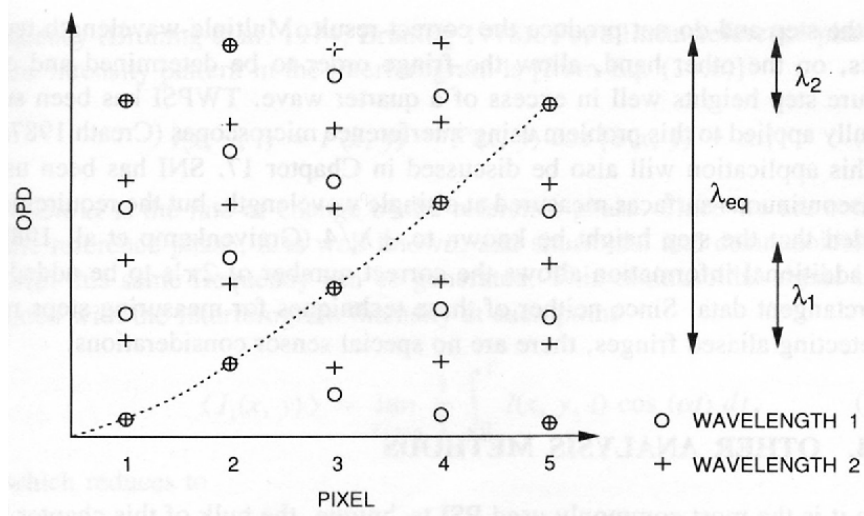
Figure 4.6 The reconstruction process of TWI (after J. E. Greivenkamp, [5])

The locations where the two sets of dots fall on top of each other indicate possible correct solutions for the wavefront. At each pixel, there are multiple locations of coincidence, and the spacing between these points is the equivalent wavelength:

$$\lambda_{eq} = \frac{\lambda_1 \lambda_2}{|\lambda_1 - \lambda_2|}, \tag{4.2.32}$$

where λ_1 and λ_2 are the two measurement wavelengths. Phase unwrapping of the common points is now done using standard PSI techniques at the equivalent wavelength. Since the equivalent wavelength is much longer than the actual wavelengths, large wavefront slopes can be handled before the algorithm breaks down. TWI requires the use of a sparse-array sensor to take a full advantage of the algorithm [10]. In addition to the typical error sources found in the conventional PSI, there are several challenges involved in implementing a practical TWI system. One is calibration: a careful ray-tracing simulation at these wavelengths is required prior to the measurement and analysis, especially when the test under surface is aspherical [11]. Another is data-matching problem: if the phase data for λ_1 and λ_2, are not for the same data points, a shearing effect

error will be superimposed on the measurement result [12]. The third is chromatic aberration: optics involved in measurements must be achromatized at both wavelengths in order to eliminate chromatic aberration [11-12]. As a result, TWI is better suited for surface profilometry, where chromatic aberration has minimal effect on measurements [12-13]. In 2003, A. Pfortner and J. Schwider reported a three-wavelength interferometer (3WI) for the metrology of discontinuous structures [13]. Using widely spaced three wavelengths (red, green, and blue) with a three-chip RGB CCD, the interference patterns at three different wavelengths are simultaneous recorded. In order to get rid of the inevitable phase jumps, the authors adapted the method of exact fractions, whose philosophy is known from length measurement of end gauges. The concept of using a three-chip RGB CCD can also be applied to TWI for simultaneous measurements at two different wavelengths, and this will ease the stability and vibration requirements for TWI. However, the optics included in the 3WI setup must still be achromatized, making it challenging for refractive cornea measurements. Also, TWI is too slow for measuring corneas of living humans.

4.3 Curvature Sensors

4.3.1 Basic Theory of Curvature Sensors

A curvature sensor measures and reconstructs the randomly distorted wavefronts from estimates of the radial tilt at the edge of the aperture and of the curvature measured within the aperture [14]. The practical version of the curvature sensing was proposed by F. Roddier in 1988 as an alternative to the methods that measure local wavefront slopes along two orthogonal directions [15]. The curvature-sensing method (CSM) is based on the irradiance transport equation (ITE) derived by M. R. Teague in 1983 [16]:

$$C_{Local}(x, y) = \frac{\partial^2 W(x, y)}{\partial x^2} + \frac{\partial^2 W(x, y)}{\partial y^2} = \nabla^2 W(x, y), \qquad (4.3.1)$$

where $C_{Local}(x, y)$ is the local wavefront curvature and $W(x, y)$ is the wavefront surface [15]. ITE is also treated in detail by F. Roddier in 1990 [17]. Radial tilts at the aperture edge must also be measured together with the curvature in order to provide the boundary conditions required to solve the Poisson equation above.

A CSM setup is schematically described in Figure 4.7:
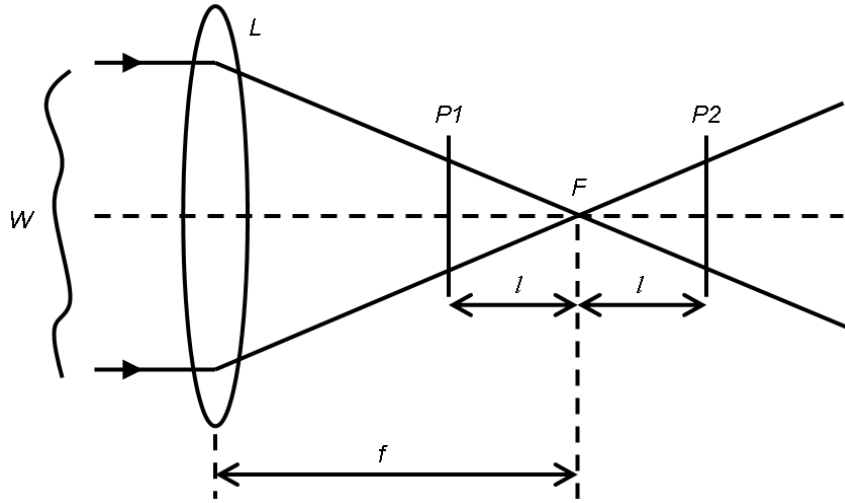
Figure 4.7   Curvature sensing with two image planes (P_1 and P_2) symmetrically displaced from the focal plane F (after F. Roddier [16])

The curvature sensor consists of two image detectors. One detects the irradiance distribution $I_1(\mathbf{r})$ in plane P_1 at a distance $(f - l)$. The other detects the irradiance distribution $I_2(-\mathbf{r})$ in plane P_2 at a distance $(f + l)$. From geometrical optics considerations, a local wavefront curvature will cause an excess of illumination in one plane and a lack of illumination in the other plane. The difference between the two illuminations will therefore provide a measure of the local wavefront curvature.

Diffraction equations show that geometrical optics is a good approximation if the inequality expressed in (4.3.2) applies.

$$\frac{\lambda}{r_0}(f - l) << \frac{l}{f} r_0, \qquad (4.3.2)$$

where r_0 is *Fried's parameter*, f is the focal length, and λ is the wavelength [16]. The term on the left side describes the blur size found in the pupil image at plane P_1 due to the wavefront fluctuations of scale r_0 (which diffracts light at an angle λ/r_0). The term on the right side describes r_0 scaled down by a factor l/f. Inequality (4.3.2) states that, in order to make good measurements, the blurriness caused by the wavefront fluctuations expressed through the *Fried's parameter* r_0 must be much smaller than r_0 scaled down by a factor l/f. Rearranging the variables, we obtain

$$l >> \frac{\lambda f^2}{\lambda f + r_0^2}, \qquad (4.3.3)$$

which gives the size of l (see Fig. 4.7) to measure wavefronts with fluctuations r_0. Keeping this requirement in mind, complete calculations show that

$$\frac{I_2(\mathbf{r}) - I_1(\mathbf{r})}{I_2(\mathbf{r}) + I_1(\mathbf{r})} = \frac{f(f - l)}{2l}\left[\frac{\partial}{\partial \mathbf{n}}W\left(\mathbf{r}\left(\frac{f}{l}\right)\right)\delta_C + \nabla^2 W\left(\mathbf{r}\left(\frac{f}{l}\right)\right)\right] \qquad (4.3.4)$$

where δ_C is a linear impulse distribution around the pupil edge weighted by the wavefront radial tilt $\partial W / \partial \mathbf{n}$ and $\nabla^2 W$ is the wavefront curvature [15]. The sensor will therefore provide all the information needed to reconstruct the wavefront. J. Hardy gives a more simplified expression in his book after making several additional approximations [14]:

$$\frac{I_2(\mathbf{r}) - I_1(\mathbf{r})}{I_2(\mathbf{r}) + I_1(\mathbf{r})} \approx \frac{2f^2}{l}\nabla^2 W(\mathbf{r}) \equiv \frac{2f^2}{l}C_{Local}(\mathbf{r}), \qquad (4.3.5)$$

Equation (4.3.5) ignores any radial tilts and directly relates the illumination difference to the wavefront curvature.

The most interesting property of CSM is that membrane or bimorph mirrors can be used as analog devices that automatically solve Eq. (4.3.5) when proper voltages are applied [15]. Hence, the signal from a curvature sensor can be amplified and directly applied to the mirror without any computer processing. For an ideal membrane, the dynamic equation of state has the form

$$\frac{\partial^2 W'}{\partial t^2} = A\nabla^2 W' + BP \qquad (4.3.6)$$

where $W'(x, y, t)$ is the membrane surface and $P(x, y, t)$ is the electrostatic pressure applied as a function of time t; A and B are constant coefficients [15]. Equilibrium is obtained when the mirror surface is the solution of a Poisson equation with appropriate boundary conditions. In other words, the effect of applying a pressure is to change the local curvature of the membrane mirror. If, in a servo loop, a pressure proportional to the signal delivered by the curvature sensor is applied, both the local curvature inside the mirror and the radial tilts at the edge will be corrected. For simplest feedback loop, it can be shown that for a membrane mirror,

$$\nabla^2 W'(\mathbf{r}) \propto P(\mathbf{r}), \qquad (4.3.7)$$

$$W'(\mathbf{r}) = KW(\mathbf{r}), \qquad (4.3.8)$$

where K is a constant [15].

4.3.2 Present Status of Curvature-Sensor Measurement

Researchers have investigated the usefulness of the curvature-sensing method (CSM) in several applications such as evaluation of the optical quality of telescopes and other optical components [18-19] as well as the detection of wavefront tilt for accurate pointing of laser beams and phase imaging of thermal atomic beams [20-21]. However,

curvature sensing is mainly used in adaptive optics (for astronomical telescopes) to perform low-order-aberration corrections including piston and tilts. For CSM, membrane or bimorph mirrors can be used as analog devices to solve a Poisson equation automatically. Since the signal from a curvature sensor can be amplified and directly applied to the mirror without any digital processing, high-speed real-time wavefront corrections are possible.

Although the implementation of the sensor looks simple, the positions of the two image planes plays a very critical role in determining the sensor's dynamic range and sensitivity. And, choosing the optimal positions can be quite challenging. Unfortunately, most researchers provide $l >> \left(\lambda f^2\right)/\left(\lambda f + r_0^2\right)$ as a guideline for selecting the detector positions. This leaves the readers with rather a large group of choices for positioning detector planes. Selecting the detector plane also requires a certain degree of *a priori* knowledge of the phase to be measured, and this requirement can make CSM impractical in certain situations [15, 22]. Using simulations, M. Soto and his colleagues showed that the optimal positions of the detector planes heavily depend on the types and magnitudes of optical aberrations being measured [23]. Unfortunately, this was the only paper found to tackle this issue systematically, and it was impossible to draw a general consensus on the effect of the optimal detector position on the wavefront estimation accuracy. CSM simulations has shown good results for very low-order aberrations (less than a dozen Zernike coefficients) [24]. F. Rigaut and his colleagues compared the performance of CSM-based adaptive optics to that of Shack-Hartmann-based adaptive optics [25]. They found that both adaptive optics systems showed similar performance for low order aberrations and predicted that Shack-Hartmann system would yield better results for

correcting high-order aberrations [25]. A more recent variation of CSM involving four image planes also has been shown to be very effective only for very low-order aberrations [22]. In 1995, P. Doel reported (based on the simulation results) that Shack-Hartmann yielded better accuracy than CSM for estimating low-order aberrations through large telescope systems [26]. Up to date, a curvature sensor's ability to estimate high-order aberrations remains to be proven [27-28].

Considering the theoretical model used for CSM, one can visualize that measuring high-order aberrations of large magnitude may not be a suitable application for CSM. The distance between the detector planes must be increased in order to accommodate the magnitude of aberrations. But, as the distance becomes larger, the sensor's sensitivity decreases [22]. Measurements with such conditions, if made, will become a very crude approximation of the wavefront curvatures [27].

Hence, the sensors' ability to measure high-order aberrations of large magnitude and their application to LASIK cannot be answered at this point.

4.4 Phase-Diversity Method

4.4.1 Basic Theory of Phase-Diversity Method

The phase-diversity (PD) method extracts the Fourier transform of a complex signal based on observation of the modulus of the signal [29-30]. One of the interesting properties is that the phase-diversity algorithm allows the joint-estimation of an object and the aberrations of an imaging system from multiple images incorporating phase diversity. A good theoretical treatments of the method can be found in the paper published by R. Paxman, T. J. Shulz, and J. R. Fienup in 1992 [31].
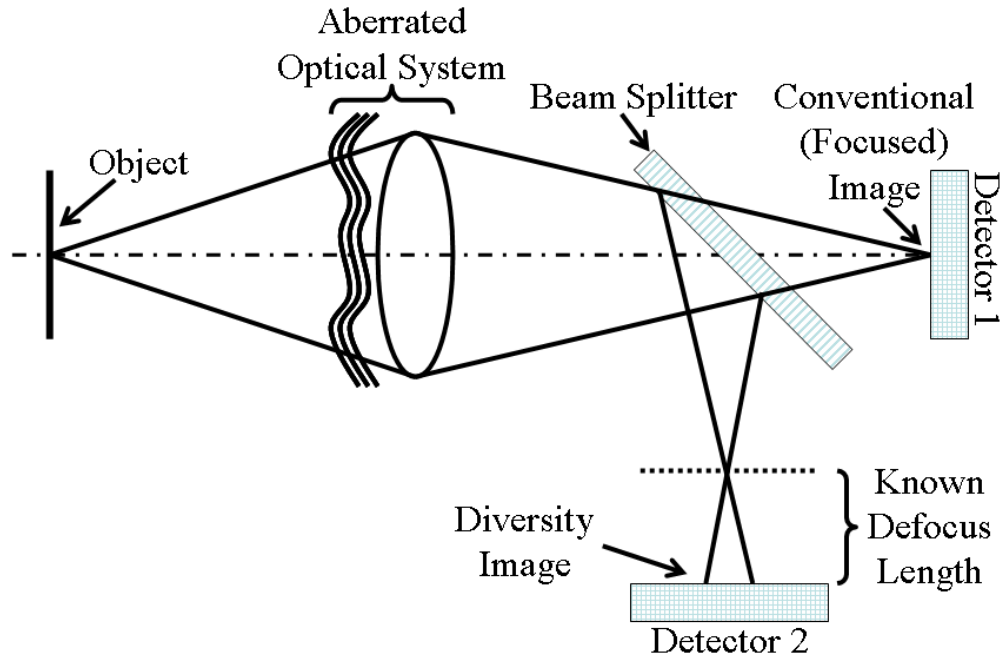
Figure 4.8   Schematic diagram of a phase-diversity system (after R. G. Paxman *et al.* [31])

If we assume that the object and its Fourier transform as discrete arrays, the incoherent image-formation process is approximated by the following discrete and cyclic convolution:

$$g_k(x) = \sum_{x' \in \chi} f(x') s_k(x - x') \equiv f * s_k(x) \qquad (4.4.1)$$

where f is the object array, s_k is a PSF having diversity k, g_k is the k_{th} diversity image, and x is a two-dimensional coordinate. We treat the object, the PSF's, and the images as periodic arrays with a period cell of size $N \times N$. These arrays are completely specified by their functional values on the set χ, where

$$\chi = \{0, 1, ..., N-1\} \times \{0, 1, ..., N-1\} \qquad (4.4.2)$$

Diversity is introduced by including a known phase function in the generalized pupil function of the system:

$$H_k(u) = |H_k(u)| \exp\{i[\phi(u) + \theta_k(u)]\},\qquad(4.4.3)$$

where ϕ is the unknown phase-aberration function that we would like to estimate, θ_k is a known phase function associated with the k_{th} diversity image, and $u \in \chi$. It is often convenient to parameterize the unknown phase-aberration function:

$$\phi(u) = \sum_{j=1}^{J} \alpha_j \phi_j(u),\qquad(4.4.4)$$

where J coefficients in the set $\{\alpha_j\}$ serve as parameters and $\{\phi_j\}$ is a convenient set of basis functions, such as discretized Zernike polynomials.

The inverse discrete Fourier transform of the generalized pupil function gives the impulse-response function for a coherently illuminated object:

$$h_k(x) = \frac{1}{N^2} \sum_{u \in \chi} H_k(u) \exp(i2\pi\langle u, x\rangle / N),\qquad(4.4.5)$$

where $\langle \cdot, \cdot \rangle$ represents an inner product. The incoherent PSF is just the squared modulus of the coherent impulse response function:

$$s_k(x) = |h_k(x)|^2.\qquad(4.4.6)$$

Given the set of K detected diversity images $\{d_k\}$, and the binary pupil functions $\{|H_k|\}$, estimate the object f and the aberration parameters α. The relationship between a noiseless image and the actual detected image d_k will depend on the specific noise mechanisms.

First we consider the case in which the noise at each detector element is modeled as an additive, independent, and identically distributed random variable with a zero-mean Gaussian probability density having a variance σ_n^2. Such a model would be appropriate,

for example, if the dominant noise were thermal noise. In this case, each detected

diversity image d_k is related to the corresponding noiseless diversity image g_k as follows:

$$d_k(x) = g_k(x) + n_k(x) = f * s_k(x) + n_k(x), \qquad (4.4.7)$$

where n_k represents the additive noise. Note that, because of the noise component, dk(x)

will be a random variable with a normal probability density:

$$p[d_k(x); f, \alpha] = \frac{1}{\left(2\pi\sigma_n^2\right)^{1/2}} \exp\left\{-\frac{[d_k(x) - f * s_k(x)]^2}{2\sigma_n^2}\right\}. \qquad (4.4.8)$$

The probability density for realizing an entire data set {dk}, consisting of all the pixels in

each detected diversity image, is given by

$$p[\{d_k\}; f, \alpha] = \prod_{k=1}^{K} \prod_{x \in \chi} \frac{1}{\left(2\pi\sigma_n^2\right)^{1/2}} \exp\left\{-\frac{[d_k(x) - f * s_k(x)]^2}{2\sigma_n^2}\right\}. \qquad (4.4.9)$$

The MLE is the estimate that is most likely to have produced a specific

measurement. It is found by maximizing the likelihood function (equation above

evaluated with a specific measurement) with respect to f and α. The maximization is

more easily carried out on a modified log-likelihood function:

$$L(f, \alpha) = -\sum_{k=1}^{K} \sum_{x \in \chi} [d_k(x) - f * s_k(x)]^2, \qquad (4.4.10)$$

which is obtained by taking the natural logarithm of the likelihood function and dropping

an inconsequential constant term and scale factor. For convenience, we refer to L as the

log-likelihood function. Applying discrete versions of both Parseval's theorem and the

convolution theorem to the above equation, we have that

$$L(f, \alpha) = -\frac{1}{N^2} \sum_{k=1}^{K} \sum_{x \in \chi} [D_k(u) - F(u) * S_k(u)]^2, \qquad (4.4.11)$$

where D_k, F, and S_k are discrete Fourier transforms of d_k, f, and s_k, respectively. Note that maximizing the log-likelihood function is equivalent to minimizing the sum of squared differences, which is the error metric used by Gonsalves.

Gonsalves showed, for the case of $K = 2$, that the aberration parameters can be estimated by optimizing an objective function that depends explicitly on the aberration parameters but only implicitly on the object pixel values. The result is a significant reduction in the dimension of the parameter space over which a numerical optimization is performed. The closed-form expression for the object that maximizes the log-likelihood function, given a fixed aberration function:

$$F_M(u) = \frac{D_1(u)S_1^*(u) + D_2(u)S_2^*(u)}{|S_1(u)|^2 + |S_2(u)|^2}, \tag{4.4.12}$$

where an asterisk used as a superscript implies complex conjugation. The new objective function that does not depend explicitly on an object estimate:

$$L_M(\alpha) = -\sum_{u \in \chi} \frac{|D_1(u)S_2(u) + D_2(u)S_1(u)|^2}{|S_1(u)|^2 + |S_2(u)|^2}, \tag{4.4.13}$$

where it has been assumed that $S_1(u)$ and $S_2(u)$ do not simultaneously go to zero for $u \in \chi$. It is important to recognize that maximizing the Gonsalves objective function L_M yields the MLE for the aberration parameters explicitly and the object parameters implicitly, under the additive Gaussian noise model.

We now proceed to generalize the Gonsalves objective function to accommodate an arbitrary number K of diversity measurements. We seek an expression for the particular F that maximizes L, given in the original log-likelihood equation. The real and imaginary parts of any such F_M will satisfy the following equations:

$$\frac{\partial}{\partial F_r(u)} L = 0, \quad u \in \chi, \tag{4.4.14}$$

$$\frac{\partial}{\partial F_i(u)} L = 0, \quad u \in \chi, \tag{4.4.15}$$

where Fr(u) and Fi(u) are the real and the imaginary parts of F(u), respectively. The

solution for the above equations is derived in the reference and is given by

$$F_M(u) = \left\{ \begin{array}{ll} \sum_{k=1}^{K} D_k(u) S_k^*(u) \Big/ \sum_{k=1}^{K} |S_l(u)|^2 & u \in \chi_1 \\ F_M^*(-u) & u \in \chi_0 \end{array} \right\}, \tag{4.4.16}$$

where the set of spatial frequencies χ has been partitioned into the subset χ_0, the set of

spatial frequencies at which all the OTF's are zero valued, and its complement, χ_1. Now

the generalized objective function becomes,

$$L_M(\alpha) = \sum_{u \in \chi_1} \frac{\left| \sum_{j=1}^{K} D_J(u) S_j^*(u) \right|^2}{\sum_{l=1}^{K} |S_l(u)|^2} - \sum_{u \in \chi} \sum_{k=1}^{K} |D_k(u)|^2. \tag{4.4.17}$$

We may employ nonlinear optimization techniques to find aberration parameters

that maximize the equation above. Many of these techniques repeatedly compute the

gradient of the objective function. An analytic expression for the partial derivative of the

objective function with respect to the aberration parameters, given a mild assumption on

the OTF's, is derived in the reference and is given by

$$\frac{\partial}{\partial \alpha_n} L_M = -\frac{4}{N^2} \sum_{u \in \chi} \phi_n(u) \operatorname{Im}\left[\sum_{k=1}^{K} H_k(u) \left(Z_k * H_k^* \right)(u) \right], \tag{4.4.18}$$

where

$$Z_k(u) \equiv \left\{ \begin{array}{ll} \left[\sum_l |S_l|^2 \left(\sum_j D_j S_j^* \right) D_k^* - \left| \sum_j D_j S_j^* \right|^2 S_k^* \right] \Bigg/ \left(\sum_l |S_l|^2 \right)^2 & u \in \chi_1 \\ 0 & u \in \chi_0 \end{array} \right\}.$$

(4.4.19)

For the case of $K = 2$, the above equation simplifies to

$$\frac{\partial}{\partial \alpha_n} L_M = -\frac{4}{N^2} \sum_{u \in \chi} \phi_n(u) \, \text{Im}\left[H_1(u)(ZS_2 * H_1^*)(u) - H_2(u)(ZS_1 * H_2^*)(u) \right],$$

(4.4.20)

where

$$Z(u) \equiv \left\{ \begin{array}{ll} \dfrac{\left(D_1 S_1^* + D_2 S_2^* \right)\left(D_2 S_1^* - D_1 S_2^* \right)}{\left(|S_1|^2 + |S_2|^2 \right)^2} & u \in \chi_1 \\ 0 & u \in \chi_0 \end{array} \right\}.$$

(4.4.21)

We now consider the case in which the data are limited by photon noise. In this case, the number of photo-conversions that occur at each detector element will be a Poisson-distributed random variable with a mean value prescribed by the noiseless image g_k given in units of mean detected photons per pixel. Therefore, the probability of detecting d_k photo-events at location x is

$$\Pr[d_k(x)] = \frac{g_k(x)^{d_k(x)} \exp[-g_k(x)]}{d_k(x)!}.$$

(4.4.22)

We assume that the number of photo-events realized will be statistically independent for each pixel. Therefore, the probability of realizing an entire data set $\{d_k\}$ will be

$$\Pr[\{d_k\}] = \prod_{k=1}^{K} \prod_{x \in \chi} \frac{g_k(x)^{d_k(x)} \exp[-g_k(x)]}{d_k(x)!}.$$

(4.4.23)

A modified log-likelihood function for the joint estimation of the object and aberration parameters is

$$L(f,\alpha) = \sum_{k=1}^{K}\sum_{x\in\chi}\left[d_k(x)\ln g_k(x) - g_k(x)\right], \tag{4.4.24}$$

where an inconsequential constant has been dropped. Consider the second term in the above equation:

$$\sum_{k=1}^{K}\sum_{x\in\chi} g_k(x) = \sum_{x'\in\chi} f(x')\frac{1}{N^2}\sum_{k=1}^{K}\sum_{u\in\chi}\left|H_k(u)\right|^2, \tag{4.4.25}$$

where we have used discrete versions of the Fourier shift theorem and Parseval's theorem. Note that the double sum over the squared moduli of the pupil functions is just a constant, independent of the object, the aberration parameters, and the phase diversity. Let

$$C \equiv \frac{1}{N^2}\sum_{k=1}^{K}\sum_{u\in\chi}\left|H_k(u)\right|^2. \tag{4.4.26}$$

The equation becomes

$$\sum_{k=1}^{K}\sum_{x\in\chi} g_k(x) = C\sum_{x'\in\chi} f(x), \tag{4.4.27}$$

and the log-likelihood function simplifies to

$$L(f,\alpha) = \sum_{k=1}^{K}\sum_{x\in\chi} d_k(x)\ln\left[\sum_{x'\in\chi} f(x')s_k(x-x')\right] - C\sum_{x\in\chi} f(x). \tag{4.4.28}$$

The desired sequence is to solve for the MLE of the object, given fixed aberration parameters, and substitute this result in to the expression for the log-likelihood function to create an objective function that does not depend explicitly on the object estimate. We begin by computing the partial derivative of the log-likelihood function with respect to the ith pixel value of the object estimate:

$$\frac{\partial}{\partial f(x_i)}L = \sum_{k=1}^{K}\sum_{x\in\chi}\frac{d_k(x)s_k(x-x_i)}{\sum_{x'\in\chi} f(x')s_k(x-x')} - C. \tag{4.4.29}$$

To find the MLE of the object for fixed aberration parameters we set this partial derivative equal to zero and attempt to solve for f:

$$0 = \sum_{k=1}^{K} \sum_{x \in \chi} \frac{d_k(x) s_k(x - x_i)}{\sum_{x' \in \chi} f(x') s_k(x - x')} - C.$$ (4.4.30)

The tractability of the computation implied by the equation above suggests the use of a gradient-search technique in maximizing the log-likelihood functions over object pixels and aberration parameters simultaneously. The expression for the partial derivatives of the log-likelihood function with respect to the aberration parameters is given by

$$\frac{\partial}{\partial \alpha_n} L = -2 \sum_{u \in \chi} \phi_n(u) \operatorname{Im}\left[\sum_{k=1}^{K} H_k(u) \frac{1}{N^2} \sum_{x' \in \chi} h_k^*(x') \times \exp(i2\pi\langle u, x'\rangle / N) \sum_{x'' \in \chi} \frac{d_k(x) f(x - x')}{f(x'') s_k(x - x'')} \right].$$ (4.4.31)

Optimization is performed using non-linear iterative methods such as a neural network. Typical neural network algorithms are steepest-descent, conjugate gradient, and quasi-Newton algorithms based on the back-propagation method [32].

4.4.2 Phase-Diversity Method: Past, Present, and Future

Several researchers have investigated the possibility of using the phase-diversity method for adaptive optics in astronomical telescopes. By running computer simulations, R. G. Paxman and J. R. Fienup as well as several other researchers investigated the use of the phase-diversity algorithm for aligning optical components in the astronomical telescope and showed that the algorithm could be effectively used to determine the misalignment parameters of the telescope optics [33-34].

As a wavefront sensor, the phase-diversity method is not as mature and (hence) widely-accepted as other available wavefront sensing technologies such as phase-shifting interferometry, Shack-Hartmann test, lateral-shearing interferometry, and curvature

sensing [35-38]. In particular, the capability of phase-diversity method for estimating high-order aberrations of large magnitude has not been demonstrated or examined up to date.

In 1993, J .R. Fienup and his colleagues reported in detail the computer-simulation results characterizing the Hubble Space Telescope (HST) from measured point spread functions by using phase-retrieval algorithms [39]. The paper shows the improved images of the point-spread functions along with the numerical values of the first eleven low-order Zernike coefficients. The authors claim that they have invested considerable effort into processing data from the HST as well as optimizing the phase-diversity system parameters over a period of several months, during which time the quality of both the data and the phase-retrieval algorithms improved. The authors reported that the values of the low-order Zernike coefficients, except the spherical aberration term, fluctuated whenever the system or algorithm parameters were slightly changed. As a result, the authors mention that the accuracy of their results (to publication date) was not sufficient to give them high confidence in the predictions of the Zernike coefficients other than the spherical aberration. The authors also mention that the error bars on their estimate are difficult to determine since the error bars depend on systematic errors, such as poorly known parameters of the system, rather than random errors whose standard deviation can be derived. The authors did not present the reconstructed phase maps (by using the phase-diversity method) in the paper, either, because the authors did not have confidence in the maps' reliability.

In 1994, R. A. Carreras, S. Restaino, and D. Duneman published their work on extracting higher-order Zernike coefficients using the phase-diversity method [40].

Unfortunately, their conference paper does not include any numerical values for estimated higher-order Zernike coefficients. The authors show only two sets of images where they claim that the quality of reconstructed images was improved by using the phase-diversity method.

Some researchers compared the performance of the phase-diversity algorithm with that of a SH sensor or a curvature sensor [35, 41]. The conclusions of these conference papers are somewhat ambiguous. The authors do not make any systematic comparison of the sensors' performance parameters such as sensitivity, precision, and dynamic range.

In 1999, L. Meynadier and his colleagues reported that, for the phase-diversity method, the noise variance on the Zernike polynomials (17 low-order terms) increases with the order of the polynomial [42]. Since there is a higher noise level for a larger number of estimated Zernike coefficients, the authors believe that the phase-diversity method is consequently better adapted for the estimation of the low-order aberrations. In addition to the noise propagation property of the phase-diversity method, L. Meynadier and his colleagues also reported the finding of the existence of an optimal defocus position that minimizes the noise propagation on the estimated phase. The optimal position varies from one case to another case, and for the particular case presented in the paper, it is approximately equal to 2π.

In 2003, J. J. Dolne and his colleagues showed that the exact amount of defocus distance does not need to be known exactly for the phase-diversity method [43]. The authors intentionally included an error of 0.2λ in the defocus distance and compared the recovered wavefront with the original wavefront. (The actual position of the defocus

image was also off by 0.03λ.) They found that the difference between the recovered wavefront and the original wavefront is less than 0.01λ rms, and without knowing the exact defocus distance, non-linear optimization required roughly twice more iteration steps. This result contradicts the fundamental assumption of the phase-diversity method: the magnitude of the defocus added to the second image must be known accurately. J. J. Dolne and his colleagues also stated that the optimal position of the defocus image was not very important in determining the accuracy of the measurements, which contradicts the claim made by L. Meynadier and his colleagues in 1999. In spite of the discord, J. J. Dolne and his colleagues show that the aberrations (the first six Zernike coefficients excluding piston and tilt) recovered by the phase-diversity method compare with those measured by a Fizeau interferometer with Strehl ratio of over 0.9.

In 2003, A. Blanc, T. Fusco, M. Hartung, L. M. Mugnier, and G. Rousset applied the phase-diversity method to characterize the static aberrations of the Nasmyth Adaptive Optics System (NAOS) and the high-resolution, near-IR camera CONICA [44-45]. From the simulation results, the authors show that only the first thirty-six Zernike coefficients can be estimated with a reasonable accuracy (using the phase-diversity method) [44]. For the experimental results, only the first eleven low-order terms of Zernike coefficients (excluding piston and tilt) were presented with good accuracy [45]. The magnitudes of the aberrations measured were very small, mostly less than 0.1 μm. The authors do not provide a detail on the limitation of the non-linear optimization algorithm that they used. Many readers probably wish to know which non-linear optimization algorithm enabled the authors to have confidence in their results since what limits the performance of the

phase-diversity method is the uncertainty originating from non-linear optimization algorithm [36-37].

D. Malacara states in his book *Optical Shop Testing* that estimating aberrations from the point spread function is generally impossible in principle [46]. Near to the focal plane, where phase-diversity sensors take their measurements, the relationship between the aberrations and the measured data is extremely nonlinear, requiring a computationally more demanding nonlinear-optimization to determine the aberrations [36]. The aberration retrieval from the image becomes even harder when the magnitudes of the aberrations are large [36]. No research works that show successful measurements of high-order aberrations of large magnitude using a phase-diversity sensor have been reported up to date. The value of using the phase-diversity method for wavefront sensing purpose in adaptive optics is also questioned [38]. The phase-diversity method is too slow to be used for measuring and correcting aberrations in real-time because it relies on iterative methods to estimate the aberrations. As a wavefront sensor, phase-diversity method is still at the rudimentary stage and has not been proven as a reliable wavefront-sensing algorithm.

Nevertheless, if considerable improvements and advances are brought to non-linear optimization or neural network algorithms, the phase-diversity method will prove to be very useful in many applications, especially in adaptive optics for astronomy. Because the measurements are made at the focal point and at a position slightly off the focal point where the image intensity is the strongest, the phase-diversity method can potentially yield extremely high signal-to-noise ratios. And, this will consequently

enable astronomers increase the coverage of currently unexplored regions of the night sky
[35].

4.5 Lateral Shearing Interferometry

Lateral shearing interferometry is an important field of interferometry and has been used extensively in diverse applications such as the testing of optical components and systems and the study of flow and diffusion phenomena in gases and liquids. Unlike wavefront-measuring interferometers, lateral shearing interferometers measure constant average wavefront slope over the shear distance. The operating principles of lateral shearing interferometry are illustrated in Figure 4.9 [47]. The defective wavefront under measurement is laterally displaced by a small amount, and the interference pattern between the original and the displaced wavefronts is obtained. For a nearly plane wavefront, the lateral shear is obtained by displacing the wavefront in its own plane. For a nearly spherical wavefront, the lateral shear is obtained by sliding the wavefront along itself by rotation about an axis passing through the center of curvature of the spherical wavefront.

One of the important considerations in the design of lateral shearing interferometers is the nature of the light source. From the point of view of lateral shearing interferometry, the sources can be classified into two categories: (a) laser sources, such as the helium-neon gas laser giving a 6328-$\Rightarrow$ light beam of very high spatial and temporal coherence, and (b) all other sources, such as gas discharge lamps, which are temporally coherent to some extent but not spatially coherent.

(a)

(b)
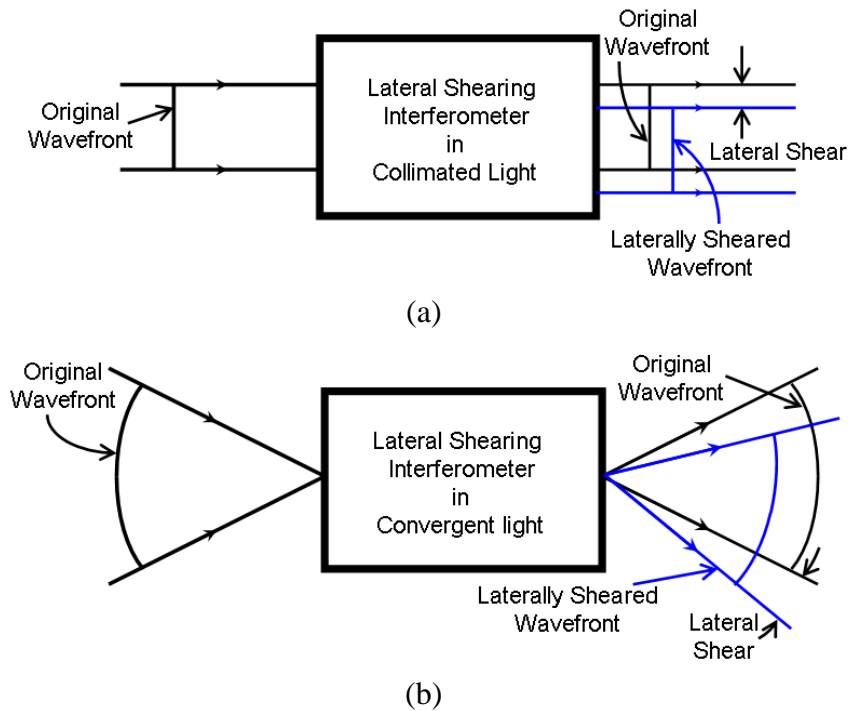
Figure 4.9   Schematic diagrams illustrating lateral shearing interferometry in (a) collimated light and (b) convergent light. (After D. Malacara [47])

4.5.1 Basic Theory of Lateral Shearing Interferometry

Consider the original wavefront and laterally sheared wavefront in Figure 4.10.
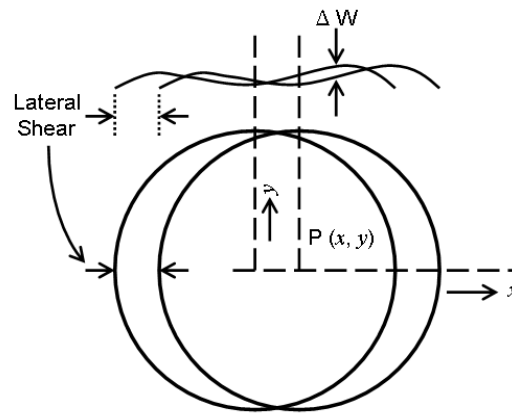
Figure 4.10   Schematic diagram illustrating the original and the sheared wavefronts. A circular aperture is assumed. The lateral shear fringes appear in the common area of the two wavefronts. (After D. Malacara [47])

The wavefront is considered nearly plane so that wavefront errors may be small

deviations from this plane. The wavefront error may be expressed as $W(x, y)$, where (x, y)

are the coordinates of the point P. When this wavefront is sheared in the *x*-direction by an amount S, the error at the same point for the sheared wavefront is $W(x - S, y)$. The resulting path difference ΔW at P between the original and sheared wavefronts is $W(x, y) - W(x - S, y)$. Thus, in lateral shearing interferometry, it is the quantity, ΔW, that is determined, and when S is zero, there is no path difference anywhere in the wavefront area and consequently no error can be seen, however large it may be. Now, the path difference ΔW may be obtained at various points on the wavefront from the usual relationship:

$$\Delta W = n\lambda \qquad (4.5.1)$$

where *n* is the order of the interference fringe and λ is the wavelength used. It is of interest that, when S is small, the previous equation may be written as

$$\left(\frac{\partial W}{\partial x}\right)S = n\lambda \qquad (4.5.2)$$

Thus the information obtained in the lateral shearing interferometer is ray aberration $(\partial W/\partial x)$ in angular measure. The equation becomes more exact a $S \to 0$, but we also have seen that the sensitivity decreases as $S \to 0$. Thus we must arrive at some compromise for the proper value of *S* if the previous equation is to be used exactly.

Defocusing:

The defocusing aberration can be written as

$$W(x, y) = D(x^2 + y^2) . \qquad (4.5.3)$$

This yields the optical path difference

$$\Delta W = 2DxS = n\lambda . \qquad (4.5.4)$$

Tilt:

If tilt exists in the direction orthogonal that of the lateral shear, the optical path difference can be written as

$$\Delta W = Ey = n\lambda. \tag{4.5.5}$$

If tilt and defocusing are simultaneously present, the optical path difference is given by

$$\Delta W = 2DxS + Ey = n\lambda. \tag{4.5.6}$$

Primary Spherical Aberration:

The wavefront error for the primary spherical aberration may be written as

$$W(x, y) = A(x^2 + y^2)^2. \tag{4.5.7}$$

Thus, the shearing interferogram can be expressed as

$$\Delta W = 4A(x^2 + y^2)xS = n\lambda. \tag{4.5.8}$$

With the addition of defocusing term and tilt, we obtain

$$\Delta W = \left[4A(x^2 + y^2)x + 2Dx\right]S + Ey = n\lambda. \tag{4.5.9}$$

If the primary spherical aberration is very small and also if the defocusing term is absent, we can approximate the previous equation as

$$\Delta W = 4Ax^3S + Ey = 0. \tag{4.5.10}$$

Primary Coma:

The expression for the primary comatic aberration is

$$W(x, y) = By(x^2 + y^2). \tag{4.5.11}$$

Due to the unsymmetrical nature of the aberration, the shape of the lateral shear fringes is dependent on the direction of the shear (x-, y-, or some other direction). If we assume that the shear is in the x-direction, then the optical path difference may be written as

$$\Delta W = 2BxyS = n\lambda. \tag{4.5.12}$$

The previous equation represents rectangular, hyperbolic fringes with asymptotes in the x- and y- directions. If the shear exists in the y-direction

$$\Delta W = B(x^2 + 3y^2)T = n\lambda. \qquad (4.5.13)$$

In this situation, the fringes form a system of ellipses with a ratio of major to minor axes of $\sqrt{3}$. Also the major axis is parallel to the x-axis.

Primary Astigmatism:

The expression for primary astigmatism is

$$W(x, y) = C(x^2 - y^2). \qquad (4.5.14)$$

As one can readily see from the expression, if the lateral shear exists in x- or y-direction, we get straight fringes orthogonal to the direction of shear. This can easily cause a misinterpretation of an astigmatic wavefront as a true spherical wavefront. However, an addition of defocusing makes it possible to detect the presence of astigmatism. In the presence of defocusing, the fringes for lateral shear in x-direction and y-direction are described, respectively, by

$$\Delta W = (2Dx + 2Cx)S = n\lambda \text{ and } \Delta W = (2Dy + 2Cy)T = n\lambda. \qquad (4.5.15)$$

Another way to detect astigmatism involves the use of lateral shear in a general direction. For example, the direction of shear may be halfway between the sagittal and tangential direction. In this case, the fringe system is described by

$$\Delta W = 2(D + C)xS + 2(D - C)yT = n\lambda. \qquad (4.5.16)$$

The previous equation describes equally spaced, straight fringes, and their slope is given by

$$Slope = \frac{(C + D)S}{(C - D)T}. \qquad (4.5.17)$$

Hence, by changing the azimuth of the direction of shear and noting the corresponding direction of the fringes, it is possible to find the particular direction the slope of which deviates most from the orthogonal direction.

Curvature of Field

Curvature of field can be simply treated as a defocusing situation because it is a displacement of focus longitudinally.

Distortion

Distortion is a function of the pupil diameter, and hence it cannot be detected using lateral shearing interferometry.

Chromatic Aberration

Longitudinal chromatic aberration is a change of focus for different wavelengths. Therefore, by changing the wavelength of the source light, one can detect a change in the number of fringes due to defocusing and thereby detect longitudinal chromatic aberration. Lateral chromatic aberration, being a linear function of the pupil diameter, is not generally detected using lateral shearing interferometry.

4.5.2 Current Status of Lateral Shearing Interferometry

Using the variable-shear LSI technique, M. P. Rimmer and J. C. Wyant reported the measurements of wavefronts having aberrations greater than 100 wavelengths and slope variations of more than 400 wavelengths per diameter [48]. (These measurement ranges fall short of those achieved by conventional Shack-Hartmann sensors.) The accuracy of the wavefront estimation rapidly deteriorates as the aberration becomes large (greater than 100 wavelengths) or the shear is reduced (smaller than 0.1). The restrictions imposed on the size of the shear fundamentally limit the sensitivity and measurement

ranges of the LSI technique. The coefficients of the polynomials that show the characteristics of the wavefront under test were calculated by solving the simultaneous equations between the Zernike coefficients of the wavefront under test and the coefficients of the difference between the two wavefronts [48]. However, the order of the polynomials that construct the difference information is lower than the order of the polynomials that construct the wavefront under test. Therefore, the number of unknown coefficients of the wavefront under test does not coincide with the number of known coefficients of the difference information. In this case, the unknown coefficients are approximately calculated by the least-squares fitting. The calculated coefficients are not precise. Also, using the monomial representation in the fitting process and converting the fitting data found to the Zernike set of functions afterward produce computational inaccuracies [48, 55].

In general, if one of the polynomial methods is used for representing wavefront under test, polynomial coefficients are determined by least squares. However, the degree of polynomial has to be chosen in advance [49]. If the degree selected is too small, the polynomial model can prove to be poor. An excessively large degree can lead to difficulties that are due to ill conditioning or over-fitting.

Another method uses Tikhonov regularization to obtain a reconstructed wavefront that is smooth. For this method, an appropriate regularization parameter has to be chosen to yield good results. Since this method leads to low-pass filtering of the frequency response, the whole Fourier transform of the wavefront is somewhat biased [50].

The biggest challenge for lateral shearing interferometry (LSI) is the reconstruction of the measured wavefronts [49-53]. Regardless of the type of

reconstruction algorithms (for example, polynomial-fitting methods or fringe-following techniques) used, the reconstruction process proves to be a highly sophisticated data analysis problem for LSI. As a result, LSI has not been a popular choice when quantitative data is to be extracted from the wavefront under analysis [48]. No researchers have reported successful quantitative measurements of high-order aberrations of large magnitude (such as measuring aspheric surfaces or lenses) or very large local-gradients using LSI.

4.6 Other Testing Methods and Instruments

4.6.1 Star Tests

The star test is conceptually basic and simple method for testing image-forming optical systems. One examines the image of a point source formed by the system and judge the image quality according to the departure from the ideal image form. In practice, the star test is almost always carried out visually and semi-quantitatively. It is generally impossible, in principle, to extract the aberrations from the form of the point spread function. As a result, one who uses the star-test method has to estimate the aberrations of the system, based on experience and on the many examples of point spread functions that have been either computed or photographed from known aberrations. Thus, the star test is a highly qualitative method, and obtaining the best results from it requires considerable experience.

For measuring large aberrations of imaging systems such as photographic objectives, projection objectives, and camera optics, the system will normally be set up on a nodal slide optical bench with a collimator, as in Figure 4.11, so that off-axis aberrations can also be measured. According to D. Malacara [56], the work published by

Wandersleb showed good photographs of point spread functions with large aberrations for comparison and estimation purposes.
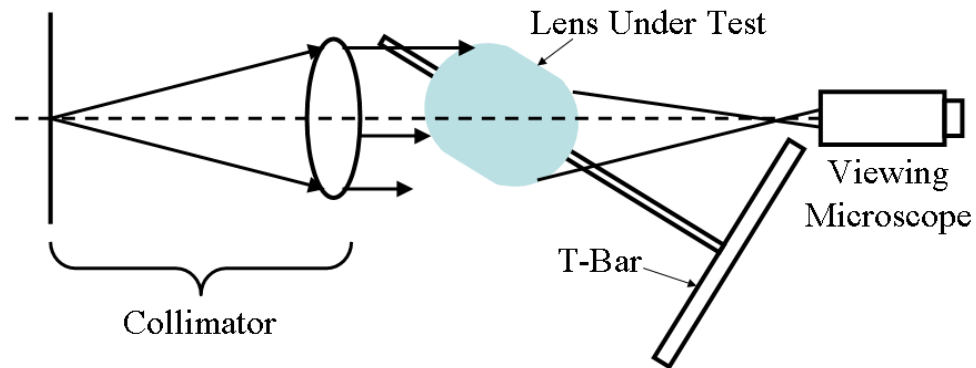
Figure 4.11   A nodal slide optical bench as used for star testing photographic imaging systems (after D. Malacara [56])

Since the star test does not make quantitative measurements accurately for large aberrations, incorporating a null test by adding an auxiliary optical system with the required aberrations was demonstrated. The auxiliary system should be precisely designed to generate known aberrations (for example, an auxiliary lens system for null-testing paraboloids), and the system must be easy to manufacture [56]. If it is possible to test the system with a laser as light source, then a computer-generated hologram can be used as the auxiliary system [57-58]. A useful description of this method is given by Birch and Green, who reported that they demonstrated the measurement accuracy of less-than $\lambda/20$-rms for primary and secondary spherical aberrations (low-order aberrations) [57]. With a high-resolution computer graphics system, the computer-generated hologram can synthesize a wavefront of any desired shape. And, usually the computer-generated hologram corrector is part of an interferometric testing scheme [57-58], but it could also be used to synthesize an aberrated wavefront for transmission through the system under test. If the system had the desired aberrations, it would form an

unaberrated final image. The most recent work is done by Heil, Wesner, Muller, and Sure [58]. They used the computer-generated holograms, in conjunction with the Twyman-Green interferometer, in order to perform the in-situ final-minute adjustment to the imaging quality of microscope objectives on production line. The researchers did not provide the accuracy and precision that could be achieved with the method. Also the maximum magnitude of the aberrations that could be measured with the method was not reported, either. The paper gave very qualitative discussion of the results on imaging correction rather than quantitative discussion on how accurately optical aberrations were estimated.

It is difficult to find publications about the star test. This is mainly due to the fact that the testing method depends heavily on the experience of the user [56]. This implies that the star test method is very qualitative rather than quantitative. Also, the earlier relevant publications are either too old that they do not show up in the digital database, or they were published in German, making it difficult to understand.

4.6.2. Ronchi Tests

In optical testing, the Ronchi test has been used widely but in a qualitative rather than a quantitative way [59]. The Ronchi test measures the transverse aberration (TA) in a direct way, as shown in Figure 4.12. In this figure, both the object and the image are on the optic axis, so the transverse aberration is measured from the axis and can be seen to include defocusing as well as other aberrations.

The wave aberration is defined in this exit pupil of the optical system under test, using a formula given by Rayces, as

$$\frac{\partial W}{\partial x} = -\frac{TA_x}{r-W} \approx -\frac{TA_x}{r} \; ; \; \frac{\partial W}{\partial y} = -\frac{TA_y}{r-W} \approx -\frac{TA_y}{r} , \tag{4.6.1}$$

since $r >> W$ (r: the radius of curvature of the wavefront). If we assume a Ronchi ruling with spacing d between the slits, for a point (x, y) on the mth fringe we may write, in general,

$$\frac{\partial W}{\partial x} \cos \varphi - \frac{\partial W}{\partial y} \sin \varphi = -\frac{md}{r} , \tag{4.6.2}$$

where it is assumed that the ruling lines are inclined at an angle φ with respect to the y-axis. This is the basic formula for the geometrical model of the Ronchi test.

The primary aberrations can be written as

$$W(x, y) = A(x^2 + y^2)^2 By(x^2 + y^2) + C(x^2 + 3y^2) + D(x^2 + y^2), \tag{4.6.3}$$

where A, B, C, and D are the spherical aberration, coma, astigmatism, and defocusing coefficients, respectively. No tilt term is included because the Ronchi test is insensitive to them. The last coefficient D is given by the distance l' from the Ronchi ruling to the paraxial focus, as

$$D = \frac{l'}{2r^2} . \tag{4.6.4}$$

Manipulating the first two equations, we obtain

$$4A(x^2 + y^2)(x \cos \varphi - y \sin \varphi) + B[2xy \cos \varphi - (3y^2 + x^2) \sin \varphi]$$
$$+ 2C(x \cos \varphi - 3y \sin \varphi) + 2D(x \cos \varphi - y \sin \varphi) = -\frac{md}{r} . \tag{4.6.5}$$

In the study of each of the aberrations, it will often be convenient to apply a rotation ψ to this expression by means of the relations

$$x = \eta \cos \psi + \xi \sin \psi,$$
$$y = -\eta \sin \psi + \xi \cos \psi, \tag{4.6.6}$$

where η and ξ are the new coordinate axes.
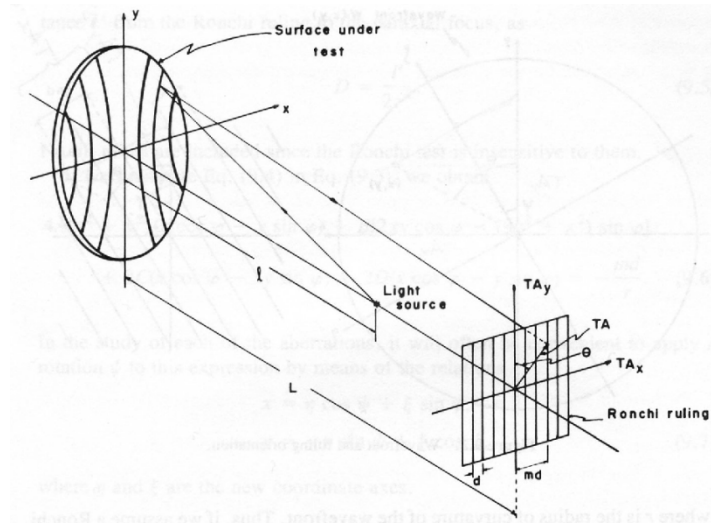
Figure 4.12   Geometry of the Ronchi Test (after D. Malacara [59])
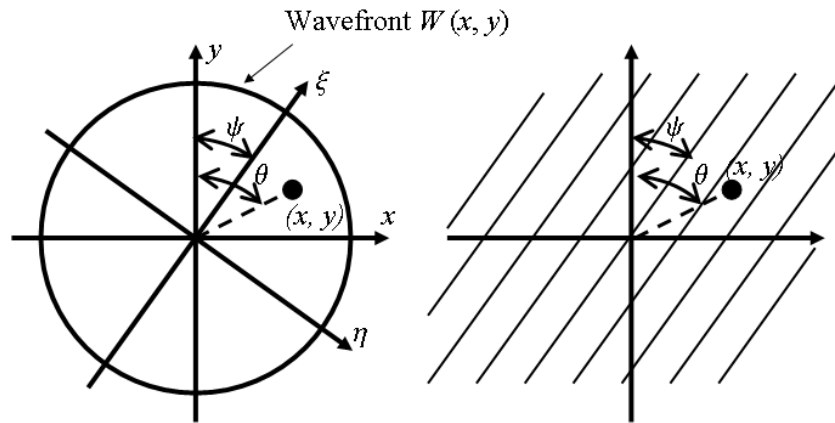
Figure 4.13   Wavefront and ruling orientation (after D. Malacara [59])

Defocusing:

By applying the rotation $\psi = \varphi$ to the defocusing term, we obtain

$$2D\eta = -\frac{md}{r}.$$
(4.6.7)

$$S = \frac{d}{2Dr}$$
(4.6.8)

Spherical Aberration with Defocusing:

By applying the rotation $\psi = \varphi$, we obtain

$$4A(\eta^2 + \xi^2)\eta + 2D\eta = -\frac{md}{r} \qquad (4.6.9)$$

Coma:

Applying a rotation $\psi = \varphi/2 + \pi/4$, we obtain

$$B\left[-\eta^2(1 + 2\sin\varphi) + \xi^2(1 - 2\sin\varphi)\right] = -\frac{md}{r}. \qquad (4.6.10)$$

Depending on the ruling inclination (φ) with respect to the meridional plane,

different patterns are obtained:

$\varphi = 0°$ Hyperbolas

$\varphi = 90°$ Ellipse with semi-axes in the ratio $\sqrt{3}$ to 1

$0° < \varphi < 90°$ Hyperbolas inclined at an angle ψ

$\varphi = 30°$ Straight bands

$30° < \varphi < 90°$ Ellipse inclined at an angle ψ

Astigmatism with Defocusing:

By applying the rotation $\psi = \varphi$, we obtain

$$2C\left[\eta(2 - \cos 2\varphi) - \xi\sin 2\varphi\right] + 2D\eta = -\frac{md}{r}. \qquad (4.6.11)$$

The angle of inclination between the Ronchigram and the ruling slits is given by

$$\tan\alpha = \frac{C\sin 2\varphi}{D + C(2 - \cos 2\varphi)}. \qquad (4.6.12)$$

The separation of the bands is given by

$$\Delta\xi = \frac{d}{2rC\sin 2\varphi}. \qquad (4.6.13)$$

Spherical Aberration with Astigmatism and Defocusing:

By applying the rotation $\psi = \varphi$, we obtain

$$4A\eta\left(\eta^2 + \xi^2\right) + 2\eta\left[D + C(2 - \cos 2\varphi)\right] - 2C\xi \sin 2\varphi = -\frac{md}{r}. \qquad (4.6.14)$$

The Ronchi test has been applied to characterize the primary aberrations of aspherical mirrors [60-62]. The measurement range can be quite large for the conventional Ronchi test [61-63], but the measurement sensitivity is on the order of magnitude of the diameter of the Airy Disc [61]. For example, the maximum sensitivity is given by $2\lambda R/D$, where λ is the test wavelength, R is the radius of the curvature, and D is the diameter of the mirror under test. In order to increase the measurement sensitivity of the Ronchi test, the number of fringes in the interferogram must be decreased so that the individual fringes become more visible [61]. However, a decrease in the number of fringes reduces the dynamic range of the phase measurements. Hence, an appropriate compromise must be made between the sensitivity and dynamic range, according to the specific measurement requirements. In addition, imperfections of the Ronchi gratings, especially binary gratings that generate large number of harmonic components, reduce the signal-to-noise ratio of the Ronchi test. Another challenge is to make digitized, quantitative measurements with the Ronchi test. In 1984, T. Yatagai reported the fringe scanning Ronchi test for aspherical surfaces [64] using a digital phase-measurement technique. He translated the Ronchi ruling sideways to vary the irradiance of the Ronchigram periodically with time, and then made synchronous phase detection in the Ronchi test. T. Yatagai was able to measure up to75-μm peak-to-peak surface deviation but did not comment on the accuracy, repeatability, and sensitivity of his method. Also

the fringe scanning algorithm is limited by the 2π phase jump usually seen in the phase-shifting interferometer. In 1997, another group of researchers made digitized aberration measurement on a lens using the Ronchi test with a phase-shifted sinusoidal grating [65]. The goal was to optimize the performance of the quantitative Ronchi test between the accuracy and the measurement range. The least-squares fitting was performed to reconstruct the wavefront, and only the spherical aberration of the lens was quantitatively calculated. They reported the accuracy of 0.014λ, which is compatible with the values yielded by high-precision PSI systems or S-H sensors. Unfortunately, the maximum deviation that could be measured at this magnitude of the error was only 9.9λ, which is much smaller than that of conventional PSI or S-H systems. More recent works of the Ronchi test concentrated on surface profilometry [66-67]. No researchers have successfully demonstrated fast, quantitative measurements of large-magnitude, high-order wavefront aberrations of optical components or systems using the Ronchi test.

4.6.3 Foucault's Knife-Edge Tests

The knife-edge test may be considered, in general, as a method for detecting the presence of transversal aberrations [68]. This is done by blocking out one part of a plane traversed by rays or diffracted light so that a shadow appears over the aberrated region (Figure 4.14). The knife-edge test is very simple and is used mainly for qualitative interpretation.

For aberrations greater than the wavelength of the illuminating radiation, geometrical theory of image formation is employed to study the characteristics of the test. Refer to Figure 4.15. The border of the knife in the Foucault test is placed at a distance r_1 from the chief ray intersection (the origin of the X_1-Y_1 plane), and an angle ϕ_1 is

subtended between the Y_1 axis and the knife edge. The angle ϕ_1 will be defined as positive if the slope of the knife edge is positive.
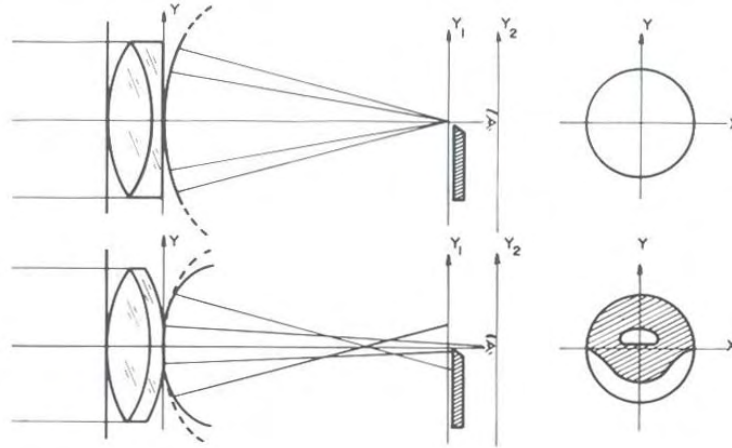
Figure 4.14   Foucault method for testing lenses (after D. Malacara [68])
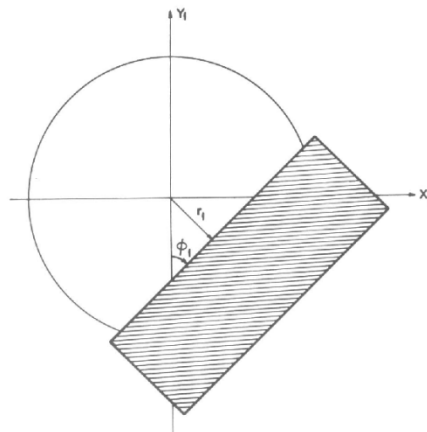
Figure 4.15   Knife-edge position projected over the entrance pupil plane of the viewing system (after D. Malacara [68])

The following equation defined the border:

$$x_1 \cos \phi_1 - y_1 \sin \phi_1 = r_1 \tag{4.6.15}$$

The transmittance over this plane may be expressed as

$$T(x_1, y_1) = \begin{cases} 1 & if \quad x_1 \cos \phi_1 - y_1 \sin \phi_1 < r_1 \\ 0 & if \quad x_1 \cos \phi_1 - y_1 \sin \phi_1 \geq r_1 \end{cases}. \tag{4.6.16}$$

But, since the X_1-Y_1 plane defines the paraxial plane of convergence of the ideal wavefront W, any point (x_1, y_1) over this plane satisfies, approximately, the following property:

$$(x_1, y_1) = \left(-R\frac{\partial W}{\partial x}, -R\frac{\partial W}{\partial y} \right);$$

(4.6.17)

where R is the distance between the X-Y plane and the X_1-Y_1 plane.

Using this result, we obtain

$$T(x_1, y_1) = \begin{cases} 1 & if & \dfrac{\partial W}{\partial x}\cos\phi_1 - \dfrac{\partial W}{\partial y}\sin\phi_1 < \dfrac{r_1}{R} \\ 0 & if & \dfrac{\partial W}{\partial x}\cos\phi_1 - \dfrac{\partial W}{\partial y}\sin\phi_1 \geq \dfrac{r_1}{R} \end{cases}.$$

(4.6.18)

If we choose the X-axis as reference so that ϕ_1 is 90°,

$$T\left(\frac{\partial W}{\partial y} \right) = \begin{cases} 1 & if & \dfrac{\partial W}{\partial y} < \dfrac{r_1}{R} \\ 0 & if & \dfrac{\partial W}{\partial y} \geq \dfrac{r_1}{R} \end{cases}.$$

(4.6.19)

Focus error:

$$W(x, y) = D\left(x^2 + y^2\right)$$

(4.6.20)

$$y_1 = \frac{r_1}{2DR}$$

(4.6.21)

Primary spherical aberration:

If both primary spherical aberration and defocus are present, the aberration function is

$$W(x, y) = A\left(x^2 + y^2\right)^2 + D\left(x^2 + y^2\right),$$

(4.6.22)

The equation of the borders of the shadow pattern is written as

$$y^3 + \left(\frac{D}{2A} + x^2\right) y - \frac{r_1}{4DR} = 0. \tag{4.6.23}$$

Setting $x = 0$, we identify the boundaries of the shadow pattern along the Y-axis for this case:

$$y^3 + \frac{D}{2A} y - \frac{r_1}{4DR} = 0. \tag{4.6.24}$$

Since the equation is cubic, we expect three roots. We define the parameter Δ as

$$\Delta = \left(\frac{r_1}{8AR}\right)^2 + \left(\frac{D}{64}\right)^3. \tag{4.6.25}$$

1. If $\Delta < 0$, there will be three real and unequal roots.

2. If $\Delta = 0$, there will be three real roots of which at least two are equal.

3. If $\Delta > 0$, there will only one real root and two conjugate imaginary roots.

The shadow pattern will show more than one dark region if conditions 1 and 2 are satisfied. This happens when A and D have different signs.

If $\Delta \leq 0$, then

$$\left(\frac{r_1}{R}\right)^2 \leq \frac{\left(-\frac{2}{3} D\right)^3}{A}. \tag{4.6.26}$$

If the knife edge is touching the optical axis ($r_1 = 0$),

$$y\left(y^2 + \frac{D}{2A}\right) = 0. \tag{4.6.27}$$

The solutions are

$$y = 0$$

$$y = \pm\sqrt{-\frac{D}{2A}}\,.$$

In this case, D and A must have different signs in order to produce real numbers as solutions.

Primary coma:

The aberration function for primary coma and defocus is given by

$$W(x, y) = By(x^2 + y^2) + D(x^2 + y^2) \tag{4.6.28}$$

If the knife edge is placed at a point on the X_1 axis at a distance r_1 from the origin (parallel to the Y_1 axis, $\phi_1 = 0$), that the shadow pattern satisfies the following equation:

$$2Bxy + 2Dx = \frac{-r_1}{R}\,. \tag{4.6.29}$$

Regrouping the previous equation gives

$$\left(y + \frac{D}{B}\right)x = \frac{-r_1}{2RB}\,. \tag{4.6.30}$$

This equation implies rectangular hyperbolas centered at the point $[0, -(D/B)]$.

If the knife edge is introduced at a point on the Y_1-axis, the partial derivative of the wavefront with respect to y is

$$\frac{\partial W}{\partial y} = B(x^2 + 3y^2) + 2yD\,. \tag{4.6.31}$$

And, the borders of the shadow pattern becomes

$$x^2 + 3\left(y + \frac{D}{3B}\right) = \frac{r_1}{RB} + \frac{1}{3}\left(\frac{D}{B}\right)^2, \tag{4.6.32}$$

which is an ellipse centered at point [0, -(D/3B)], with the major axis parallel to the X-axis.

Astigmatism:

Astigmatism, together with defocus yields the aberration function:

$$W(x, y) = Cy(x^2 + 3y^2) + D(x^2 + y^2).$$

(4.6.33)

Assuming the knife edge is introduced along an axis that subtends an angle ϕ_1 with the Y_1-axis. The partial derivative with respect to x is

$$\frac{\partial W}{\partial x} = 2Cx + 2Dx.$$

(4.6.34)

And, with respect to y, the partial derivative is

$$\frac{\partial W}{\partial y} = 6Cy + 2Dy.$$

(4.6.35)

The border of the shadow pattern becomes

$$-(C + D)x \cos \phi_1 + -(3C + D)y \sin \phi_1 = \frac{r_1}{2R}.$$

(4.6.36)

Depending on the magnitude of aberrations, a proper mathematical model for the Foucault's test must be chosen to analyze the measured data. For wavefront aberrations smaller than the test wavelength, the diffraction theory of the Foucault knife-edge should be applied. For optical aberrations larger than the test wavelength, the geometrical theory is used, and as a result the sensitivity is degraded [68].

A few papers can be found regarding the Foucault's knife-edge test for quantitative measurements. In 1975, R. G. Wilson applied the diffraction theory of the Foucault test to quantitatively characterize the figure-error of a spherical mirror [69]. A precision knife-edge scanner (driven by a reversible clock motor) was used together with

three photomultiplier scanners to make the measurements on figure-errors (low orders or low spatial frequencies) of a spherical mirror. The power of the irradiance bypassing the knife edge was recorded as a function of the edge position. The scanning measurements were made in two orthogonal orientations of the mirror under test. R. G. Wilson reported the rms figure-error of 0.007λ, which is close to the precision found in high-end SH sensors or PSI systems. But, the author showed little confidence in measuring wavefront aberrations larger than 1λ and recommended the method for measuring very small aberrations of nearly diffraction-limited optical elements or systems. In 1999, F. Zamkotsian and K. Dohlen reported the quantitative Foucault's knife-edge method for measuring Texas Instruments' micro-mirror array [70]. Translating a high-precision knife-edge scanner ($\pm 1\mu m$ positioning accuracy) through the source image, twenty-nine images of the same field of view for different positions of the knife edge were recorded with a CCD. The authors demonstrated the measurement of 2-nm maximum deviation with a sub-nanometer (± 0.82 nm) precision. However, the way the authors validated the method was questionable. Using their Foucault's scanning method, they measured a conventional spherical mirror with a radius of curvature of 252 mm. Then instead of comparing with the measurements made on the same mirror using a well-established technology (such as white-light interferometry), the authors compared the measured profile with the theoretical profile. The detailed specifications of the conventional spherical mirror were not shown in the paper.

No researchers, up-to-present, using the Foucault's knife-edge test, have successfully demonstrated the fast, quantitative measurements of large-magnitude, high-order wavefront aberrations.

4.7 Conclusions

In this chapter, we have examined the status today and considered the future development of various types of wavefront sensors: phase-shifting interferometers, lateral-shearing interferometers, curvature sensing, the phase-diversity method, the Foucault (knife-edge) test, the Ronchi test, and the star test. None of these wavefront sensors are suitable for precisely characterizing high-order wavefront aberrations of large magnitude. In the next chapter, we will introduce our Shack-Hartmann sensor with addressable microlens array demonstrating how it will eventually be capable of characterizing: corneal scarring, tear-film effects, LASIK-flap wrinkles, and keratoconics and post-LASIK corneas.

References

[1]   S. A. Klein, "Problems with wavefront aberrations applied to refractive surgery: Developing Standards," Ophthalmic Technologies XI, SPIE Vol. 4245, pp47-56.

[2]   C. E. Joslin, S. M. Wu, T. T. McMahon, M. Shahidi, "Higher-order wavefront aberrations in corneal refractive therapy," Optometry & Vision Science, vol.80, no.12, Dec. 2003, pp.805-11.

[3]   D. R. Neal, D. M. Topa, J. Copland, "The effect of lenslet resolution on the accuracy of ocular wavefront measurements," SPIE-Int. Soc. Opt. Eng. Proceedings of Spie - the International Society for Optical Engineering, vol.4245, 2001, pp.78-91.

[4]   D. Malacara, *Optical Shop Testing* Wiley-Interscience, (New York, 1992), Chap. 14.

[5]   J. E. Greivenkamp, "Sub-Nyquist interferometry," Applied Optics, vol.26, no.24, Dec. 1987, pp.5245-58.

[6]   M. Servin, D. Malacara, Z. Malacara, and V. I. Vlad, "Sub-Nyquist null aspheric testing using a computer-stored compensator," Applied Optics, vol.33, no.19, Jul. 1994, pp.4103-08.

[7]   J. C. Wyant, "Testing Aspherics Using Two-Wavelength Holography," Applied Optics, vol.10, no.9, Sep. 1971, pp.2113-18.

[8]   J. C. Wyant, B. F. Oreb, and P. Hariharan, "Testing aspherics using two-wavelength holography: use of digital electronic techniques," Applied Optics, vol.23, no.22, Nov. 1984, pp.4020-23.

[9]   Y. Cheng and J. C. Wyant, "Two-wavelength phase shifting interferometry," Applied Optics, vol.23, no.24, Dec. 1984, pp.4539-43.

[10]   J. E. Greivenkamp, "Sub-Nyquist interferometry," Applied Optics, vol.26, no.24, Dec. 1987, pp.5245-58.

[11]   D. Malacara, *Optical Shop Testing* Wiley-Interscience, (New York, 1992), Chap. 14.

[12]   N. Ninane and M. P. Georges, "Holographic interferometry using two-wavelength holography for the measurement of large deformations," Applied Optics, vol.34, no.11, Apr. 1995, pp.1923-28.

[13]   A. Pfortner and J. Schwider, "Red-green-blue interferometer for the metrology of discontinuous structures," Applied Optics, vol.42, no.4, Feb. 2003, pp.667-73.

[14] J. W. Hardy, *Adaptive Optics for Astronomical Telescopes*, Oxford University Press, New York, 1998, Chap. 5.

[15] F. Roddier, "Curvature sensing and compensation: a new concept in adaptive optics," Applied Optics, vol. 27, no.7, Apr. 1988, pp. 1223-25.

[16] M. R. Teague, "Deterministic phase retrieval: a Green's function solution," Journal of the Optical Society of America, vol.73, no.11, Nov. 1983, pp. 1434-41.

[17] F. Roddier, "Wavefront sensing and the irradiance transport equation," Applied Optics, vol. 29, no.10, Apr. 1990, pp. 1402-03.

[18] C. Roddier and F. Roddier, "Wave-front reconstruction from defocused images and the testing of ground-based optical telescopes," Journal of the Optical Society of America A - Optics & Image Science, vol.10, no.11, Nov. 1993, pp. 2277-2287.

[19] A. Barty, K. A. Nugent, A. Roberts, and D. Paganin, "Quantitative opticalphase microscopy," Optics Letters, vol.23, no.11, Jun. 1998, pp. 817-819.

[20] M. Toyota, K. Araki, and Y. Suzuki, "Wave-front tilt sensor with two quadrant detectors and its application to a laser beam pointing system," Applied Optics, vol. 41, no.12, Apr. 2002, pp. 2219-2223.

[21] P. J. Fox, T. R. Mackin, L. D. Turner, I. Colton, K. A. Nugent, and R. E. Sholten, "Noninterferometric phase imaging of a neutral atomic beam," Journal of the Optical Society of America B-Optical Physics, vol.19, no.8, Aug. 2002, pp.1773-6.

[22] J. R. Fienup, B. J. Thelen, R. G. Paxman, and D. A. Carrara , "Comparison of Phase Diversity and Curvature Wavefront Sensing," SPIE-Int. Soc. Opt. Eng. Proceedings of Spie - the International Society for Optical Engineering, Conference: Adaptive Optical System Technologies, Kona, Hawaii, vol.3353, 1998, pp.930-40.

[23] M. Soto and E. Acosta, "Performance analysis of curvature sensors: optimum positioning of the measurement planes," Optics Express, vol.11, no.20, Oct. 2003, pp.2577-88.

[24] R. Kupke, F. Roddier, and D. L. Mickey, "Curvature-based Wavefront Sensor for use on Extended Patterns," SPIE-Int. Soc. Opt. Eng. Proceedings of Spie - the International Society for Optical Engineering, Conference: Adaptive Optics in Astronomy, vol.2201, 1994, pp.519-27.

[25] F. Rigaut, B. L. Ellerbroek, and M. J. Northcott, "Comparison of curvature-based and Shack-Hartmann based adaptive optics for the Gemini telescope," Applied Optics, vol.36, no.13, May 1997, pp.2856-68.

[26]   P. Doel, "A comparison of Shack-Hartmann and curvature sensing for large telescopes," SPIE-Int. Soc. Opt. Eng. Proceedings of Spie - the International Society for Optical Engineering, Conference: Adaptive Optical Systems and Applications, San Diego, California, vol.2534, 1995, pp.265-76.

[27]   Cerro Tololo Inter-American Observatory, Adaptive Optics Tutorial Chapter 3, Web Address - http://www.ctio.noao.edu/.

[28]   Gary Chanan, Wavefront Sensing Part 3, CFAO Summer School on Adaptive Optics 2004, Web Address - http://cfao.ucolick.org/aosummer/aosummer2004/lectures.php.

[29]   R. A. Gonsalves, "Phase retrieval from modulus data," Journal of the Optical Society of America, vol.66, no.9, Sept. 1976, pp.961-4.

[30]   R. A. Gonsalves, "Phase retrieval and diversity in adaptive optics," Optical Engineering, vol. 21, no. 5, September - October 1982, pp. 829-832.

[31]   R. G. Paxman, T. J. Schulz, and J. R. Fienup, "Joint estimation of object and aberrations by using phase diversity," Journal of the Optical Society of America A - Optics & Image Science, vol.9, no.7, July 1992, pp.1072-85.

[32]   T. L. Fine, *Feedforward Neural Network Methodology*, Springer-Verlag, New York, 1999, Chap. 5.

[33]   R. G. Paxman and J. R. Fienup, "Optical misalignment sensing and image reconstruction using phase diversity," Journal of the Optical Society of America A - Optics & Image Science, vol.5, no.6, Jun. 1988, pp.914-23.

[34]   M. A. van Dam and R. G. Lane, "Tip/tilt estimation from defocused images," Journal of the Optical Society of America A - Optics & Image Science, vol.19, no.4, Apr. 2002, pp.745-752.

[35]   J. R. Fienup, B. J. Thelen, R. G. Paxman, and D. A. Carrara , "Comparison of Phase Diversity and Curvature Wavefront Sensing," SPIE-Int. Soc. Opt. Eng. Proceedings of Spie - the International Society for Optical Engineering, Conference: Adaptive Optical System Technologies, Kona, Hawaii, vol.3353, 1998, pp.930-40.

[36]   J. W. Hardy, *Adaptive Optics for Astronomical Telescopes*, Oxford University Press, New York, 1998, Chap. 5.

[37]   Adaptive Optics at University of Hawaii, The University of Hawaii Adaptive Optics System, Web Address - http://www.ifa.hawaii.edu/ao/.

[38]   Cerro Tololo Inter-American Observatory, Adaptive Optics Tutorial Chapter 3, Web Address - http://www.ctio.noao.edu/.

[39] J. R. Fienup, J. C. Marron, T. J. Schulz, and J. H. Seldin, "Hubble Space Telescope characterized by using phase-retrieval algorithms," Applied Optics, vol.32, no.10, Apr. 1993, pp.1747-67.

[40] R. A. Carreras, S. Restaino, and D. Duneman, "A Laboratory Experiment Using Phase Diversity to Extract Higher Order Zernike Coefficients," SPIE-Int. Soc. Opt. Eng. Proceedings of Spie - the International Society for Optical Engineering, Conference: Image Reconstruction and Restoration, San Diego, California, vol.2302, 1994, pp.323-29.

[41] B. L. Ellerbroek, B. J. Thelen, D. J. Lee, D. A. Carrara, and R. G. Paxman, "Comparison of Shack-Hartmann wavefront sensing and phase-diverse phase retrieval," SPIE-Int. Soc. Opt. Eng. Proceedings of Spie - the International Society for Optical Engineering, Conference: Adaptive Optics and Applications, San Diego, California, vol.3126, 1997, pp.307-20.

[42] L. Meynadier, V. Michau, M-T Velluet, J-M Conan, L. M. Mugnier, and G. Rousset, "Noise propagation in wave-front sensing with phase diversity," Applied Optics, vol.38, no.23, Aug. 1999, pp.4967-79.

[43] J. J. Dolne, R. J. Tansey, K. A. Black, J. H. Deville, P. R. Cunningham, K. C. Widen, and P. S. Idell, "Practical issues in wave-front sensing by use of phase diversity," Applied Optics, vol.42, no.26, Sep. 2003, pp.5284-89.

[44] A. Blanc, T. Fusco, M. Hartung, L. M. Mugnier, and G. Rousset, "Calibration of NAOS and CONICA static aberrations - Application of the phase diversity technique," Astronomy & Astrophysics, vol.399, no.1, Feb. 2003, Publisher: EDP Sciences, France, pp.373-83.

[45] M. Hartung, A. Blanc, T. Fusco, F. Lacombe, L. M. Mugnier, G. Rousset, and R. Lenzen, "Calibration of NAOS and CONICA static aberrations – Experimental results," Astronomy & Astrophysics, vol.399, no.1, Feb. 2003, Publisher: EDP Sciences, France, pp.385-94.

[46] D. Malacara, *Optical Shop Testing* Wiley-Interscience, (New York, 1992), Chap. 11.

[47] D. Malacara, *Optical Shop Testing* Wiley-Interscience, (New York, 1992), Chap. 4.

[48] M. P. Rimmer and J. C. Wyant, "Evaluation of Large Aberrations Using a Lateral-Shear Interferometer Having Variable Shear," Applied Optics, vol.14, no.1, Jan. 1975, pp.142-150.

[49] G. Harbers, P. J. Kunst, and G. W. R. Leibbrandt, "Analysis of lateral shearing interferograms by use of Zernike polynomials," Applied Optics, vol.35, no.31, Nov. 1996, pp.6162-72.

[50]   M. Servin, D. Malacara, and J. L. Marroquin, "Wave-front recovery from two orthogonal sheared interferograms," Applied Optics, vol.35, no.22, Aug. 1996, pp.4343-8.

[51]   C. Elster and I. Weigartner, "Solution to the shearing problem," Applied Optics, vol.38, no.23, Aug. 1999, pp.5024-31.

[52]   S. Okuda, T. Nomura, K. Kamiya, H. Miyashiro, K. Yoshikawa, and H. Tashiro, "High-precision analysis of a lateral shearing interferogram by use of the integration method and polynomials," Applied Optics, vol.39, no.28, Oct. 2000, pp.5179-5186.

[53]   C. Elster, "Exact two-dimensional wave-front reconstruction from lateral shearing interferograms with large shears," Applied Optics, vol.39, no.29, Oct. 2000, pp5353-59.

[54]   DeVon W. Griffin, "Phase-shifting shearing interferometer," Optics Letters, vol.26, no.3, Feb. 2001, pp.140-141.

[55]   H. van Brug, "Zernike polynomials as a basis for wave-front fitting in lateral shearing interferometry," Applied Optics, vol.36, no.13, May 1997, pp.2788-90.

[56]   D. Malacara, *Optical Shop Testing* Wiley-Interscience, (New York, 1992), Chap. 11.

[57]   K. G. Birch and F. J. Green, "The application of computer-generated holograms to testing optical elements," Journal of Physics D-Applied Physics, vol.5, no.11, Nov. 1972, pp.1982-92, UK.

[58]   J. Heil, J. Wesner, W. Müller, T. Sure, "Artificial Star Test by Real-Time Video Holography for the Adjustment of High-numerical-aperture Micro-Objectives," Applied Optics, Vol. 42 Issue 25, Sep. 2003, pp. 5073-5085.

[59]   D. Malacara, *Optical Shop Testing* Wiley-Interscience, (New York, 1992), Chap. 11, pp. 397-426.

[60]   D. Malacara, "Geometrical Ronchi Test of Aspherical Mirrors," Applied Optics, vol.4, no.11, Nov. 1965, pp.1371-74.

[61]   A. Cornejo and D. Malacara, "Ronchi Test of Aspherical Surfaces, Analysis, and Accuracy," Applied Optics, vol.9, no.8, Aug. 1970, pp.1897-1901.

[62]   D. Malacara and A. Cornejo, "Null Ronchi Test for Aspherical Surfaces," Applied Optics, vol.13, no.8, Aug. 1974, pp.1778-80.

[63]   L. Carretero, C. Gonzalez, A. Fimia, and I. Pascual, "Application of the Ronchi test to intraocular lenses: A comparison of theoretical and measured results," Applied Optics, vol.32, no.22, Aug. 1993, pp.4132-4137.

[64]   T. Yatagai, "Fringe scanning Ronchi test for aspherical surfaces," Applied Optics, vol.23, no.20, Oct. 1984, pp.3676-79.

[65]   K. Hibino, D. I. Farrant, B. K. Ward, and B. F. Oreb, "Dynamic range of Ronchi test with a phase-shifted sinusoidal grating," Applied Optics, vol.36, no.25, Sep. 1997, pp.6178-89.

[66]   J. Arasa, S. Royo, and N. Toms, "Simple Method for Improving the Sampling in Profile Measurements by use of the Ronchi Test," Applied Optics, vol.39, no.25, Sep. 2000, pp.4529-34.

[67]   S. Roy, J. Arasa, and C. Pizarro, "Profilometry of Toroidal Surfaces with an Improved Ronchi Test," Applied Optics, vol.39, no.31, Nov. 2000, pp.5721-31

[68]   D. Malacara, *Optical Shop Testing* Wiley-Interscience, (New York, 1992), Chap. 8.

[69]   R. G. Wilson, "Wavefront-error evaluation by mathematical analysis of experimental Foucault-test data," Applied Optics, vol.14, no.9, Sep. 1975, pp.2286-97.

[70]   F. Zamkotsian and K. Dohlen, "Surface characterization of micro-optical components by Foucault's knife-edge method: The case of a micromirror array," Applied Optics, vol.38, no.31, Nov. 1999, pp.6532-39.

CHAPTER 5

Addressable Microlens Array to Improve Dynamic Range of Shack-Hartmann Sensors

NOMENCLATURE

$A_{comb\_overlap}$	Overlapping area between moving and fixed comb fingers
$A_{structure}$	Area of the top surface of the resonant structure
$A_{structure\_overlap}$	Overlapping area between the resonant structure and substrate
b	Damping factor
d_a	Actuation distance
d_{lens}	Diameter of microlens
E_{Si}	Young's modulus of elasticity of silicon
f_{lens}	Focal length of the lens
f_r	Resonant frequency
g_c	Gap between moving and fixed combs
g_f	Gap between two parallel flexures
k	Stiffness or spring constant
$k_{x\text{-}comb}$	Stiffness or spring constant of the combs in x-direction
$k_{x\text{-}flex}$	Stiffness or spring constant of the flexures in x-direction
$k_{y\text{-}flex}$	Stiffness or spring constant of the flexure in y-direction
$k_{y\text{-}max}$	Maximum stiffness or spring constant of the flexure in y-direction allowed in a single row
l_c	Length of combs
l_f	Length of flexures
l_{ol}	Length of overlap between fixed and moving combs
m	Total mass of the microlens resonant unit
$m_{\,moving\,structure}$	Mass of the moving structure without lens and flexures
$m_{\,flexures}$	Mass of the flexures attached to the unit
$m_{\,lens}$	Mass of the lens
n	The number of moving comb fingers
t_{SOI}	Thickness of the device layer of the SOI wafer
t_{BOX}	Thickness of the buried oxide layer of the SOI wafer
V_{dc}	DC driving voltage
V_{ac}	AC driving voltage
V_{dc_dyn}	Maximum dc-driving voltage before side thrust occurs (at resonance)
V_{dc_st}	Maximum dc-voltage before a side thrust occurs (at stationary position)
w_f	Width of flexures
w_c	Width of combs

y_0	Initial overlap length between the fixed and moving combs
y_d	Desired actuation distance at resonance in y-direction
y_{max_is}	Maximum actuation distance before a side thrust occurs (at resonance) in y-direction
y_r	Actuation distance at resonance in y-direction
θ	Wavefront slope
ε	Permittivity of air
ρ_{Si}	Density of single crystal silicon
ρ_{Lens}	Density of lens material
τ	Identification (readout) time
ω	Angular frequency ($2 \cdot \pi \cdot f$)
ω_r	Angular resonant frequency ($2 \cdot \pi \cdot f_r$)
μ	Viscosity of air
ν	Kinetic viscosity of air

5.1 Introduction

Shack-Hartmann sensors are widely used in astronomical telescopes and ophthalmic-analysis systems as monitors for wavefront aberrations. They are fast, accurate and, in contrast to interferometers, generally insensitive to vibrations. When they are used in conjunction with adaptive mirrors, Shack-Hartmann sensors are able to improve the image quality of astronomical telescopes by performing real-time corrections on the wavefront aberrations that are inherently generated as starlight traverses the earth's atmosphere [1]. Shack-Hartmann sensors have also proven to be the most suitable wavefront monitors for ophthalmic-analysis applications (such as pre- and/or post-LASIK surgery and keratoconus analysis) because measuring the optical aberrations in illumination passing through constantly moving human eyes requires fast measurement speed and high accuracy [2-6].
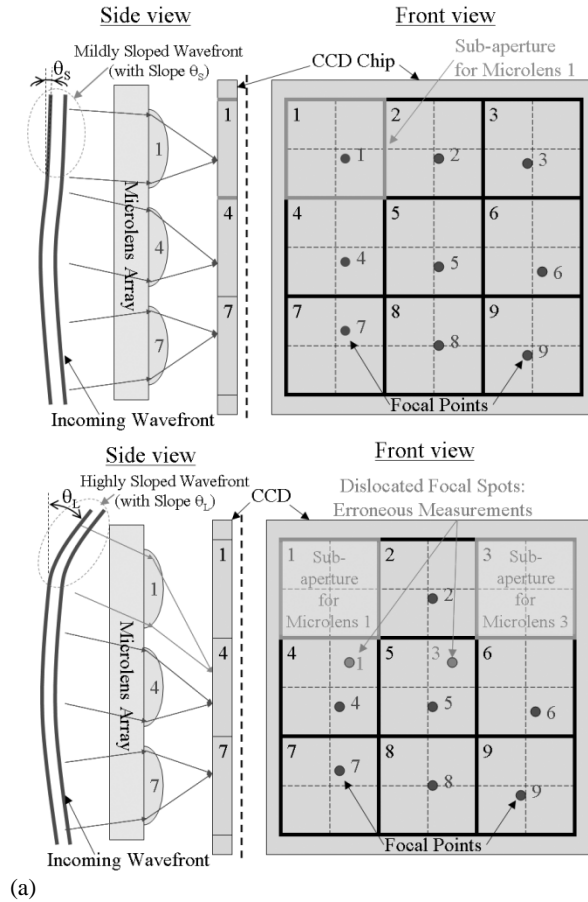
Figure 5.1   (a) Wavefront-slope measurement using microlens array: Each microlens has its own sub-aperture consisting of approximately forty CCD pixels (divided into four quadrants), and the focal point of the microlens must be located within the assigned sub-apertures; (b) Limited dynamic range of a conventional Shack-Hartmann sensor (left): A highly aberrated wavefront has a very large local slope, which causes the focal points of microlenses #1 and #3 to become focused onto the sub-apertures assigned to microlenses #4 and #5, respectively, causing erroneous measurements.

In Shack-Hartmann systems, a microlens array dissects an incoming wavefront into a number of segments (Figure 5.1(a)) [7]. Each microlens in the array creates a focal spot within the assigned sub-aperture on the CCD (typically made of 40 CCD pixels). Because light travels in a straight path normal to the wavefront, the positions of these focal spots are related to the average wavefront slope (θ_S or θ_L in Figure 5.1) over each microlens aperture. Thus the pattern of spots at the focal plane contains information

about the spatially resolved waveform slope that can be integrated to reconstruct the wavefront. The dynamic range (the range of measurable wavefront slope) of a conventional SH system has fundamental design limits that affect its performance; a SH system produces false results if the slope of the wavefront being measured is too large [2]. Figure 5.1(b) shows one of these cases in which a focal point of one microlens, as a result of extreme aberration in the incoming wave, moves into an adjacent sub-aperture that has been pre-assigned to register the focal point of another microlens. The typical maximum values of θ that can be measured by a commercially available SH system are between 5.5 mrad and 12.5 mrad over a microlens aperture.

Researchers have attempted to overcome this dynamic-range limitation of SH systems using at least three methods: (1) by employing a modified unwrapped algorithm [8], (2) by using a SH array of microlenses with well-defined astigmatism [9], or (3) by positioning a spatial-light modulator in front of the SH microlens array as a shutter [10]. Research showed that the first two methods had limited practical use providing accurate measure of wavefront aberration. Method (1) does not work with wavefronts that exhibit localized aberrations of large magnitudes. Method (2) requires that the elliptical focal spots must have enough space between them along the major and minor axes, in order to obtain proper measurements. Hence, the spatial density of the astigmatic microlens array has to be much lower than that of a circular microlens array, and this in turn lowers the accuracy of the sensor. Method (3), which employs a spatial-light modulator, is also impractical on three grounds: the modulator absorbs a great deal of light (at least 50% in the case of an LCD illuminated with unpolarized light); it increases the noise in the measurement; and it introduces additional aberrations to the wavefront being measured.

In addition, spatial-light modulators can have polarization dependences, and these modulators are typically very expensive.

Nonetheless, expanding the dynamic range of Shack-Hartmann sensors is highly desired, especially in consideration of their increasing uses in refractive surgery ($600M market in 2001) and in Keratoconus analysis. In the case of refractive surgery, the development of a transition zone (resultant from scar tissues) at the boundary separating surgically treated and untreated areas results in large optical aberrations [11] when the tissue is examined. Also analyzing ophthalmic diseases such as Keratoconus (meaning cone-shaped cornea) requires large dynamic ranges and sensitivities that cannot be achieved by conventional Shack-Hartmann sensors [2].

Using MEMS technologies developed in the Berkeley Microlab, we have created densely packed active microlens arrays in which each of the lenses is designed so that it can be driven to resonate at a pre-designed frequency. When a lens resonates, its focal point moves parallel to its motional direction [12-13]; hence by selecting the frequency of the driving voltage on a string of parallel-connected lenses, we can select only the lens that is resonant at the driving frequency. We can then identify the focal point of that resonating lens by detecting a line instead of a point image (Figure 5.2). To build the system, we have designed the individual lens carriages for the array of lenses to have separated natural resonant frequencies so that, by changing the frequency of the drive voltage, we require only two electrical connections per lens-carriage row to identify the selected lens.
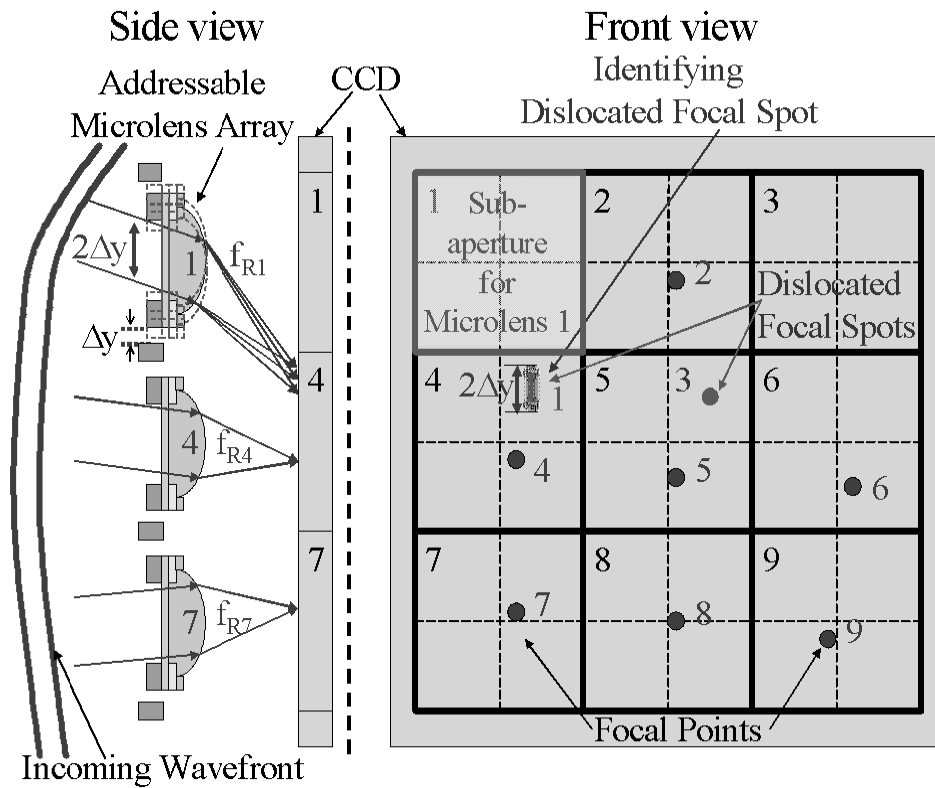
Figure 5.2 By making each microlens resonate individually, we can identify its associated focal point, even if the focal point is located outside the assigned sub-aperture.

With our design, a lens focal point can be identified even when it falls outside of its associated sub-aperture (usually 40 pixels for Shack-Hartmann sensors for ophthalmic analysis), anywhere in the sensing array. This identification will allow the dynamic range of the Shack-Hartmann sensor to be dramatically improved -- a factor of 12 to 46 better than that achieved in conventional Shack-Hartmann systems. In this chapter, we discuss the design, fabrication, and experimental results on our addressable microlens array.

5.2 Addressable Microlens-Array Design

5.2.1 Design Objectives and Considerations for Addressable Microlens Array

The design of our addressable microlens array for Shack-Hartmann sensors has been guided by the following objectives: 1. Maximize the clear aperture of the system (or microlens area) by minimizing the areas for MEMS actuators and electrical interconnects; and 2. Assure that only the desired lens moves appreciably while all other lenses in its row remain essentially stationary, even when the lens carriage with the stiffest flexures (highest resonant frequency) in the row is actuated with the highest drive voltage. The first objective is reached by designing and building the lens-carriages using the most efficient surface-micromachining capabilities available in our laboratory. Achieving the second objective requires the simultaneous consideration of the frequency responses of all the units in a single row and the analysis of side instabilities of the resonating units. The side-instabilities are caused by the electrostatic pull-in phenomena [14], which we discuss in more detail later in this chapter. The frequency responses and side-thrust issues will determine the maximum number of the MEMS-microlens units per row that can be reliably addressed by our frequency-addressing method.

5.2.2 Layout and Dimensions of the Addressable-Microlens Array

Figure 5.3 shows an enlarged view of an individual MEMS-microlens unit and the schematic diagram of our addressable-microlens array.

Truss-Joined Double Flexure
Upper Comb Set
y-axis
x-axis
w_f
Truss-Joined Double Flexures
Lower Comb Set

Unit1 Unit2 Unit3 Unit4 Unit5

Row1 f_{r1} f_{r2} f_{r3} f_{r4} f_{r5}

Row2 f_{r1} f_{r2} f_{r3} f_{r4} f_{r5}

Row3 f_{r1} f_{r2} f_{r3} f_{r4} f_{r5}

Row4 f_{r1} f_{r2} f_{r3} f_{r4} f_{r5}

Row5 f_{r1} f_{r2} f_{r3} f_{r4} f_{r5}

$V_{DC}+V_{AC}\exp(j\omega t)$
GND via Substrate
$V_{DC}+V_{AC}\times\exp(j(\omega+\pi/4)t)$

(a)   (b)
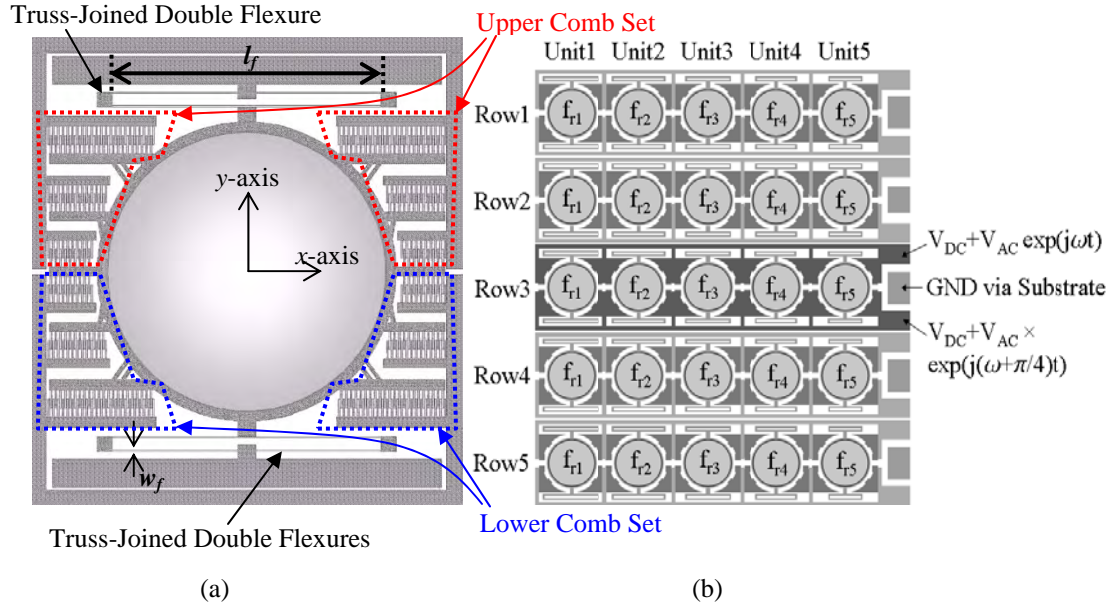
Figure 5.3   Schematic diagrams showing features of addressable-microlens array: (a) Individual resonant unit; (b) Our resonant-frequency addressing method requires only a single pair of electrical lines per row to control each unit individually. Rows 1 through 5 are identical; each row contains five MEMS-microlens units having five different resonant frequencies (f_{r1}-f_{r5}).

In order to utilize the area inside the unit rectangular cell (1360 μm by 1460 μm) efficiently, the microlens is placed at the center of the cell, the two truss-joined double flexures are placed at the top and bottom of the cell, and comb-fingers (numbering 172 moving and 184 fixed) are concentrated between the two flexures, around the microlens (Figure 5.3 (a)), inside the cell. The comb-fingers are grouped into upper and lower comb sets, as shown in Figure 5.3 (a). The upper comb sets are mirror images of the lower comb sets reflected across the x-axis. The truss-joined double flexures have been chosen to maximize pliability along the actuation directions of the resonant structures as well as to stiffen their resistances to undesired sideway motions.

Each row contains five adjacent microlens-resonant units designed to have five different mechanical-resonant frequencies. The frequencies are varied by decreasing the support-flexure lengths from 900 to 500 μm in steps of 100 μm, from the left (Unit 1) to

the right (Unit 5) (Figure 5.3 (b)). Using our frequency-addressing method, we need only

a single pair of interconnects per row to select and energize each unit, reducing and

simplifying the area and complexity necessary for alternative selection designs. A 5-by-5

addressable array is then obtained by stacking five identical rows (Row1 – Row5), as

shown in Figure 5.3 (b). The dimensions of the MEMS-microlens resonant structures are

summarized in Table 5.1 while other relevant material parameters are listed in Table 5.2.

The reasons for choosing the listed values for the dimensions will be clarified in the

following sections.

Table 5.1   Relevant parameters of the MEMS-microlens units

Number of moving comb-fingers per unit	172
Length (l_c) and width (w_c) of comb-fingers (µm)	60, 5
Length (l_f) and width (w_f) of flexures (µm)	500-900, 4
Gap between comb-fingers (g_c) (µm)	3
Thickness of SOI-wafer device layer (t_{SOI}) (µm)	20
Thickness of SOI-wafer buried-oxide-layer (t_{BOX}) (µm)	2
Diameter of integrated microlens (d_{lens}) (µm)	800
Focal length of microlens (f_{lens}) (mm)	2

Table 5.2   Relevant material parameters for the MEMS-microlens units

Young's Modulus (E_{Si}) of silicon (GPa)	170
Density of silicon (ρ_{Si}) (kg/m^3)	2330
Density of microlens material (ρ_{lens}) (g/cm^3)	1.08
Refractive index of microlens material (n)	1.51
Viscosity of air (µ) (N·s/m^2)	$1.8 \cdot 10^{-5}$
Kinetic viscosity of air (ν) (m^2/s)	$1.5 \cdot 10^{-5}$
Permittivity of air (ε) (F/m)	$8.854 \cdot 10^{-12}$

5.2.3 Design of MEMS Resonators with Electrostatic Actuators

In order to assure the successful, distinctive resonant motion of each MEMS-

microlens unit, the following requirements must be met. Please refer to Figure 5.4. First,

each unit must be able to achieve ±20-µm amplitude at resonance stably and without

appreciable sideway motions. Second, when the unit with the highest resonant frequency

(which has the stiffest flexures and therefore requires the highest driving voltage) achieves ±20-µm resonant amplitude, all other units must move only negligibly and be free from any undesired side thrust. Third, the resonant peak of each MEMS-microlens unit should be sufficiently separated in frequency from the resonant peaks of the other units in the same row.

The target amplitude of ±20-µm is chosen by considering typical sizes of CCD-/CMOS-imager pixels, which range between 5-10 µm. Since the total amplitude of 40 µm will guarantee that the focal spot of the selected lens will move across at least 4 pixels of the CCD-/CMOS-imager, the computer can identify the moving spot and the lens that generated it.
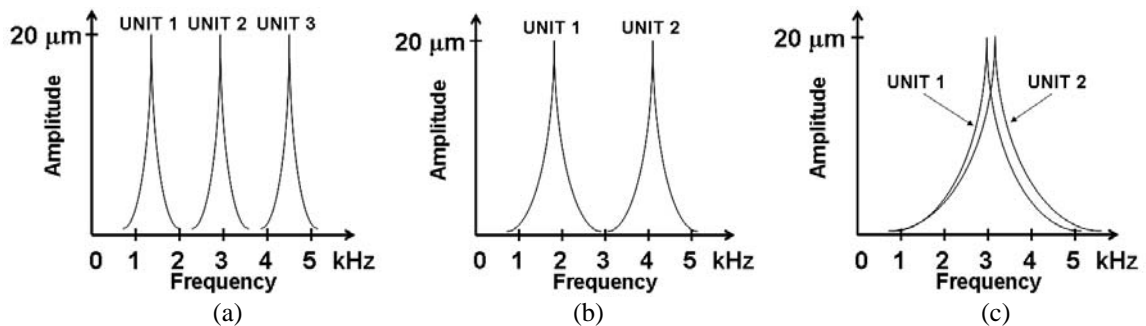
Figure 5.4 Examples of frequency response of MEMS-microlens units in a row: (a) Three resonant peaks sufficiently spaced for clear identification (higher Q); (b) resonant peaks sufficiently spaced for clear identification (lower Q); and (c) Resonant peaks insufficiently spaced for identification: When Unit 1 is at resonance, Unit 2 will also show considerable movements, making it difficult to identify the units.

A side thrust mentioned in the first and the second requirements are caused by the electrostatic pull-in phenomenon [14], which is illustrated in Figure 5.5. The moving combs are sometimes not perfectly centered between the fixed combs due to the processing variations (Figure 5.5(c)). And, even if the combs were initially aligned perfectly, they can slightly deviate from the ideal line of actuation when the structures are

actuated or some external vibrations are present. This slight misalignment results in an unbalanced net electrostatic force in the direction (x-axis) perpendicular to the desired actuation (y-axis) (Figure 5.5(c)). When the changes in these electrostatic forces with respect to x become larger than the stiffness of the flexures along the x-axis, the moving comb-fingers will bend and in all likelihood stick to the fixed combs, causing the proper operation of the structure to fail when the driving signal becomes short-circuited, as shown in Figure 5.5(d). We call the voltage at which the structure begins to fail in this way, *the side-thrust voltage*.
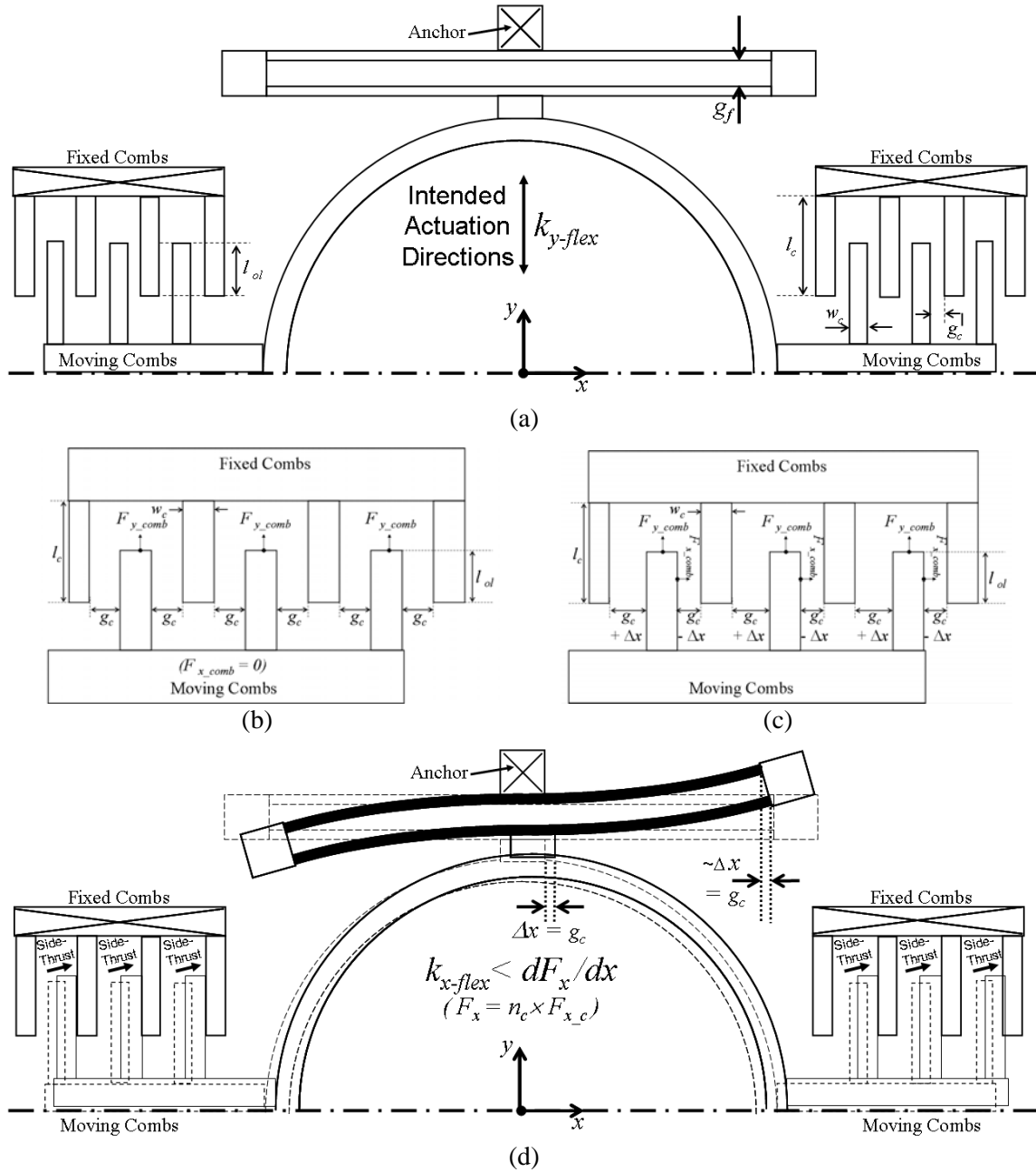
Figure 5.5 (a) Sketches of the upper half of a the MEMS-microlens unit; (b) perfectly aligned fixed and moving combs, (c) misaligned fixed and moving combs – the gaps on the right side of the moving combs are smaller than those the gap on the left side of the moving combs, causing unbalanced electrostatic force in the x-direction; (d) The force F_x generated by the misaligned combs causes the unit to shift to the left by Δx. If the change in F_x is larger than the stiffness of the flexures in x-direction, Δx becomes as large as g_c, and the moving- comb fingers become sufficiently displaced to cause electrical contact with the fixed-comb fingers, shorting out the drive voltage.

There are two different cases of side thrust that we consider. The first case, which we call *dynamic side thrust*, may occur to the unit at resonance when its drive voltage is increased to achieve the intended resonant amplitude. The second case, *stationary side thrust*, occurs when the unit with the highest resonant frequency is driven to the desired resonant amplitude while the others are stationary. We need to consider them separately because the overlapping areas between the moving- and fixed-comb fingers remain constant for *stationary side thrust* yet change in the case of *dynamic side thrust*. For *stationary side thrust*, some of the other lower-resonant-frequency units may experience side thrust because the highest-frequency unit has the stiffest flexures and requires the highest drive voltage. This high drive voltage is applied to all the units in the row, possibly causing one or more of them to move in an undesired direction and to fail.

Considering both types of failures and the needed selectivity among the lenses in a given row, we see that the number of units in a row is determined by: a) the upper and lower limits on resonant frequencies set by the side-thrust issues, and b) the quality factors of the resonant units in the row, which determines the spacing needed between adjacent units in the frequency domain for clear distinction.

To analyze the effects of these limitations, we begin by formulating expressions for the resonant frequencies, quality factors, and resonant amplitudes of the lens units. Then we consider the range of resonant frequencies allowed in a single row as set by the physical dimensions of the unit cell as well as by the side-thrust issues.

5.2.3.1 Calculations of resonant frequencies, quality factors, and resonant amplitudes

The resonant frequency of each MEMS-microlens unit is [15]:

$$f_r = \frac{1}{2 \cdot \pi}\sqrt{\frac{k}{m}} \,, \tag{5.2.1}$$

where m is [16]

$$m = m_{moving\ structure} + 0.3714 \cdot m_{flexures} + m_{lens} \,. \tag{5.2.2}$$

The stiffness k of the flexures is calculated using rectangular beam theory [17]:

$$k_{y-flex} = \frac{16 \cdot t_{SOI} \cdot w_f^3 \cdot E_{Si}}{l_f^3} \,. \tag{5.2.3}$$

From Equations (5.2.1) and (5.2.3), we see that increasing the stiffness k by reducing the flexure length l_f increases the resonant frequency f_r. The mechanical quality factor Q for the resonant carriages is [15]

$$Q = \frac{\sqrt{k \cdot m}}{b} \,. \tag{5.2.4}$$

The damping factor b is calculated by summing (i) Couette-flow damping between the fixed and moving comb-fingers, (ii) Couette-flow damping between the resonant structure and the substrate, and (iii) Stokes-flow damping over the resonant structure [18]:

$$b = \frac{\mu \cdot A_{comb\_overlap}}{g_c} + \frac{\mu \cdot A_{structure\_overlap}}{t_{BOX}} + \frac{\mu \cdot A_{structure}}{\delta} \,; \quad \delta = \sqrt{\frac{2 \cdot \nu}{\omega_r}} \,. \tag{5.2.5}$$

Using the fundamental resonant frequencies and the Q factors, we predict the frequency response of the microlens resonant structures in a row as [15]:

$$y_{ac}(\omega) = \frac{n_c \cdot \varepsilon \cdot t_{SOI} \cdot (V_{dc} + V_{ac})^2}{g_c \cdot \left[(k - m \cdot \omega^2)^2 + \left(\frac{\omega \cdot \omega_r \cdot m}{Q} \right)^2 \right]^{1/2}} \,. \tag{5.2.6}$$

In Eq. (5.2.6), ω is the angular frequency of the drive voltage, and ω_r is the angular resonant frequency of the unit under consideration. As shown in Figure 5.3, each

MEMS-microlens unit has two sets of comb fingers, an upper and a lower set. The upper and lower sets actuate the MEMS-microlens unit upward and downward, respectively. Each of these sets has an equal number of paired fixed- and moving-comb fingers. Hence, dc voltage simultaneously applied to both upper- and lower-comb sets causes balanced forces and no displacement; only an ac voltage, that is applied to the upper and lower comb sets with a 90°-phase lag one from the other, will cause displacement. In this case, Eq. (5.2.6) for the resonant displacement becomes

$$y_{ac}(\omega) = \frac{n_c \cdot \left(2 \cdot V_{dc} \cdot V_{ac} + V_{ac}^2\right)^2 \cdot \varepsilon \cdot t_{SOI}}{g_c \cdot \left[\left(k - m \cdot \omega^2\right)^2 + \left(\frac{\omega \cdot \omega_r \cdot m}{Q}\right)^2\right]^{\frac{1}{2}}} \qquad (5.2.6\text{-}1)$$

Using a large dc Voltage V_{dc} improves the linearity of actuator response to an applied ac voltage V_{ac}.. Also increasing V_{dc} decreases the magnitude of V_{ac} required to achieve a target amplitude of motion, thereby easing the performance requirements for the ac driviing amplifier. For cases in which V_{dc} is much larger than V_{ac}, Eq.(5.2.6-1) can be further simplified

$$y_{ac}(\omega) \approx \frac{n_c \cdot \left(2 \cdot V_{dc} \cdot V_{ac}\right) \cdot \varepsilon \cdot t_{SOI}}{g_c \cdot \left[\left(k - m \cdot \omega^2\right)^2 + \left(\frac{\omega \cdot \omega_r \cdot m}{Q}\right)^2\right]^{\frac{1}{2}}}. \qquad (5.2.6\text{-}2)$$

The designer must consider Eq. (5.2.6-1) when it is applied over the frequency range of interest in order to assure that each unit in a given row achieves the desired amplitude at its resonant frequency while movements in the other units in the row are negligible at that frequency. The selected unit must also resonate at the desired amplitude without suffering from excessive dynamic side thrust. At resonance, the amplitude is

$$y_r = y_{ac}(\omega_r) = \frac{n_c \cdot Q \cdot \varepsilon \cdot t_{SOI}}{k_{y\_flex} \cdot g_{comb}} (V_{dc} + V_{ac})^2 . \tag{5.2.7}$$

For cases in which V_{dc} is much larger than V_{ac}, the expression for the maximum amplitude at the resonant frequency can be approximated as

$$y_r \approx \frac{n_c \cdot Q \cdot \varepsilon \cdot t_{SOI}}{k_{y\_flex} \cdot g_{comb}} (2 \cdot V_{dc} \cdot |V_{ac}|) . \tag{5.2.7-1}$$

Turning now to the *dynamic side thrust* issue, we calculate the maximum attractive electrostatic force between the moving and fixed combs that causes side-thrust at the resonant frequency [14]

$$F_{side} = \frac{(n_c/2) \cdot t_{SOI} \cdot (y_0 + y_r)}{2(g_c - x)^2} (V_{dc} + |V_{ac}|)^2 - \frac{(n_c/2) \cdot t_{SOI} \cdot (y_0 + y_r)}{2(g_c + x)^2} (V_{dc} + |V_{ac}|)^2$$

$$+ \frac{(n_c/2) \cdot t_{SOI} \cdot (y_0 - y_r)}{2(g_c - x)^2} (V_{dc})^2 - \frac{(n_c/2) \cdot t_{SOI} \cdot (y_0 - y_r)}{2(g_c + x)^2} (V_{dc})^2 . \tag{5.2.8}$$

In Eq. (5.2.8), the number of comb fingers (n_c) is divided by two because V_{ac} is sinusoidal and its peak voltage is applied either to the upper or to the lower comb each half cycle. The stable operation of the resonant unit requires that [14]

$$k_{x\_flex} >> \left[\frac{\partial F_{side}}{\partial x} \right]_{x \to 0} \tag{5.2.9}$$

where

$$\left[\frac{\partial F_{side}}{\partial x} \right]_{x \to 0} = \left(\frac{n_c \cdot t_{SOI}}{g_c^3} \right) \left[(y_0 + y_r)(V_{dc} + |V_{ac}|)^2 + (y_0 - y_r)V_{dc}^2 \right]$$

In Eq. (5.2.9), k_{x_flex}, is the effective stiffness of the truss-joined double-flexures in the *x*-direction,; this parameter can be calculated by considering the slope developed at the end of the flexure beams when stiction takes place [17]:

$$k_{x-flex} = \frac{4 \cdot t_{SOI} \cdot E_{Si} \cdot w_f^3}{3 \cdot l_f \cdot g_f^2}.$$ (5.2.10)

When the drive voltage exceeds the side-thrust voltage ($V_{s\_d} = V_{dc\_dyn} + |V_{ac}|$), the comb drive becomes unstable, leading the moving comb finger to stick to its fixed counterpart. If we express y_r using Eq. (5.2.7-1) in Eq. (5.2.9) and assume a reasonable value for $|V_{ac}|$ (for example $V_{dc} \gg |V_{ac}|$, $|V_{ac}| = 4$ V), we can solve for V_{dc_dyn}.

$$V_{dc\_dyn} = \frac{-B + \sqrt{B^2 - 4 \cdot A \cdot C}}{2 \cdot A}$$ (5.2.11)

where

$$A = 2 \cdot \left(y_0 + |V_{ac}|^2 \cdot \frac{n_c \cdot Q \cdot \varepsilon \cdot t_{SOI}}{k_{y\_flex} \cdot g_c} \right),$$

$$B = 2 \cdot |V_{ac}|^3 \left(\frac{y_0}{|V_{ac}|^2} + \frac{n_c \cdot Q \cdot \varepsilon \cdot t_{SOI}}{k_{y\_flex} \cdot g_c} \right), \text{ and}$$

$$C = |V_{ac}|^4 \left(\frac{y_0}{|V_{ac}|^2} + \frac{n_c \cdot Q \cdot \varepsilon \cdot t_{SOI}}{2 \cdot k_{y\_flex} \cdot g_c} \right) - \frac{k_{x\_flex} \cdot g_c^3}{n_c \cdot \varepsilon \cdot t_{SOI}}.$$

We now use Eq. (5.2.11) to express V_{dc_dyn} in Eq. (5.2.7) and calculate the maximum displacement that the resonant unit can achieve before experiencing electrostatic pull-in.

$$y_{max\_is} = \frac{n_c \cdot Q \cdot \varepsilon \cdot t_{SOI}}{k_{y\_flex} \cdot g_{comb}} \left(V_{dc\_dyn} + |V_{ac}| \right)^2$$ (5.2.12)

For stable operation of MEMS-microlens units, this maximum displacement before side thrust must be larger than the desired resonant amplitude.

5.2.3.2 Lower and Upper Limits on Resonant Frequencies

The lower limit on the resonant frequencies is related to the physical size of the rectangular unit cell. In our design, the maximum length of flexures that can be placed

inside the unit cell is 1250 μm, which gives rise to the lowest resonant frequency of 0.99 kHz. However, to provide a margin of safety (because of possible variations in voltage values as well as tolerance limits in surface micromachining) it is reasonable to set the maximum length (and corresponding minimum resonant frequency) to 900 μm and 1.56 kHz, respectively.

After we have the flexure length for the lowest-frequency unit, we can calculate the flexure length for the highest-frequency unit based on the stationary side-thrust condition of the lowest-frequency unit. The worst case that we need to consider occurs when the highest-frequency unit (unit 5 in Figure 5.3) is resonating. In this condition, we need to assure that the lowest frequency unit, which has the most pliant flexures, remains stationary and stable. Hence we first calculate the stationary side-thrust voltage for the lowest frequency unit at the stationary (rest) position. This side-thrust voltage of the lowest-frequency unit is the highest voltage that can be applied to the common electrical interconnects in the row without causing stationary side thrust in any of the units. Then, using the stationary side-thrust voltage (V_{dc_st}) of the lowest-frequency unit at the stationary position, we calculate the minimum flexure length of the highest-frequency unit that will allow $\pm$20-μm displacement at resonance when driven at a voltage $\leq V_{dc\_st}$ of the lowest frequency unit.

$$F_{side} = \frac{(n_c/2) \cdot t_{SOI} \cdot (y_0)}{2(g_c - x)^2}(V_{dc} + |V_{ac}|)^2 - \frac{(n_c/2) \cdot t_{SOI} \cdot (y_0)}{2(g_c + x)^2}(V_{dc} + |V_{ac}|)^2$$

$$+ \frac{(n_c/2) \cdot t_{SOI} \cdot (y_0)}{2(g_c - x)^2}(V_{dc})^2 - \frac{(n_c/2) \cdot t_{SOI} \cdot (y_0)}{2(g_c + x)^2}(V_{dc})^2 . \qquad (5.2.13)$$

$$k_{x\_flex} > \left[\frac{\partial F_{side}}{\partial x}\right]_{x \to 0} = \left(\frac{2 \cdot (n_c/2) \cdot t_{SOI}}{g_c^3}\right)\left[(y_0)(V_{dc} + |V_{ac}|)^2 + (y_0)V_{dc}^2\right] \qquad (5.2.14)$$

Solving Eq. (5.2.9) for V_{dc}, we obtain

$$V_{dc\_st} = \frac{-2 \cdot |V_{ac}| + \sqrt{4 \cdot |V_{ac}|^2 - 8(|V_{ac}|^2 - D)}}{4} \quad \text{where} \quad D = \frac{k_{x\_flex} \cdot g_c^3}{n_c \cdot \varepsilon \cdot t_{SOI} \cdot y_0}. \tag{5.2.15}$$

For $l_f = 900$ μm and $|V_{ac}| = 4$ V, V_{dc_st} is 44.74 V. Using Eq. (5.2.7-1), we now calculate the maximum stiffness of the flexures (k_{y_max}) that can still achieve ±20-μm resonant amplitude (y_d) at this voltage:

$$y_d \approx \frac{n_c \cdot Q \cdot \varepsilon \cdot t_{SOI}}{k_{y\_max} \cdot g_{comb}} \left(2 \cdot V_{dc\_st} \cdot |V_{ac}|\right) = \frac{n_c \cdot \sqrt{k_{y\_max} \cdot m} \cdot \varepsilon \cdot t_{SOI}}{k_{y\_max} \cdot g_{comb} \cdot b} \left(2 \cdot V_{dc\_st} \cdot |V_{ac}|\right)$$

$$k_{y\_max} \approx \left[\frac{n_c \cdot \varepsilon \cdot t_{SOI} \cdot \sqrt{m}}{y_d \cdot g_{comb} \cdot b} \left(2 \cdot V_{dc\_st} \cdot |V_{ac}|\right) \right]^2 \tag{5.2.16}$$

The damping factor b (Eq. (5.2.5)) increases gradually as the flexure lengthens; however, for resonant frequencies between 1-10 kHz, the change in b is typically less than 10 % of its original value in our design. Hence, to simplify calculation, we assume that b is fixed at 0.49×10^{-5} N·s/m. Assuming $|V_{ac}| = 4$ V, we obtain $k_{y\_max} = 79.57$ N/m, and the corresponding maximum resonant frequency and quality factor are 5.84 kHz and 437.91, respectively. Using the numerical value of k_{y_max} in Eq. (5.2.3) and solving for l_f, we obtain

$$l_f = \left(\frac{16 \cdot t_{SOI} \cdot w_f^3 \cdot E_{Si}}{k_{y\_max}} \right)^{1/3} = 352 \; \mu m \tag{5.2.17}$$

Equation (5.2.17) shows that the minimum length of the flexures allowed in a row (that can achieve ±20-μm displacement at resonance without causing side-thrust in low-frequency units) is 352 μm. This minimum length determines that the upper limit on the resonant frequencies allowed in the row (using Eqs (5.2.1-5.2.3)) is 5.84 kHz. As before,

if we provide a safety factor (e.g. select $l_f = 500$ instead of 352 µm as the minimum flexure length), we calculate an upper limit for the resonant frequency of 4 kHz.

5.2.3.3 Frequency Response of the Resonant Units in a Single Row: Resonant Frequencies and Quality Factors

After choosing the design values that bracket upper and lower resonant frequencies of the MEMS-microlens units in a given row, we calculate the number of units having addressable resonant frequencies that can be placed in the row. We predict the frequency response of the MEMS-microlens resonant structures in a row using Eq. (5.2.6-1). Using Equation (5.2.6-1), we ensure that at the resonant frequency of the unit of interest, the other units in the row do not show any significant movement.

As a design example, we fabricated a lens array in which five MEMS-microlens units (as described in Table 5.1) were placed in a row having the dimensions indicated in Table 5.3. Predicted resonant frequencies and mechanical quality factors for the units are also given in Table 5.3, while in Table 5.4 we show predicted amplitudes for the units when they are driven at five different drive frequencies and voltages. Theory predicts that when a designated unit is at full resonance reaching amplitudes of ±20 µm, the other four units move less than ±1 µm as shown in Figure 5.6. The appropriate spacing between neighboring resonant frequencies together with stability condition determines the maximum number of units that can be placed in each row for a given maximum frequency of driving voltage. Between the lowest resonant frequency ($f_r = 1.56$ kHz) and the highest resonant frequency ($f_r = 4$ kHz), we calculate that the maximum number of units (of different resonant frequencies) that can be placed in a single row is approximately 25. Using only two electrical interconnects, we can realize an array of 25×25 (or 625 lenses on a 37.5mm×37.5mm aperture).

Table 5.3   Predicted resonant frequencies and quality factors of the five MEMS-microlens resonant units in a row

	Unit1	Unit2	Unit3	Unit4	Unit5
l_f (µm)	900	800	700	600	500
w_f (µm)	4	4	4	4	4
f_r (kHz)	1.56	1.88	2.33	3.00	4.05
Q	116.13	139.67	172.44	220.43	295.80

Table 5.4   Predicted amplitudes for the MEMS-microlens units at differing drive frequencies: Bold characters indicate the resonant unit. (*A*: Amplitude)

	Unit1	Unit2	Unit3	Unit4	Unit5
l_f (µm)	900	800	700	600	500
A (in µm) (S1: Unit 1 Designated) (V $_{Applied}$=20 V$_{ac}$, $f_{Applied}$= f_r_unit1)	**20.45**	0.44	0.17	0.08	0.04
A (in µm) (S2: Unit 2 Designated) (V $_{Applied}$=25 V$_{ac}$, $f_{Applied}$= f_r_unit2)	0.52	**20.25**	0.32	0.11	0.05
A (in µm) (S3: Unit 3 Designated) (V $_{Applied}$=32 V$_{ac}$, $f_{Applied}$= f_r_unit3)	0.24	0.39	**20.40**	0.22	0.07
A (in µm) (S4: Unit 4 Designated) (V $_{Applied}$=42 V$_{ac}$, $f_{Applied}$= f_r_unit4)	0.14	0.17	0.27	**20.23**	0.14
A (in µm) (S5: Unit 5 Designated) (V $_{Applied}$=53 V$_{ac}$, $f_{Applied}$= f_r_unit5)	0.09	0.10	0.12	0.18	**20.01**
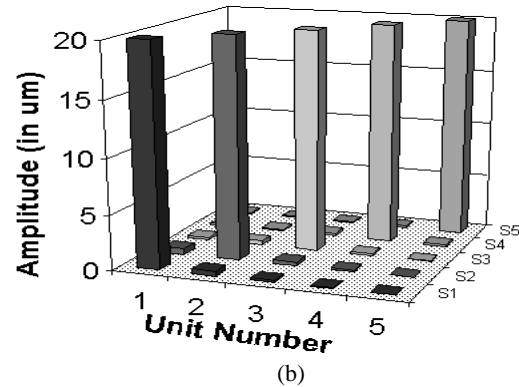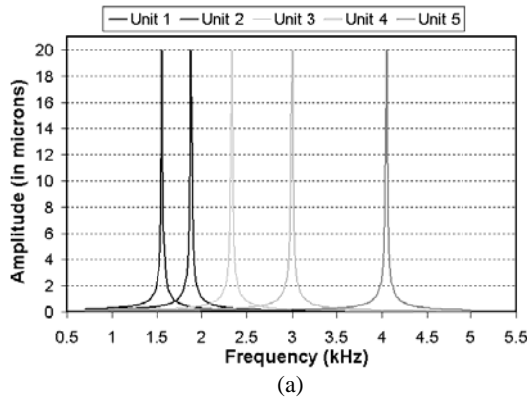
Figure 5.6   (a) Predicted frequency responses of the MEMS-microlens units, and (b) graph representing the data in Table 5.4 to emphasize the selectivity of the mechanical-resonance method.

5.3 Fabrication of Addressable Microlens Array

Our addressable-microlens array is fabricated in two steps: *1.* the MEMS-microlens carriages are built using a BSAC-conventional silicon-MEMS process; and *2.*

microlenses are formed on the MEMS carriages using polymer-jet printing technology developed in our laboratory [19].

5.3.1 Fabrication of MEMS-Microlens Carriages

Steps in the fabrication process of MEMS-microlens carriages are shown in Figure 5.7 and described in the figure caption.

☐ Silicon	■ Polysilicon	▨ Thick PR
▨ Oxide	▨ Silicon Nitride	☐ Microlens

1 Thermal Oxide

2 Oxide Mask

3 Trench for Anchor & Electrical Connection

4 Polysilicon   Anchor

5 Well for Microlens

6 Silicon Nitride

7

8

9 Combs   Flexure

10 Microlens
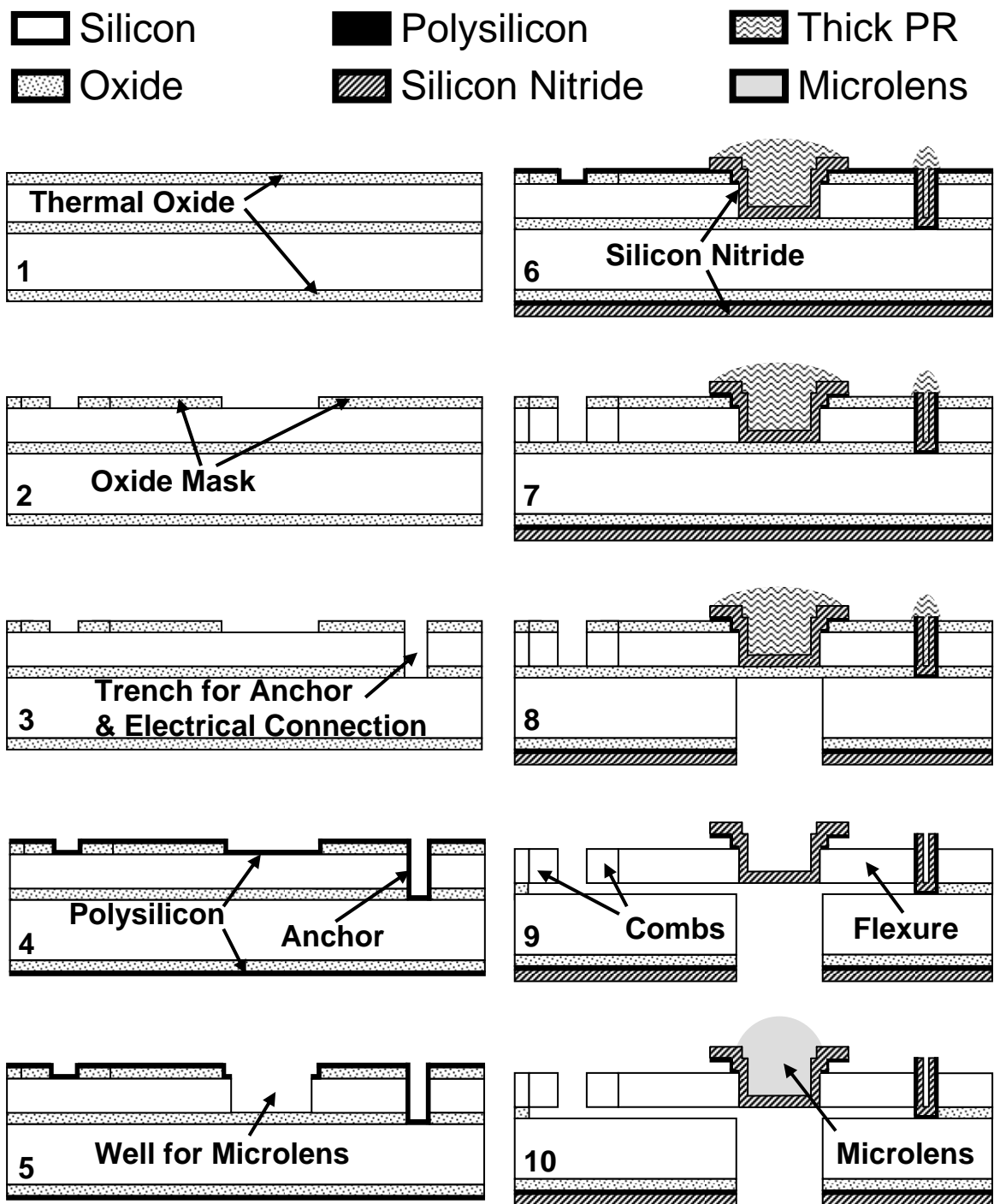
1. Grow a 1μm-thick thermal-silicon dioxide layer on a SOI wafer.

2. Pattern the layer to make a mask that will later define combs, flexures, supports, and lens frames.

(Figure 5.7 continues on the next page)

170

3. Deep-reactive-ion-etch (DRIE) trenches that will be used to form anchors and electrical connections between the device layer and the handling layer of the SOI wafers.

4. Deposit a 0.5μm-thick LPCVD polysilicon layer to create electrical contacts from the device layer to the handling layer (which serves as a GND). The polysilicon layer also protects the oxide mask.

5. DRIE circular trenches in the device layer. These trenches will serve as wells for droplet microlenses later.

6. Deposit (using LPCVD) a 2-μm-thick silicon nitride layer (tensile stress, ~250MPa) and pattern the layer.

7. DRIE silicon parts (combs, flexures, supports, and lens frame) using the silicon dioxide mask layer defined in step 2.

8. Open the backside of the wafers using DRIE to make clear apertures for microlenses.

9. Release the devices in concentrated HF.

10. Make microlenses using polymer-jet printing technology. The boundary of the trench defines the diameter of the lens.

Figure 5.7   Fabrication process of addressable microlens array

In order to make high-quality lenses using polymer-jet printing technology it is necessary to form very flat, optically transparent diaphragms on the MEMS carriage structures. We have used LPCVD-deposited silicon nitride thin-film membranes (Step 6 in Figure 5.7) and found them to be excellent for this purpose. As demonstrated in previous work [20, 21], low tensile-stress (~250 MPa) LPCVD-deposited silicon nitride membranes (5 mm squares) are virtually flat (radius of curvature ~ 51 m) and physically very robust [22]. Additionally, the spectral transmission of silicon nitride membranes is above 75% and nearly uniform (75-95%) for wavelengths in the visible region [20]. These excellent qualities combine to make silicon nitride membranes very good choices for microlens substrates.

5.3.2 Direct Fabrication/Integration of Microlenses on MEMS-Carriages

Fabrication of high-quality droplet microlenses using hydrophobic effects [22] or polymer-jet printing technology [23-24] has been reported by other researchers. In Chapter 1, we have discussed the fabrication of high-quality microlenses with excellent

uniformity by combining the hydrophobic-effect method with polymer-jet printing technology [19]. To form the SH lens array, we repeated this established method depositing the polymer lenses on preformed silicon nitride substrates supported by the individual lens carriages.

The photograph on the right-hand-side of Figure 5.8 shows the microlens-fabrication setup in our laboratory. The microlenses are precisely formed by polymer-jet printing on 2μm-thick silicon nitride layers that are uncovered by etching circular wells (20 μm in diameter) into the device layer of SOI wafers. The boundaries of the circular wells precisely define the lens diameters, and surface tension in the polymer creates a high-quality optical surface. The polymer-jet printing head used in our system is the Microfab MJ-AT-01-40, which operates at room temperatures [25]. The MJ-AT-01-40 requires that the viscosity of the printed material not exceed 40 cps [25]. We used Epoxy Technology's *uv-curable* Epo-Tek OG146,which meets this requirement at room temperature [26]. In addition to its low viscosity, Epo-Tek OG146 possesses excellent optical properties: more than 95% spectral transmission after curing in the 0.4-2μm (visible to near-IR regions) range and a refractive index of 1.51 [26].

Figure 5.8   Microlens Fabrication Process: (a) Fabrication diagram; (b) Fabrication setup in our laboratory
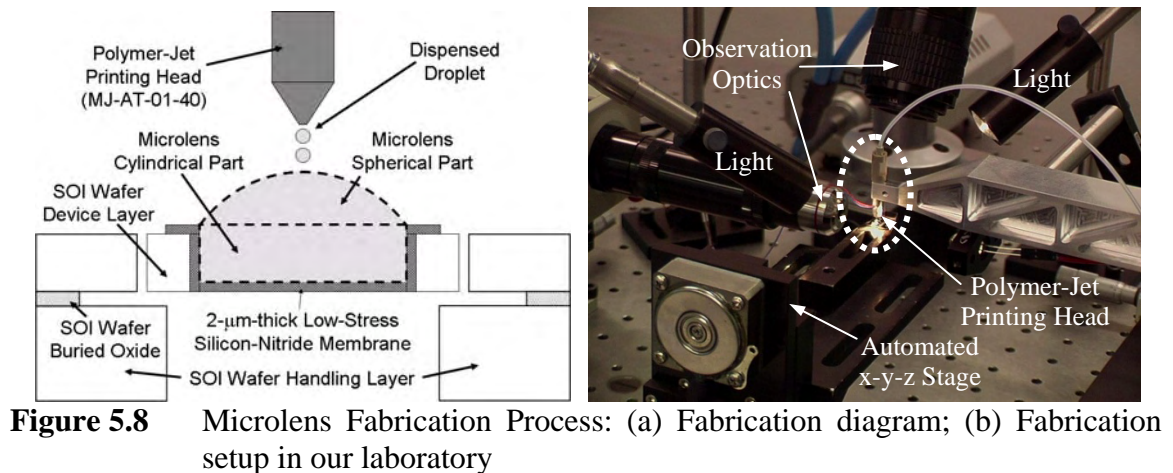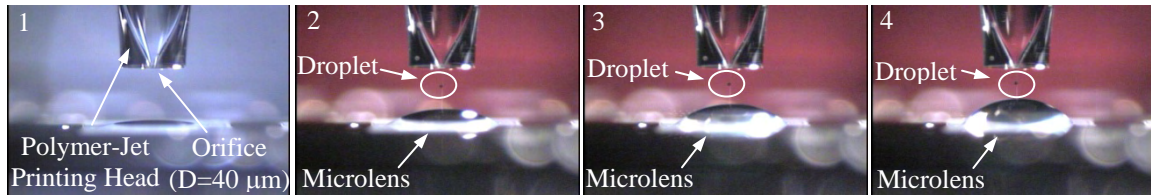
Figure 5.9   Microlens Fabrication Process: Stroboscopic observation – the focal length is controlled by varying the volume of the microlens

Optical properties such as the focal length for a microlens are adjusted by controlling the volume of deposited polymer material [19]. The total microlens volume is the sum of a spherical part and a cylindrical part, as shown in Figure 5.8 (a). To give an example: we fabricate a 2-mm-focal-length microlens on the MEMS-microlens carriage by depositing 2.98×10^{-11} m^3 (or 29.8 nl) of the microlens material. Since the polymer-jet printing head generates a droplet of volume 0.025 nl, we need to deposit 1192 drops to fabricate a microlens having the required properties on the MEMS carriage.

5.4 Experimental Results and Discussion

Examples of our 5×5 addressable-lens arrays, fabricated using SOI wafers, are pictured in the SEM photographs shown in Figures 5.10-11. Each addressable unit (1.5mm square) contains one 800μm-diameter microlens with lens-support carriage and actuators.
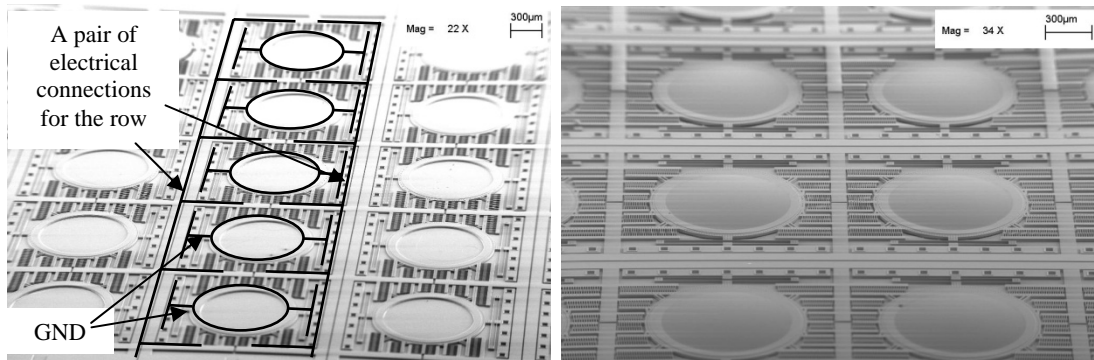
Figure 5.10   SEM picture of the fabricated addressable microlens array (a) before and (b) after microlens fabrication
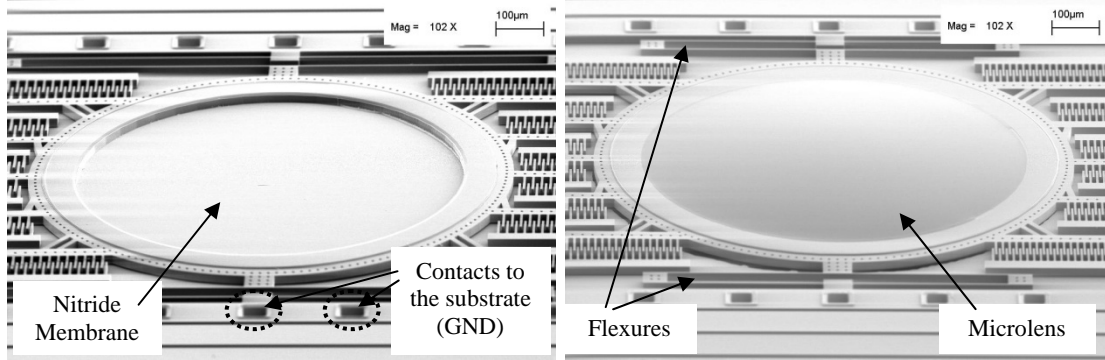
Figure 5.11   SEM picture of the fabricated individual MEMS-microlens unit before and after microlens fabrication

5.4.1 Microlens

Using WYKO-NT3300, we measured the surface profiles of the low-stress (~250MPa) tensile-silicon nitride-membranes and microlenses (EFL=5.5mm) (Figures 5.12-13). Within a 200μm-radius, the membranes are virtually flat (radius-of-curvature ≥ 3m) (Figure 5.12). Near the edge, the membrane profiles deviate slightly from ideal flat surfaces, but the maximum deviation across its 800μm-diameter is still lower than 0.5 μm. The average surface roughness is measured at 8.7 nm.
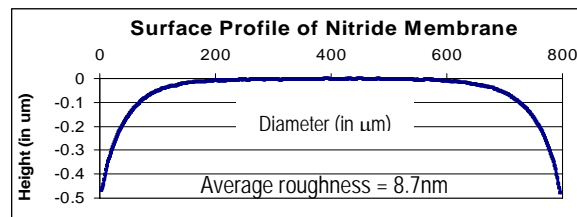
Figure 5.12   WYKO measurement of low tensile-stress (250MPa) nitride-membrane surface profile: very flat (radius of curvature≥3m) within 200μm radius

Using our polymer-jet printing technique in circular wells, we have been able to produce microlenses with effective focal lengths (EFL) ranging from 1.94 to 7.48 mm as adjusted by controlling the deposited polymer volumes forming the microlenses. Figure 5.12 shows the surface profile of a microlens (f = 5.5 mm) and its deviation from that of an ideal circle. The microlens surfaces closely approximate a circle having radius 2.2mm.
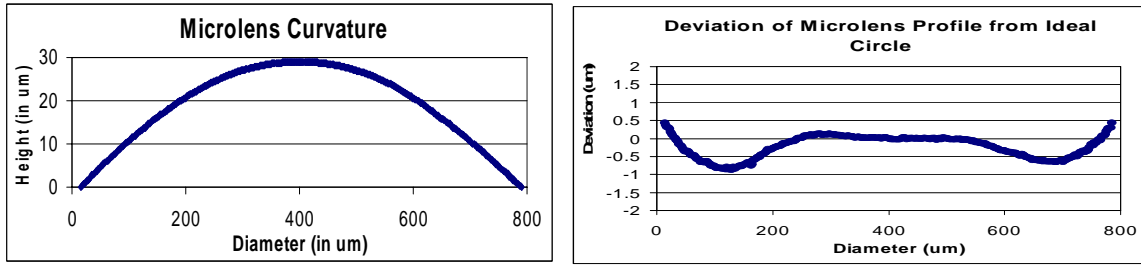
Figure 5.13 The microlens (f=5.5mm) profile follows closely with an ideal circle (radius=2.2mm) within 200μm radius. Its deviation near the edge may be influenced by the profile of the nitride membrane underneath it.

For our addressable-microlens array, microlenses having a designed focal length of 2.0 mm were fabricated. The 25 fabricated microlenses have an average effective focal length (EFL) of 2.09 mm, and the peak-to-peak variation in EFL is ≤ 7%.

5.4.2 Mechanical Performance

The measured mechanical resonant frequencies of the MEMS-microlens units 1 through 5 (microlens EFL=2.09mm) are 1.31, 1.58, 1.98, 2.48, and 3.49 kHz, respectively. The corresponding mechanical Q-factors (microlens EFL=2.09mm) are 65.4, 105.1, 142.1, 174.8, and 205.2. Across the same chip, the maximum variation in resonant frequencies of five identical units is less than 5 %. All units achieve 40μm resonant excursions (±20μm) when applying actuation voltages equal to or lower than $4V_{ac\_peak-to-peak} + 44V_{dc}$ are applied. Using an optical microscope, we could not observe any mechanical crosstalk for these drive conditions.

The experimentally measured resonant frequencies deviate from their design values by as much as 17 % due mainly to imprecision in control of the deep-reactive-ion-etch process as revealed by SEM measurements and shown in Figure 5.14 and Table 5.5.
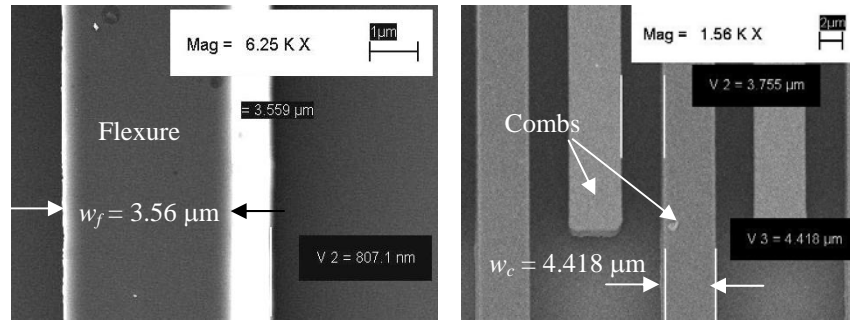
Figure 5.14   Over-etched combs and flexures during the DRIE process

Table 5.5   Processing variation on structure dimensions

	Design	Measured
w_f (μm)	4	3.57
w_c (μm)	5	4.418

Using the dimensions given in Table 5.5, our calculations for the resonant frequencies

nearly match the measured values as indicated in Table 5.6.

Table 5.6   Experimentally measured and theoretically predicted resonant frequencies and quality factors

	Unit1	Unit2	Unit3	Unit4	Unit5
l_f(μm)	900	800	700	600	500
f_r (kHz) calculated	1.32	1.59	1.97	2.53	3.42
f_r (kHz) measured	1.31	1.58	1.98	2.48	3.49
Q calculated	99.0	119.1	147.1	188.2	252.6
Q measured	65.4	105.1	142.1	174.8	205.2

Precisely estimating the quality factors using theoretical models can be quite challenging

[27]. As other researchers have found previously, our Equation (5.2.5) underestimates

the damping factor and, as a result, the quality factors are overestimated [18, 27].
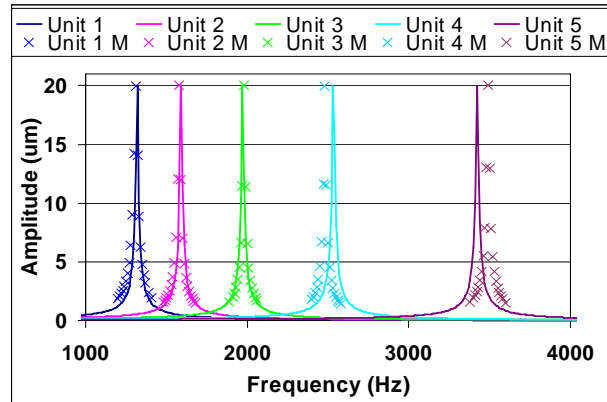
Figure 5.15   Comparison between the theoretical model and experimentally measured data: Unit 1 – Unit 5 indicate the theoretical prediction while Unit 1 M – Unit 5 M present the experimental measurements.

Individual frequency-addressing of MEMS-microlens resonant units in a row is demonstrated in Figures 5.16 and 5.17. In all five cases, the targeted unit achieves highly distinguishable resonance (±20 μm) while the others in the row are effectively still.
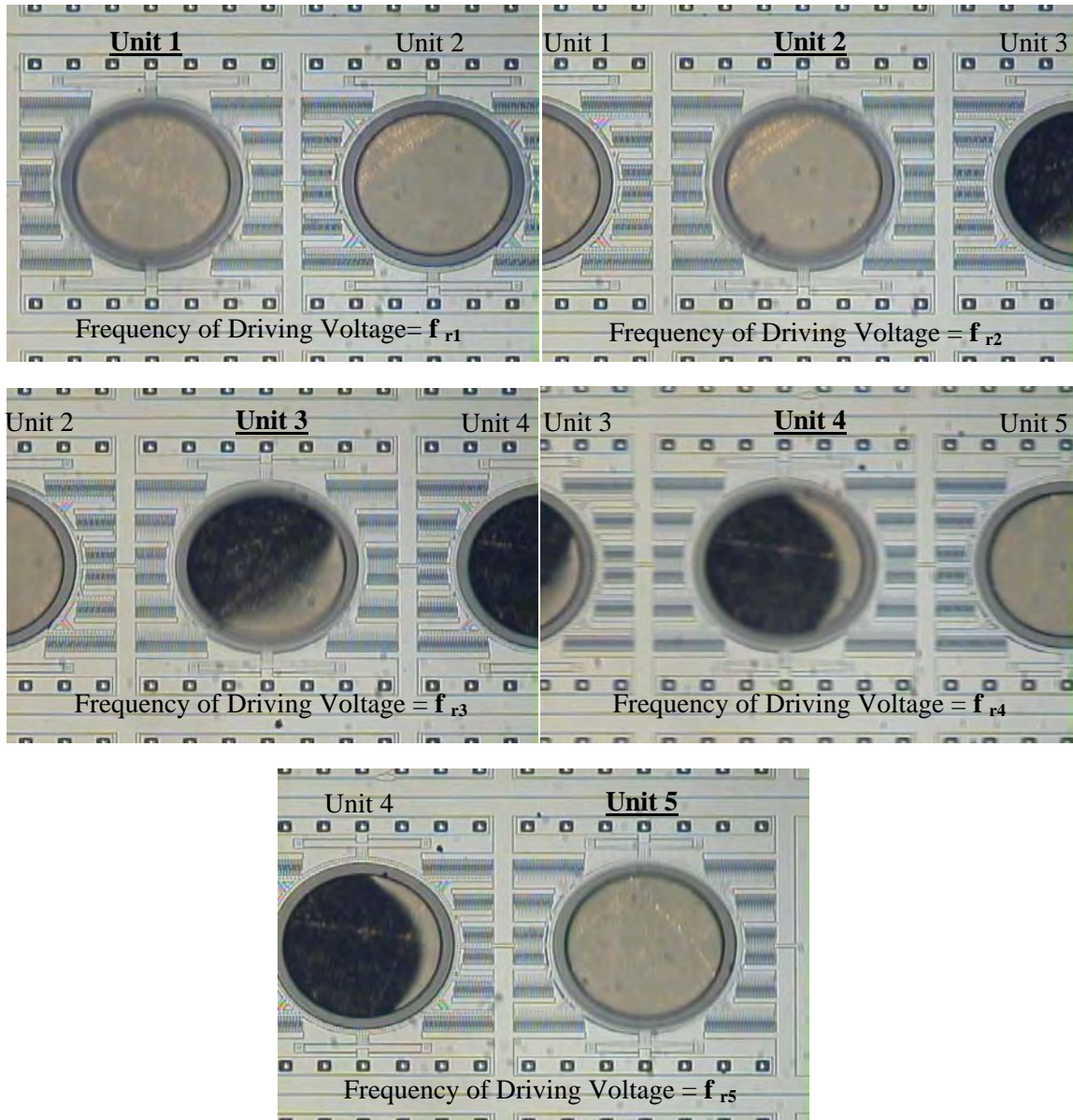
Figure 5.16 To be aware of the motions, note the flexures of the each unit shown in the images: (a) Unit 1 is at resonance. Unit 2 is still; (b) Unit 2 is at resonance. Unit 1 and Unit 3 are still; (c) Unit 3 is at resonance. Unit 2 and Unit 4 are still; (d) Unit 4 is at resonance. Unit 3 and Unit 5 are still; and (e) Unit 5 is at resonance. Unit 4 is stationary. (Non-uniform metallic texture seen on the nitride membrane is a reflection of the surface of the copper wafer-chuck. The dark shadows on the membranes for Units 3 and 4 are due to the objective lens of the optical microscope.)
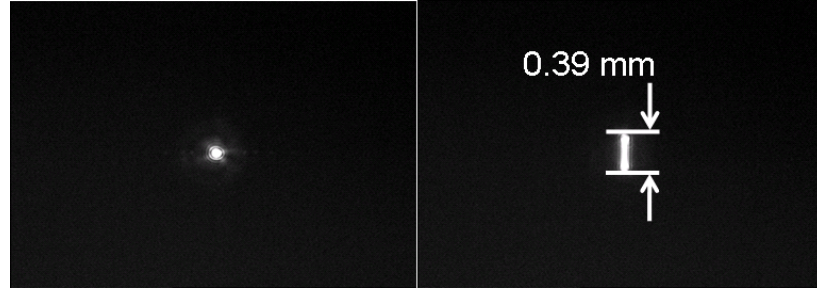
Figure 5.17   Demonstration of focal-point identification: As the microlens resonates, its focal point generates a scanning line, and the focal point and its associated microlens can thereby be identified. The focal length f of the microlens is 2.09 mm, and the CCD imager is placed at 9.84f from the lens. The focal point travels ~40μm×9.84f or ~0.39 mm on the CCD imager.

For our 5×5 array, the serial identification (readout) time τ can be approximated as

$$\tau = 5 \times 2 \times \sum_{i=1}^{5} Q_i / f_{ri} \ . \tag{5.4.2}$$

where Q_i and f_{ri} are the quality factor and resonant frequency of each unit in the row, where i indicates the unit number. It is well known that for $Q \gg \frac{1}{2}$, the impulse response of a resonator decays by the factor $e^{-\pi}$ in Q cycles, which is approximately 96% decay or -27 dB.   The serial identification (readout) time τ is obtained by adding the time increments needed for a lens unit to reach its resonant full amplitude and then to become stationary again. For our 5-by-5 array (25 lenses), we calculate $\tau_{1\sim5} = 3.175$ seconds.

The improvement in the dynamic range by employing the addressable microlens array is limited by the number of photons passing through each microlens and by the sensitivity of the CCD imager. As the slope of the wavefront continues to increase, the effective aperture size for each microlens decreases, which consequently reduces the number of photons passing thorough it. Depending on the sensitivity of the CCD imager and the thickness of the wafer used, the maximum dynamic range will vary. As an

example, Figure 5.18 shows the maximum dynamic range for a wafer thickness of 500 μm, with three representative effective aperture sizes. Our addressable microlens array will allow a SH sensor to achieve dynamic-range values between 144 and 574 mrad. This is an improvement by a factor of 12-46 above values reported for conventional SH designs whose dynamic range is usually limited at 12.5 mrad. This improvement is subject to an experimental verification because coma and astigmatism (off-axis aberrations) can reduce the accuracy of measurements at such large angles.

Wafer thickness = 500 μm		
EA = 90 % Aperture	EA = 75 % Aperture	EA = 50 % Aperture
Max θ = 144 mrad	Max θ = 323 mrad	Max θ = 574 mrad
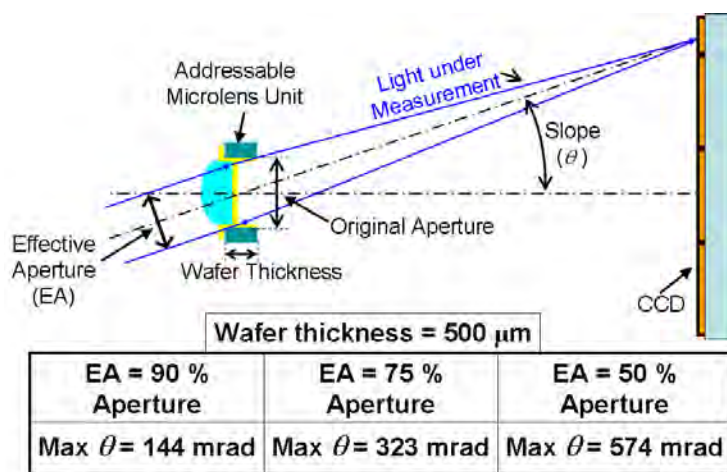
Figure 5.18   Expected improvements in dynamic range for different effective aperture sizes: The diameters of EAs are 90, 75, and 50 % of the original aperture diameter.

5.5 Conclusions

We have designed, built, and tested an array of MEMS structures that are nearly identical except that each structure is designed to have a unique mechanical-resonance frequency. We have arranged these structures along rows and columns and mounted nearly identical optical lenses on them to form a lens array that can be used as a Shack-Hartmann sensor having the special capability to identify the light passing through a particular lens by driving the carriage supporting that lens to mechanical resonance. In particular, we have demonstrated a (5 by 5) addressable array of high-quality microlenses

that can be applied to a Shack-Hartmann (SH) sensor in a micro-optical system to improve its dynamic range. Specific lenses in the array can be addressed using our design in which the mechanical resonant frequencies of individual lens-support carriages are varied. The measured mechanical resonant frequencies of the MEMS-microlens units 1 through 5 with microlenses (EFL=2.09mm) range from 1.31 up to 3.49 kHz and the corresponding Q-factors were between 65.4and 205.2. All units achieve 40μm resonant excursions (±20μm) when applying actuation voltages ($|V_{ac}+V_{dc}|$) lower than 50V. Optically observed mechanical cross talk between different units is negligible. Use of the frequency-selection scheme to address individual MEMS structures in an array is not limited to the optical application demonstrated in this project. This scheme clearly has value for other MEMS applications such as print-head activation in multi-color printers or activated drug dispensing, to site only two examples. In each of these cases, an important advantage of the selection technique is that it does away with the need for multiple input-addressing leads or for the use of sophisticated electronics.

In continued research, we have been working to shorten the time needed for an SH readout measurement by implementing lens units that have faster responses as well as by developing more efficient data-handling algorithms. We are also carrying through research on new designs to increase our lens-array fill factor from its present 40%. Although we believe that we can double this percentage, we need to develop experimental proof before discussing these new designs.

References

[1] E. Viard, M. Le Louarn, N. Hubin, "Adaptive optics with four laser guide stars: correction of the cone effect in large telescopes," *Applied Optics, vol.41, no.1*, Jan. 2002, pp.11-20, Opt. Soc. America, USA.

[2] L. N. Thibos and X. Hong, "Clinical applications of the Shack-Hartmann aberrometer," *Optometry & Vision Science, vol.76, no.12*, Dec. 1999, pp.817-25, Lippincott Williams & Wilkins, USA.

[3] K. Munson, X. Hong, and L. N. Thibos, "Use of a Shack-Hartmann Aberrometer to Assess the Optical Outcome of Corneal Transplantation in a Keratoconic Eye," *Optometry & Vision Science, vol.78, no.12*, Dec. 2001, pp.866-871, Lippincott Williams & Wilkins, USA.

[4] L. Llorente, L. Diaz-Santana, D. Lara-Saucedo, and S. Marcos, "Aberrations of the human eye in visible and near infrared illumination," *Optometry & Vision Science, vol.80, no.1*, Jan. 2003, pp.26-35, Lippincott Williams & Wilkins, USA.

[5] X. Cheng, N. L. Himebaugh, P. S. Kollbaum, L. N. Thibos, and A. Bradley, "Validation of a clinical Shack-Hartmann aberrometer," *Optometry & Vision Science, vol.80, no.8*, Aug. 2003, pp.587-95, Lippincott Williams & Wilkins, USA.

[6] C. E. Joslin, S. M. Wu, T. T. McMahon, M. Shahidi, "Higher-order wavefront aberrations in corneal refractive therapy," *Optometry & Vision Science, vol.80, no.12*, Dec. 2003, pp.805-11, Lippincott Williams & Wilkins, USA.

[7] R. V. Shack and B. C. Platt, "Production and use of lenticular Hartmann screen," *Programme of the 1971 spring meeting of the Optical Society of America*, Optical Society of America, 1971, pp.15, Washington, DC, USA.

[8] J. Pfund, N. Lindlein, J. Schwider, "Dynamic range expansion of a Shack-Hartmann sensor by use of a modified unwrapping algorithm," *Optics Letters, vol.23, no.13*, July 1998, pp.995-7. Opt. Soc. America, USA.

[9] N. Lindlein, J. Pfund, J. Schwider, "Expansion of the dynamic range of a Shack-Hartmann sensor by using astigmatic microlenses," *Optical Engineering, vol.39, no.8,* Aug. 2000, pp.2220-5. SPIE, USA.

[10] N. Lindlein, J. Pfund, J. Schwider, "Algorithm for expanding the dynamic range of a Shack-Hartmann sensor by using a spatial light modulator array," *Optical Engineering, vol.40, no.5,* May 2001, pp.837-40. SPIE, USA.

[11] S. A. Klein, ""Problems with wavefront aberrations applied to refractive surgery: Developing Standards," Ophthalmic Technologies XI, SPIE Vol. 4245, January 2001, pp47-56, SPIE, USA.

[12] A. Tuantranont, V. M. Bright, J. Zhang, W. Zhang, J. A. Neff, and Y. C. Lee, "Optical beam steering using MEMS-controllable microlens array," *Elsevier Sensors & Actuators A-Physical, vol.A91, no.3*, July 2001, pp.363-72. Switzerland.

[13] H. Toshiyoshi, G-DJ Su, J. LaCosse, and M. C. Wu, "A surface micromachined optical scanner array using photoresist lenses fabricated by a thermal reflow process," *Journal of Lightwave Technology, vol.21, no.7*, July 2003, pp.1700-8, IEEE, USA.

[14] R. Legtenberg, A. W. Groeneveld, and M. Elwenspoek, "Comb-drive actuators for large displacements," *Journal of Micromechanics & Microengineering*, *vol.6*, *no.3*, Sept. 1996, pp.320-9, UK.

[15] G. T. A. Kovacs, "MICROMACHINED TRANSDUCERS: SOURCEBOOK," McGraw-Hill Companies, Chap. 3, New York, New York, USA.

[16] W. C. Tang, T.-C. H. Nguyen, and R. T. Howe, "Laterally driven polysilicon resonant microstructures," *Sensors and Actuators, vol. 20*, 1989, pp.25-32.

[17] A. C. Ugural, "MECHANICS OF MATERIALS," McGraw-Hill Companies, Chap. 9, New York, New York, USA.

[18] X. Zhang and W. C. Tang, "Viscous air damping in laterally driven microresonators," in *Tech. Dig. IEEE Micro Electro Mechanical Systems Workshop*, Jan. 1994, pp.199-204.

[19] H. Choo and R. S. Muller, "Optical properties of microlenses fabricated using hydrophobic effects and polymer-jet-printing technology," *2003 IEEE/LEOS International Conference on Optical MEMS and Their Applications,* August 18-21, 2003, pp.169-170. Waikoloa Beach Marriot, Waikoloa, Hawaii.

[20] D. R. Ciarlo, "Silicon Nitride Thin Windows for Biomedical Microdevices," *Biomedical Microdevices, vol.4, no.1*, March 2002, pp.63-8, USA.

[21] K. Gupta, H. Choo, H. Kim, and R. S. Muller, "Micromachined polarization beam splitters for the visible spectrum," *2003 IEEE/LEOS International Conference on Optical MEMS and Their Applications,* August 18-21, 2003, pp.171-172. Waikoloa Beach Marriot, Waikoloa, Hawaii.

[22] D. M. Hartmann, O. Kibar, and S. C. Esener, "Optimization and theoretical modeling of polymer microlens arrays fabricated with the hydrophobic effect," *Applied Optics, vol.40, no.16,* 1 June 2001, pp.2736-46, Opt. Soc. America, USA.

[23] D. L. MacFarlane, V. Narayan, J. A. Tatum, W. R. Cox, T. Chen, and D. J. Hayes, "Microjet fabrication of microlens arrays," *IEEE Photonics Technology Letters, vol.6, no.9*, Sept. 1994, pp.1112-14, USA.

[24] C. Ting, W. R. Cox, D. Lenhard, D. J. Hayes, "Microjet printing of high-precision microlens array for packaging of fiber optic components," *SPIE-Int. Soc. Opt. Eng. Proceedings of Spie - the International Society for Optical Engineering, vol.4652,* 2002, pp.136-41, USA.

[25] Microfab Technologies, Inc., Plano, Texas, USA.

[26] Epoxy Technology, Billerica, Massachusetts, USA.

[27] Y.-H. Cho, A. P. Pisano, and R. T. Howe, "Viscous damping model for laterally oscillating microstructures," *Journal of Microelectromechanical Systems*, *vol.3*, *no.2*, June 1994, pp.81-7, USA.

CHAPTER 6

Fast, MEMS-Based, Phase-Shifting Interferometer

NOMENCLATURE

f_r	Mechanical resonant frequency
l	Length of the optically active area
w	Width of the optically active area
l_f	Length of flexure
w_f	Width of flexure
l_c	Length of comb finger
w_c	Width of comb finger
l_s	Length of stress-relieving beam
w_s	Width of stress-relieving beam
h	Height of flexure
k	Vertical stiffness of the MEMS resonant structure
m	Total mass of resonant structure
t_{SOI}	Thickness of the device layer of the SOI wafer
E_{Si}	Young's modulus for silicon
$I(x, y)$	Intensity measurement as a function of x and y
$I'(x, y)$	Intensity bias
$I''(x, y)$	Amplitude of intensity modulation
λ	Wavelength of interest
$\delta(t)$	Phase shift (angular variation)
$\phi(x, y)$	Phase information of the surface of the sample under measurement

6.1 Introduction

Phase-shifting interferometry (PSI) is a well-established optical-characterization technique [1]. Typically, a conventional phase-shifting interferometer is constructed with both reference and test optical paths arranged in what is known as a Twyman-Green configuration, as shown in Figure 6.1.
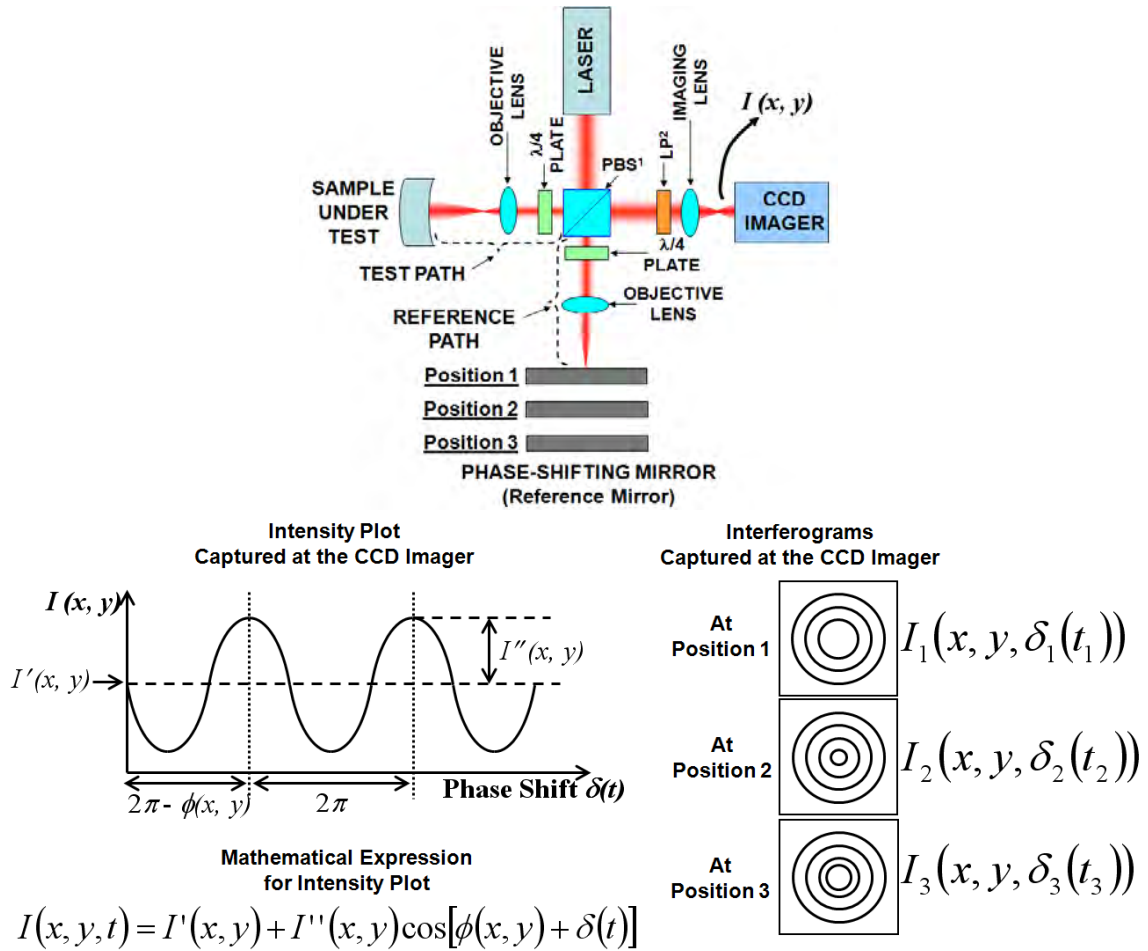
Figure 6.1 Conventional three-step phase-shifting interferometric setup using a Twyman-Green configuration [1]

The laser beam from the source is directed into two orthogonal optical paths by the polarizing beam splitter (PBS). The two beams travel their designated paths and are then directed towards a CMOS/CCD imager. As a consequence of the difference in optical path lengths, the beams constructively and destructively interfere to form fringe patterns. The phase-shifting mirror is moved from position 1 to 2, and then finally to position 3 to form three different intensity-measurement patterns. The intensity of each pattern, captured by the CMOS/CCD imager, can be expressed mathematically as [2]

$$I(x, y, t) = I'(x, y) + I''(x, y)\cos[\phi(x, y) + \delta(t)] \qquad (6.1.1)$$

In (1), $I(x, y, t)$ is the intensity captured by the CCD imager, $I'(x, y)$ is the intensity bias, $I''(x, y)$ times the cosine term is the intensity modulation, and $\delta(t)$ is the angular variation that results from the modulated phase-shifting distance. The wavefront phase $\phi(x, y)$ contains the phase information for the wave reflected off the surface of the sample-under-test, and it is the information that we want to retrieve [2]. Knowing $\phi(x, y)$, for example, we can generate the surface profile of the sample-under-measurement. The angular variation $\delta(t)$ is known precisely because we control it in the experiment, and therefore the three unknowns to be determined are: $I'(x, y)$, $I''(x, y)$, and $\phi(x, y)$. To solve for these quantities, we need at least three independent intensity measurements which we obtain by physically translating the reference mirror to three different, yet precisely known, positions [2]. After we make the three intensity measurements, we can solve for $\phi(x, y)$. The three-step algorithm requires the minimum amount of data and is the simplest to use. However, this algorithm is also very sensitive to errors in the phase-shift between frames [1]. Because of this sensitivity, researchers often use a four-step algorithm or a five-step "Hariharan algorithm" [1].

The rate at which a PSI makes measurements is limited by how quickly and precisely one can position the phase-shifting mirror. Piezoelectric actuators (usually made with lead-zirconium titanate (PZT)), which are typically used in existent PSI systems, are limited in speed owing to unavoidable transients that need to subside before accurate measurements become possible. When a PZT actuator stops after a commanded phase step, there is a transient oscillation of the reference mirror (mounted on the PZT actuator) that must be allowed to decay [3]. As a result, in PZT systems, measurements

are taken over intervals that vary between 0.5 and 5 seconds. Over time spans of these lengths, however, PSI measurements can be corrupted by changes that are due to variations in beam transmission over the optical path. As a result, PSI has generally been used to characterize the surfaces of static optical components such as mirrors and lenses or of device structures in optical systems built using such components. In order to apply PSI systems to measure transient phenomena such as turbulent flows, non-steady-state motions of structural elements, or crystal growth, to name a few examples [4-6], the required data sets must be taken at higher rates than are possible in PZT-driven systems. Another drawback to the use of conventional PZT actuators is that these components require relatively sophisticated control electronics, making them a costly part of the PSI system.

In this chapter, we discuss a fast, MEMS-based, phase-shifting interferometer. In our MBPSI, the cost-effective micromachined mirror replaces the PZT actuator and serves as a phase-shifting component (Figure 6.2). Other changes include replacing the laser with a laser diode and the CCD imager with a faster CMOS imager. The micromachined mirror operates at resonance, with an amplitude at resonance that exceeds the wavelength of the laser used for measurement. We have implemented the four-step algorithm for measurement-data reduction in order to achieve processing speed while maintaining accuracy.
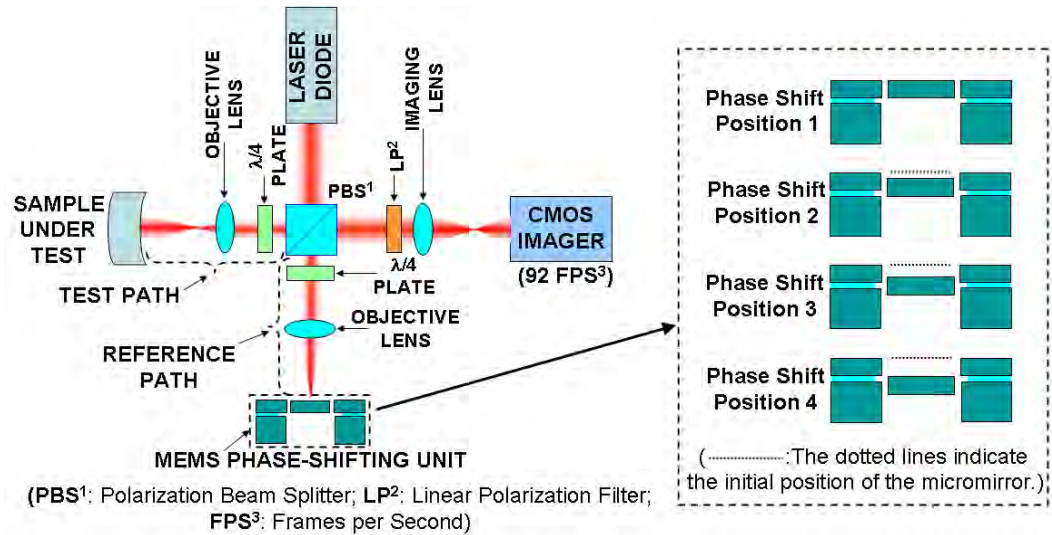
Figure 6.2 MBPSI setup using the Twyman-Green configuration: The micromachined MEMS mirror, laser diode, and CMOS imager replace the PZT mirror, continuous-wave laser, and CCD imager, respectively, in the conventional setup. The diagram in the inset shows the instantaneous visualization of four different phase-shift positions which occur in the path of mirror's resonant motion. The distances of motions have been vastly exaggerated in the drawing for illustration purpose.

Figure 6.2 shows the optical setup used for the MBPSI. The MEMS mirror is driven at resonance, and a single PSI measurement is completed by making four intensity measurements at four different mirror positions that correspond to four phase angles in the resonant path of its surface. The laser illumination is pulsed precisely when the micromirror passes each phase position, and the resulting interference pattern for each phase position is captured in a single frame of the imaging sensor. Using the CMOS imager which is programmed to capture images at 92 frames per second (fps), a single four-step PSI measurement takes only 43.5 msec, a speed 12-115 times faster than conventional PZT-based PSI systems. Our system takes 23 measurements per second and produces as many as 700 successive measurements, which is limited by the size of the computer's system memory. This successive measurement capability enables the observation of transient optical phenomena for the duration of 30 seconds at the time-

resolution of 43.5 msec. Achieving such successive measurements is a very unique capability that is impossible and impractical to achieve using conventional PSI systems.

6.2 Fast Phase-Shifting Method

Our phase-shifting technique for MBPSI is directly related to the well-known stroboscopic method for observing vibrating specimens. By flashing the laser pulses synchronously at successively lengthened delays to the resonating micromirror in the reference path of the system, we capture repeated interference patterns for beams that traverse the two optical paths.
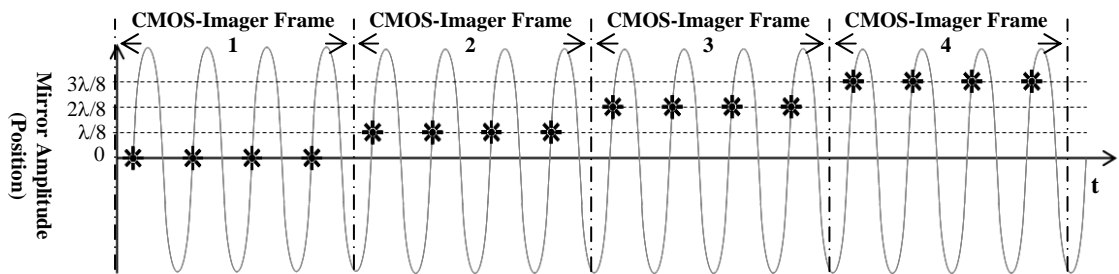
Figure 6.3   Phase-shifting technique using our vertically resonating micromirror and a pulsed laser diode: '✳' indicates when the laser pulse is flashed. In this example, there are four phase steps; each frame of the CMOS imager integrates images generated by four laser pulses flashed for each phase step.

In Figure 6.3, the sinusoidal wave represents the time-varying position of the resonating MEMS micromirror used as a phase shifter. The interference patterns corresponding to 0, $\lambda/4$, $\lambda/2$, and $3\lambda/4$ phase shifts are captured within the CMOS-imager frames 1, 2, 3, and 4, respectively. In each frame, while driving a MEMS mirror at its resonant frequency, we pulse the laser diode at the instant when the mirror is precisely displaced by the desired fraction of the illuminating wavelength from the initial position. For example, to achieve the phase shift of a 0 displacement, we flash the laser diode whenever the MEMS mirror passes the initial position. Similarly, to achieve the phase shift of a $\lambda/4$

displacement, we flash the laser diode whenever the MEMS mirror passes the position that is precisely λ/4 units away from the initial position. We do this by adding a precise amount of delay time with respect to the zero-crossing in the voltage wave that actuates the MEMS mirror before pulsing the laser-diode driving current. Because the integrating-bucket technique (the most common PSI data-collection technique) requires that the movement of the phase shifter be linear [7], we take the phase-shifted measurements in the quasi-linear region of the micromirror path. The path is approximately linear near the beginning of each resonant period as shown in Figure 6.3. Using this technique, the maximum profile-measurement rate is equal to the imager frame rate (fps) divided by the number of phase steps required by the PSI algorithm. For a MBPSI setup having a CMOS imager that operates at 92 fps and employs the 4-step algorithm, the measurement rate is 23 Hz. At this rate, the system can continuously capture 700 successive, PSI measurements in 30 seconds. The rate of measurements and the number of successive measurements can further be improved by using a faster imager and by installing a larger computer-system memory for storing captured images, respectively.

6.3 Fast Phase-Shifting MEMS Mirrors: Design, Fabrication, and Characterization

6.3.1 Design

The sizes of the reflective areas of the micromirrors are determined by their uses in specific interferometric configurations. For example, in order to measure the quality of a laser beam using the Mach-Zehnder configuration, the size of the reflective area of the micromirror must be larger than the diameter of the laser beam, which can be as large

as a few mm in diameter. For our Twyman-Green configuration, the objective lens in the reference path of the system focuses the beam onto a small spot (usually smaller in diameter than a few hundred micrometers) on the reference-mirror surface. As a result, the required size of the micromirror reflective area is just slightly larger than the size of the spot formed by the objective lens. Although we report experimental results obtained using the Twyman-Green configuration in this chapter, we plan other experiments using the Mach-Zehnder configuration and for these, we would need a square mirror that could be as large as 3 mm on a side. Hence, we designed our micromirror to have an optically reflective area larger than 3 mm by 3 mm (actual size: 3.6 mm by 3.6 mm). Figure 6.4 shows the schematic diagram of the representative micromirror that we used in our experiments.
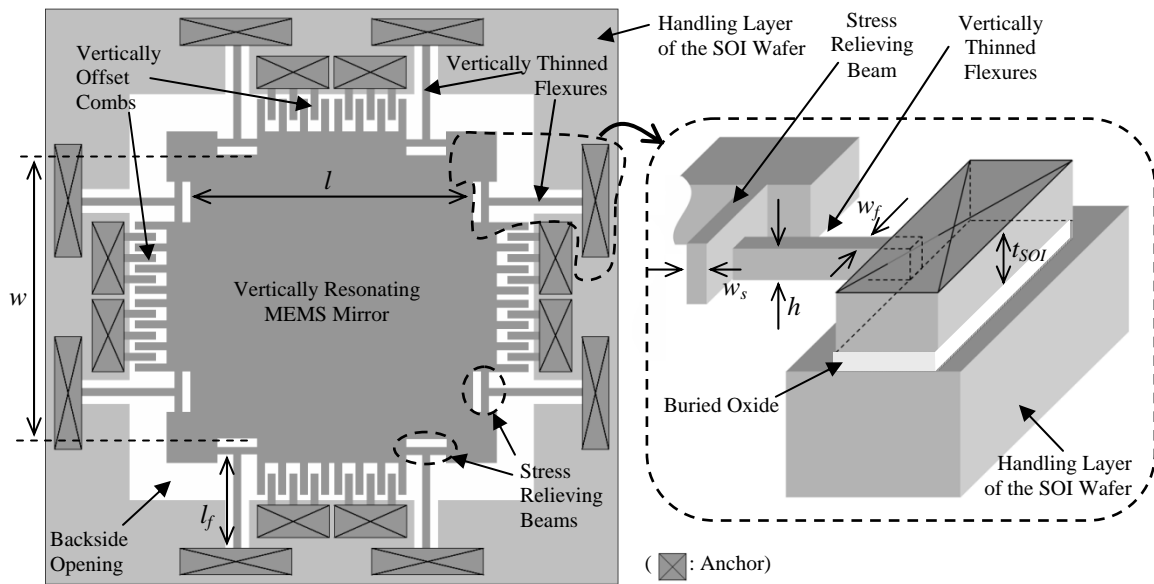

Figure 6.4   Top view of the MEMS phase-shifting micromirror: The inset shows one of the four corners of the MEMS micromirror. Both the flexure and the fixed comb fingers are vertically thinned in order to increase their pliancy in the desired actuation (vertical) direction.

We have placed eight vertically-thinned, rectangular-beam flexures at the four corners of the micromirror so that the resulting stiffness to forces applied either rotationally or laterally in-plane or else torsionally out-of-plane will be much larger than that in the vertical direction (perpendicular to the substrate) and will prevent any unwanted motions. To fabricate the mirrors, using SOI (silicon-on-insulator) wafers, we made use of a process that we had described in earlier publications [8, 9]. In this process, the vertically offset actuating combs are formed when we use deep-ionic reactive etching to thin the fixed combs without eroding the surfaces of the moving combs. The flexing elements are simultaneously thinned vertically.

The vertical resonant frequency of the MEMS phase-shifting micromirror is calculated using (6.3.1) [10]

$$f_r = \frac{1}{2 \cdot \pi} \sqrt{\frac{k}{m}} \qquad (6.3.1)$$

where k is the combined vertical stiffness of the 8 flexures and m is the mass of the moving structure. The stress-relieving beams are found to be 768 times stiffer in the vertical direction than the flexures, and we can assume that the stress-relieving beams will not bend in the vertical direction. Hence, the vertical stiffness k of the moving structure is given by [11]

$$k = \frac{8 \cdot (h)^3 \cdot w_f \cdot E_{Si}}{l_f^3}. \qquad (6.3.2)$$

The actual values of the design parameters are given below in Table 1.

Table 6.1   Design parameters of the micromirror

t_{SOI} (thickness of the device layer of the SOI wafer)	50 μm
l_f (length of flexure)	1000 μm
w_f (width of flexure)	50 μm
h (height of flexure)	25 μm
l_c (length of comb finger)	280 μm
w_c (width of comb finger)	15 μm
Number of moving comb fingers	208 comb fingers
l_s (length of stress-relieving beam)	500 μm
w_s (width of stress-relieving beam)	75 μm
l (length of the optically active area)	3600 μm
w (width of the optically active area)	3600 μm
m (total mass of resonant structure)	2.06×10^{-6} kg
E_{Si} (Young's modulus for silicon)	1.70 GPa
k	1.06×10^3 N/m

The precise value of the resonant frequency f_r is relatively unimportant; it is important, however, that f_r be much higher than the frame rate (*fps*) of the photo-sensor array. Our MEMS phase-shifting micromirror chosen for our MBPSI experiment has the design resonant frequency of 3.61 kHz. We calculated this resonant frequency using the parameters given in Table 6.1 in (6.3.1) and (6.3.2). For a CMOS-image array (fps ~ 30-100 Hz), indicating that each image frame will capture 36-120 pulses. The advantage of having a larger number of pulses-per-frame is that unavoidable reference phase-shift errors contained in interferometric images, which can be introduced by the system electronics, can be averaged out improving the phase-shift accuracy in the image sets.

6.3.2 Micromirror Fabrication

The MEMS phase-shifting mirror with its support and actuator structures measures 7.9 by 7.9 by 0.05 mm (the optically reflective area is 3.6 by 3.6 mm), and is micromachined using a fabrication process that we have described earlier [8-9]. The process uses three photolithography masks (two for defining features in the device layer of a SOI wafer and one for opening the backside of the microscanners). All process steps

are made with conventional silicon-processing tools that have proven their effectiveness and user-friendliness through large-scale use in the integrated-circuits industry. All required processing temperatures are low enough to allow pre-fabrication of CMOS electronics directly on the same wafer as the microscanner devices. Steps in the fabrication process are illustrated in Figure 6.5.

1. Figure 6.5-1: Start with an SOI wafer. Grow 0.5-µm thermal or low-temperature oxide (LTO). Using the photolithography mask #1, pattern and remove the thermal oxide (or LTO) selectively where fixed combs will be later defined and vertically thinned.

2. Figure 6.5-2: Using mask #2, create patterns of micromirror including moving and fixed combs, flexures, and mirrors. The fixed combs must be defined within the windows from which the oxide has been removed to expose the silicon surface in the previous step, and the minimum gap between the moving and fixed comb fingers can be as small as twice the alignment accuracy of the photolithography process.

3. Figure 6.5-3: Use deep-reactive-ion-etch (DRIE) to define the micromirror structures in the device layer.

4. Figure 6.5-4: Remove the photoresist layer and deposit a very thin layer (~0.2 µm) of LTO.

5. Figure 6.5-5: Use timed-anisotropic-plasma etch to remove 0.2-µm thick LTO from the top-facing surfaces. This step exposes the silicon surface on top of the fixed combs, but leaves all other surfaces covered by an approximately 0.5µm-thick oxide layer.

6. <u>Figure 6.5-6</u>: Then use timed-isotropic silicon-etch to create a set of vertically thinned combs. Only the fixed combs, which do not have any protective layer on top, will be vertically thinned.

7. <u>Figure 6.5-7</u>: Using mask #3, pattern and open the backside of the micromirror using DRIE process. Release the devices in HF and perform critical-point drying.

More detailed description of the fabrication process, including additional comments on creating vertically offset-combs, is found in references [8-9].

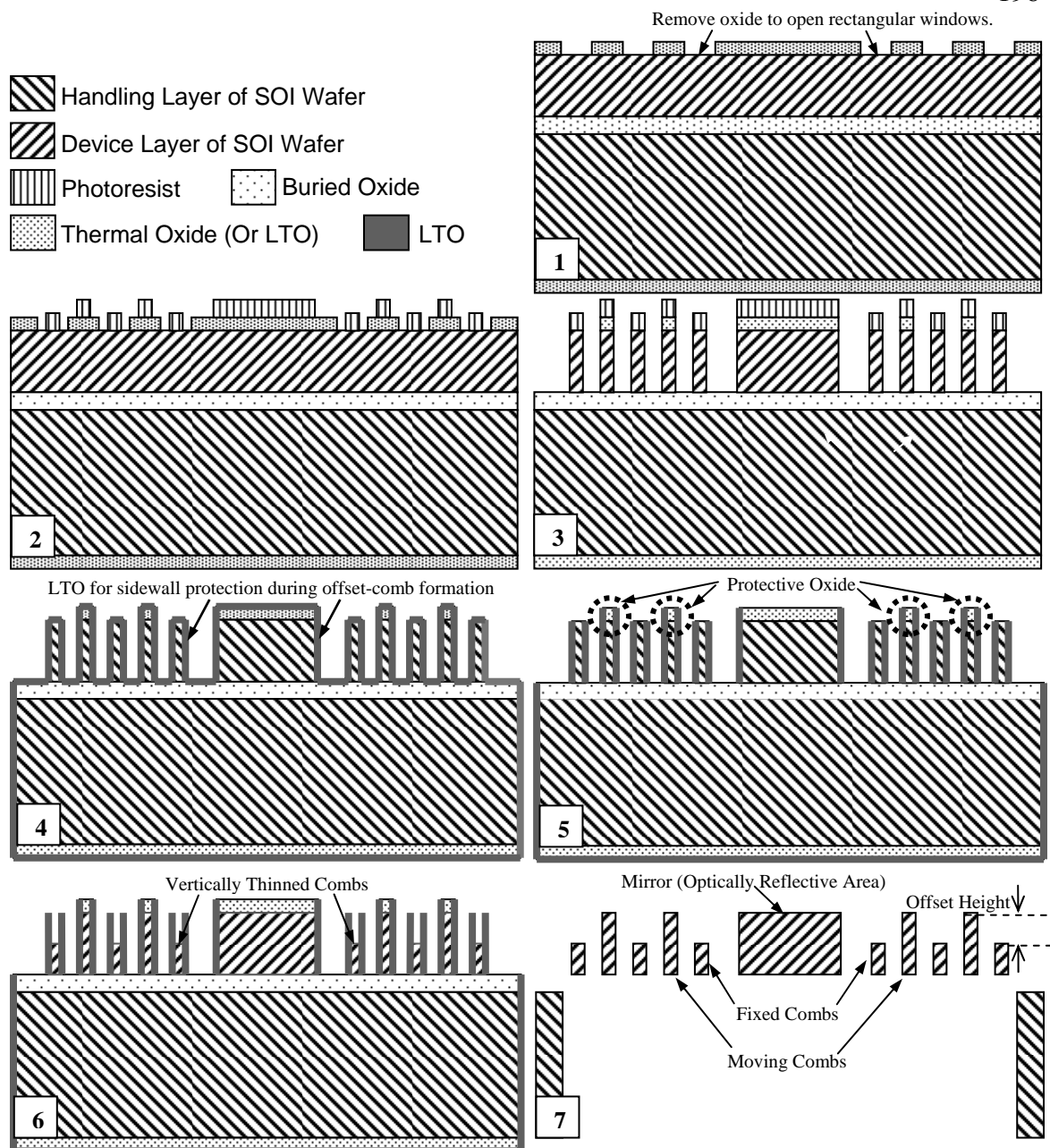**Figure 6.5** Fabrication process for vertically actuated microscanners with self-aligned, vertically offset combs

Figure 6.6 shows photos of five different fabricated micromirrors. Three of the micromirrors are mounted and wire-bonded on ceramic packages that have circular openings (indicated by white-dashed line in the photo) in the mounting area in order to minimize air damping and thus improve the mechanical quality factors.
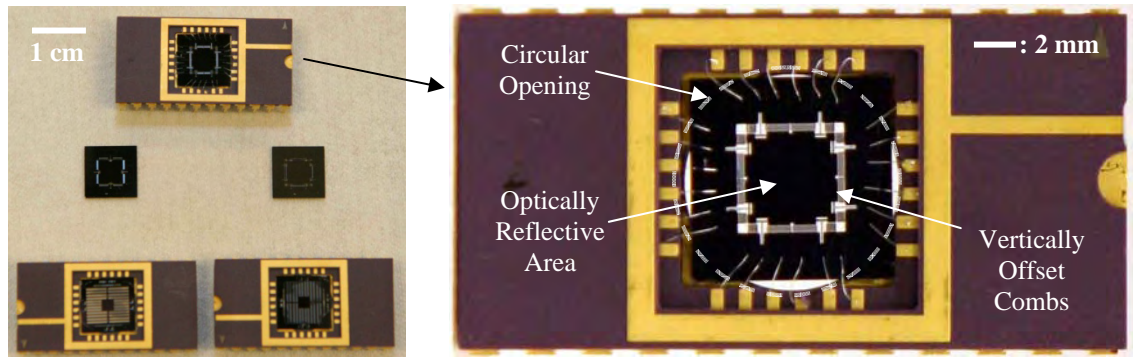
Figure 6.6 Photos of fabricated MEMS phase-shifting micromirrors: Three micromirrors are mounted and wire-bonded on ceramic packages which have circular backside holes. The micromirror shown on right is the representative micromirror used to produce the results reported in this chapter.

In Figure 6.7, the SEM image on the right-hand-side shows the vertically thinned flexures with reduced vertical stiffness. The SEM images show that the fabricated structures, including vertically offset combs and vertically thinned flexures, are sharply defined, precisely aligned, and uniformly etched. Using the WYKO white light interferometer, we have measured that the average offset height across the wafer is 24.9 μm, and the offset height shows excellent uniformity (less than or equal to ±1.5 % peak-to-peak deviation from the average value).
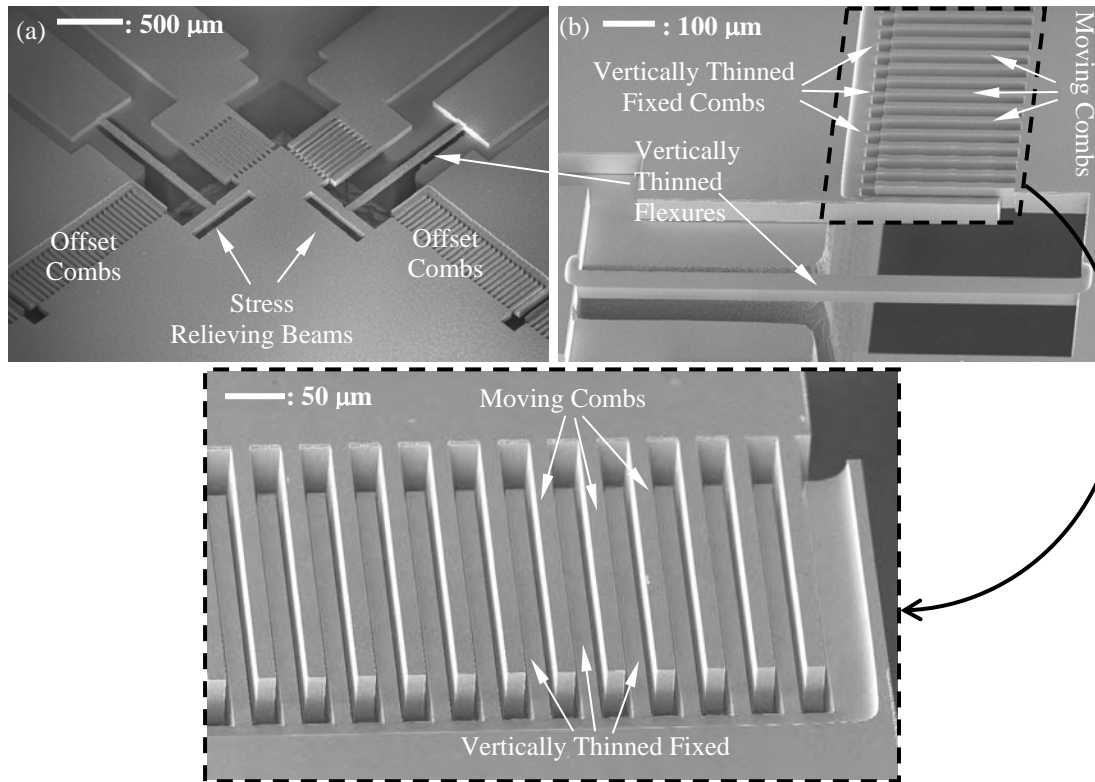
Figure 6.7   SEM images showing the key sections of the phase-shifting MEMS mirror: (a) A corner of the MEMS phase-shifting micromirror; and (b) close-up image of vertically offset combs as well as vertically thinned flexure – The offset height is 24.9 μm. The inset at bottom shows the magnified SEM image of precisely-aligned vertically-offset combs

6.3.3 Micromirror Characterization

Using a white-light interferometer (WYKO NT3300), we measured the surface profile of one representative micromirror (of 18 that we have produced). An image from this measurement is shown in Figure 6.8; the radius-of-curvature at all points on the mirror surface is greater than 20 m, and the surface roughness is consistently below 20 nm. We carried out the radius-of-curvature measurements on all 18 fabricated micromirrors and found in all cases a value greater than 10 m.
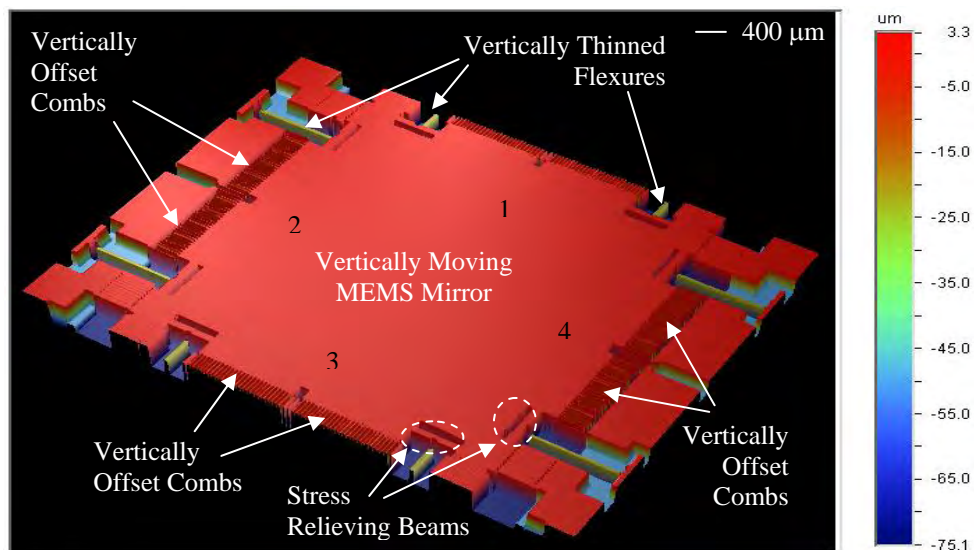
Figure 6.8   3-D picture of WYKO-profile measurement of fabricated MEMS mirror
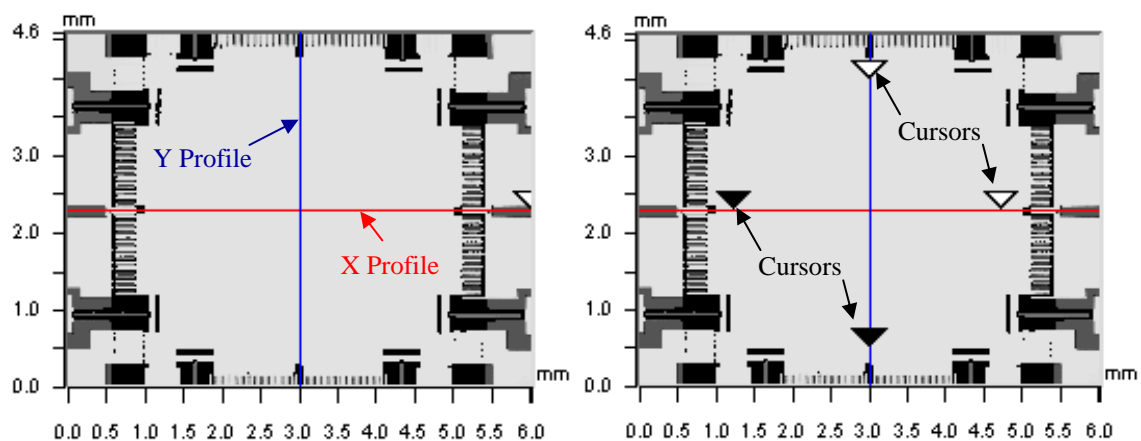
Figure 6.9   Top views of WYKO-profile measurement: The first picture (left) without analysis cursors (reversed triangles); the second picture (right) with analysis cursors (reversed triangles) in place (over the optical active area)

X Profile

Rq	0.00	um
Ra	0.00	um
Rt	0.00	um
Rp	-49.27	um
Rv	-49.27	um

Angle	0.00	mrad
Curve	0.00	nm
Terms	None	
Avg Ht	-49.27	um
Area	0.00	mm2

Optically
Active Area

X Profile

X: 3.5 mm

Cursor   Cursor

Y: 0.0 um

Rq	0.02	um
Ra	0.02	um
Rt	0.08	um
Rp	3.24	um
Rv	3.16	um

Angle	1.66	urad
Curve	-23.12	m
Terms	None	
Avg Ht	3.21	um
Area	0.01	mm2

Curvature
Measurement Area

Curvature
Measurement

Y Profile

Rq	0.03	um
Ra	0.03	um
Rt	0.13	um
Rp	3.24	um
Rv	3.11	um

Angle	0.00	mrad
Curve	-22.85	m
Terms	None	
Avg Ht	3.20	um
Area	0.01	mm2

Curvature
Measurement Area

(Figure 6.10 continues on the next page)

(Figure 6.10 continues)

Figure 6.10   X- and Y-profiles of the phase-shifting MEMS mirror: The pictures with cursors in place and without cursors are shown because the mirror is extremely flat and the gray lines that show the difference in height between two cursor points cover the red and blue profile lines. In both cases, the radii of curvature are larger than 20 m.

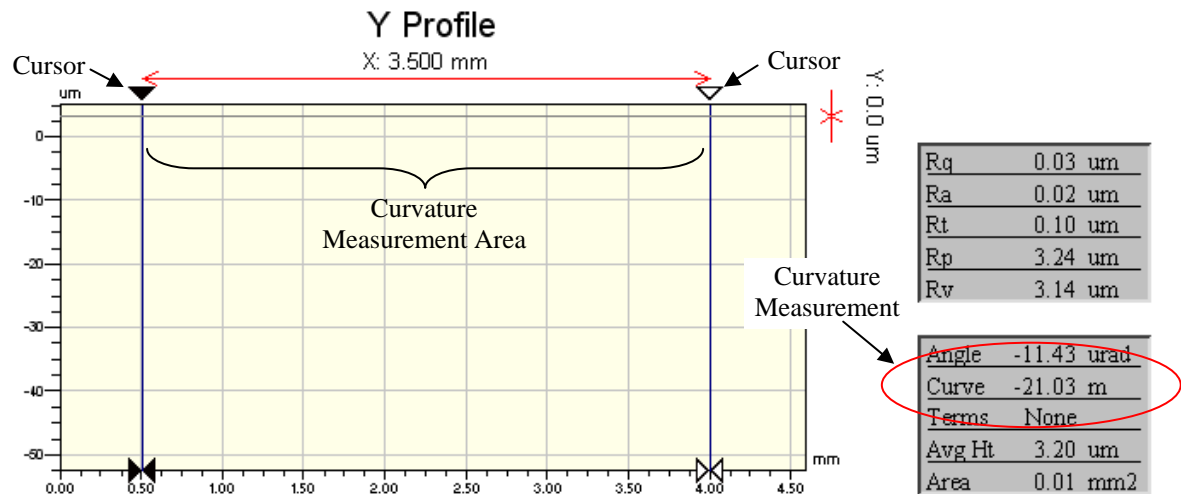In order to find the precise flash timings for laser pulses (synchronized with the micromirror's resonant motion) required for MBPSI operation, we studied the resonance behavior of the micromirrors using a piezo-based, calibrated stroboscopic interferometer [12], which has an rms-measurement accuracy of 5nm.   In these measurements we tracked the relative motions of each of the four corners on the mirror and at the mirror center and recorded these measurements over one period of resonant motion to obtain the measurements shown in Figure 6.11. The measurement results indicate that a relatively small, peak-to-peak 0.75-μm resonant amplitude achieved with 18 V (peak to peak sinusoidal drive voltage) is sufficient for performing PSI measurements. With this drive voltage, the micromirror surface passes the desired phase-shifting positions of 0, $\lambda/8$, $2\lambda/8$, and $3\lambda/8$ at intervals of 0, 10, 20, and 30 μsec (see the inset of Figure 6.11),

respectively. Using these intervals as delay times, we can achieve precise timings for the laser pulses which have a 1-μsec duration.
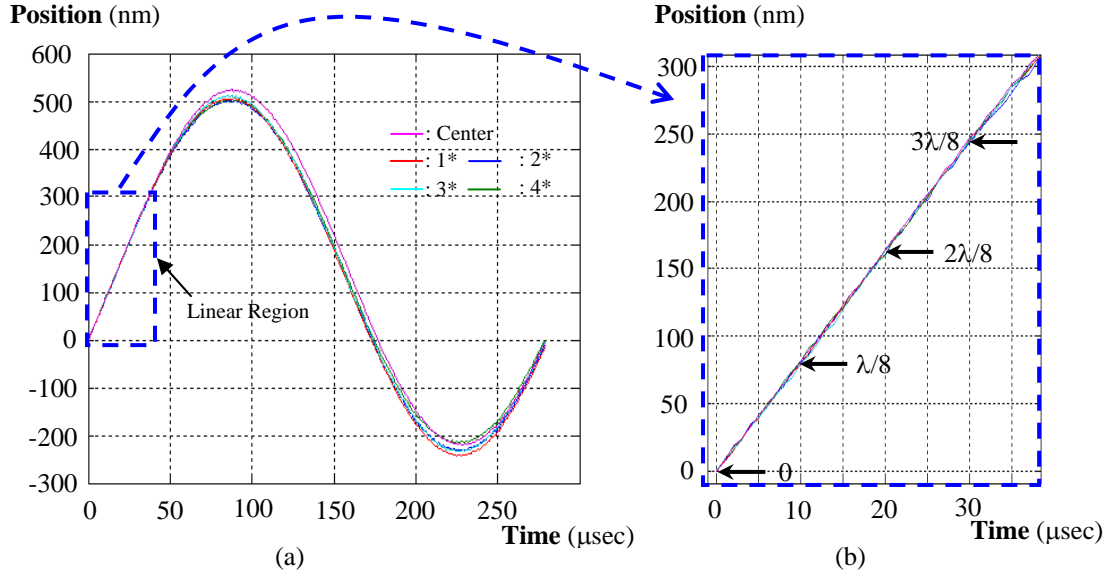

Figure 6.11   Resonant-motion analysis for our phase-shifting MEMS mirror measured with a calibrated laboratory Stroboscopic Interferometer developed at BSAC [11] – (a): One full period of resonant motion, with the quasi-linear region indicated by the dashed rectangle, (b): Quasi-linear region used for phase-shifting (peak-to-peak deviation in position: < 6 nm) (*1-4: Please refer to Figure 6.8.)

The dynamic deformation of the mirror, between the center and the four corners of the micromirror, within this quasi-linear region of operation, is less than 3 nm or λ/220, which is quite close to the measurement accuracy of the stroboscopic interferometer. We measured a resonant frequency of 3.55 kHz for this micromirror (design value is 3.61 kHz) and a mechanical Q of 63.

6.4 Optical Measurements Using MBPSI

Details of our experimental setup are shown in Figure 6.12. The CMOS imager has a maximum frame rate of 100 fps [13]. We ran the imager at a conservative 92 fps and employed the four-step phase-shifting algorithm in order to measure sample motions

at a rate of 23 Hz. We used the surface of a flat, reflective mirror mounted on a commercial PZT actuator as a measurement sample [14] because we know its traveled distance with a precision of ±10 nm as read directly from a feedback-position sensor that is built directly into the PZT actuator package. The MEMS phase-shifting micromirror was driven by a 3.55 kHz sine wave of amplitude 18 $V_{ac\_p\text{-to-}p}$. For a light source, we drove a pig-tailed laser diode (λ = 660 nm) [15] with 1μsec-wide synchronized pulses having rise/fall times shorter than 50 nsec. The laser driver was a precision-pulsed current source [16] controlled by a digital controller installed in an IBM-PC computer [17]. The entire setup was enclosed in a transparent Acrylic plastic cover in order to prevent the influence of air turbulence on the measurements.

(PBS[1]: Polarization Beam Splitter; LP[2]: Linear Polarization Filter; FPS[3]: Frames per Second)
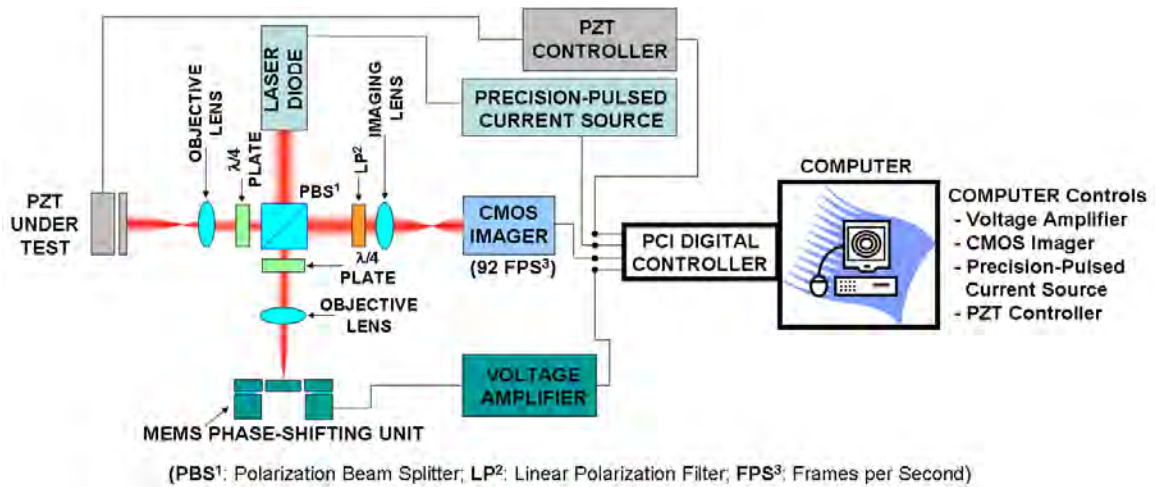
Figure 6.12 MBPSI optical-test setup (Twyman-Green configuration): PZT is not used as a phase-shifting element but rather serves as the object-under-test as well as a calibration reference.

In the experiments, we first used the PZT actuator as a calibration reference to measure repeatability of the system for transient measurements. We repeatedly measured the changing positions of the PZT actuator and found that the system repeatability was < ± 5 nm (±λ/132) over a 30-second period and < ± 10 nm (±λ/66) over a 20-minute period.

Next, we measured the accuracy of the system also by using the moving PZT as a reference. We found that the system's accuracy was $< \pm 5.5$ nm ($\pm\lambda/120$).

In order to demonstrate the fast measuring capability of our system, we used it to track, in real time, the fast-changing, transient motion of the PZT actuator. The actuator was stepped at intervals of 50 nm every 0.5 sec over a 6.478-sec period. We measured the surface profile of the central area (0.52 by 0.4 mm) of the mirror mounted on the PZT actuator. Since our system continuously measured at a rate of 23 Hz, the total number of recorded profile measurements was 150, where each profile measurement contained 4 separate phase-shifted intensity measurements. After using noise reduction (averaging over the entire area within same measurement), the transient measurement was precise to within ± 3 nm ($\pm \lambda/220$), lower than the 10nm-accuracy limit of the PZT-actuator's position-read-out sensor (Figure 6.13).
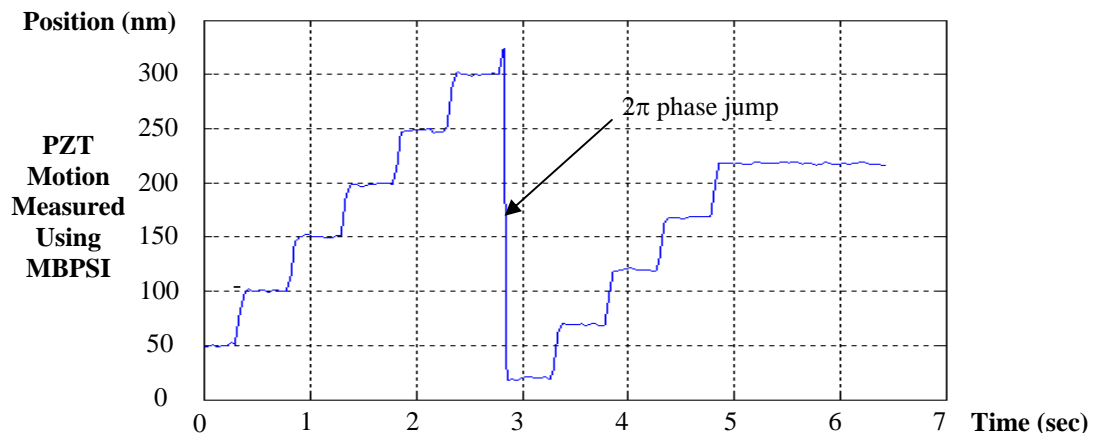

Figure 6.13 Section of a total 150 measurements made with our MBPSI system showing a PZT actuator moving at a step of 50 nm every 0.5 seconds during the 6.478-second period (PZT movement resolution: $<\pm10$ nm from the readings of the PZT built-in feedback position sensor)

6.5 Conclusions

We have demonstrated a fast, accurate, MEMS-based PSI that can measure transient optical phenomena at measurement frequencies up to 23Hz. A cost-effective, batch-produced MEMS micromirror is used as the phase-shifting element. Proven, robust conventional PSI algorithms can be applied to our system without any modifications. The repeatability of the system was measured to be $< \pm 5$ nm for 30-second interval and $< \pm 10$ nm for 20-minute interval. The accuracy of the system was measured to be $< \pm 5.5$ nm (without noise reduction). The system has successfully tracked the fast changing motion of a PZT actuator. The transient measurement was precise to within ± 3nm ($\pm \lambda/220$, after noise reduction), lower than the 10nm-accuracy limit of the PZT-actuator movement.

References

[1] D. Malacara, Ed., "Optical Shop Testing," 2nd Edition, Chap. 14, New York: Wiley, 1992, USA

[2] D. Malacara, Ed., "Optical Shop Testing," 2nd Edition, Chap. 14, Section 14-2, New York: Wiley, 1992, USA

[3] J. L. Seligson, C. A. Callari, J. E. Greivenkamp, and J. W. Ward, "Stability of a Lateral-Shearing Heterodyne Twyman-Green Interferometer," *Optical Engineering, vol.23*, 1984, pp.353-356

[4] D. Malacara, Ed., "Optical Shop Testing," 2nd Edition, Chap. 14, Section 14-4 and Section 14-14-3, New York: Wiley, 1992, USA

[5] G. M. Burgwald and W. P. Kruger, "An Instant-on Laser for Distance Measurement," *Hewlett-Packard Journal*, vol.21, 1970, pp.14, USA

[6] K. Onuma, K. Tsukamoto, and S. Nakadate, "Application of real-time phase shift interferometer to the measurement of concentration field," J. of Crystal Growth, vol. 129, 1993, pp. 706-718

[7] D. Malacara, Ed., "Optical Shop Testing," 2nd Edition, Chap. 14, Section 14-7, New York: Wiley, 1992, USA

[8] H. Choo, D. Garmire, J. Demmel, and R. S. Muller, "A Simple Process to Fabricate Self-Aligned, High-Performance Torsional Microscanners: Demonstrated Use in a Two-Dimensional Scanner," 2005 IEEE/LEOS International Conference on Optical MEMS and Their Applications, August 1-4, 2005, pp.21-22, Oulu, Finland (Journal version submitted and presently under review)

[9] H. Choo, D. Garmire, J. Demmel, and R. S. Muller, "Simple Fabrication Process for Self-Aligned, High-Performance Microscanners; Demonstrated Use to Generate a Two-Dimensional Ablation Pattern," Journal of Microelectromechanical Systems (Submitted and presently under review)

[10] W. C. Tang, T.-C. H. Nguyen, and R. T. Howe, "Laterally driven polysilicon resonant microstructures," *Sensors and Actuators, vol. 20*, pp.25-32, 1989

[11] A. C. Ugural, "MECHANICS OF MATERIALS," McGraw-Hill Companies, Chap. 9, 1990, New York, New York, USA

[12] M. R. Hart, R. A. Conant, K. Y. Lau, and R. S. Muller, "Stroboscopic Interferometer System for Dynamic MEMS Characterization," *J. MEMS*, vol. 9, no. 4, December 2000, pp. 409-418, USA

[13]   Basler A600f: High-Speed, Area-Scan CMOS Camera

[14]   PZT Actuator: PI P-753 LISA, PZT Controller: PI E-501

[15]   Thorlabs LPS-660 FC Single Mode Pig-Tailed Laser Diode System

[16]   ILX DLP 3840 Precision Pulsed current source

[17] National Instrument PCI-6259 Multifunction DAQ (Digital Input/Output Card)

CHAPTER 7

Conclusions

New fabrication processes and devices that expand the design and application space for optical MEMS are presented in this thesis. In Chapter 1, we describe a method to fabricate and place high-quality microlenses in an optical MEMS. The microlenses are fabricated using polymer-jet printing and hydrophobic effects. Fabricated microlenses, whose diameters are 200, 400, 600, and 1000 μm, have focal lengths ranging between 0.3 and 7.44 mm. The *f*-numbers for these lenses range from 1.5-2.1, 2.0-5.5, 3.4-6.3, and 2.9-7.4 for lenses with these respective sizes. They are produced with a focal-length uniformity of 3.09% within the chip and 4.22 % from chip to chip. The microlens profiles are nearly spherical; the maximum deviation from an ideal radius-of-curvature is 4.51 %. The rms wavefront errors (WFE) of the microlenses are also excellent. Over the microlens area included by 90% of its diameter, all microlenses show rms WFEs lower than λ/6, which is the quality typically assured in high-end commercial camera lenses. The low optical aberration we have achieved proves that these microlenses are capable of imaging very fine features (2.5-μm wide lines and gaps). When we compare our microlens imaging system (pairing it with a miniature CCD) with that of a commercial microscope, we demonstrate its ability to resolve 2.5-μm wide lines and gaps. Our microlenses also demonstrate good imaging qualities when used to observe macro-scale objects.

In Chapter 2, we describe batch-processed polarization-beam splitters (PBS), important optical components to separate the orthogonal TE and TM components of light.

The devices, fabricated using thin-film, low-stress silicon nitride membranes show excellent performance: extinction ratios (σ_R for reflected and σ_T for transmitted light) of (21dB, 10dB), (21dB, 14dB), and (21dB, 16dB) for single-, double-, and triple-layer systems, respectively with corresponding insertion losses of 3, 10, and 13%. We show that stacking PBS devices improves performance over single elements, especially increasing the extinction ratio for transmitted light. The measured level of performance is comparable to that obtained with commercially available PBS.

In Chapter 3, we describe the design, fabrication, and test of microscanners produced using a new fabrication technique, that derives from well-developed integrated-circuit processing tools. It is simple, high-yielding, and reliable. The major advance in our fabrication process results from its straightforward method to produce vertically offset comb pairs that provide for robust electrostatic drive of torsion-bar suspensions. The gap between the comb fingers is ultimately limited to twice the alignment accuracy of the photolithography process. However, practical minimum gap sizes are typically 1-μm or wider because they are determined by other fabrication-process limitations and variations. In practice, we achieve uniform offset-heights for vertical comb fingers spaced across the 10-cm wafers. Microscanners produced using this new technique have resonant frequencies ranging from 50 Hz to 24 kHz and optical-scanning-angle values typically approximating 20° but varying from 8 to 48°. The actuation voltages required range from 14.1 to 67.2 V_{ac_rms}. A 2-D scanning system, built using these microscanners, is demonstrated to produce emulated-ablation patterns that compare favorably to published results obtained with a state-of-the-art macro-scale ablative surgery system.

Chapters 4 and 5 are closely related. In Chapter 4, we discuss published results that show the present status and predicted development of various types of wavefront sensors: phase-shifting interferometers, lateral-shearing interferometers, curvature sensing, phase-diversity methods, the Foucault (knife-edge) test, the Ronchi test, and the star test. The purpose of Chapter 4 is to consider wavefront sensors that may be suitable for specific ophthalmic-analysis applications (such as corneal refractive-surgery evaluations and Keratoconus analysis), that require large dynamic ranges and sensitivities. We conclude that no presently available wavefront sensors are capable of precisely characterizing high-order wavefront aberrations of large magnitude.

In Chapter 5, we describe an addressable MEMS-microlens array that vastly improves the dynamic range and sensitivity of Shack-Hartmann wavefront sensors. We present our successful research to produce an array of MEMS structures that are nearly identical except that each structure is designed to have a unique mechanical-resonance frequency. We arranged these structures along rows and columns and mounted nearly identical optical lenses on them to form a lens array that can be used as a Shack-Hartmann sensor having the special capability to identify the light passing through a particular lens by driving the carriage supporting that lens to mechanical resonance. Use of the frequency-selection scheme to address individual MEMS structures in an array is not limited to the optical application demonstrated in this project. This scheme has value for other MEMS applications such as print-head activation in multi-color printers or activated drug dispensing, to cite only two examples. In each of these cases, an important advantage of the selection technique is that it does away with the need for multiple input-addressing leads to the array or for the use of sophisticated electronics. In continued

research, the time needed for an SH readout measurement will be shortened by implementing lens units that have faster responses as well as by developing more efficient data-handling algorithms. We will also carry through research on new designs to increase our lens-array fill factor from its present 40%.

In Chapter 6, we describe a fast, accurate, MEMS-based PSI that can measure transient optical phenomena at measurement frequencies up to 23Hz. A cost-effective, batch-produced MEMS micromirror is used as the phase-shifting element. We show that proven, robust, conventional PSI algorithms can be applied to our system without any modifications. The repeatability of the system is measured to be less than $\pm$ 5 nm for 30-second intervals and less than $\pm$ 10 nm for 20-minute intervals. The accuracy of the system is measured to be less than $\pm$ 5.5 nm (without noise reduction). The system has successfully tracked the fast changing motion of a PZT actuator. Precise transient measurement to within $\pm$3nm ($\pm\lambda/220$, after noise reduction) is demonstrated, a measurement accuracy lower than the 10nm-motional accuracy achieved in the commercial PZT-actuator movement.

Appendix I: Publication List

Reviewed Archival Journals

1. H. Choo and R. S. Muller, "**Devices, Structures, and Processes for Optical MEMS**," *Invited Paper, Special Issue on IEEJ (Institute of Electrical Engineers of Japan) Transactions of Electrical and Electronic Engineering* (To be published in May 2007).

2. H. Choo, D. Garmire, J. Demmel, and R. S. Muller, "**A Simple Process to Fabricate Self-Aligned, High-Performance Torsional Microscanners: Demonstrated Use in a Two-Dimensional Scanner**," Journal of Microelectromechanical Systems, vol. 16, no. 2, April 2007, pp. 260-268.

3. H. Choo and R. S. Muller, "**Addressable Microlens Array to Improve Dynamic Range of Shack-Hartmann Sensors**," Journal of Microelectromechanical Systems, vol. 15, no. 6, December 2006, pp. 1555-1567.

4. J. B. Kim, H. Choo, L. Lin and R. S. Muller, "**Microfabricated Torsional Actuator Using Self-Aligned Plastic Deformation**," Journal of Microelectromechanical Systems, vol. 15, no. 3, June 2006, pp.553-562.

5. H. Choo, R. Kant, D. Garmire, J. Demmel, and R. S. Muller, "**Fast, MEMS-Based, Phase-Shifting Interferometer**," Journal of Microelectromechanical Systems (Submitted and Being Reviewed).

6. D. Garmire, H. Choo, R. S. Muller, S. Govindjee, and J. Demmel, "**MEMS Process Characterization with an on-Chip Device**," Journal of Microelectromechanical Systems (In Preparation).

7. H. Choo and R. S. Muller, "**Optical Properties of Microlenses Fabricated Using Hydrophobic Effects and Polymer-jet-printing Technology**," Optics Letters (In Preparation).

Reviewed Conference Proceedings and Presentations

1. H. Choo, R. Kant, D. Garmire, J. Demmel, and R. S. Muller, "**Fast, MEMS-Based, Phase-Shifting Interferometer,**" Solid-State Sensor and Actuator Workshop, June 4-8, 2006, pp.94-95, Hilton Head, SC USA (Late News Oral Presentation).

2. D. Garmire, H. Choo, R. S. Muller, S. Govindjee, and J. Demmel, "**MEMS Process Characterization with an on-Chip Device**," 2006 Nano Science and Technology Institute Nanotech, May 8-11, 2006, Boston, MA USA (Oral Presentation).

3. D. Garmire, H. Choo, R. S. Muller, S. Govindjee, and J. Demmel, "**Device for in situ Electronic Characterization of MEMS Applicable to Conducting Structural**

Materials," Material Research Symposium 2006 Spring Meeting, April 17-20, 2006, San Francisco, CA USA (<u>Oral Presentation</u>).

4. H. Choo, D. Garmire, J. Demmel, and R. S. Muller, "**A Simple Process to Fabricate Self-Aligned, High-Performance Torsional Microscanners: Demonstrated Use in a Two-Dimensional Scanner**," 2005 IEEE/LEOS International Conference on Optical MEMS and Their Applications, August 1-4, 2005, pp. 21-22, Oulu, Finland (<u>Oral Presentation</u>).

5. H. Choo and R. S. Muller, "**Addressable Microlens Array to Improve Dynamic Range of Shack-Hartmann Sensors**," Solid-State Sensor and Actuator Workshop, June 6-10, 2004, pp. 79-82, Hilton Head, SC USA (<u>Oral Presentation</u>).

6. H. Choo and R. S. Muller, "**Optical Properties of Microlenses Fabricated Using Hydrophobic Effects and Polymer-jet-printing Technology**," 2003 IEEE/LEOS International Conference on Optical MEMS and Their Applications, August 18-21, 2003, pp. 169-170, Kona, Hawaii USA (<u>Oral Presentation</u>).

7. K. Gupta, H. Choo, H. Kim and R. S. Muller, "**Micromachined Polarization Beam Splitters for the Visible Spectrum**," 2003 IEEE/LEOS International Conference on Optical MEMS and Their Applications, August 18-21, 2003, pp. 171-172, Kona, Hawaii USA (<u>Oral Presentation</u>).

8. J. B. Kim, H. Choo, L. Lin and R. S. Muller, "**Microfabricated Torsional Actuator Using Self-Aligned Plastic Deformation**," TRANSDUCERS 2003, The 12th International Conference on Solid-State Actuators, Sensors, and Microsystems, June 5-10, 2003, pp. 1015-1018, Boston, MA USA (<u>Oral Presentation</u>).

Appendix II: Non-Provisional US and International Patent List

1. H. Choo, D. Garmire, J. Demmel, and R. S. Muller, "**CMOS-compatible high-performance microscanners, including structures, high-yield simplified fabrication methods and applications**," US Patent Application Number: 20070026614 (Pending).

2. H. Choo, and R. S. Muller, "**Optical system applicable to improving the dynamic range of Shack-Hartmann sensors**," US Patent Application Number: 20050275946 (Pending).

3. H. Choo, and R. S. Muller, "**Optical switch using frequency-based addressing in a microelectromechanical systems array**," US Patent Application Number: 20060262379 (Pending).

4. H. Choo, D. Garmire, R. Kant, J. Demmel, and R. S. Muller, "**Fast, MEMS-Based, Phase-Shifting Interferometer**," UC Case Number: B06-136-1 (Pending).

5. D. Garmire, H. Choo, S. Govindjee, J. Demmel, and R. S. Muller, "**Integrated MEMS Metrology Device Using Complementary Measuring Combs**," UC Case Number: B06-028 (Pending).